Titre: Title:	Quantification de la microstructure de la moelle épinière humaine par IRM et application chez des patients avec sclérose en plaques
Auteur: Author:	Tanguy Duval
Date:	2017
Type:	Mémoire ou thèse / Dissertation or Thesis
Référence: Citation:	Duval, T. (2017). Quantification de la microstructure de la moelle épinière humaine par IRM et application chez des patients avec sclérose en plaques [Thèse de doctorat, École Polytechnique de Montréal]. PolyPublie. https://publications.polymtl.ca/2871/

URL de PolyPublie: PolyPublie URL:	https://publications.polymtl.ca/2871/
Directeurs de recherche: Advisors:	Julien Cohen-Adad, & Eric C. Klawiter
Programme: Program:	Génie biomédical

UNIVERSITÉ DE MONTRÉAL

QUANTIFICATION DE LA MICROSTRUCTURE DE LA MOELLE ÉPINIÈRE HUMAINE PAR IRM ET APPLICATION CHEZ DES PATIENTS AVEC SCLÉROSE EN PLAQUES

TANGUY DUVAL

INSTITUT DE GÉNIE BIOMÉDICAL

ÉCOLE POLYTECHNIQUE DE MONTRÉAL

THÈSE PRÉSENTÉE EN VUE DE L'OBTENTION

DU DIPLÔME DE PHILOSOPHIÆ DOCTOR

(GÉNIE BIOMÉDICAL)

OCTOBRE 2017

UNIVERSITÉ DE MONTRÉAL

ÉCOLE POLYTECHNIQUE DE MONTRÉAL

Cette thèse intitulée :

QUANTIFICATION DE LA MICROSTRUCTURE DE LA MOELLE ÉPINIÈRE HUMAINE PAR IRM ET APPLICATION CHEZ DES PATIENTS AVEC SCLÉROSE EN PLAQUES

présentée par : DUVAL Tanguy

en vue de l'obtention du diplôme de : Philosophiæ doctor

a été dûment acceptée par le jury d'examen constitué de :

M. STIKOV Nikola, Ph. D., président

M. COHEN-ADAD Julien, Ph. D., membre et directeur de recherche

M. KLAWITER Eric C., MD, membre et codirecteur de recherche

M. LESAGE Frédéric, Ph. D., membre

Mme TARDIF Christine, Ph. D., membre externe

DÉDICACE

À Naïn et Thérèse,

À Djadjo et Jean,

REMERCIEMENTS

Je souhaite en premier lieu remercier mon directeur de recherche, Julien Cohen-Adad, pour m'avoir fait confiance et m'avoir largement soutenu et accompagné. Merci de m'avoir introduit ainsi à la communauté d'imagerie par résonance magnétique, et d'avoir créé cet écosystème novateur et dynamique qui m'a servi à atteindre mes objectifs. Nous n'avons pas chômé, c'était passionnant, merci mille fois.

Je remercie aussi Nikola Stikov et Jennifer Campbell, mes premiers collaborateurs pour leur accueil si chaleureux.

Merci à Eric Klawiter, mon co-directeur, pour son accueil et sa générosité pendant mon stage à Boston. Merci aux collègues de Boston, notamment Jason et Amanda de m'avoir hébergé.

Merci aux étudiants du laboratoire Neuropoly, de Yves Goussard et de Frédéric Lesage pour avoir amené la bonne humeur. Merci à Corentin, Marion, Mahsa, Qinyi, Benjamin, Benjamin bis, Ryan, Nibardo, Alex, Simon et Gabriel. Merci aussi à Jean-François, Marc, Amélie, William, Geoffrey, Paolantonio, Tanguy 2, Costas, Ritesh et William bis. Merci à Julien, Paul, Sid, Thomas, Tom et Pierre-Louis. Merci enfin à Grégoire, Tung, Victor, Camille, Charley Gros, Sara, Mr. Bean, Banniii, Tommy, Darya, Ilana, Mathieu, Jean-François, Maxime, Alexandre, Dodominique, Agah, Pascale, Atef, Aldo, Ariane, Christian, Georges, Ian… et les autres.

Merci à mes collaborateurs pour tous ces échanges : le groupe d'Aviv Mezer à Tel Aviv, de Rachid Deriche à Sophia-Antipolis, de Virgnie Callot à Marseille, de Bruce Pike à Montréal, de Maxime Descoteaux à Sherbrooke, de Noam Shemesh à Lisbonne, de Yogesh Rathi à Boston.

Merci aux collègues internationaux d'avoir égayer les conférences. Je tiens à rendre hommage au bon esprit de la communauté d'IRM, où la coopération, le partage, et la franchise sont de mise.

Merci à Yves de m'avoir éclairé sur les problèmes de maths. Merci à Philippe, Frédéric, Caroline, pour les problèmes d'imagerie d'IRM et d'optique. Merci à tous les collaborateurs qui ont permis l'histologie à grand champ de vue de la moelle, notamment Micheline, Philippe et Diane.

Merci finalement à ma chère Michelle pour avoir rendu ces années heureuses.

Beaucoup de monde sont passés au cours de ces 4 années, et beaucoup resterons des amis fidèles.

RÉSUMÉ

Les pathologies dégénératives de la moelle épinière sont encore aujourd'hui mal diagnostiquées et laissent les patients dans un état de souffrance et de doute. L'imagerie par résonance magnétique (IRM) permet d'obtenir des informations quantitatives sur la microstructure de la matière blanche. Nous avons démontré la faisabilité d'estimer la densité et le diamètre des axones dans la moelle épinière humaine en utilisant une IRM unique au monde installée à Boston, le "scanner Connectom", capable d'atteindre des gradients de champ magnétique de 300mT/m. Cependant cette méthode ne donne qu'une information partielle de la microstructure de la matière blanche et ne tient pas compte de la gaine de myéline entourant les axones. Cette gaine de myéline permet d'assurer une bonne conductivité des axones et peut dégénérer dans certaines pathologies comme la sclérose en plaques. Nos collaborateurs de l'université McGill ont proposé de combiner cette technique avec l'IRM quantitative de la myéline afin de mesurer son g-ratio, ou ratio du diamètre interne sur externe de la myéline. Durant cette thèse, j'ai mis en place les techniques d'IRM de la microstructure, j'ai validé ces méthodes en utilisant l'histologie à large champ de vue, puis je les ai appliquées chez des patients avec sclérose en plaques pour une application clinique.

ABSTRACT

Degenerative pathologies of the spinal cord are still difficult to diagnose today, leaving patients in a state of constant suffering and constant doubt about their future. Magnetic Resonance Imaging (MRI) can gather quantitative information about the white matter microstructure by playing on the phase and relaxation of the spins. Using a unique MRI system capable of magnetic gradients of 300mT/m, the "Connectom scanner", we showed that neuronal fibers (axons) density and diameter can be measured in the human spinal cord *in vivo* using diffusion MRI. Although very informative, this method only provides a partial description of the tissue and no direct information about the myelin sheath that surrounds the axons is extracted. The myelin sheath improves the speed and frequency of action potentials that are transmitted through the axons, and an alteration of myelin integrity leads to paralysis in diseases such as multiple sclerosis. Our collaborators at McGill University proposed to combine the diffusion technique with quantitative myelin imaging technique in order to measure the thickness of the myelin sheath. In this thesis, I developed quantitative MRI techniques in the spinal cord, I validated these methods using large-scale histology, and I applied them on patients with multiple sclerosis.

TABLE DES MATIERES

DÉDICACE III

REMERCIEMENTS IV

RÉSUMÉ VI

ABSTRACT VII

TABLE DES MATIERES VIII

LISTE DES TABLEAUX XIII

LISTE DES FIGURES XIV

LISTE DES SIGLES ET ABREVIATIONS XXVII

CHAPITRE 1 INTRODUCTION 1

CHAPITRE 2 REVUE CRITIQUE DE LA LITTÉRATURE 3

2.1 Anatomie et cytoarchitecture de la moelle épinière 3

2.1.1 Système anatomique de référence 3

2.1.2 Anatomie de la moelle épinière 3

2.2 Imagerie par résonance magnétique 6

2.2.1 Spin et moment magnétique 6

2.2.2 Pondération en T1, T2 ou bien en densité protonique 8

2.2.3 De la RMN à l'IRM 10

2.2.4 Séquence IRM 11

2.2.5 La RMN sensible à la diffusion 14

2.2.6 Limitations et sujets de recherche 16

2.3 Article 1: Modeling white matter microstructure 19

2.3.1 Introduction 20

2.3.2 White matter microstructure 22

2.3.3 Quantitative MRI modalities 26

2.3.4 Challenges 34

2.3.5 Performance of quantitative MRI metrics 37

2.3.6 Example of quantitative MRI images 42

2.3.7 Concluding remarks 44
2.3.8 Acknowledgments 44
2.3.9 References 45

CHAPITRE 3 DÉMARCHE DE L'ENSEMBLE DU TRAVAIL 54

CHAPITRE 4 ARTICLE 2: IN VIVO MAPPING OF HUMAN SPINAL CORD MICROSTRUCTURE AT 300 MT/M 59

4.1 Introduction 61
4.2 Methods 64
4.2.1 Acquisition 64
4.2.2 Preprocessing 67
4.2.3 Motion Correction 67
4.2.4 Model fitting 70
4.2.5 Post-processing 71
4.2.6 Statistics 73
4.3 Results 75
4.3.1 Quality of the data 75
4.3.2 SNR analysis 78
4.3.3 Quality of q-space Fitting 80
4.3.4 Mapping of axon diameter 82
4.3.5 Orientation dependence and reproducibility 85
4.4 Discussion 87
4.4.1 Interpretation of axon diameter maps 87
4.4.2 Acquisition and preprocessing 91
4.4.3 Diffusion model 94
4.4.4 Applications and future work 98
4.5 Conclusion 99
4.6 Bibliography 100
4.7 Supplementary Material 106

CHAPITRE 5 ARTICLE 3: G-RATIO WEIGHTED IMAGING OF THE HUMAN SPINAL CORD *IN VIVO* 115

5.1 Introduction 117

5.2 Methods 120
5.2.1 Acquisition 120
5.2.2 Preprocessing 122
5.2.3 Metric quantification 125
5.2.4 Effect of spinal cord curvature 127
5.2.5 Template registration and atlas-based analysis 128
5.3 Results 129
5.3.1 SNR and noise analysis 129
5.3.2 Effect of spinal cord curvature 130
5.3.3 Registration 131
5.3.4 Quantitative MRI metric mapping 132
5.3.5 Tract-by-tract analysis 136
5.4 Discussion 138
5.4.1 Comparison with histology 138
5.4.2 Myelin versus macromolecular volume fraction 140
5.4.3 Reproducibility of quantitative metrics 141
5.4.4 Comparison with previous work 143
5.4.5 Interpretation of g-ratio measurements 145
5.5 Conclusion 149
5.6 Acknowledgements 149
5.7 Bibliography 150
5.8 Supplementary Material 157
CHAPITRE 6 ARTICLE 4: SCAN-RESCAN OF AXCALIBER, MACROMOLECULAR TISSUE VOLUME AND G-RATIO IN THE SPINAL CORD 158
6.1 Introduction 159
6.2 Methods 162
6.2.1 Acquisition 162
6.2.2 Processing 162
6.2.3 Statistics 163
6.3 Results 165
6.4 Discussion 167
6.4.1 Voxel-wise correlation 168

6.4.2 Intra-Class Correlation Coefficient 168
6.4.3 Laterality difference 169
6.4.4 Model assumptions 169
6.4.5 Data quality 170
6.4.6 Applicability of the results 170
6.5 Conclusion 171
6.6 References 172
6.7 Supplementary Material 175
6.7.1 Supporting Information S1: ANOVA 175
6.7.2 Supporting Information S2: Simulation of the impact of diffusion model assumptions on repeatability and accuracy 176

CHAPITRE 7 ARTICLE 5: VALIDATION OF QUANTITATIVE MRI METRICS USING FULL SLICE HISTOLOGY WITH AUTOMATIC AXON SEGMENTATION 180
7.1 Introduction 181
7.2 Methods 183
7.2.1 Tissue preparation 183
7.2.2 MRI acquisition 183
7.2.3 Histology 186
7.2.4 Voxel-wise comparison 187
7.3 Results 188
7.4 Discussion 191
7.5 Acknowledgments 192
References. 193

CHAPITRE 8 HISTOLOGIE A GRANDE ECHELLE DE LA MOELLE EPINIERE HUMAINE : UNE ANATOMIE DETAILLEE DE LA MICROSTRUCTURE 197
8.1 Introduction 199
8.2 Méthodes 202
8.2.1 Préparation du tissue 202
8.2.2 Microscopie 206
8.2.3 Traitement d'image 206
8.2.4 Statistiques 209

Résultats 209
8.2.5 Imagerie de la moelle entière 209
8.2.6 Morphologie axonale dans des petites régions 211
8.2.7 Cartes de la microstructure 215
8.2.8 Analyse basée sur l'atlas 217
8.3.1 Modèle de microstructure 223
8.4 Discussion 224
8.4.1 Interprétation 224
8.4.2 Limitations de la méthode 225
8.5 Conclusion 229
8.6 Remerciements 229
8.7 Matériel supplémentaire 230
8.7.1 S1 : Correction des valeurs aberrantes de l'algorithme de collage 230
8.7.2 S2 : Correction de AxonSeg 231
CHAPITRE 9 TRANSLATION CLINIQUE 234
9.1 600 mT/m par rapport au protocole optimisé 80 mT/m 234
9.1.1 Méthodes 234
9.1.2 Résultats 236
9.1.3 Conclusion 239
9.2 Application sur un patient atteint de sclérose en plaques 240
9.2.1 Méthodes 240
9.2.2 Résultats 241
9.2.3 Conclusions 242
9.2.4 Références 243
CHAPITRE 10 DISCUSSION GÉNÉRALE 245
CHAPITRE 11 CONCLUSION ET RECOMMANDATIONS 249
BIBLIOGRAPHIE 251

LISTE DES TABLEAUX

Table 4.1: SNR computed per subject and per vertebral level at b=0 and b=39,011 s/mm^2 (b_{max}) 79

Table 4.2: Goodness of fits using $\chi red2$ statistics. α represents the probability that our data are well described with the AxCaliber model (the higher the better). 80

Table 5.1: Fitting parameters used in the interior-point algorithm, with initialization and boundaries 126

Table 5.2: SNR and L (non-central χ parameter) values for each subject 129

Table 5.3: White matter normative values. Mean value, standard deviation within the white matter (computed per subject and then averaged), the standard deviation across subjects (of the mean white matter values obtained per subject) and the resulting coefficient of variation (COV) across subjects (STD across subjects divided by the mean). 135

Table 6.1: Review of the scan-rescan studies in the spinal cord and brain white matter. ..161

Tableau 8.1: Liste des échantillons. C: niveau cervical, T: niveau thoracique et L: niveau lombaire. Lorsque plusieurs tranches ont été extraites au même niveau, les lettres A, B et C ont été utilisés avec A la tranche la plus rostrale. 204

LISTE DES FIGURES

Figure 2.1: Système anatomique de référence. 3

Figure 2.2: tranche axial de moelle épinière..... 4

Figure 2.3: voies spinales (ou tractus) de la moelle épinière humaine. ©Polarlys and Mikael Häggström, 2010. Reproduit avec permission. 5

Figure 2.4: spin ayant un mouvement de précession autour d'un champ magnétique B_0. ..7

Figure 2.5: exemple de pondération, souvent les tissus ayant des T_2 longs ont des T_1 court et inversement, c'est pourquoi, les images ont des contrastes inversés..... 9

Figure 2.6: Image pondérée en densité protonique.....10

Figure 2.7: Exemple de détermination axonale par IRM a diffusion. a. b. c. les courbes obtenues expérimentalement du signal reçu en fonction de q. d. carte de la provenance des signaux. e. Probabilité de distribution axonale par zone. (McNab, et al., 2013). Reproduit avec permission..... 17

Figure 2.8: Modeling of the white matter tissue. a. Transmission electron microscopy of an axial slice of white matter fiber bundles extracted from the corpus callosum of a mouse (West et al., 2016a). b. Schematic representation of the white matter. c. Proportions of the different white matter tissue components. The top left pie chart divides white matter into two general components: water (blue) (the component that produces the MRI signal) and lipids/macromolecules (red). The top right pie chart divides white matter into three spaces (used in diffusion and myelin imaging models): the myelin sheath (purple), the extra-axonal volume (yellow) and the intra-axonal volume (green). The bottom pie chart subdivides these three spaces into water and lipid/macromolecular content. d. Definitions of most commonly used MRI (gray boxes) and tissue modeling (light blues boxes) metrics and their rough values..... 25

Figure 2.9: Diffusion reveals the underlying microstructure of the tissue. The diffusion of a drop of ink on isotropic (left) or anisotropic (right) fibrous tissue is Gaussian and can be modeled with an ellipse. The main axis of this ellipse (horizontal axis in this case)

defines the main direction of the fibers that form the tissue. The ratio between the main and the secondary axis defines the degree of anisotropy of the paper. Similarly, diffusion in the white matter tissue is modeled with an ellipsoid in diffusion tensor imaging experiments. This figure was inspired by Dr Gordon Kindlmann (University of Chicago)..... 27

Figure 2.10: Timeline for encoding the diffusion of the water molecules in MRI. Just after being excited, the position of each molecule is tagged based on the phase of its spins, by applying gradient #1 (parametrized by its strength G and duration δ). During a time Δ, the spins (illustrated by small circles) move (due to Brownian motion or convection). The longer the time Δ is, the further the molecules can move. A second and identical gradient is applied to quantify this displacement through a signal loss in the MR response. 28

Figure 2.11: MRI signal as a function of b-value in voxels presenting Gaussian (left) or non-Gaussian (right) diffusion of water molecules. While conventional diffusion MRI assumes Gaussian diffusion characterized by dependence on the b-value only, diffusion perpendicular to neuronal fibers (right) is non-Gaussian, which allows the extraction of additional microstructural information such as axon diameter..... 30

Figure 2.12: Example of multi-parametric quantitative MRI maps of a multiple sclerosis patient. Myelin volume fraction (MVF) was obtained using a qMT (Henkelman et al., 1993), axon volume fraction (AVF) was computed using the NODDI model (Zhang et al., 2012), and g-ratio was calculated from AVF and MVF (Stikov et al., 2015a). Conventional FLAIR contrast indicates the presence of three hyperintense lesions. These lesions are associated with a reduction in MVF and AVF, but only one lesion show an abnormal g-ratio (>0.8). 42

Figure 2.13: A comparison of ex vivo quantitative MRI maps with histology. Once segmented, histology can provide mean axon diameter or myelin volume fraction in a voxel. Visually, MRI and histology are in agreement, supporting the sensitivity of MRI to these specific microstructural properties. 43

Figure 3.1: Structure de la thèse..... 58

Figure 4.1: Placement of slices (yellow), saturation bands (red) and shimming volume (green). Four slices were placed in the middle of the vertebral body at levels C1, C2, C3 and C4, by adjusting the slice gap for each subject. Slices were orthogonal to the SC. Optimal shim coefficients (up to 2nd order) were calculated within a small box encompassing the spinal cord. To prevent aliasing associated with reduced FOV, two saturation bands were prescribed anteriorly and posteriorly. 65

Figure 4.2: Illustration of the diffusion encoding gradients used in the AxCaliber protocol (a) and in the protocol for probing orientation dependence (b). The latter protocol aims at exploring fibers that are not oriented along Z (e.g., collateral fibers entering the dorsal aspect of the cord)..... 66

Figure 4.3: Examples of DW images with selected b-values in the lowest range ($430<b<4000$ s/mm^2) used for motion correction. These images offer sufficient SNR for robust estimation of motion parameters without CSF contamination. 68

Figure 4.4: Estimated motion in anteroposterior direction (raw moco) and fitted spline functions (smooth moco) at each cervical level in one subject. All data with different Δ were concatenated. Here, "moco" stands for motion correction..... 69

Figure 4.5: a: Mean high b-values images. b: image of the template used for registration. c: registered image after applying the deformation field. d: Five major axonal pathways with different morphological features were selected from the white matter atlas in order to extract model-based diffusion MRI metrics..... 72

Figure 4.6: Example of images acquired at different q-vectors. Data are not interpolated. Contrast is kept the same for better comparison. Notice the low SNR at very-high q-value (orange), which was compensated by averaging over the four directions. 75

Figure 4.7: Data averaged along q-values in one subject (excluding images acquired at $b < 430$s/mm^2), before and after applying the correction for eddy-currents and subject motion. 76

Figure 4.8: Top: Rician corrected q-space data in one voxel of the spinal cord white matter for one subject before LPCA correction (normalized by b=0). Bottom: same data averaged over the four directions. The purple dashed box shows the data collected for probing the orientation dependence (see Figure 2.b.). 77

Figure 4.9: Standard deviation of noise along q (blue curve) in one voxel and one subject before LPCA correction. Values are shown as percentage of the b=0 signal. This estimated noise includes thermal and physiological noise. Notice that the standard deviation is fairly constant along q. 78

Figure 4.10: a: Cuneatus (blue), gracilis (yellow) and rubrospinal (red) tracts highlighted on the mean DWI in one subject. b. Histological images of axons stained for myelin (luxol fast blue cross) over corresponding pathways of a human spinal cord ("Histology at the University of Michigan," n.d.), reproduced with permission. c. Model fitting on signal decay acquired in one subject on a single voxel in the corresponding regions. 81

Figure 4.11: Maps of fitted parameters using single diameter model. Data histograms with range and mean value are shown at the bottom. The black arrows points to the posterior funiculus,..... 82

Figure 4.12: Top left: Mean DWI with overlay of ROIs for computing parameters within specific white matter tracts. Top right: Bar graph showing estimated axon diameter within tracts, laterality and subject. The estimated axon diameters range between 3.5 and 5.5 μm, suggesting fairly precise estimate of axon diameters on an individual basis. Bottom table: Estimated parameters averaged across subjects. Mean axon diameter was 3.51 (+/-0.54), 4.15 (+/-0.46) and 3.71 (+/- 0.36) μm in the gracilis, cuneatus and spinothalamic tracts, respectively. The restricted water fraction (1-fh), which correlates with axon density, was 55% and 44% (+/- 2%) in the cuneatus and spinothalamic tracts, respectively. Results of the three-way ANOVA show a significant effect of pathway and subjects but no effect for laterality..... 84

Figure 4.13: Difference in axon diameter estimated using two sub-sets of data with orthogonal diffusion gradient direction (X,Y;-X,-Y) and (-X,Y; X,-Y) in one subject.

Symmetrical differences (red versus blue) are observed in the lateral region (especially at C1 and C2), which could be attributed to the presence of collateral fibers. 85

Figure 4.14: a. q-space sampling for orientation dependence study. b. Signal at different gradient orientations, which was detrended using cosines into a function representing the signal variation as a function of gradient orientation ("orientation dependence" plot). c. Directions of collateral fibers averaged across subjects at level C2. This map was obtained by extracting the angular value corresponding to the highest diffusion (i.e. lower signal). d. Corresponding map of orientation dependence obtained using the peak-to-peak amplitude from the orientation dependence plot. 86

Figure 4.15: Comparison of AxCaliber results with two histological resources. Left: Optical images (50x50μm^2) of human thoracic spinal cord ("Histology at the University of Michigan," n.d.), reproduced with permission. Middle: Cytoarchitecture of human spinal cord white matter at vertebral levels C1 and C5 (Nieuwenhuys et al., 2007), reproduced with permission. Axon size is gray-level coded (the darker the bigger). Note that this representation of axon diameter is qualitative. Notice that some tracts have monodisperse axonal sizes (e.g. spinocerebellar and gracilis), while others present some super-axons surrounded by tiny axons (e.g. Pyramidal tracts). For direct comparison, AxCaliber results (averaged over five subjects) are overlaid on the right portion of the cytoarchitecture map at the corresponding levels (note: given that we did not acquire lower than C4, the C4 level is shown next to the C5 level from the cytoarchitecture map). Regions corresponding to the optical imaging panel are circled on the AxCaliber maps: gracilis (yellow), cuneatus (blue), rubrospinal (green) and spinocerebellar (red). 89

Figure 4.16: χ_{red}^2 histograms (top) and maps (bottom) in one subject per vertebral level. Values close to 1 (blue) represent the best fits. Values are smaller than 1.5 (red), which shows that all fitting errors were close to the noise standard deviation. 106

Figure 4.17: Example of fits at extreme **α**-values for two voxels in the white matter (each plot corresponds to one voxel). The right plot shows overfitting at Δ=50ms and underfitting at Δ=20ms for high q-values (>0.08μm^{-1}) 107

Figure 4.18: Histograms of mean axon diameter in spinal cord white matter for each subjects with m. Bottom right: Maps of estimated axon diameter at vertebral level C4 for each subject. All histograms present a dominant peak centered at around 4μm. 108

Figure 4.19: Results of the analysis using Gaussian Phase Distribution (GPD) approximation. Top left: Mean DWI with overlay of ROIs for computing parameters within specific white matter tracts. Top right: Bar graph showing estimated axon diameter within tracts, laterality and subject. Bottom table: Estimated parameters averaged across subjects. Overall, axon diameters estimated with GPD approximation were greater than that with the short pulse approximation (6.00μm versus 3.89μm in average between subjects and tracts). Fraction of hindered compartment was similar between models although the standard deviation was higher using the GPD model (0.08 versus 0.01). 110

Figure 4.20: Effect of maximal gradient strength on AxCaliber results with maximal gradient strength of 300mT/m (first column) versus 80mT/m (second and third column). Column three is equivalent to column two except that colorbars were rescale for more clarity. Top row: Axon diameter maps at C2 vertebral level. Bottom row: Fraction of hindered water maps. 111

Figure 4.21: Results of axon diameter estimation at Gmax = 80 mT/m. Top left: example of q-space fitting in the spinal cord white matter in one subject. right: Estimated axon diameter in five different tracts for each subject. Bottom left: Table showing the 3-way Anova results for estimated axon diameter. No significant differences between tracts were found at 80 mT/m (p=0.79, versus p=3.5x10^{-6} at 300mT/m). 112

Figure 4.22: Results of AxCaliber analysis using an additional free water compartment in the model. Top: Maps of estimated parameters averaged across the five subjects.

Bottom: bar plot showing estimated axon diameter per tract in each subject and results from the three-way ANOVA analysis. 113

Figure 5.1: Slices, shim box and saturation bands position on subject #4. 121

Figure 5.2: Illustration of the noise mask manually drawn on a slice of subject #5 at b = 5,050 s/mm^2 and b = bmax = 34,357 s/mm^2. Note that the high diffusion-weighting suppresses signal from CSF and fat, and thus allows to estimate the noise distribution close to the spinal cord..... 123

Figure 5.3: Non-central χ fitting of noise histogram for each subject. Noise was assessed on images acquired at b > 5,000 s/mm^2. Noise distribution was found to be Rician (L < 1.05 for all subjects). 129

Figure 5.4. Effect of the spinal cord's angle with respect to the slice-selection direction on diffusion metrics. a. angle values (in degree) for each subject (here, extracted at C3 for illustration purpose). b. Diffusion metrics fr and axon diameter averaged in the white matter (at levels C2 and C3) as a function of spinal cord angle (at C2-C3 disc). c. Illustration of two subjects (#3 and #4) with different spinal cord angle at the C3 disc location. 130

Figure 5.5: Registration result of the mean DWI to the template space. Subjects #6 (orange panel) and #4 (red panel) are presented here for illustration purpose. For each subject, the mean DWI was registered to the MNI-Poly-AMU white matter template (Blue panel) using a combination of affine and SyN transformations. Gracilis (blue), cuneatus (cyan), corticospinal (green), rubrospinal (orange) and spinothalamic (red) tracts are overlaid on the registered data for visualization purpose. Note that the mean DWIs shown here were generated using data acquired at b-values between 2,000 s/mm^2 and 20,000 s/mm^2 (also see the Methods section). 131

Figure 5.6: Maps of quantitative MRI metric averaged over nine subjects. Top: schematic cross-section of axons. Left: metrics obtained using MTV protocol. Middle: metrics obtained using diffusion MRI. Right: multimodal metrics combining myelin and diffusion measures. The gray matter was masked using the probabilistic template on

metrics where the model isn't adapted (mainly due to the orientation dispersion of the fibers). 133

Figure 5.7: Illustration of the quality of *fr* (left column) and MTV (right column) at C3 level on two representative subjects: one with a large (subject #7) and another with a small spinal cord (subject #5). The relatively high precision and good sensitivity of these two metrics is suggested by the low level of noise and strong contrast in the white matter, allowing us to distinguish the fasciculus cuneatus and lateral corticospinal tracts, even on a single-subject basis. 134

Figure 5.8: Tract-by-tract analysis of quantitative metrics. Metrics were extracted in five different tracts (color-coded) in the left and right hemispheres of the spinal cord. A three-way ANOVA analysis was done to assess reproducibility across tracts, laterality and subjects. 137

Figure 5.9: Comparison of axon diameter (left) and fr (right) between (Duval et al., 2015) and the current study (2016). Note that these maps were averaged across five subjects in the previous study (Duval et al., 2015) and seven other subjects in the current study. 144

Figure 5.10: Voxel-wise comparison of subject-averaged MTV and fr metrics in the white matter with lines of constant g-ratio. The grayscale encodes for voxel count. The two different MRI metrics seem to tend toward a constant g-ratio. 147

Figure 5.11: Results per tract of quantitative metrics (T1, MTV, *fr*, Dh, axon diameter, g-ratio). For each metric, the mean and the standard deviation across subjects were highlighted in red. Sensory tracts are highlight in blue and motor tracts in red. 157

Figure 6.1: Scan-rescan repeatability of the different quantitative metrics, assessed voxel-wise, in the template space, in the white matter. Bottom right. the correlation between MTV and fr seems to follow the line of iso-g-ratio g=0.75, thus reducing the dynamic of the g-ratio metric (achievable values are emphasized by the dashed box). 165

Figure 6.2: Intra-class correlation coefficient (ICC) assessed per tract using the atlas of spinal cord tracts. An ICC close to 1 shows the capability of the metric to detect differences between subjects. 166

Figure 6.3: Result of the three-way ANOVA (tracts, subjects, and laterality) for each metric along with the bar plot of metric values in each tract, and scan-rescan error. 167

Figure 6.4: *Result of the three-way ANOVA (tracts, subjects, and laterality) for each metric along with the bar plot of metric values in each tract, and scan-rescan error.* 175

Figure 6.5: Simulation of the impact of model assumptions (X-axis) on the fitted parameters (Y-axis) using qMRLab. In order to improve the precision of fitting parameters, the number of parameters is reduced by fixing some of them to a particular value (vertical dotted lines). Violation of these assumptions can introduce biases, illustrated by the deviation of the average fitted values (blue circles) from the ground truth (horizontal black lines), or reduce precision of the fitted values (blue error bars). 178

Figure 7.1. qspace sampling of the diffusion protocols. a. AxCaliber b. NODDI and ActiveAx 185

Figure 7.2: Optical image of the full spinal cord before (left) and after (right) myelin segmentation (color-coded for axon diameter). 186

Figure 7.3: Framework for the comparison of MRI quantitative metrics with histology. Histology was downsampled (a) by computing the average axonal metrics in 150x150µm2 pixels. Metrics were then registered on the MRI (b) using affine transform. MRI quantitative metrics (c) were compared with histology (d) voxel by voxel using Pearson correlation coefficient (e). 187

Figure 7.4: Quantitative MRI metrics mapping (left 2 columns) and histology mapping (right column). Top row: Axon diameter metrics. Middle row: Fraction of restricted water. Bottom row: FA and myelin volume fraction metrics. 188

Figure 7.5: Correlation matrix comparing histology (green) quantitative diffusion MRI metrics (orange) and quantitative myelin imaging (blue). Note the numbered cases.

Box 1 exhibits a high correlation (0.62) between histology and MRI for axon diameter. Box 2 presents a moderate correlation (0.48) between histology and MRI for the restricted fraction. Box 3 highlights the agreement between 2D and 3D sampled q-pace metrics. Box 4 highlights the link between diffusion and myelin imaging.....190

Figure 8.1. dissection de la moelle épinière. La moelle épinière a été entièrement exposée (à gauche) et une 24 tranches de un centimètre de moelle épinière ont été extraites et post-fixées (à droite).....202

Figure 8.2: Microtomie. Une lame en carbure de tungstène a été utilisé pour exposer la surface de la moelle épinière. L'angle de découpe a été ajusté afin d'éviter de couper plus profond que 100 microns. 205

Figure 8.3: Recalage de l'atlas (en bas à droite) vers l'histologie (« histo »). Le recalage a été estimé sur la base des masques de la matière blanche et grise de l'atlas (source) et histologie (destination). Plusieurs étapes ont été utilisées: affines, et de multiples déformations non linéaires régularisés avec BSplines (bspline-syn). La transformation inverse (de histo2atlas) utilise uniquement la déformation douce afin de maintenir la forme de la structure interne intacte. 208

Figure 8.4: Images MEB de moelle entières (recollées), acquises à une résolution allant jusqu'à 129 nm (à droite), et segmentées (code couleur pour diamètre axonal) en utilisant AxonSeg. La forme de la moelle épinière et de la matière grise correspond correctement à l'anatomie du Grays (Gray et al., 2005). 210

Figure 8.5: Extraction de l'information microstructurale. Suite à la détection de l'axone (c) et de la segmentation de la myéline (d) des images MEB (b), les coupes complètes (a) sont sous-échantillonnées en petits pixels de 100x100μm^2, où l'information morphologique est extraite (indiquée sur la droite).....211

Figure 8.6: images MEB de la moelle épinière dans trois régions différentes (rouge, vert et bleu), à trois niveaux différents de la colonne vertébrale (C3, T9 et L1). Les axones myélinisés peuvent être facilement distingués sur les images MEB.....212

Figure 8.7: Morphologie axonale en fonction du diamètre axonal dans trois régions de 1mm2 (code couleur en rouge pour spinocérébellar, vert et bleu pour gracilis pour faisceau cortico-spinal) de l'échantillon C5B. Tracés de gauche. La distribution des diamètres axonal ajustées en utilisant de multiples fonctions de probabilité (limite de résolution a été estimée à environ 1 µm, voir Figure 8.17). Milieu. Tracés de la densité volumique de fibres en fonction du diamètre axonal. Tracés de droite. g-Ratio en fonction du diamètre axonal. 214

Figure 8.8: Les cartes de microstructure axonale. Le diamètre moyen des axones (première colonne), la densité de 1-4µm (nombre d'axones par pixel de 100µm2) (deuxième colonne), de 4-8µm (troisième colonne), de 8-12µm (quatrième colonne), la densité des fibres (axones plus myéline) (cinquième colonne), et l'excentricité moyenne axonale (sixième colonne) dans des pixels de 100x100µm à différents niveaux de la colonne vertébrale (lignes). Ces cartes peuvent être comparés avec le dessin manuel de cytoarchitecture extrait de (Nieuwenhuys et al., 2007) (à gauche). 216

Figure 8.9: analyse basée sur l'atlas de la Figure 8.3 (s'y référer pour le nom des voies spinales). L'atlas de la substance blanche de la moelle épinière, construit à partir de l'anatomie de Gray (Gray et al., 2005) et disponible dans la boîte à outils de la moelle épinière SCT (Lévy et al., 2015), a été recallé sur les coupes histologiques afin d'extraire la morphologie axonale dans les différentes voies spinales. La répartition des diamètres moyen des axones (rangée du milieu) et la fraction volumique des fibres (rangée du bas) au sein du même voie spinale (code couleur) a été tracée. Les médianes (lignes rouges), avec l'intervalle de confiance de 95% (lignes noires) montrent que chaque tube présente des microstructures caractéristiques. La plupart des régions présentes des microstructures assez homogènes comme le montrent leur distribution étroite. 218

Figure 8.10: Cohérence de l'analyse basée sur un atlas à travers les différentes coupes de moelles (en utilisant les plus grands tractus, numérotés de 1 à 6 sur la Figure 8.9). La plupart des tranches du cervical sont fortement cohérents (r> 0,8) entre eux (par exemple C3 versus C2 à la ligne du haut). Cependant, C1 et les niveaux thoraciques

étaient moins consistants (par exemple C5 versus C1 à la rangée du bas), notamment en raison de la déformation de l'atlas particulièrement forte. 219

Figure 8.11: Evolution de la morphologie axonale le long de la moelle épinière. Les propriétés morphologiques ont été moyennées dans la matière blanche pour chaque échantillon (points bleus), et une fonction de lissage (ligne rouge) a été ajustée pour la visualisation des tendances. 221

Figure 8.12: Comparaison de la morphologie axonale dans la partie gauche et droite. Les différences de morphologie axonale entre voies gauche et droite sont très limitées : pour le diamètre axonale 0,01 um, 1% pour la densité axonale, et 0,4% pour le contenu de la myéline. 222

Figure 8.13: Modèle de la microstructure de la moelle épinière. Coronale (en haut) et vue axiale (en bas) du modèle généré. Les coupes histologiques ont été recalées au niveau des vertèbres correspondantes, puis interpolées entre des coupes à l'aide de déformations non-linéaires. Le modèle résultant présente des transitions en douceur entre les tranches. 223

Figure 8.14: Axon equivalent diameter overestimates the true axon diameter for axons that are not running along the spinal cord main axis. Oblique axons are filtered by AxonSeg based on the minor over major axis ratio of the axon to prevent dramatic failure... 227

Figure 8.15: la performance AxonSeg dans la matière grise. Similaire à la Figure 8.5, mais dans une région de la matière grise 228

Figure 8.16: Correction d'outliers de l'algorithme de collage de mosaïques. Mosaïque poste (des croix bleues), estimée à l'aide de l'algorithme de couture, a été trouvé pour être disposé dans une grille oblique (polarisation constante dans X et Y). Sur la base de cette hypothèse, les valeurs aberrantes peuvent être détectés (points rouges) et corrigés (croix verte). 230

Figure 8.17: Pipeline de correction AxonSeg en utilisant deux méthodes distinctes pour différentes mesures 232

Figure 8.18: Les parcelles Bland-Altman comparant la segmentation AxonSeg (après correction) avec la segmentation manuelle. La première courbe représente la corrélation linéaire tandis que la seconde courbe représente l'accord entre la Groundtruth et la segmentation. Le RPC est le coefficient de reproductibilité avec le pourcentage de la valeur à côté. Le CV est le coefficient de variation, qui est essentiellement l'écart-type des valeurs moyennes pour cent en forme. 233

Figure 9.1: Résultats de l'optimisation SOMA. Gauche. Convergence du CRLB pour le protocole optimisé. Droite. Écart-type et erreur sur 200 simulations pour différents SNR. 237

Figure 9.2: Comparaison expérimentale des mesures AxCaliber en utilisant des protocoles acquis à 600mT / m (colonne bleue), 80mT / m avec échantillonnage en grille de l'espace (| G |, Δ, δ) (colonne rouge) et 80mT / m optimisé (colonne verte). a. Visualisation des trois protocoles expérimentaux. b. exemple de fit dans un pixel de la matière blanche. c et d. cartes quantitatives avec (c) ou sans (d) estimation du diamètre axonal. 238

Figure 9.3: L'IRM quantitative est sensible aux lésions de SEP et permet de distinguer différents phénotypes. Haut. Fraction volumique de myéline (MVF) obtenue à partir de MTV. Milieu. Densité axonale obtenue à partir de l'IRM de diffusion en utilisant le modèle AxCaliber. Bas. Cartes pondérées par rapport au G obtenues en combinant la MVF et la densité axonale. Les flèches rouges mettent en évidence des valeurs anormales. 242

LISTE DES SIGLES ET ABREVIATIONS

AVF	Axon Volume Fraction
DWI	Diffusion-weighted images
δ	duration of the diffusion encoding gradients
Δ	Diffusion time (time delay between diffusion encoding gradients)
fr	Fraction of Restricted water
Gmax	Maximal magnetic gradient strength
FVF	Fiber Volume Fraction
Gmax	Maximal magnetic Gradient strenght
MTV	Macromolecular Tissue Volume
MVF	Myelin Volume Fraction
MS	Multiple Sclerosis
MRI	Magnetic Resonance Imaging
qMR	quantitative Magnetic Resonance
SC	Spinal Cord
SEP	Sclérose en plaques
STD	Standard Deviation

CHAPITRE 1 INTRODUCTION

La matière blanche de la moelle épinière est constituée de fibres nerveuses, appelées axones, et regroupées en différents tractus. Chaque tractus permet la transmission de signaux nerveux en provenance ou en direction d'une région spécifique du cerveau. Tout endommagement de ces axones, que ce soit d'origine pathologique ou accidentelle, peut entraîner une paralysie, un déficit sensoriel, ou des douleurs neuropathiques (Dijkers et al., 2009). Le pronostic des patients atteints de lésions médullaires dépend fortement du tractus endommagé (Rossignol et al., 2006) et, dans certaines pathologies, de la morphologie des axones endommagés : ainsi la sclérose en plaques affecte préférentiellement les petits axones (DeLuca et al., 2004), tandis que les maladies des neurones moteurs endommagent les gros axones en premier (Cluskey and Ramsden, 2001).

Pour diagnostiquer et pronostiquer l'évolution des patients atteints de lésions médullaires, l'IRM est souvent privilégiée. Cette méthode d'imagerie est particulièrement appréciée pour la qualité de ses images, son aspect non-invasif, son absence de rayonnement ionisants, et la multitude de contrastes disponibles (e.g. T1, T2, PD, FLAIR, STIR, DWI et beaucoup d'autres). Mais malgré ces atouts, il n'existe aujourd'hui que peu de liens entre l'activité des lésions observées par IRM conventionnelle et l'état clinique des patients (Guttmann et al., 1995; Rovira et al., 2013). Pour autant ceci n'est pas une fatalité, car l'IRM a un fort potentiel d'innovation, avec notamment le développement de l'IRM quantitative et multimodale, deux mots qui constituent les deux aspects clés de cette recherche. L'imagerie quantitative est une technique qui touche toutes les méthodes d'imagerie biomédicale (e.g. ultrason, tomographie par rayons X), et qui consiste à faire des mesures absolues des propriétés du tissue à partir des images, reproductibles entre les scans, et si possible avec une interprétation simple (e.g. élasticité, densité, volume d'eau). L'imagerie multimodale consiste à combiner plusieurs contrastes sensibles à différents phénomènes physiques, afin de gagner en spécificité ou sensibilité.

Ainsi, l'IRM permet l'obtention de contrastes différents souvent découverts de longue date lors d'expériences de spectroscopie par résonance magnétique nucléaire (RMN). Une de ces

application, déjà exploitée et largement médiatisée, est l'IRM fonctionnelle par effet BOLD (Singleton, 2009). Cette méthode a permis depuis 30 ans de localiser l'activité cérébrale et ainsi d'aider à comprendre l'organisation du cerveau. Au cours des prochaines décennies, l'IRM permettra aussi de visualiser l'architecture du cerveau, son réseau de fibres nerveuses (Johansen-Berg and Behrens, 2013), son réseau vasculaire (Schneider et al., 2006), la microstructure ou la composition moléculaire des tissus (Brandão and Domingues, 2004; Cohen-Adad and Wheeler-Kingshott, 2014; Tofts, 2003; Wu et al., 2016).

Ces méthodes, potentiellement révolutionnaires pour le pronostic des maladies neurodégénératives, sont rendues possible sur l'IRM humaine grâce aux récentes innovations technologiques qu'a observées l'IRM. L'amélioration des aimants (puissance et homogénéité du champ) et des antennes IRM, notamment par l'augmentation du nombre de canaux de réception et par leur plus grande proximité à la moelle (Keil et al., 2013), permet d'avoir suffisamment de signal pour atteindre des niveaux de détails inégalés (Cohen-Adad et al., 2012), jusqu'à environ 0.5mm isotropique. Mais une autre révolution technologique a eu un impact tout aussi important pour l'imagerie de la moelle : l'accélération des acquisitions par l'essor de l'echo planar imaging (Stehling et al., 1991), de l'imagerie parallèle (Griswold et al., 2002; Pruessmann et al., 1999), du simultaneous multi-slice (Barth et al., 2016; Saritas et al., 2014), et des techniques de réduction de champ de vue (Saritas et al., 2008; Wilm et al., 2007). Alors que les mouvements non rigides de la moelle et les variations spatiale et temporelle du champ magnétique (dûs aux différences de susceptibilité magnétique des os des vertèbres et de l'air des poumons) introduisaient des déformations importantes de l'image (Bammer and Fazekas, 2003; Verma and Cohen-Adad, 2014), celles-ci sont devenues négligeables avec l'accumulation de ces techniques. D'autre part, l'accélération des séquences permet désormais d'acquérir une multitude d'images et de contrastes différents en une seule session IRM, permettant ainsi de faire des mesures quantitatives et multimodales. Une introduction à la moelle et à l'IRM, suivie d'une revue des techniques quantitatives existantes et des problématiques associées est détaillée au prochain chapitre.

CHAPITRE 2 REVUE CRITIQUE DE LA LITTÉRATURE

2.1 Anatomie et cytoarchitecture de la moelle épinière

2.1.1 Système anatomique de référence

Le système anatomique de référence est nécessaire pour comprendre l'orientation des images médicales. La figure 1 montre les différents termes des plans anatomiques. Dans l'imagerie de la moelle épinière, le plan transversal, également appelé plan axial, est principalement utilisé en imagerie quantitative de la microstructure, car cette dernière varie principalement dans le plan transverse et présente une certaine cohérence le long de la moelle.

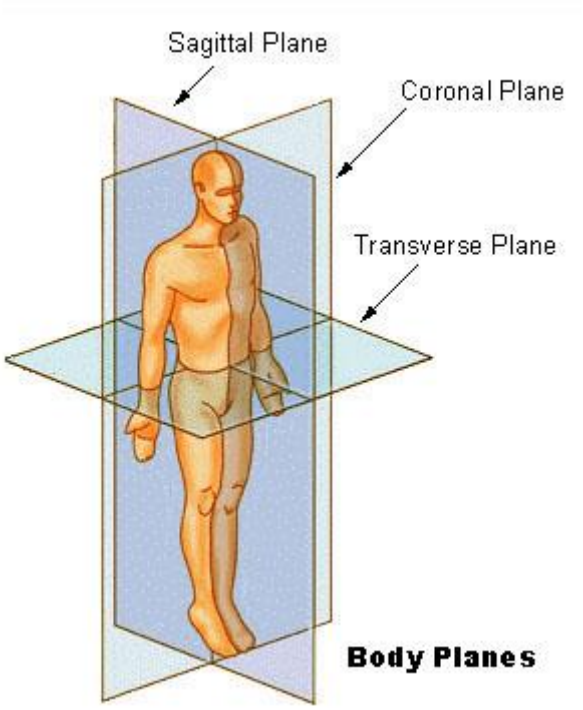

Figure 2.1: Système anatomique de référence.

2.1.2 Anatomie de la moelle épinière

La moelle épinière est composée de fibres neuronales qui relient le cerveau aux nerfs périphériques des organes et des muscles à travers les épines dorsales (ventral roots). Il est

protégé et encerclé par la colonne vertébrale et peut être segmenté par niveaux vertébraux (8 niveaux cervicaux, 12 thoraciques et 5 lombaires). Alors que la matière blanche (voir Figure 2) transmet l'information entre le cerveau et le reste du corps, la matière grise calcule l'information comme les réflexes musculaires.

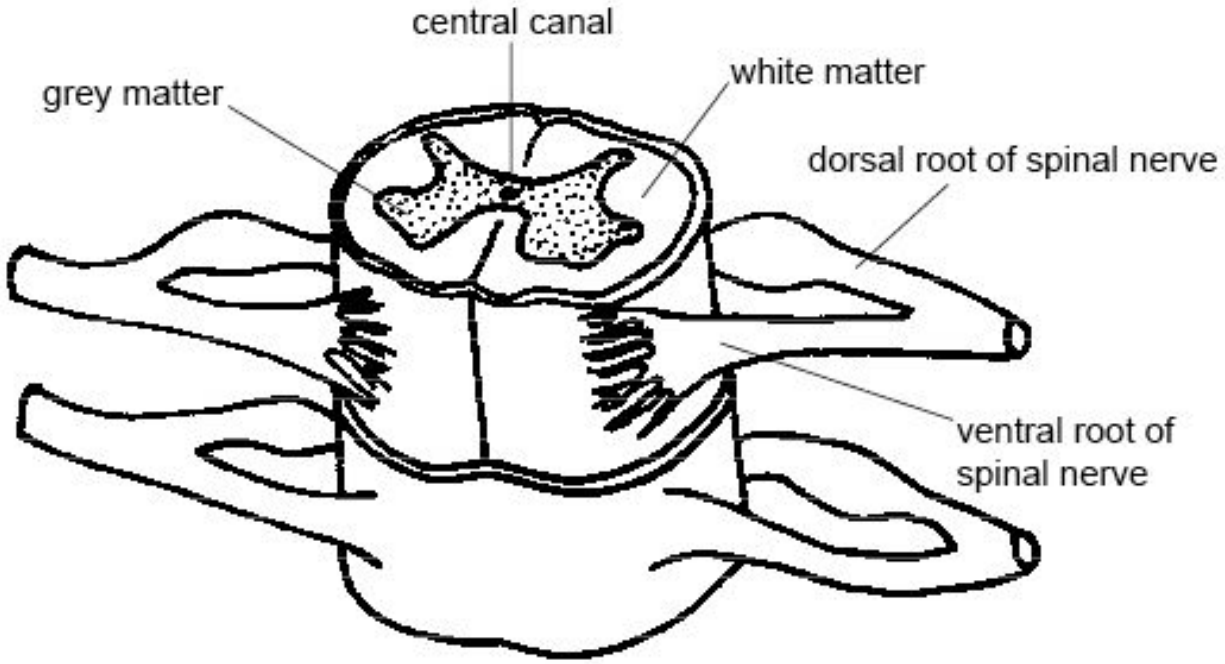

Figure 2.2: tranche axial de moelle épinière.

À une échelle plus petite (quelques millimètres), la moelle épinière peut être segmentée en différentes voies spinales, comme le montre la figure 3. Les voies motrices sont descendantes et leur nom se termine par «-spinal». Les voies sensorielles sont ascendantes et leur nom est composé de "spin-" suivi de la partie du cerveau à laquelle ils sont connectés. Ces différentes voies présentent une grande diversité de microstructures.

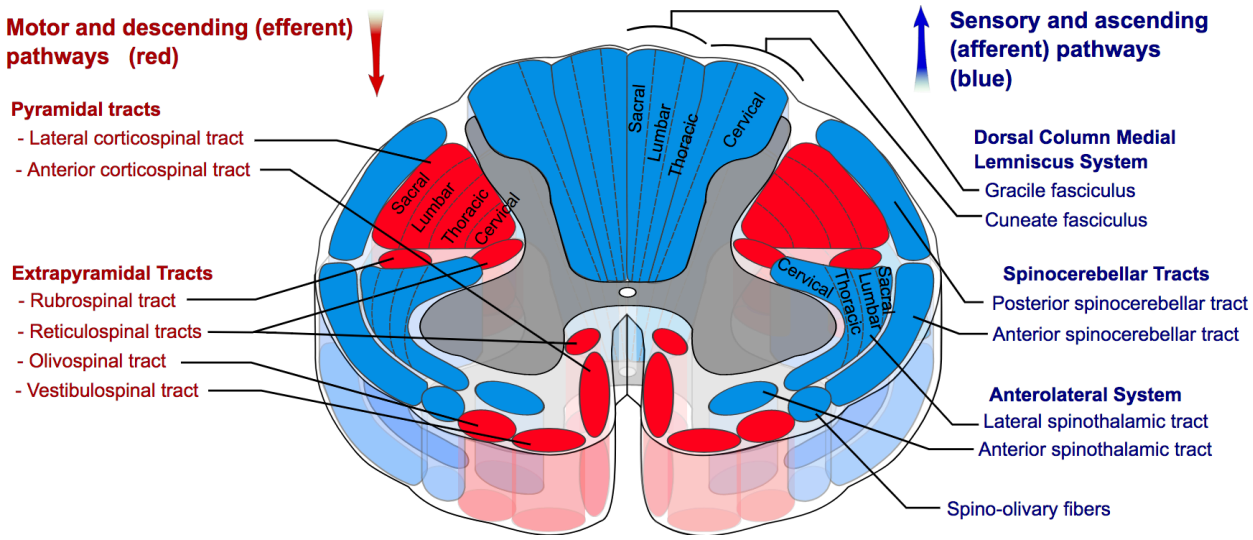

Figure 2.3: voies spinales (ou tractus) de la moelle épinière humaine. ©Polarlys and Mikael Häggström, 2010. Reproduit avec permission.

2.2 Imagerie par résonance magnétique

2.2.1 Spin et moment magnétique

La résonance magnétique nucléaire est une technique en développement depuis une cinquantaine d'années tandis que l'imagerie date des années 1970. Aujourd'hui, l'IRM est devenue une technique majeure de l'imagerie médicale moderne.

Lorsqu'un noyau possède un nombre impair de nucléons et du fait de la rotation individuelle et propre de ce nucléon célibataire, il possède un moment magnétique intrinsèque. On le représente par le vecteur d'aimantation $\boldsymbol{\mu}$**.** Au sein d'un corps biologique, c'est le noyau d'hydrogène présent dans les molécules d'eau qui en quantité suffisamment abondante pour présenter un intérêt.

Au repos, la résultante (somme des moments magnétiques) $\boldsymbol{M} = \sum \boldsymbol{\mu}$ est nulle. Lorsque les protons sont plongés dans un champ magnétique **B0**, leurs moments magnétiques de spin **μ** s'alignent localement sur la direction de **B0**. En pratique seulement deux positions sont possibles : chaque spin fait un angle α ou π – α avec le champ **B0**. Ces spins sont alors animés d'un mouvement de précession autour de **B0** à une fréquence précise dépendant directement de **B0**, la fréquence de Larmor :

$$\omega_0 = \gamma B_0$$

γ étant le rapport gyromagnétique spécifique à chaque noyau

L'orientation parallèle est la plus probable, car le niveau d'énergie est plus bas qu'en position antiparallèle. Ceci génère une résultante **M** orientée dans la direction du champ **B0** (Dugas-Phocion, 2006)**.**

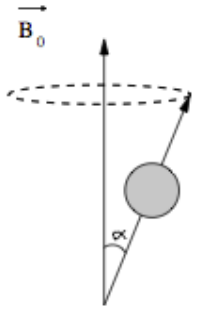

Figure 2.4: spin ayant un mouvement de précession autour d'un champ magnétique B_0.

Les scanners IRM sont constitués d'un champ permanent (de champ magnétique **B0** suivant un axe z). Ainsi les noyaux d'hydrogène ont un mouvement de précession autour de l'axe z. Le principe de l'IRM est de faire entrer en résonnance les protons d'hydrogène en appliquant une onde électromagnétique **B1** suivant l'axe x à la fréquence de Larmor. Le moment magnétique **M** décrit alors au cours du temps une spirale associé à un basculement.

Lorsque l'angle de bascule entre **Mz** et **Mxy** est de 90° (ou 180°) on parle d'une impulsion de 90° (ou 180°). Cet état est instable et dès la fin de l'excitation, il y a un phénomène de relaxation au cours duquel les phénomènes inverses vont avoir lieu. D'une part, la composante longitudinale **Mz** « repousse » progressivement et d'autre part, par déphasage des spins, la composante transversale va disparaitre.

Les spins sont spontanément en déphasage du fait des inhomogénéités de champs magnétique dans l'espace. En effet, selon l'environnement des protons, le champ **B0** sera plus ou moins important (« inhomogénéité d'origine moléculaire ») et, par conséquent les spins tourneront à des vitesses légèrement différentes ce qui induit un déphasage entre les spins. Le temps de relaxation transversale dépend donc directement du milieu moléculaire des protons et donc des différents tissus.

Le contraste des images va largement dépendre de ces temps caractéristiques de relaxation longitudinale (T1) et transversale (T2).

2.2.2 Pondération en T1, T2 ou bien en densité protonique

On réceptionne le signal pendant le phénomène de relaxation grâce à une antenne positionnée dans le plan xy, de manière à obtenir le signal associé à l'aimantation **Mxy**. En effet il est inutile de chercher à obtenir les variations d'amplitude du vecteur **Mz** car celles-ci sont noyées sous la puissance du signal du champ **B0**. On remonte à **Mz** en considérant le fait que la norme du vecteur **Mxy** est égale à celle de **Mz** lorsque les spins sont en phase (donc à la fin de l'impulsion RF).

Les temps de relaxation T1 et T2 sont en fait régis par l'équation de Bloch :

$$\frac{d\boldsymbol{M}}{dt} = \gamma(\boldsymbol{M}\times\boldsymbol{B}) - \frac{Mz - M0}{T1}\boldsymbol{k} - \frac{Mx\,\boldsymbol{i} + My\,\boldsymbol{j}}{T2}$$

où **i**, **j**, **k** sont les vecteurs du repère, **M0** norme du vecteur d'aimantation à l'équilibre, γ le rapport gyromagnétique, T1 la constante de temps de relaxation longitudinale et T2 la constante de temps de relaxation transversale.

On remarque que **Mz** repousse selon une exponentielle croissante (de constante de temps T1) tandis que **Mx** et **My** évoluent selon une exponentielle décroissante (de constante de temps T2).

Pendant une séquence d'acquisition IRM, on définit le temps de repousse (TR) entre deux émissions de pulses RF. Il correspond au temps que l'on laisse à **Mz** pour repousser. De plus on définit le temps d'écho (TE) le temps entre l'excitation par le signal RF et la lecture du signal reçu. Ces deux durées sont choisies par l'opérateur. Comme indiqué précédemment on mesure la composante transversale **Mxy** du signal émis par les spins. En jouant sur TR et TE on peut obtenir un contraste pondéré en T1, en T2 ou en densité protonique. En effet deux tissus distincts ont des temps T1 et T2 différents, ainsi qu'une densité protonique différente. Au bout d'un temps TR les vecteurs **Mz** n'auront pas atteint les mêmes valeurs de « repousse » dans tous les tissus. De même au bout d'un temps TE, les vecteurs **Mxy** n'auront pas diminué de la même valeur.

Pour un temps TR long il n'y aura pas de différence entre le signal du tissus L et le signal du tissus R qui n'ont pourtant pas la même constante T1. Par contre, si l'on réduit le temps TR,

la différence de signal entre le tissu R et L est significative. Autrement dit pour obtenir une image pondérée en T1 il faut un TR court. Le même raisonnement permet de conclure qu'il faut un TE long pour obtenir une image pondérée en T2. Mais cela ne suffit pas. Si on a un T1 court mais un TE long, les deux pondérations vont se mêler ce qui ne permettra pas de discriminer les tissus entre eux. Il faut donc, pour obtenir une pondération en T1, avoir non seulement un TR court mais aussi un TE court de manière à que les différences de constante de temps T2 n'ont pas le temps de s'exprimer.

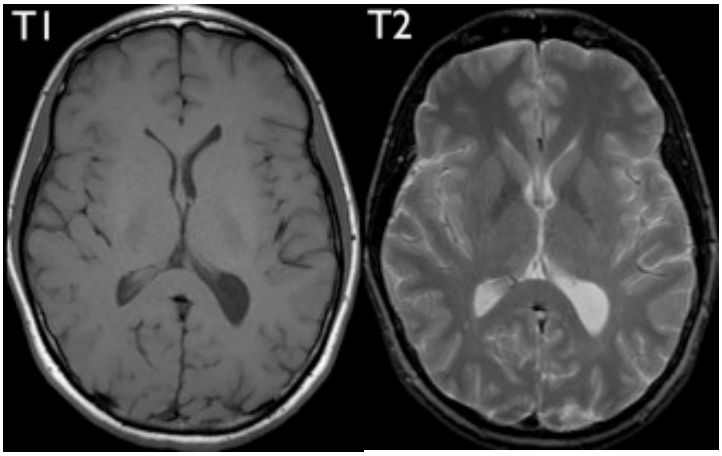

Figure 2.5: exemple de pondération, souvent les tissus ayant des T_2 longs ont des T_1 court et inversement, c'est pourquoi, les images ont des contrastes inversés

La valeur d'équilibre initiale de l'aimantation longitudinale est aussi proportionnelle à la densité protonique des tissus. Il faut donc un T_1 long et un TE court pour obtenir une image pondérée en densité protonique.

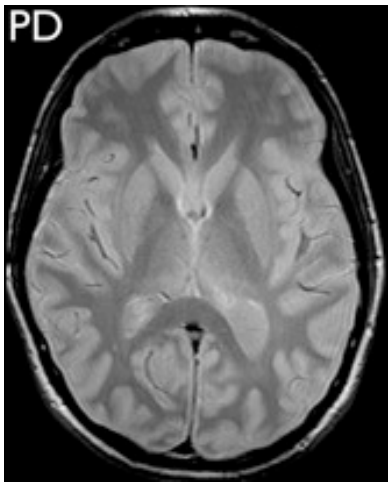

Figure 2.6: Image pondérée en densité protonique

2.2.3 De la RMN à l'IRM

L'Imagerie par Résonnance Magnétique Nucléaire (IRM) a pour but de mesurer le signal RMN des molécules d'eau en un point donné de l'espace. La puissance du signal reçu nous indiquera la concentration en molécules d'eau à cet endroit précis et nous permettra de former une image d'un corps de manière non-intrusive.

Comme expliqué précédemment, la fréquence de résonnance des protons (fréquence de Larmor) dépend de son environnent, mais aussi du champ magnétique dans lequel il est plongé. C'est cette dernière dépendance qui a permis la conception de l'IRM : en appliquant un gradient de champ magnétique au lieu d'un champ constant, nous pouvons exciter qu'une zone localisée de l'espace.

Cette technique a été proposée en 1950 pour reconstruire une imagerie 1D, et a été améliorée ensuite pour de l'imagerie 3D (1973).

2.2.4 Séquence IRM

2.2.4.1 Excitation sélective 2D

Nous avons vu qu'avec un champ magnétique externe **B0**, les spins s'orientent dans la direction de ce champ. L'application d'une excitation magnétique radiofréquence (RF) à la fréquence de Larmor fait tourner les spins. Ils sont alors en état excité et sont basculés de 90°. Ils se retrouvent alors dans le plan perpendiculaire au champ constant **B0**.

Si le corps est plongé dans **B0** seul, tous les spins ont la même fréquence de résonnance, et le signal RF fera basculer tous les spins de l'espace. Afin de former une image 3D, nous devons exciter un plan et non plus l'espace entier. Puis en formant l'image de plans successifs, nous reconstruirons une image 3D. Si nous souhaitons exciter un plan seul, l'idée est d'ajouter un gradient de champ **Gz** (dans la direction **Z**) au champ magnétique **B0**. Ainsi tous les spins n'auront pas la même fréquence de Larmor. Si notre signal RF a une bande passante étroite, il excitera seulement les spins possédant une fréquence de Larmor dans cet bande, donc un plan perpendiculaire à la direction **Z**. Nous avons donc effectué une excitation sélective de notre espace.

2.2.4.2 Méthode d'imagerie 2D

Nous avons donc réussi à exciter les spins situés dans un plan de l'espace. Le signal que nous recevons est donc la contribution de tous les spins de ce plan. Afin de faire une image de ce plan nous devons réussir à calculer la contribution d'une zone restreinte de ce plan. Cette zone est appelée voxel et sa taille déterminera la résolution de notre image. Nous noterons $m(x,y)$ l'amplitude du signal émis par le voxel de coordonnées [x,y].

Une première étape consiste à « étaler » le signal reçu, actuellement à la fréquence de Larmor, sur une bande de fréquence plus large où le signal à une fréquence donnée correspondra au signal à une position x donnée. Encore une fois un gradient de champ Gx (dans la direction x cette fois) sera appliqué pendant la lecture du signal reçu (donc après

la phase d'excitation). Les spins ne se relaxeront plus à la fréquence de Larmor $\omega = \gamma B_0$ mais à la fréquence $\omega(x) = \gamma(B_0 + G_x x)$.

En filtrant le signal reçu $s_{\omega_p}(t)$ à une fréquence donnée $\omega_p(x_p)$, nous lisons les contributions des spins situés à une position x_p donnée :

$$s_{\omega_p}(t) = \int_y m(x,y)e^{-i\omega_p t}dy = \int_y m(x,y)dy\, e^{-i\omega_p t}$$

Nous obtenons donc la projection sur l'axe des x de $m(x,y)$.

Nous devons donc à présent déterminer la provenance du signal sur la dernière direction : la direction y. Pour cela nous allons jouer sur la phase des spins excités. En effet, les spins excités se mettent à tourner dans le plan [x,y] en phase avec le signal excitant RF. Les spins étant tous en phase (prise comme phase de référence), leurs signaux émis s'ajoutent, et nous obtenons un fort signal. En appliquant un champ magnétique pendant une courte durée δ aux spins, ceux-ci vont tourner à une fréquence légèrement différente pendant ce temps δ, et leur phase va être modifiée. L'idée est donc de déphaser les spins entre eux en fonction de leur position y. Nous allons donc appliquer un gradient de champ Gy dans la direction y entre la phase d'excitation et la phase de lecture. Les spins vont donc tourner à la fréquence $\omega(y) = \gamma\big(B_0 + G_y y\big) = \omega_0 + \gamma G_y y$ pendant δ. Leur nouvelle phase sera donc $\phi(y) = \gamma G_y y \delta$. L'amplitude du signal émis par les spins d'un voxel pendant la phase de lecture sera donc $m(x,y)e^{-i\phi(y)}$. Le signal filtré reçu $s_{\omega_p}(t)$ est alors :

$$s_{\omega_p}(t) = \int_y m(x,y)e^{-i\phi(y)}dy\, e^{-i\omega_p t}$$

En notant $k_y = \frac{\gamma}{2\pi} G_y \delta$, l'amplitude du signal reçu filtré S_{ω_p} vaut :

$$S_{\omega_p}(k_y) = \int_y m(x,y)e^{-ik_y y}dy\, e^{-i\omega_p t}$$

On reconnaît ici la transformée de Fourrier de notre signal $m(x,y)$. On reconstruit cette transformée de manière discrète en prenant différentes valeurs de k_y (on joue sur G_y et δ). La transformée de Fourrier inverse de cette fonction nous donne enfin $m(x,y)$.

Reprenons à présent le signal total reçu $s(t)$:

$$
\begin{aligned}
s(t) &= \int_{\omega_p} s_{\omega_p}(t)\, d\omega_p \\
&= \int_{\omega_p} \left[\int_y m(x,y) e^{-ik_y y} dy \right] e^{-i\omega_p t}\, d\omega_p \\
&= \int_x \left[\int_y m(x,y) e^{-ik_y y} dy \right] e^{-i\omega_0 t} e^{-i\gamma G_x x t}\, dx \\
&= \left[\int_x \int_y m(x,y) e^{-ik_y y} e^{-ik_x x}\, dx\, dy \right] e^{-i\omega_0 t} \Big\|_{\substack{k_x = \gamma G_x t \\ k_y = \frac{\gamma}{2\pi} G_y \delta}}
\end{aligned}
$$

On constate bien ici de manière mathématique que le signal reçu correspond à la transformée de Fourrier 2D de $m(x,y)$ à un vecteur d'onde donné **k**. Nous pouvons reconstruire cette transformée de Fourrier de manière discrète à l'aide des paramètres Gx, Gy et δ. Finalement une transformée de Fourrier inverse permet de retrouver $m(x,y)$. En faisant de même pour tout une série de plan de hauteur z, on obtient $m(x,y,z)$ et on peut faire une image 3D.

2.2.4.3 Écho de spin

Le signal reçu est cependant perturbé par des artefacts, et notamment celui du décalage de phase. Celui-ci est dû aux inhomogénéités du champ magnétique constant. En effet le champ B0 n'est pas tout à fait constant car la susceptibilité magnétique du corps n'est pas constante (entre l'air des sinus ou des poumons et l'eau du corps par exemple). De plus l'environnement chimique du proton perturbe le champ magnétique ressenti par le spin. Ainsi, entre le moment où l'impulsion RF est donnée et la lecture du signal, nos spins se déphasent entre eux. Si nos spins restent à la même position, ce déphasage évolue de manière linéaire avec le temps.

Une technique largement utilisée actuellement est l'écho de spin. L'idée pour supprimer ce déphasage entre nos spins est d'inverser les phases de tous les spins à l'instant moitié entre l'excitation et la lecture. Ainsi les spins qui étaient en avance de phase (donc avec une fréquence de rotation plus rapide, i.e. plongés dans un plus haut champ), se retrouveront en retard de phase. Comme ils ont une fréquence de rotation plus rapide, ils rattraperont progressivement leur retard et seront parfaitement en phase au moment de la lecture. Nous observons donc un écho sur le signal reçu à cet instant précis où les spins retournent en phase. Pour inverser les phases de nos spins, un pulse RF à 180° est envoyé au système. On appelle temps d'écho le temps séparant l'excitation de l'écho, ce temps pouvant être choisi par l'utilisateur par le pulse à 180° (qui correspond à TE/2).

2.2.5 La RMN sensible à la diffusion

Afin de tirer encore plus d'informations du signal IRM, une nouvelle technique a été mise en place pour détecter la diffusion des molécules d'eau dans le corps. Les molécules d'eau joueront alors le rôle de sonde de notre système nerveux en détectant des zones de mauvaise circulation (La première application clinique de l'IRM à Diffusion est la détection précoce d'une ischémie cérébrale), ou en détectant la direction des fibres neuronales pour retracer une cartographie des neurones de la matière blanche.

Pour cela le déphasage entre les spins va encore être exploitée. L'idée est cette fois de déphaser les spins qui se déplaceront pendant un intervalle Δ, et ce de manière proportionnelle à la distance parcouru. Ainsi dans les zones de grande diffusion, les spins seront beaucoup déphasés entre eux, et nous observeront une perte de signal. Afin de déphaser les spins un nouveau gradient de champ **g** est appliqué pendant une durée δ avant le pulse à 180°. Les spins vont donc recevoir un déphasage linéaire entre elles dans la direction de **g**. Les spins qui ont reçu un champ g élevé vont être en avance de phase par rapport à ceux qui ont reçu un champ g faible. Après le pulse à 180°, le même champ **g** va être appliqué pendant la même durée δ. On s'aperçoit bien ici que les spins qui n'ont pas bougé vont retourner en phase, tandis que les autres seront déphasées d'autant plus que le champ g reçu lors du deuxième pulse sera différent du premier (i.e. d'autant plus que la

molécule se sera déplacée dans la direction du champ). On mesure alors l'atténuation du signal pour en déduire la diffusion dans la direction de **g**.

De même que précédemment (Méthode d'imagerie 2), nous définissons un vecteur d'onde **q** par :

$$\vec{q} = \frac{1}{2\pi}\gamma\delta\vec{g}$$

On suppose en effet que la diffusion des molécules d'eau pendant δ est négligeable par rapport à celle mesurée pendant Δ (ie $\delta \ll \Delta$), donc le champ **g** perçu est quasi constant.

Le déphasage introduit par les deux pulses de **g** pour une molécule s'étant déplacée de **r** sera alors :

$$\phi = \vec{q} * \vec{r}$$

Ainsi l'atténuation du signal E sera alors :

$$E(\vec{q}) = \int_{\mathbb{R}^3} P(\vec{r}, \Delta) e^{-2i\pi\vec{q}*\vec{r}} d\vec{r}$$

Avec $P(\vec{r}, \Delta)$ la densité de probabilité qu'une molécule se soit déplacée de **r** pendant Δ, Cette densité étant fonction du tenseur de diffusion.

Nous avons une fois de plus une transformée de Fourrier. Que l'on peut reconstruire de façon discrète en balayant les valeurs du vecteur d'onde **q**. On appelle l'ensemble de ces valeurs le q-space qui peut être décrit en jouant sur les paramètres des gradients de diffusion : le gradient **g**, la largeur du pulse δ et la séparation Δ.

Nous avons plusieurs limitations ici dans les performances : nous sommes limités par le gradient de champ qui dépasse difficilement les 80 mT m^{-1} (Daniel C. Alexander, 2010) pour les scanners IRM humains. Le temps d'acquisition est trop long pour respecter le critère de Shannon (on ne peut dépasser 1h pour une application clinique). Afin de contourner ces limitations, la technique actuellement employée est de simplifier le problème en considérant que le déplacement des molécules suit une probabilité Gaussienne multi-

variable. L'équation d'atténuation se simplifie alors, et avec un algorithme de moindres carrés on peut en déduire le tenseur de diffusion (Caruyer et al., 2012).

Une cartographie de ce tenseur dans l'espace permet finalement les applications citées au début : détection d'ischémies, ou fiber tracking (cartographie du réseau neuronal).

2.2.6 Limitations et sujets de recherche

Interpréter ce tenseur de diffusion est actuellement le sujet de nombreuses recherches. Il concerne d'ailleurs exactement mon sujet de recherche et mes recherches bibliographiques se sont beaucoup concentrées sur ce sujet.

2.2.6.1 Nouvelles métriques

Pour détecter des anomalies spécifiques, de nombreuses métriques ont été produites. Ces métriques joueront le rôle de marqueurs facilement interprétable par le médecin lorsqu'elles sont imagées. Ainsi une liste des principales métriques est (avec λ_i la i^e valeur propre du tenseur de diffusion) (Basser et al., 1994) :

- Le déplacement moyen (Mean Square Value) : $MSD = \int_{\mathbb{R}^3} P(\vec{r}) r^2 d\vec{r}$
- La probabilité de retour à l'origine : $RTO(\Delta) = P(\vec{0}, \Delta)$
- La diffusivité moyenne (Mean Diffusivity): $MD = \frac{1}{3}\sum_{i=1}^{3} \lambda_i$
- La fraction d'anisotropie : $FA = \sqrt{\frac{3\sum_{i=1}^{3}(\lambda_i - MD)^2}{2\sum_{i=1}^{3}{\lambda_i}^2}}$

2.2.6.2 Extension du model gaussien

L'utilisation du model gaussien précédent pour la diffusion des molécules d'eau nous limite dans notre interprétation de la diffusion. En effet nous calculons grâce à cette technique qu'un tenseur de diffusion moyen au sein d'un voxel. Cependant un voxel peut être le lieu d'un croisement de fibres axonales de direction totalement différentes. Ainsi le tenseur de diffusion que nous calculons donne une fausse information sur la direction des fibres dans le voxel. Pour résoudre ce problème, un modèle multi-tenseur peut être utilisé en place du model simple-tenseur (D.C. Alexander, 2002).

Lorsque l'on veut aller encore plus dans les détails, c'est à dire avoir des informations sur les cellules (leur taille, leur densité…) comme la détermination du diamètre des axones, nous devons aussi modéliser différents compartiments où diffuse l'eau. Encore une fois un model multi-tenseur est nécessaire (Assaf and Cohen, 2002).

De nombreuses recherches se sont aussi intéressées au calcul de la diffusion sans l'utilisation de modèles, nous pouvons mentionner ici la technique du q-ball qui échantillonne le q-space (E. Caruyer, 2012).

2.2.6.3 Détermination du diamètre axonal

L'idée ici est de modéliser le tissu en différent compartiments de diffusion différentes, puis d'affiner les paramètres de notre modèle pour s'approcher du signal expérimental obtenu : technique de l'ajustement de courbes.

L'information sur le diamètre axonale vient du fait que la diffusion sature lorsque l'on augmente le temps *Δ*. En effet les molécules d'eau « rebondissent » contre la paroi de myéline des axones. Si on laisse diffuser pendant un temps très long, les molécules ne se seront pas déplacées d'une distance plus grande que du diamètre de l'axone.

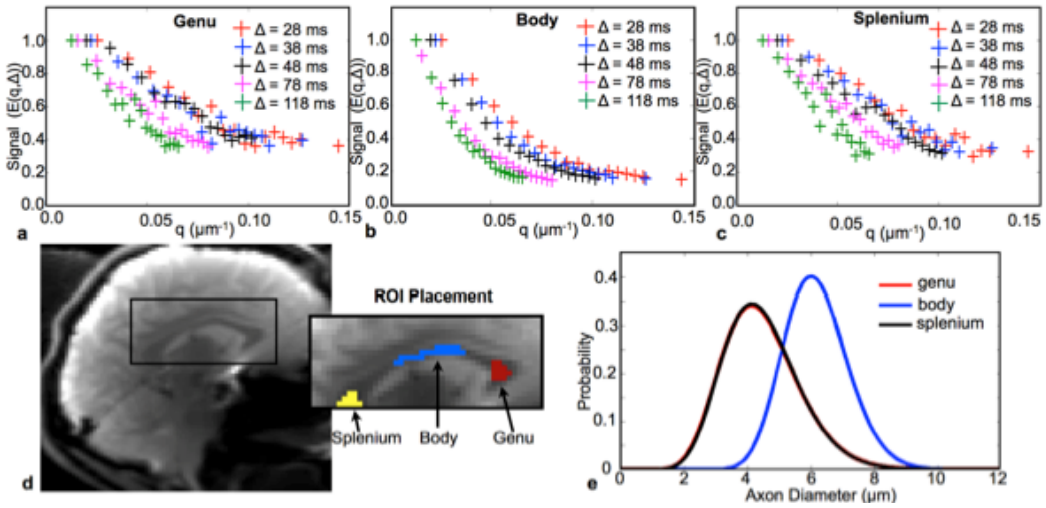

Figure 2.7: Exemple de détermination axonale par IRM a diffusion. **a. b. c.** les courbes obtenues expérimentalement du signal reçu en fonction de q. **d.** carte de la provenance des signaux. **e.** Probabilité de distribution axonale par zone. (McNab, et al., 2013)**.** Reproduit avec permission.

Cependant la réalité est plus compliquée. En effet il y a de nombreux échanges de molécules d'eau entre les différents compartiments (parfois plus efficaces que la diffusion), ainsi que de nombreuses interactions moléculaires (avec les parois par exemple). De plus nous sommes limités par le matériel (toujours la problématique du gradient de champ limité (donc qmax limité), d'un temps d'acquisition minimum pour avoir assez de signal etc….).

Nous avons d'autre part les problèmes exposés précédemment avec la modélisation de la diffusion dont on voudrait bien se passer (Extension du model gaussien).

2.3 Article 1: Modeling white matter microstructure

Journal – Functional Neurology

Tanguy Duval[1], Nikola Stikov[1,2], Julien Cohen-Adad[1,3]

[1] *NeuroPoly Lab, Institute of Biomedical Engineering, Polytechnique Montreal, Montreal, QC, Canada*

[2] *Montreal Heart Institute, Montreal, QC, Canada*

[3] *Functional Neuroimaging Unit, CRIUGM, Université de Montréal, Montreal, QC, Canada*

Quantitative magnetic resonance imaging can be combined with advanced biophysical models to measure microstructural features of white matter. Non-invasive microstructural imaging has the potential to revolutionize neuroscience, and acquiring these measures in clinically feasible times would greatly improve patient monitoring and clinical studies of drug efficacy. However, a good understanding of microstructural imaging techniques is essential to set realistic expectations and to prevent over-interpretation of results. This review explains the methodology behind microstructural modeling and imaging, and gives an overview of the breakthroughs and challenges associated with it.

Keywords*: diffusion, g-ratio, microstructure, MRI, myelin imaging, white matter*

Contribution: *Redaction of the article and generation of the figures.*

Submitted: *28 August 2016*

Accepted: *12 October 2016*

2.3.1 Introduction

Magnetic resonance imaging (MRI) is an attractive, non-invasive modality that can provide information about the integrity of the central nervous system (CNS) at a resolution in the order of $1mm^3$. To produce an image, an MRI scanner excites the magnetic moments of hydrogen atoms in water molecules, or spins, using radio waves. The excited spins will then re-emit a radio wave that is characterized by the water density as well as the time constants T1 and T2, which reflect the tissue chemical environment, thereby providing the image contrast. Thanks to its high sensitivity to soft tissue (not shown by X-ray), conventional MRI can distinguish different structures and detect lesions (e.g. inflammation, scar tissue, low-grade tumors). This good sensitivity is limited, however, by a lack of specificity, and it is usually difficult to establish a relationship between lesion activity observed by MRI and clinical score and patient prognosis (Rovira et al., 2013). However, the potential of MRI goes far beyond its capacity to provide simple contrast between tissues. By varying, in a controlled fashion, the excitation and the dephasing of the spins that produce the MR signal, researchers are able to measure several chemical and physical properties, such as the local change in oxygenation in functional MRI, the diffusion profile of water molecules in diffusion MRI, and the proportion of different macromolecules or metabolites (e.g. myelin lipids or iron) in relaxometry, magnetization transfer and magnetic resonance (MR) spectrometry. Instead of providing arbitrary numbers, these different MRI modalities can be calibrated in order to extract quantitative metrics, reproducible across sites (with different brands of scanner and with different coils). These techniques are commonly called "quantitative MRI" (Cohen-Adad and Wheeler-Kingshott, 2014; Tofts P, 2003). While many quantitative MRI metrics, such as T1 or fractional anisotropy (FA) from diffusion MRI, are now widely used by clinicians, they are still difficult to interpret, notably because they lack specificity (Alexander et al., 2007). To further understand how the complex chemical environment influences these quantitative metrics, researchers have proposed to take up the challenge of modeling mathematically the relationship between the white matter

microstructure and the generated MRI signal. Using the resulting models, they can extract meaningful numbers, such as the size and density of tissue fibers, the concentration of myelin or iron within a voxel, and the thickness of the myelin sheath surrounding the axons. These microstructural metrics are usually called “model-based quantitative metrics” as opposed to “physical quantitative metrics” (e.g. T1 or ADC, i.e. apparent diffusion coefficient). The ability to measure quantitatively many different properties with a single system allows comprehensive characterization of white matter tissue, from its composition to its microstructure. While the different information is usually exploited separately, complementary MRI metrics can also be combined to extract complete and specific information about the tissue, which can help with diagnosis and prognosis of neurodegenerative disorders.

In practice, quantitative MRI metrics are extracted by acquiring multiple images of the same modality (e.g. diffusion MRI), using different acquisition parameters (e.g. diffusion time). By modeling the signal change as a function of these acquisition parameters, one can extract quantitative information. In this review, we focus on model-based quantitative MRI metrics (which exclude physical quantitative metrics) and describe the methodology for modeling the white matter microstructure and the associated MRI signal. The challenges and limits of these techniques will also be addressed.

2.3.2 White matter microstructure

To model the MRI signal, it is essential to have sufficient knowledge of the underlying tissue microstructure. For instance, precise knowledge of the volume fraction of a certain water component makes it easier to understand its contribution to the MRI signal: the bigger this component is, the more it contributes to the signal (weighted by the T1 and T2 relaxations).

Figure 2.8 shows an example of white matter electron microscopy (a) along with a schematic drawing of white matter microstructure (b). The white matter is composed of four main components: neurons, glial cells (e.g. astrocytes, microglia, oligodendrocytes), the extracellular space, and blood vessels.

Neurons can be subdivided into fibers, cell bodies and dendrites. In the white matter, we observe very few neuronal bodies and dendrites[1], and the majority of the space is occupied by neuronal fibers (~60%) (Mottershead et al., 2003; Perge et al., 2009; Stikov et al., 2015a). The extracellular space constitutes about 20% of the volume (Bourne, 2012; Syková and Nicholson, 2008), blood vessels constitute less than 3% (Syková and Nicholson, 2008), while the rest of the volume is occupied by glial cells. 70 to 95% of the nerve fibers are enveloped by a myelin sheath (Biedenbach et al., 1986; Liewald et al., 2014) (myelin is responsible for the white appearance of the white matter). Furthermore, myelinated fibers are, on average, much larger than unmyelinated fibers (20 to 50% larger) (Biedenbach et al., 1986; FitzGibbon and Nestorovski, 2013), with the result that the majority of the space is occupied by myelinated fibers. The term fiber refers to the axon plus its myelin sheath. About 33%[2] of the white matter volume is composed of axons (Nilsson et al., 2013; Perge et al., 2009).

---

[1] The soma to glial cell ratio is 1:15 in white matter versus 1:1 in gray matter (Azevedo et al., 2009), while glial cell density is similar in white and gray matter (Herculano-Houzel, 2014).

[2] Note that an axon volume fraction of 33% and a fiber volume fraction of 60% leads to a g-ratio of $\sqrt{(33/60)}=0.74$, which is close to the optimal value of 0.77 as mentioned in (Chomiak and Hu, 2009).

All these components are highly hydrated [the water content of white matter is ~72% (Lajtha, 2013; Tofts PS, 2003)]. The axoplasm is composed largely of water (87%) and contains 2.5% proteins (assessed in squid giant axons) (Johansen-Berg and Behrens, 2013; Adelmann et al., 2013). Glial cells and blood vessels are composed of ~80% water (Shepherd, 2006); The extracellular space contains mainly fluid supplemented by long macromolecules that constitute the extracellular matrix (Syková and Nicholson, 2008); only the myelin sheath presents a relatively low water content of 40% (Morell and Quarles, 1999; Norton and Cammer, 1984). In fact, 50 to 60% of the dry tissue weight in white matter is myelin (Norton and Autilio, 1966), and this proportion reaches 75% in peripheral nerves (O'Brien and Sampson, 1965).

Glial cell density is very constant in the brain [~10^5 cells/mm^3 (Herculano-Houzel, 2014)], suggesting a homogeneous contribution of glial cells to the MRI signal strength. Axon density, however, varies greatly (10^4 to 10^5/mm^3) due to large differences in mean axon diameter between regions (Herculano-Houzel, 2014).

Axons are myelinated by oligodendrocytes (one oligodendrocyte for up to 50 axons [(Baumann and Pham-Dinh, 2001)], which wrap multiple layers of myelin around the axons until the ratio of the inner to the outer diameter of the fiber, called the g-ratio, achieves an optimal value of around 0.77 (Chomiak and Hu, 2009). The myelin sheath is thus a succession of impermeable bi-lipid layers, separated by layers of water (myelin water). In adults, the myelin sheath occupies approximately 25–30% of the white matter volume (Mottershead et al., 2003; Perge et al., 2009; Stikov et al., 2015a). The function of the myelin layers is to improve the speed of propagation of action potentials by inhibiting ionic exchanges between the intra- and the extra-axonal space. Instead, these exchanges mostly take place at the regularly spaced nodes of Ranvier. These nodes are ~2µm long and spaced ~1 mm apart (depending on the axon diameter), and thus constitute only 0.2% of the axon surface (Giuliodori and DiCarlo, 2004). This anatomical feature explains why water diffuses preferentially along the nerve fibers (about four times faster than perpendicular to the fibers), as observed in diffusion tensor imaging experiments (Alexander et al., 2007), and also explains the presence of a slow diffusion component perpendicular to the fibers that is

attributed to water “trapped” inside the axons (Clark and Le Bihan, 2000). Nuclear magnetic resonance (NMR) experiments have established that the exchange rate between the intra- and the extra-axonal space is ~600 ms (Duong et al., 1998; Meier et al., 2003; Nilsson et al., 2013), an order of magnitude longer than the typical diffusion time used in diffusion MRI. Axons can thus be considered impermeable to water in diffusion MRI models. As for glial cells, their membrane is more permeable thanks to the presence of aquaporin pores on their surface (Arciénega et al., 2010; Nielsen et al., 1997). This is confirmed by the greater restriction (50% decrease of the diffusion coefficient) of water molecules after deactivation of these aquaporin pores (Badaut et al., 2011), and the appearance of a new water compartment, isotropically restricted, in fixed tissue (~30% of the MRI-visible water) (Panagiotaki et al., 2012), much larger than in *in vivo* tissue (Ferizi et al., 2014). Similarly to glial cells, water molecules in blood vessels are not restricted, because of the rapid exchange (exchange rate of 15-30ms) with the extracellular space and the glial cells. (Johansen-Berg and Behrens, 2013).

The pie charts in Figure 2.8 summarize the above information and give rough estimates of the volume fraction of the different constituents of white matter, values that are particularly useful in myelin imaging.

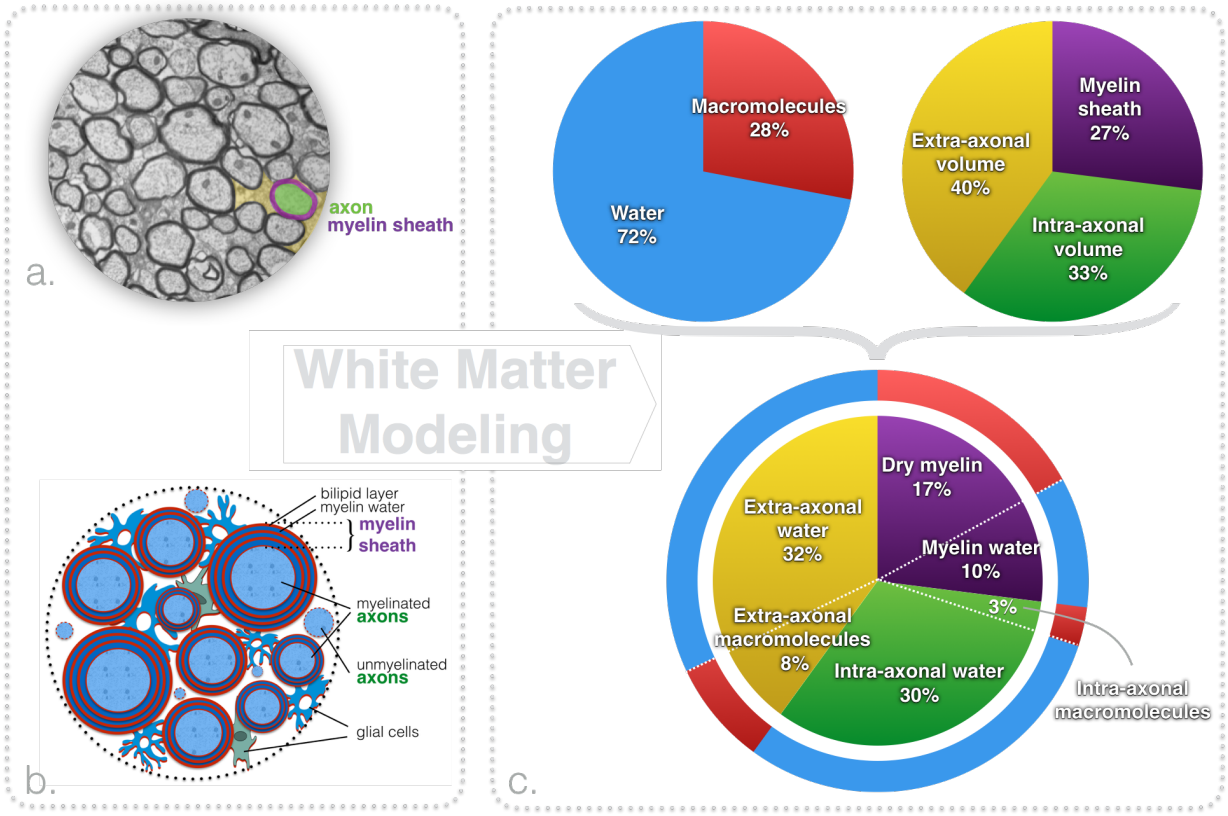

d.

Acronym	Definition	Rough value in white matter	Pie chart correspondence (%)
AVF	Axon Volume Fraction	33 %	33
FVF	Fiber Volume Fraction	60 %	33 + 27
MVF	Myelin Volume Fraction	27 %	27
MTV[1]	Macromolecular Tissue Volume	28 %	28
PD[1]	Normalized Proton Density	72 %	72
fr[2]	Water Fraction with Restricted diffusion	48 %	30 / (32 + 30)
MWF[1]	Myelin Water Fraction	14 %	10 / 72

[1] See section *Myelin imaging* [2] See section *Diffusion MRI*

Figure 2.8: Modeling of the white matter tissue. **a.** Transmission electron microscopy of an axial slice of white matter fiber bundles extracted from the corpus callosum of a mouse (West et al., 2016a). **b.** Schematic representation of the white matter. **c.** Proportions of the different white matter tissue components. The top left pie chart divides white matter into two general components: water (blue) (the component that produces the MRI signal) and lipids/macromolecules (red). The top right pie chart divides white matter into three spaces (used in

diffusion and myelin imaging models): the myelin sheath (purple), the extra-axonal volume (yellow) and the intra-axonal volume (green). The bottom pie chart subdivides these three spaces into water and lipid/macromolecular content. **d.** Definitions of most commonly used MRI (gray boxes) and tissue modeling (light blues boxes) metrics and their rough values.

2.3.3 Quantitative MRI modalities

In this section, important quantitative MRI modalities are briefly presented, focusing on the fundamental physics that allows to retrieve meaningful measures of tissue microstructure. This section also highlights the advantages of these metrics compared to conventional MRI and clarifies the limitations in their interpretation.

2.3.3.1 Diffusion MRI

2.3.3.1.1 Theory

A popular modality for assessing tissue microstructure is diffusion MRI. Diffusion MRI takes advantage of the diffusion of water molecules to probe the microenvironment. Just as the diffusion of a drop of ink on a fibrous tissue reveals the direction of the microscopic fibers that compose that tissue (Figure 2.9), diffusion MRI reveals the direction of the fibers that compose the white matter tissue, a technique called diffusion tensor imaging (DTI). In each voxel and in multiple directions, the diffusion of water molecules is measured thanks to an equation that relates MRI signal reduction to the diffusion rate of water molecules (Stejskal and Tanner, 1965) (see next paragraph). If the diffusion is modeled in 2D, it can be described by an ellipse, as illustrated with the drop of ink (Figure 2.9). In 3D the diffusion can be described by a tensor (a 3x3 symmetric matrix with six parameters), therefore at least six diffusion-weighted MR images need to be acquired to resolve its shape. This can be done for each individual voxel in the MRI acquisition. This principle can be pushed further to measure the amount of water trapped inside the myelinated fibers, and the size distribution of these fibers (Assaf et al., 2008). Indeed, these water molecules present restricted diffusion and result in a small MRI signal decrease. Although models exist for different

tissues (e.g. kidney cells, gray matter), the majority of the models have been adapted to white matter tissue, because white matter presents fewer dendrites and many myelinated fibers in relatively coherent orientations.

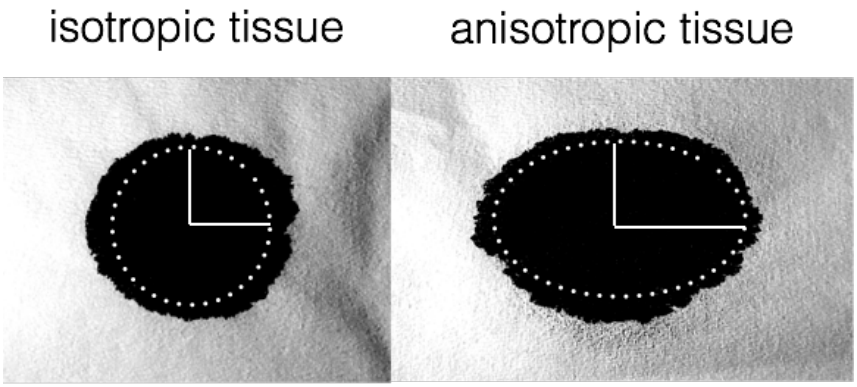

Figure 2.9: Diffusion reveals the underlying microstructure of the tissue. The diffusion of a drop of ink on isotropic (left) or anisotropic (right) fibrous tissue is Gaussian and can be modeled with an ellipse. The main axis of this ellipse (horizontal axis in this case) defines the main direction of the fibers that form the tissue. The ratio between the main and the secondary axis defines the degree of anisotropy of the paper. Similarly, diffusion in the white matter tissue is modeled with an ellipsoid in diffusion tensor imaging experiments. This figure was inspired by Dr Gordon Kindlmann (University of Chicago).

Diffusion encoding in MRI is performed through the dephasing and rephasing of the spins using magnetic field gradients, referred to in this paper as "diffusion gradients". The standard diffusion protocol is the pulsed-gradient spin echo sequence, which is composed of two diffusion gradients characterized by three parameters: their duration δ, amplitude G, and separation Δ (Figure 2.10). The relationship between diffusion gradients and MRI signal was first expressed by Stejskal and Tanner (1965) assuming a Gaussian diffusion:

$$S = S_0 e^{-bD}$$

where S_0 represents the MR signal when no diffusion encoding is applied (i.e. $b = 0$), $b = (\gamma\delta G)^2 \cdot (\Delta - \delta/3)$ (s/mm^2), and D (mm^2/s) is the diffusion coefficient in the direction of the diffusion gradients.

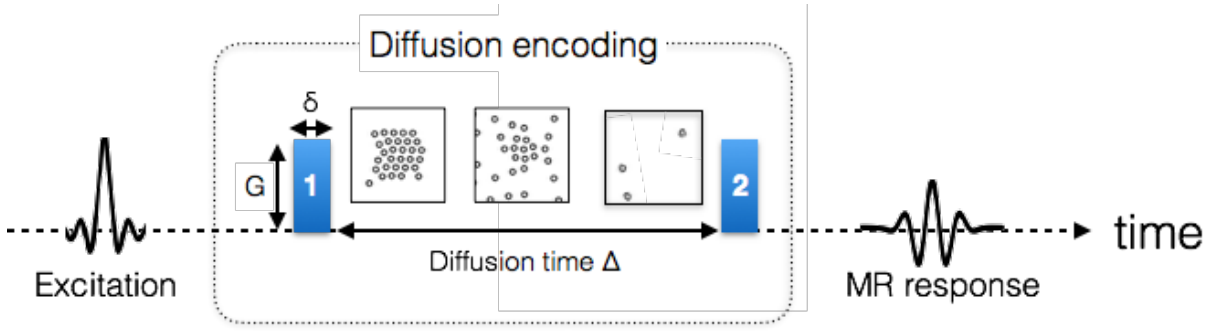

Figure 2.10: Timeline for encoding the diffusion of the water molecules in MRI. Just after being excited, the position of each molecule is tagged based on the phase of its spins, by applying gradient #1 (parametrized by its strength G and duration δ). During a time Δ, the spins (illustrated by small circles) move (due to Brownian motion or convection). The longer the time Δ is, the further the molecules can move. A second and identical gradient is applied to quantify this displacement through a signal loss in the MR response.

2.3.3.1.2 Advanced modeling

The MR model for Gaussian diffusion is thus characterized by a single parameter *b* instead of three (Δ, δ, and G). This equation can be validated experimentally by measuring the evolution of the MR signal in water for different combinations of Δ, δ, and G (Figure 2.11). However, the same experiment in the white matter (with diffusion gradient directions perpendicular to the main axis of the axons) shows that: i) a single exponential is not sufficient to model the MR signal decay as a function of the *b*-value, and ii) the MR signal is not a function of the b-value only (see Figure 2.11). The first observation led to the development of the models with multiple compartments, a slow diffusion compartment that corresponds to the trapped water (within myelinated axons for instance), and a fast diffusion compartment that corresponds to the water that is diffusing in the extracellular matrix or is in active exchange with glial cells (e.g. astrocytes via the aquaporin pores). The

second observation (signal is not dependent only on the *b*-value) requires the use of non-Gaussian diffusion equations to model the slow compartment. The equation of restricted diffusion within cylinders of known diameter (Wang et al., 1995) correctly models this non-Gaussianity of diffusion in white matter (Alexander et al., 2010; Assaf and Basser, 2005; Avram et al., 2004; Ferizi et al., 2014, 2015; Nilsson et al., 2013; Panagiotaki et al., 2012; Zhang et al., 2012). This non-Gaussian compartment is usually attributed to the water restricted in myelinated fibers. Although the extra-axonal compartment is a complex structure, assuming Gaussian diffusion in this compartment correctly models the MRI signal (Alexander et al., 2010; Assaf and Basser, 2005; Ferizi et al., 2015; Nilsson et al., 2013; Zhang et al., 2012), probably due to the good permeability of the membranes (see section "White matter microstructure"), although this assumption can be refined when varying the diffusion time (Burcaw et al., 2015).

While Gaussian diffusion, notably used in DTI experiments, is a good approximation at low *b*-values (typically b = 1500 s/mm^2) for a fixed diffusion time, advanced models, such as those from the previous paragraph, are necessary for larger *b*-values or in experiments with various diffusion times in order to get measurements (e.g. diffusion coefficients) that are independent of the acquisition protocol (e.g. choice of *b*-values and diffusion times). Another asset of these more advanced models is their robustness to partial volume effects or contamination with cerebrospinal fluid (CSF). Not accounting for these effects leads to abnormally low values of FA, for instance at the periphery of the white matter tissue, notably close to ventricles or at the periphery of the spinal cord, even if the tissue is healthy.

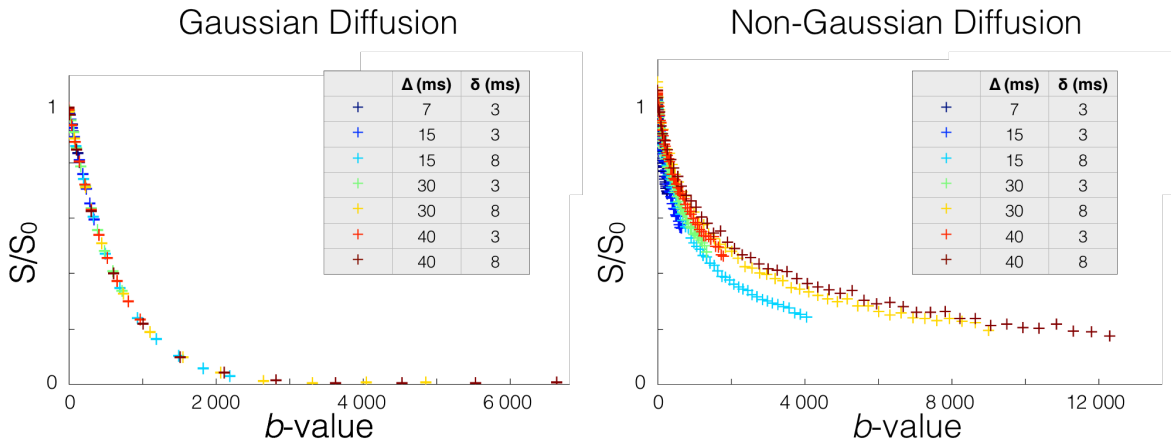

Figure 2.11: MRI signal as a function of b-value in voxels presenting Gaussian (left) or non-Gaussian (right) diffusion of water molecules. While conventional diffusion MRI assumes Gaussian diffusion characterized by dependence on the b-value only, diffusion perpendicular to neuronal fibers (right) is non-Gaussian, which allows the extraction of additional microstructural information such as axon diameter.

These models can thus be used to describe tissue microstructure. The relative proportion between the restricted water trapped inside axons and the water presenting Gaussian diffusion outside the axons can be retrieved (metric *fr* in Figure 2.8), and some models also feature the orientation dispersion or the permeability of the myelin sheath (Clark and Le Bihan, 2000; Nilsson et al., 2012, 2013; Panagiotaki et al., 2012; Zhang et al., 2012). Some of these parameters can be measured robustly only with a system that can achieve very high gradient strengths, while others are adapted for clinical scanners.

2.3.3.2 Myelin imaging

In one important field of MRI research, the aim is to measure the myelin content within a tissue. Myelin imaging is particularly interesting in neurodegenerative diseases, as well as in several neurological disorders (e.g. autism, schizophrenia), because of the presence of demyelination or abnormal myelination of neuronal fibers (Fields, 2008). Unfortunately, measuring the signal directly from myelin is challenging due to the ultra-short myelin relaxation times (T2~10 μs), and because the signal from myelin gets lost in the strong water signal. Although some groups showed very promising results of direct myelin imaging in humans *in vivo* (Sheth et al., 2016), such techniques are very recent and further validation is required. Instead of detecting the myelin directly, researchers have developed strategies to retrieve quantitative metrics that correlate with absolute myelin content (or myelin volume fraction, MVF) from the water signal. As a consequence, it should be kept in mind that the term myelin imaging can be misleading. Indeed, these techniques provide quantitative metrics that need to be calibrated, assuming a linear relationship with MVF, in order to retrieve the true myelin content. Usually, the coefficients of this linear relationship are not perfectly known and might change in pathology (e.g. effect of the non-compact myelin sheath in multi-component T2 experiments). Also, some of these techniques are sensitive to all lipids and macromolecules in general (e.g. magnetization transfer) and not only to myelin. Different physical properties have been used to obtain metrics sensitive to myelin content.

2.3.3.2.1 Magnetization transfer

One strategy is to take advantage of the phenomenon called magnetization transfer (MT) (Wolff and Balaban, 1989), where the hydrogen spins bound to macromolecules, once excited by a dedicated radiofrequency pulse, transfer a part of their energy to the neighboring free water spins. The more the macromolecules ~~are~~ present in the voxel, the greater the number of free water spins ~~are~~ excited via this phenomenon, which impacts on the MR signal. The most common metric utilizing this phenomenon is the magnetization transfer ratio (MTR), which has been shown to correlate with myelin content (Schmierer et

al., 2004), but also with other properties such as the T1 relaxation time (Henkelman et al., 2001). A particularly interesting improvement of MTR is the saturated magnetization transfer metric (MTsat) (Helms et al., 2008): MTsat decouples MTR from T1, but is still protocol-dependent. In order to derive truly quantitative metrics from the MT phenomenon, researchers proposed modeling it in white matter and introduced equations of the MR signal change as a function of acquisition parameters (e.g. frequency or power of the radiofrequency pulse that excites the macromolecules), a technique called quantitative MT (qMT) (Henkelman et al., 1993). While comprehensive models are theoretically able to quantify myelin content (Harrison et al., 1995), fitted parameters are too unstable to be estimated *in vivo (Levesque and Pike, 2009)*. Alternatively, qMT extracts the volume fraction of all macromolecules in a voxel (i.e. not only myelin, but also membranes of other cells and organelles).

2.3.3.2.2 Myelin water fraction

Another strategy is to exploit the relationship between myelin content and spin relaxometry. Indeed, the water contained in the myelin sheath (myelin water amounts to approximately 40% of the myelin volume) presents a very short T2 relaxation time compared with the rest of the water molecules. By measuring the amount of water with a short T2 relaxation time, it is possible to measure the myelin water fraction (MWF) (MacKay et al., 1994). It is also possible to infer the myelin volume fraction from the MWF if we assume that 40% of myelin water is in the myelin sheath. While initial implementations of this technique suffered from high noise level, new acquisition strategies and models have been developed to obtain higher quality images and to make this technique usable for clinical studies (Deoni et al., 2008; Oh et al., 2013; Prasloski et al., 2012). Note that T1 relaxation time can also be used for myelin imaging as proposed by Stüber et al. (2014), keeping in mind that T1 is potentially biased by axon diameter (Harkins et al., 2016).

2.3.3.2.3 Normalized proton density

Another relevant metric for microstructure modeling is the measurement of the water content obtained using normalized proton density (PD) mapping (Tofts PS, 2003; Volz et al., 2012). The complement of this metric is the non-water volume; this provides a measure of the macromolecular tissue volume (MTV), which includes lipids (Mezer et al., 2013). While all raw MR images are PD weighted, obtaining quantitative measurement of the water content requires challenging corrections of coil excitation (B1+) and sensitivity (B1–) profiles, as well as a calibration of the signal with relatively pure water (e.g. CSF) (Mezer et al., 2013; Tofts PS, 2003; Volz et al., 2012). With a good correction and calibration pipeline, water content can be measured precisely and with high reproducibility in the brain (Mezer et al., 2013).

2.3.3.3 Multimodal MRI

Thanks to ongoing improvements in acquisition sequences, protocols and hardware, it is now possible to obtain quantitative maps rapidly (in less than 10 min). By obtaining multiple quantitative MRI maps in a reasonable time it is possible to get complementary information on the tissue microstructure. The different metrics can be combined using models to derive more robust and relevant quantitative metrics, commonly called multimodal or multi-parametric measurements. One example is the computation of the fiber g-ratio, defined as the ratio of the axon caliber to the fiber caliber (axon plus myelin). The g-ratio can be computed by combining the restricted water fraction (*fr*) obtained with quantitative diffusion MRI, and the MVF obtained with myelin imaging. Taken independently, both *fr* and MVF are affected by CSF contamination or edema. In the computation of the g-ratio, these effects are compensated for; this simplifies the interpretation in case of demyelination, and is expected to improve the specificity of the technique to myelin sheath thickness.

The recent development of MR fingerprinting also offers interesting ways to obtain multi-parametric maps in a rapid manner (Ma et al., 2013), although further validation is still required before these techniques can be applied to pathological cases.

2.3.4 Challenges

In addition to practical and technical challenges, quantitative MRI presents fundamental challenges that make the modeling and interpretation of quantitative MRI results difficult.

2.3.4.1 Inferring the microscopic from the macroscopic

The signal is an average of many micro- and nanoscopic processes occurring over space (one voxel is composed of millions of magnetic spins) and time (usually in the order of milliseconds). The diffusion, for instance, is due to the Brownian movement and convection of water molecules within cells, between cells and through membrane aquaporin pores. Although very complex at nanoscopic scale, these chaotic displacements of water molecules can be described through probability functions [e.g. Gaussian in free water (Einstein, 1956)] that are highly reproducible on a macroscopic scale, and can therefore be modeled. But these probability functions also depend on the microscopic structure of the tissue (e.g. size of the cells and direction of the fibers), which hinders or restricts the global diffusion and thus modifies the MRI signal. Explaining the macroscopic features from the micro- and nanoscopic processes requires the isolation of the main effects from the negligible ones, a task that is particularly difficult because i) many of the parameters involved are difficult to measure directly (e.g. diffusion coefficients, membrane permeabilities, exchange rates); ii) the precision of the measurements, hardware capability and experiment duration are limited, and iii) the observed signal usually shows a simple behavior (e.g. bi-exponential) with only subtle changes.

2.3.4.2 Choosing the right model

Due to this difficulty in relating the macroscopic to the microscopic, many models have been developed for each MRI modality. While most diffusion models share the same approach (i.e., they are based on a mixture of free, hindered and restricted water compartments), they usually propose to take into account additional effects or to make additional simplifications and assumptions. Choosing the right model is not straightforward and multiple criteria need to be taken into account. The complexity of the

model, which can be defined by the number of parameters to fit, is one important criterion; while the most complex models are supposedly more accurate and specific, they produce less precise metrics with worse image quality, and thus cannot detect a subtle change in tissue integrity. On the other hand, simple models produce metrics that are harder to interpret because of the difficulty in decoupling the contributions from multiple sources. Another criterion for choosing the right model is the targeted tissue. Indeed, in the majority of the white matter, the large dispersion of orientation (and crossing) of the fibers needs to be taken into account in the diffusion model (via additional parameters). Zhang et al. proposed a popular model called NODDI (Zhang et al., 2012) that can quantify this dispersion of orientation as well as the intra-axonal volume. However, this aspect can be neglected (which simplifies the modeling) in the spinal cord white matter where there is good coherence of orientation (Grussu et al., 2016). Choosing the right model also goes hand in hand with deciding the acquisition strategy: instead of building very complex models that would work with any acquisition protocol, another interesting strategy is to adapt the acquisition in order to simplify the modeling. For instance, acquiring diffusion data only in one direction perpendicular to the direction of the fibers (in tissues with good coherence of orientation) allows simpler modeling than a complete 3D acquisition, and thus the extraction of more robust metrics with shorter protocols. Another example is the choice of diffusion time in the protocol: the longer the diffusion time, the more hindered the diffusion in the extra-axonal compartment (Burcaw et al., 2015). Acquisition protocols that have only long diffusion times will thus be modeled differently from those consisting only of short durations. Some groups even proposed changing the acquisition paradigm: oscillating instead of pulsed magnetic gradients have been used successfully to encode the diffusion (Lundell et al., 2015; Shemesh et al., 2015); additional preparatory pulses have been used in myelin imaging to cancel the signal from free water protons (VISTA) (Oh et al., 2013).

2.3.4.3 Validating the models

Testing and validating the different models requires a good ground truth, which is hard to get. The comparison of the MRI signal with histology, as well as the fabrication of realistic

and well-controlled synthetic phantoms is an active field of research in microstructural imaging. Histology is technically complex due to tissue deterioration during the preparation stages (e.g. fixation, staining, slicing) and it is limited due to the many coupled variables that cannot be controlled independently. While histology is a great method for demonstrating the sensitivity to a particular microstructural feature, it cannot easily be used to show the specificity. Indeed, microstructural properties (g-ratio, T1, absolute myelin content, water content, axon diameter) generally correlate with each other. Hence, assessing with confidence the specificity of each individual metric is an inherently ill-posed problem.

The issue of validation from *ex vivo* data is further complicated by the difficulty in generating, from histology, ground truth data that match the resolution of MRI: within a single MRI voxel there lie thousands of axons, which need to be individually labeled in order to retrieve aggregated ground truth metrics such as axon diameter and myelin. Fortunately, recent efforts in open-source software[3] for automatic axon and myelin segmentation (Zaimi et al., 2016) will make it easier for researchers to use large-scale histology and validate the relationship of their metric with the desired microstructural feature. Although numerical and synthetic phantoms allow for better-controlled experiments, this approach needs to be complemented with more realistic white matter tissue. In summary, there is no perfect validation method and the research community relies on the accumulation of evidence from diverse approaches to validate quantitative MRI methods.

2.3.4.4 Translating the models to the damaged tissue

Tissue characteristics can change drastically in pathology. The proliferation of microglia, inflammation, the presence of axonal debris, or the constitution of a glial scar in nervous tissue limit the validity of some assumptions used in models [e.g. impermeability of the myelin sheath in demyelination, unrestricted diffusion in the extra-axonal compartment

[3] https://github.com/neuropoly/axonseg

(Syková et al., 1999)]. Choosing a model that is robust to all pathological cases is one of the biggest challenges of quantitative MRI.

2.3.5 Performance of quantitative MRI metrics

Quantitative MRI has seen many improvements thanks to better acquisition strategies (Deoni et al., 2003; Marques et al., 2010; Oh et al., 2013; Prasloski et al., 2012; Van et al., 2014), optimized experimental designs (Alexander, 2008), more robust models (Zhang et al., 2012), and advanced data processing, such as faster and more stable equation solvers (Daducci et al., 2015; Sepehrband et al., 2016). On top of that, acquisition time, noise level and image artifacts (e.g. sensitivity to movement) have been improved thanks to improvements in hardware, in terms of field and gradient strength, coils and sequences (e.g. parallel imaging, simultaneous multislice excitation, reduced field of view). By combining all these improvements, the quantitative MRI metrics cited in previous sections can provide high-quality maps, with image quality similar to that of conventional MRI images, in just a couple of minutes. Beyond these improvements in acquisition time and image quality, quantitative MRI also requires accurate and reproducible ways of extracting the values in specific regions, a task facilitated by the development of automatic and robust segmentation, registration and metric extraction software and pipelines (Dupont et al., 2016; Vollmar et al., 2010). Unfortunately integrating all these improvements is difficult and time-consuming; in practice, basic or unoptimized methods are always used at some point, which leaves space for even better results in the future.

2.3.5.1 Qualitative assessment

One approach to estimate the sensitivity and precision of a quantitative metric is to qualitatively assess the level of noise and detail in the maps. In the latest implementations, model-based diffusion MRI metrics can produce highly detailed maps with high contrast-to-noise ratio (Daducci et al., 2015). Although MWF mapping was particularly noisy when it was first introduced (MacKay et al., 1994), relatively good quality MWF maps can now be obtained rapidly (Deoni et al., 2008; Oh et al., 2013; Prasloski et al., 2012). qMT generates maps with similar noise level as MWF (depending on acquisition time), but with

particularly small contrast in the white matter (Dula et al., 2010; Levesque et al., 2010). Proton density maps are highly detailed with relatively good quality and correlate with qMT and MWF (Mezer et al., 2013).

2.3.5.2 Reproducibility

The reproducibility of quantitative metrics is usually assessed by the coefficient of variation (CoV) and/or the voxel-wise Pearson correlation coefficient (r) in scan-rescan experiments of the same subject at two different time points (the subject is removed from the scanner between scans).

Most model-based quantitative metrics have a good CoV (<10%). These include *fr* (Grussu et al., 2015), MWF (Wu et al., 2006), PD (Mezer et al., 2013) and qMT (Levesque et al., 2010). Some metrics, however, are less stable on clinical setups and are adapted essentially for research scanners and studies; axon diameter measurements, for instance, present relatively large CoV values on clinical scanners (>11%) (Clayden et al., 2015) due to the requirement of strong gradients (Dyrby et al., 2012; Huang et al., 2015).

Particularly good whole-brain scan-rescan correlations (r >0.9) have been shown for the metrics *fr* (Tariq et al., 2012) and PD (Mezer et al., 2013). While such high values are quite remarkable, comparing correlation coefficients between quantitative metrics is particularly risky because r is highly dependent on the dynamic of the metric. For example, the g-ratio is relatively constant in healthy tissue, leading to low correlation coefficients. On the contrary, metrics that present high contrast between CSF and white matter would have high correlation coefficients as a result of CSF contamination. Also, the same metric can present very different correlation coefficients depending on the region of interest selected to perform the comparison (e.g. including both gray and white matter, as opposed to white matter only, usually improves the correlation coefficient). Future studies where several metrics are acquired within the same sample would shed light on this issue.

Another interesting metric that can be used to assess metric reproducibility is the intraclass correlation coefficient (ICC); indeed, the ICC shows the capability of a metric to detect differences between subjects that are significantly higher than the intra-subject scan-rescan

difference. In the presence of significantly higher inter-subject differences the ICC should be close to 1. Instead, if the values are similar, ICC will be close to 0.5. Using this statistic, it has been shown that both diffusion MRI (ICC=0.84 for *fr* in the spinal cord) (Grussu et al., 2015) and myelin imaging techniques (ICC=0.76 for MWF in the brain) (Meyers et al., 2013) are able to detect differences of white matter microstructure between two healthy subjects.

2.3.5.3 Sensitivity

Within the white matter, the microstructure can change drastically, mainly due to large differences in axon diameters between regions (see section "White matter microstructure"). While the white matter appears homogeneous on conventional MRI scans, quantitative MRI reveals microstructural differences, notably between different regions of the corpus callosum (Alexander et al., 2010; Barazany et al., 2009; Mezer et al., 2013; Stikov et al., 2015a) or between spinal cord tracts (Duval et al., 2015; T. Duval et al., 2016a; Fujiyoshi et al., 2016; Taso et al., 2016). These metrics can also track the microstructural changes related to brain development (Dean et al., 2016; MacMillan et al., 2011; Saito et al., 2012) or tissue deterioration in pathology (Chong et al., 2016; Fujiyoshi et al., 2016; Klawiter et al., 2011; Schmierer et al., 2008; Stikov et al., 2015a). The good sensitivity and reproducibility of these metrics suggest an improved capacity to detect subtle changes. Note that the sensitivity of quantitative MRI metrics implies the sensitivity of the non-quantitative MRI contrasts that produced this metric. However, compensating effects (e.g. simultaneous increase of T1 and MT) can conceal subtle changes in non-quantitative MRI contrast.

2.3.5.4 Specificity

Specificity is supposed to be the main asset of quantitative MRI metrics since these metrics disentangle the information from different sources. Unfortunately, assessing the specificity of quantitative MRI metrics is challenging due to the inter-correlation of many microstructural and MR parameters in the white matter (e.g. axon diameter, axon density, myelin content, water content, T1, T2*) (see the section "Challenges"). This issue can lead to incorrect interpretation of tissue structure: T1, for instance, has been considered

successively as a semi-quantitative marker for myelin (Koenig et al., 1990), for water content (Fatouros and Marmarou, 1999), and even for axon diameter (Harkins et al., 2016). While the lack of specificity of the early quantitative MRI metrics is commonly pointed out (Alexander et al., 2007; Schwartz et al., 2005; Wheeler-Kingshott and Cercignani, 2009), model-based metrics bring new information (i.e. not perfectly correlated with conventional metrics) (Alexander et al., 2010; Zhang et al., 2012) that correlates with histology (Alexander et al., 2010; Barazany et al., 2009; Dula et al., 2010; Duval et al., 2015, 2016b; Ong and Wehrli, 2010; West et al., 2016b), and improves specificity in lesions (Kipp et al., 2016; Stikov et al., 2015a). More comprehensive models (Burcaw et al., 2015), as well as a new paradigm for measuring myelin (Sheth et al., 2016), should further improve the specificity of these metrics.

2.3.5.5 Accuracy

In the early stages of MRI biomarker development, accuracy could be considered a secondary issue. Indeed, if a quantitative metric presents good reproducibility across sites, as well as good sensitivity and specificity to microstructure integrity, this metric requires only normative values from healthy subjects in order to decide whether or not a patient presents abnormal values. An atlas of widely used semi-quantitative metrics has already been generated [e.g. FMRIB58_FA (Smith et al., 2004)].

However, accuracy is important in model-based quantitative MRI for validating the models and for allowing accurate interpretation of tissue integrity in different case scenarios. Accuracy is notably important when several metrics are combined, such as in computing the g-ratio, to prevent misinterpretation (Campbell et al., 2016). Accuracy is usually assessed by comparing MRI metrics with features extracted from *ex vivo* tissue such as those reported in Figure 2.13. Some metrics can be directly compared such as PD, *fr* or axon diameter distribution. While PD and *fr* present relatively good accuracy (Nilsson et al., 2013; PS Tofts, 2003), axon diameter measurement has been reported to be overestimated by a factor of ~3 (Alexander et al., 2010; Horowitz et al., 2015; Innocenti et al., 2015; Zhang et al., 2011), and this was recently shown to be due to modeling issues (Burcaw et al., 2015)

that were affecting the specificity of this metric. Unfortunately, many metrics, such as MWF and qMT, cannot be compared directly because they are specific to different microstructural features (myelin water for MWF, macromolecules for qMT). However, the MRI metric (e.g. MWF) can be calibrated to get accurate measurements of the microstructural feature (in this case, the myelin volume fraction, or MVF). Usually this calibration assumes a linear relationship between the MRI metric and the targeted microstructural parameter (i.e. MWF $\propto$ MVF), and is performed using synthetic phantoms (e.g. agar-agar solution with a known concentration) or using a few normative values measured with histology on healthy tissue (e.g. white matter and gray matter myelin content). While these calibration strategies might be a good approximation for healthy tissue, a linear assumption might not hold in pathology. For instance, how should we define the MWF or the *fr* in axons presenting unwrapped myelin sheaths? For these reasons, special care should be taken in evaluating the accuracy of quantitative MRI metrics.

2.3.6 Example of quantitative MRI images

In this section, we present some examples of quantitative MRI maps. These maps are often easily distinguished from conventional MRI by the presence of a colorbar associating a pixel color with a quantitative value. Figure 2.12 shows maps of MVF, axon volume fraction (AVF) and g-ratio obtained using qMT and NODDI on a multiple sclerosis patient. As shown in section *reproducibility*, the variation of these metrics across healthy subjects is relatively low (CoV<10%) which means that the underlying microstructure within a healthy population does not vary much. Knowing this, alteration of tissue integrity can be detected, not from the contrast with surrounding tissue, but directly from the quantitative value. Thanks to robust registration procedures, it is also possible to detect abnormal values automatically, segment a lesion, and provide statistics. Conventional fluid attenuated inversion recovery (FLAIR) contrast clearly indicates the presence of three hyperintense lesions. While these three lesions are associated with a reduction of myelin content MVF and axon density AVF, only one of them presents an abnormal g-ratio, suggesting a gain in specificity of the g-ratio metric.

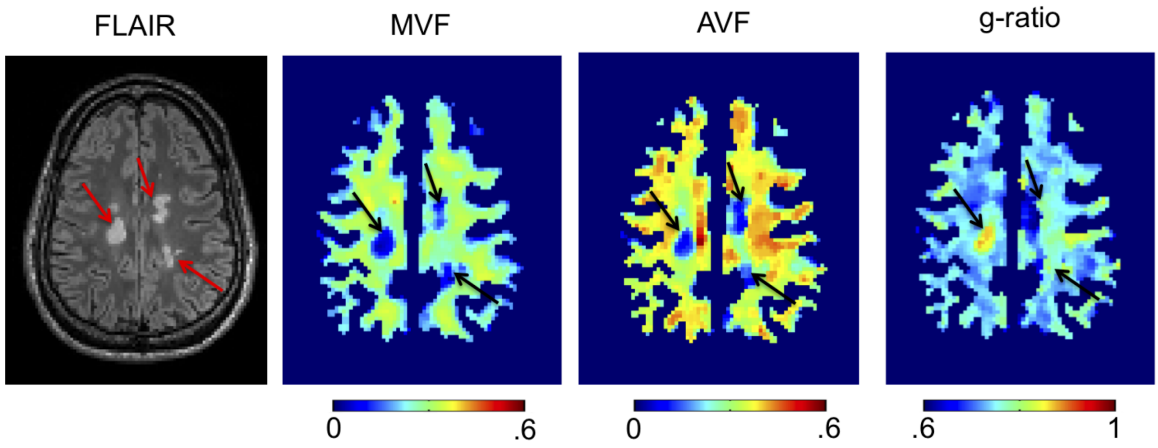

Figure 2.12: Example of multi-parametric quantitative MRI maps of a multiple sclerosis patient. Myelin volume fraction (MVF) was obtained using a qMT (Henkelman et al., 1993), axon volume fraction (AVF) was computed using the NODDI model (Zhang et al., 2012), and g-ratio was calculated from AVF and MVF (Stikov et al., 2015a). Conventional FLAIR contrast indicates the presence of three

hyperintense lesions. These lesions are associated with a reduction in MVF and AVF, but only one lesion show an abnormal g-ratio (>0.8).

Ex vivo experiments, such as that presented in Figure 2.13, enable comparison between MRI and histology to assess the sensitivity and accuracy of models. Because microstructural parameters are correlated between each other (e.g. axon diameter, axon density and g-ratio), assessing their specificity is not straightforward, and would require a number of comparisons, not only in healthy white matter, but also in pathological tissue (West et al., 2016b).

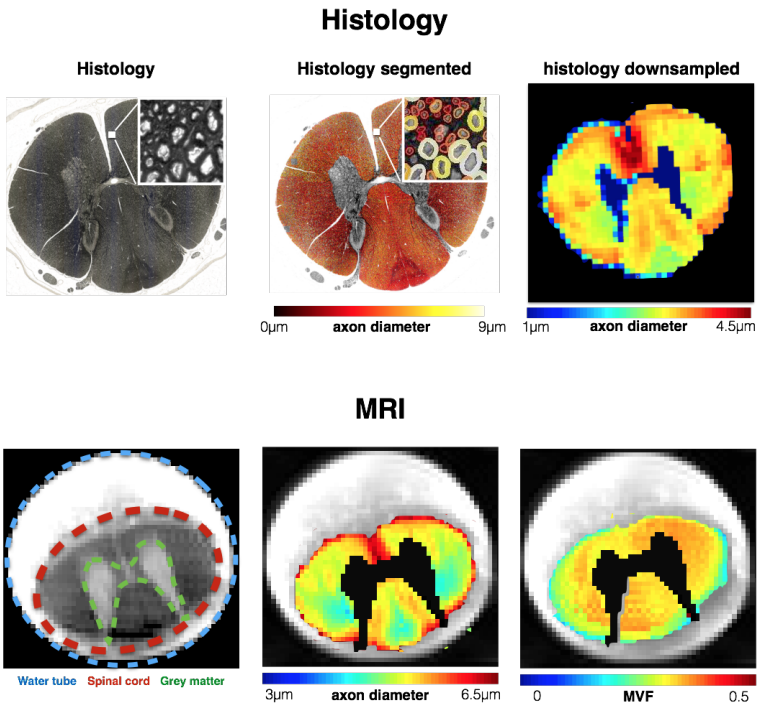

Figure 2.13: A comparison of ex vivo quantitative MRI maps with histology. Once segmented, histology can provide mean axon diameter or myelin volume fraction in a voxel. Visually, MRI and histology are in agreement, supporting the sensitivity of MRI to these specific microstructural properties.

2.3.7 Concluding remarks

In this brief review, we have described the most common quantitative MRI metrics and the methodology for modeling white matter. We showed that state-of-the-art quantitative MRI techniques produce reproducible maps that are highly sensitive to particular microstructural parameters. These maps are more specific to white matter microstructure than conventional MRI metrics, and can be calibrated to give meaningful numbers. While the long-term objective is to be able to retrieve the exact tissue microstructure and assess its integrity non-invasively, current quantitative MRI metrics should be interpreted carefully. With automatic processing pipelines, quantitative MRI should see more clinical applications in the next few years, notably for diagnosis and prognosis of diseases, as well as the monitoring of the effects of treatment.

2.3.8 Acknowledgments

We would like to thank Jennifer Campbell for her contribution to this presentation of an example dataset. This work was funded by the MS Society of Canada [EGID 2370], the Canada Research Chair in Quantitative Magnetic Resonance Imaging (JCA), the Canadian Institute of Health Research [CIHR FDN-143263], the Fonds de Recherche du Québec - Santé [28826], the Fonds de Recherche du Québec - Nature et Technologies [2015-PR-182754], the Natural Sciences and Engineering Research Council of Canada [435897-2013, 06774-2016], the Montreal Heart Foundation (NS) and the Quebec BioImaging Network (NS).

2.3.9 References

Adelman WJ Jr, Arnold JM, Gilbert DL (2013). Squid as Experimental Animals. New York, US, Springer.

Alexander DC, Hubbard PL, Hall MG, et al (2010). Orientationally invariant indices of axon diameter and density from diffusion MRI. Neuroimage 52:1374-1389.

Alexander DC (2008). A general framework for experiment design in diffusion MRI and its application in measuring direct tissue-microstructure features. Magn Reson Med 60:439-448.

Alexander AL, Lee JE, Lazar M, et al (2007). Diffusion tensor imaging of the brain. Neurotherapeutics 4:316-329.

Arciénega II, Brunet JF, Bloch J, et al (2010). Cell locations for AQP1, AQP4 and 9 in the non-human primate brain. Neuroscience 167:1103-1114.

Assaf Y, Basser PJ (2005). Composite hindered and restricted model of diffusion (CHARMED) MR imaging of the human brain. Neuroimage 27:48-58.

Assaf Y, Blumenfeld-Katzir T, Yovel Y, et al (2008). AxCaliber: a method for measuring axon diameter distribution from diffusion MRI. Magn Reson Med 59:1347-1354.

Avram L, Assaf Y, Cohen Y (2004). The effect of rotational angle and experimental parameters on the diffraction patterns and micro-structural information obtained from q-space diffusion NMR: implication for diffusion in white matter fibers. J Magn Reson 169:30-38.

Azevedo FAC, Carvalho LRB, Grinberg LT, et al (2009). Equal numbers of neuronal and nonneuronal cells make the human brain an isometrically scaled-up primate brain. J Comp Neurol 513:532-541.

Badaut J, Ashwal S, Adami A, et al (2011). Brain water mobility decreases after astrocytic aquaporin-4 inhibition using RNA interference. J Cereb Blood Flow Metab 31:819-831.

Barazany D, Basser PJ, Assaf Y (2009). In vivo measurement of axon diameter distribution in the corpus callosum of rat brain. Brain 132:1210-1220.

Baumann N, Pham-Dinh D (2001). Biology of oligodendrocyte and myelin in the mammalian central nervous system. Physiol Rev 81:871-927.

Biedenbach MA, De Vito JL, Brown AC (1986). Pyramidal tract of the cat: axon size and morphology. Exp Brain Res 61:303-310.

Bourne G (2012). The Structure and Function of Nervous Tissue, V2: Structure I. London, UK, Elsevier.

Burcaw LM, Fieremans E, Novikov DS (2015). Mesoscopic structure of neuronal tracts from time-dependent diffusion. Neuroimage 114:18-37.

Campbell JSW, Leppert IR, Boudreau M, et al (2016). Mapping the myelin g-ratio: promises and pitfalls. In: Proceedings of the 24th Annual Meeting of ISMRM. Singapour, p. 1501.

Chomiak T, Hu B (2009). What is the optimal value of the g-ratio for myelinated fibers in the rat CNS? A theoretical approach. PLoS One 4:e7754.

Chong AL, Chandra RV, Chuah KC, et al (2016). Proton density MRI increases detection of cervical spinal cord multiple sclerosis lesions compared with T2-weighted fast spin-echo. AJNR Am J Neuroradiol 37:180-184.

Clark CA, Le Bihan D (2000). Water diffusion compartmentation and anisotropy at high b values in the human brain. Magn Reson Med 44:852-859.

Clayden JD, Nagy Z, Weiskopf N, et al (2015). Microstructural parameter estimation in vivo using diffusion MRI and structured prior information. Magn Reson Med 75:1787-1796.

Cohen-Adad J, Wheeler-Kingshott C (2014). Quantitative MRI of the Spinal Cord. London, UK, Elsevier Science.

Daducci A, Canales-Rodríguez EJ, Zhang H, et al (2015). Accelerated Microstructure Imaging via Convex Optimization (AMICO) from diffusion MRI data. Neuroimage 105:32-44.

Dean DC 3rd, O'Muircheartaigh J, Dirks H, et al (2016). Mapping an index of the myelin g-ratio in infants using magnetic resonance imaging. Neuroimage 132:225-237.

Deoni SC, Rutt BK, Arun T, et al (2008). Gleaning multicomponent T1 and T2 information from steady-state imaging data. Magn Reson Med 60:1372-1387.

Deoni SC, Rutt BK, Peters TM (2003). Rapid combined T1 and T2 mapping using gradient recalled acquisition in the steady state. Magn Reson Med 49:515-526.

Dula AN, Gochberg DF, Valentine HL, et al (2010). Multiexponential T2, magnetization transfer, and quantitative histology in white matter tracts of rat spinal cord. Magn Reson Med 63: 902-909.

Duong TQ, Ackerman JJ, Ying HS, et al (1998). Evaluation of extra- and intracellular apparent diffusion in normal and globally ischemic rat brain via 19F NMR. Magn Reson Med 40:1-13.

Dupont SM, De Leener B, Taso M, et al (2016). Fully-integrated framework for the segmentation and registration of the spinal cord white and gray matter. Neuroimage doi: 10.1016/j.neuroimage.2016.09.026.

Duval T, Lévy S, Stikov N, et al (2016a). g-Ratio weighted imaging of the human spinal cord in vivo. Neuroimage doi: 10.1016/j.neuroimage.2016.09.018.

Duval T, Perraud B, Vuong M-T, et al (2016b). Validation of quantitative MRI metrics using full slice histology with automatic axon segmentation. In: Proceedings of the 24th Annual Meeting of ISMRM. Singapour, p. 928.

Duval T, McNab JA, Setsompop K, et al (2015). In vivo mapping of human spinal cord microstructure at 300mT/m. Neuroimage 118:494-507.

Dyrby TB, Søgaard LV, Hall MG, et al (2012). Contrast and stability of the axon diameter index from microstructure imaging with diffusion MRI. Magn Reson Med 70:711-721.

Einstein A (1956). Investigations on the Theory of the Brownian Movement. Dover Books on Physics Series. Mineola, Dover Publications.

Fatouros PP, Marmarou A (1999). Use of magnetic resonance imaging for in vivo measurements of water content in human brain: method and normal values. J Neurosurg 90:109-115.

Ferizi U, Schneider T, Witzel T, et al (2015). White matter compartment models for in vivo diffusion MRI at 300mT/m. Neuroimage 118:468-483.

Ferizi U, Schneider T, Panagiotaki E, et al (2014). A ranking of diffusion MRI compartment models with in vivo human brain data. Magn Reson Med 72:1785-1792.

Fields RD (2008). White matter in learning, cognition and psychiatric disorders. Trends Neurosci 31:361-370.

FitzGibbon T, Nestorovski Z (2013). Human intraretinal myelination: axon diameters and axon/myelin thickness ratios. Indian J Ophthalmol 61:567-575.

Fujiyoshi K, Hikishima K, Nakahara J, et al (2016). Application of q-Space diffusion MRI for the visualization of white matter. J Neurosci 36:2796-2808.

Giuliodori MJ, DiCarlo SE (2004). Myelinated vs. unmyelinated nerve conduction: a novel

way of understanding the mechanisms. Adv Physiol Educ 28: 80-81.

Grussu F, Schneider T, Yates RL, et al (2016). A framework for optimal whole-sample histological quantification of neurite orientation dispersion in the human spinal cord. J. Neurosci Methods 273:20-32.

Grussu F, Schneider T, Zhang H, et al (2015). Neurite orientation dispersion and density imaging of the healthy cervical spinal cord in vivo. Neuroimage 111:590-601.

Harkins KD, Xu J, Dula AN, et al (2016). The microstructural correlates of T1 in white matter. Magn Reson Med 75:1341-1345.

Harrison R, Bronskill MJ, Henkelman RM (1995). Magnetization transfer and T2 relaxation components in tissue. Magn Reson Med 33:490-496.

Helms G, Dathe H, Kallenberg K, et al (2008). High-resolution maps of magnetization transfer with inherent correction for RF inhomogeneity and T1 relaxation obtained from 3D FLASH MRI. Magn Reson Med 60:1396-1407.

Henkelman RM, Stanisz GJ, Graham SJ (2001). Magnetization transfer in MRI: a review. NMR Biomed 14:57-64.

Henkelman RM, Huang X, Xiang QS, et al (1993). Quantitative interpretation of magnetization transfer. Magn Reson Med 29:759-766.

Herculano-Houzel S (2014). The glia/neuron ratio: how it varies uniformly across brain structures and species and what that means for brain physiology and evolution. Glia 62:1377-1391.

Horowitz A, Barazany D, Tavor I, et al (2015). In vivo correlation between axon diameter and conduction velocity in the human brain. Brain Struct. Funct 220:1777-1788.

Huang SY, Nummenmaa A, Witzel T, et al (2015). The impact of gradient strength on in vivo diffusion MRI estimates of axon diameter. Neuroimage 106:464-472.

Innocenti GM, Caminiti R, Aboitiz F (2015). Comments on the paper by Horowitz et al. (2014). Brain Struct Funct 220:1789-1790.

Johansen-Berg H, Behrens TEJ (2013). Diffusion MRI: From Quantitative Measurement to In vivo Neuroanatomy. London, Elsevier Science.

Kipp L, Cawley N, Prados F, et al (2016). Neurite Orientation Dispersion and Density Imaging (NODDI) in RRMS. In: (Proceedings) 31st Congress of the European-Committee-for-Treatment-and-Research-in-Multiple-Sclerosis (ECTRIMS). Barcelona, p. 9.

Klawiter EC, Schmidt RE, Trinkaus K, et al (2011). Radial diffusivity predicts demyelination in ex vivo multiple sclerosis spinal cords. Neuroimage 55:1454-1460.

Koenig SH, Brown RD 3rd, Spiller M, et al (1990). Relaxometry of brain: why white matter appears bright in MRI. Magn Reson Med 14:482-495.

Lajtha A (2013). Pathological Neurochemistry. New York, NY, US, Springer.

Levesque IR, Pike GB (2009). Characterizing healthy and diseased white matter using quantitative magnetization transfer and multicomponent T2 relaxometry: a unified view via a four-pool model. Magn Reson Med 62:1487-1496.

Levesque IR, Sled JG, Narayanan S, et al (2010). Reproducibility of quantitative magnetization-transfer imaging parameters from repeated measurements. Magn Reson Med 64:391-400.

Liewald D, Miller R, Logothetis N, et al (2014). Distribution of axon diameters in cortical white matter: an electron-microscopic study on three human brains and a macaque. Biol Cybern 108:541-557.

Lundell H, Sønderby CK, Dyrby TB (2015). Diffusion weighted imaging with circularly polarized oscillating gradients. Magn Reson Med 73:1171-1176.

MacKay A, Whittall K, Adler J, et al (1994). In vivo visualization of myelin water in brain by magnetic resonance. Magn Reson Med 31:673-677.

MacMillan EL, Mädler B, Fichtner N, et al (2011). Myelin water and T(2) relaxation measurements in the healthy cervical spinal cord at 3.0T: repeatability and changes with age. Neuroimage 54:1083-1090.

Ma D, Gulani V, Seiberlich N, et al (2013). Magnetic resonance fingerprinting. Nature 495:187-192.

Marques JP, Kober T, Krueger G, et al (2010). MP2RAGE, a self bias-field corrected sequence for improved segmentation and T1-mapping at high field. Neuroimage 49: 1271-1281.

Meier C, Dreher W, Leibfritz D (2003). Diffusion in compartmental systems. II. Diffusion-weighted measurements of rat brain tissue in vivo and postmortem at very large b-values. Magn Reson Med 50: 510-514.

Meyers SM, Vavasour IM, Mädler B, et al (2013). Multicenter measurements of myelin water fraction and geometric mean T2 : intra- and intersite reproducibility. J Magn Reson

Imaging 38:1445-1453.

Mezer A, Yeatman JD, Stikov N, et al (2013). Quantifying the local tissue volume and composition in individual brains with magnetic resonance imaging. Nat Med 19:1667-1672.

Morell P, Quarles RH (1999). Myelin Formation, Structure and Biochemistry. Philadelphia, PA, Lippincott-Raven, Chapter 4.

Mottershead JP, Schmierer K, Clemence M, et al (2003). High field MRI correlates of myelin content and axonal density in multiple sclerosis--a post-mortem study of the spinal cord. J Neurol 250:1293-1301.

Nielsen S, Nagelhus EA, Amiry-Moghaddam M, et al (1997). Specialized membrane domains for water transport in glial cells: high-resolution immunogold cytochemistry of aquaporin-4 in rat brain. J Neurosci 17:171-180.

Nisson M, van Western D, Ståhlberg F, et al (2013). The role of tissue microstructure and water exchange in biophysical modelling of diffusion in white matter. MAGMA 26:345-370.

Nilsson M, Lätt J, Ståhlberg F, et al (2012). The importance of axonal undulation in diffusion MR measurements: a Monte Carlo simulation study. NMR Biomed 24:279-805.

Norton WT, Autilio LA (1966). The lipid composition of purified bovine brain myelin. J Neurochem 13: 213-222.

Norton WT, Cammer W (1984). Isolation and characterization of myelin. In: Morell P (Ed), Myelin. Boston, Springer US, pp. 147-195.

O'Brien JS, Sampson EL (1965). Lipid composition of the normal human brain: gray matter, white matter, and myelin. J Lipid Res 6:537-544.

Oh SH, Bilello M, Schindler M, et al (2013). Direct visualization of short transverse relaxation time component (ViSTa). Neuroimage 83:485-492.

Ong HH, Wehrli FW (2010). Quantifying axon diameter and intra-cellular volume fraction in excised mouse spinal cord with q-space imaging. Neuroimage 51:1360-1366.

Panagiotaki E, Schneider T, Siow B, et al (2012). Compartment models of the diffusion MR signal in brain white matter: a taxonomy and comparison. Neuroimage 59:2241-2254.

Perge JA, Koch K, Miller R, et al (2009). How the optic nerve allocates space, energy capacity, and information. J Neurosci 29: 7917-7928.

Prasloski T, Rauscher A, MacKay AL, et al (2012). Rapid whole cerebrum myelin water imaging using a 3D GRASE sequence. Neuroimage 63:533-539.

Rovira A, Auger C, Alonso J (2013). Magnetic resonance monitoring of lesion evolution in multiple sclerosis. Ther Adv Neurol Disord 6:298-310.

Saito N, Watanabe M, Sakai O, et al (2012). Human lifespan age-related changes of the brain proton density by quantitative MRI. In: Proceedings of the 20th Annual Meeting of ISMRM. Melbourne, p. 780.

Schmierer K, Scaravilli F, Altmann DR, et al (2004). Magnetization transfer ratio and myelin in postmortem multiple sclerosis brain. Ann Neurol 56:407-415.

Schmierer K, Wheeler-Kingshott CA, Tozer DJ, et al (2008). Quantitative magnetic resonance of postmortem multiple sclerosis brain before and after fixation. Magn Reson Med 59:268-277.

Schwartz ED, Duda J, Shumsky JS, et al (2005). Spinal cord diffusion tensor imaging and fiber tracking can identify white matter tract disruption and glial scar orientation following lateral funiculotomy. J Neurotrauma 22:1388-1398.

Sepehrband F, Alexander DC, Kurniawan ND, et al (2016). Towards higher sensitivity and stability of axon diameter estimation with diffusion-weighted MRI. NMR Biomed 29:293-308.

Shemesh N, Álvarez GA, Frydman L (2015). Size Distribution Imaging by Non-Uniform Oscillating-Gradient Spin Echo (NOGSE) MRI. PLoS One 10: e0133201.

Shepherd VA (2006). The cytomatrix as a cooperative system of macromolecular and water networks. Curr Top Dev Biol 75:171-223.

Sheth V, Shao H, Chen J, et al (2016). Magnetic resonance imaging of myelin using ultrashort Echo time (UTE) pulse sequences: phantom, specimen, volunteer and multiple sclerosis patient studies. Neuroimage 136:37-44.

Smith SM, Jenkinson M, Woolrich MW, et al (2004). Advances in functional and structural MR image analysis and implementation as FSL. Neuroimage 23 Suppl 1: S208-219.

Stejskal EO, Tanner JE (1965). Spin diffusion measurements: spin echoes in the presence of a time-dependent field gradient. The Journal of Chemical Physics 42:288-292.

Stikov N, Campbell JS, Stroh T, et al (2015a). Quantitative analysis of the myelin g-ratio from electron microscopy images of the macaque corpus callosum. Data Brief 4:368-373.

Stikov N, Campbell JS, Stroh T, et al (2015b). In vivo histology of the myelin g-ratio with magnetic resonance imaging. Neuroimage 118:397-405.

Stüber C, Morawski M, Schäfer A, et al. (2014). Myelin and iron concentration in the human brain: a quantitative study of MRI contrast. Neuroimage 93 Pt 1:95-106.

Syková E, Nicholson C (2008). Diffusion in brain extracellular space. Physiol Rev 88: 1277-1340.

Syková E, Vargová L, Prokopová S, et al (1999). Glial swelling and astrogliosis produce diffusion barriers in the rat spinal cord. Glia 25:56-70.

Tariq M, Schneider T, Alexander DC, et al (2012). Scan-rescan reproducibility of neurite microstructure estimates using NODDI. In: Xie X (Ed) Medical Image Understanding and Analysis 2012: Proceedings of the 16th Conference on Medical Image Understanding and Analysis. Swansea, UK, pp. 255-261.

Taso M, Girard OM, Duhamel G, et al (2016). Tract-specific and age-related variations of the spinal cord microstructure: a multi-parametric MRI study using diffusion tensor imaging (DTI) and inhomogeneous magnetization transfer (ihMT). NMR Biomed 29:817-832.

Tofts P (2003). Quantitative MRI of the Brain: Measuring Changes Caused by Disease. Chichester, UK, John Wiley & Sons.

Tofts PS (2003). PD: proton density of tissue water. In: Tofts (Ed), Quantitative MRI of the brain. Chichester, UK, John Wiley & Sons, 85-109.

Van AT, Holdsworth SJ, Bammer R (2014). In vivo investigation of restricted diffusion in the human brain with optimized oscillating diffusion gradient encoding. Magn Reson Med 71:83-94.

Vollmar C, O'Muircheartaigh J, Barker GJ, et al (2010). Identical, but not the same: intra-site and inter-site reproducibility of fractional anisotropy measures on two 3.0T scanners. Neuroimage 51: 1384-1394.

Volz S, Nöth U, Deichmann R (2012). Correction of systematic errors in quantitative proton density mapping. Magn Reson Med 68:74-85.

Wang LZ, Caprihan A, Fukushima E (1995). The Narrow-Pulse Criterion for Pulsed-Gradient Spin-Echo Diffusion Measurements. J Magn Reson A 117:209-219.

West KL, Kelm ND, Carson RP, et al (2016a). A revised model for estimating g-ratio from

MRI. Neuroimage 125:1155-1158.

West KL, Kelm ND, Gochberg DF, et al (2016b). Quantitative estimates of myelin volume fraction from T2 and magnetization transfer. In: Proceedings of the 24th Annual Meeting of ISMRM, . Singapour, p. 1277.

Wheeler-Kingshott CA, Cercignani M (2009). About “axial” and “radial” diffusivities. Magn Reson Med 61:1255-1260.

Wolff SD, Balaban RS (1989). Magnetization transfer contrast (MTC) and tissue water proton relaxation in vivo. Magn Reson Med 10: 135-144.

Wu Y, Alexander AL, Fleming JO, et al (2006). Myelin water fraction in human cervical spinal cord in vivo. J Comput Assist Tomogr 30: 304-306.

Zaimi A, Duval T, Gasecka A, et al (2016). AxonSeg: open source software for axon and myelin segmentation and morphometric analysis. Front Neuroinform 10:37.

Zhang H, Hubbard PL, Parker GJM, et al (2011). Axon diameter mapping in the presence of orientation dispersion with diffusion MRI. Neuroimage 56: 1301-1315.

Zhang H, Schneider T, Wheeler-Kingshott CA, et al. (2012). NODDI: practical in vivo neurite orientation dispersion and density imaging of the human brain. Neuroimage 61: 1000-1016.

CHAPITRE 3 DÉMARCHE DE L'ENSEMBLE DU TRAVAIL

Les mesures quantitatives en IRM passent donc par l'acquisition de plusieurs images IRM avec des contrastes différents, jusqu'à plusieurs centaines pour l'imagerie IRM de diffusion. Se posent alors plusieurs défis pour les chercheurs : (i) comment combiner ces différents contrastes pour obtenir une mesure quantitative (problème de modélisation du signal), (ii) quels contrastes (et donc quels paramètres d'acquisition IRM) doivent être acquis pour faire des mesures précises et exactes (problème d'optimisation des protocoles), (iii) quels sont les facteurs pouvant biaiser les mesures (problèmes de correction d'artefact, de calibration) et (iv) comment extraire les mesures de façon systématique et reproductible (problèmes de traitement d'image). Prenons l'exemple de l'IRM de diffusion qui encode le mouvement brownien (diffusion) des molécules d'eau au sein d'un tissu par une perte de signal (Le Bihan et al., 1986; Stejskal and Tanner, 1965). Chaque image contrastée en diffusion (DWI) informe sur la proportion de molécules d'eau qui s'est déplacée d'une distance de plus de 1/q (définie par l'intensité Gmax et la durée δ d'application d'une paire de gradient de champ magnétique), pendant un temps Δ (délai séparant l'application des deux champs magnétique) et dans une direction donnée $\vec{u}$ (direction des gradients). Il s'agit donc d'une mesure très indirecte de la diffusion. Le premier défi consiste donc à décrire analytiquement le phénomène, en faisant des hypothèses probabilistes (e.g. diffusion gaussienne), puis interpréter la solution. Ceci a donné naissance à une multitude de modèles bio-physiques plus ou moins simplistes, plus ou moins applicables en clinique, et difficiles à valider.

Ces dernières années, plusieurs expériences d'IRM quantitative, exploitant ces modèles bio-physiques, ont été effectuées sur la moelle épinière animale *ex vivo* montrant (i) un bon contraste entre les tractus de la moelle (Ong and Wehrli, 2010; Shemesh et al., 2013) et (ii) une meilleure sensibilité aux lésions traumatique par rapport aux images d'IRM anatomique classique (Nossin-Manor et al., 2002). La première étape de cette thèse fût d'appliquer ces modèles afin d'obtenir des valeurs quantitatives *in vivo* dans les différents tractus de la moelle épinière humaine. Pour cela, nous avons mis en place un protocole IRM puis une chaîne de traitement (voir articles des **chapitres 4, 5 et 6**). Le protocole choisi s'est appuyé

sur les innovations technologiques qu'a observé l'IRM ces dernières années, abordées en introduction, afin d'obtenir des images de moelle épinière *in vivo* de haute qualité, très rapidement, et pour différents contrastes.

Bien que des expériences sur l'humain *in vivo* ont déjà montré que des biomarqueurs IRM liés à la microstructure des fibres peuvent être extraits sur des scanners cliniques (i.e. Gmax=60mT/m) (Alexander et al., 2010; Grussu et al., 2015; Schneider et al., 2012), il y a cependant une limitation intrinsèque au diamètre axonal minimum auquel on peut être sensible (Bar-Shir et al., 2008; Huang et al., 2015; Nilsson and Alexander, 2012). Le diamètre minimum est ainsi aux alentour de 6µm à 60mT/m et 3µm à 300mT/m (Nilsson and Alexander, 2012), soit du même ordre de grandeur que les axones myélinisés de la moelle humaine où 90% des axones ont un diamètre compris entre 1 et 4µm (Lassek, 1945). Ainsi, grâce à ses gradients élevés (Gmax=300mT/m), l'IRM "Connectom" a montré des résultats encourageant pour l'estimation de diamètre axonale sur le corps calleux humain (Huang et al., 2015; McNab et al., 2013). L'utilisation de ce scanner pour extraire une information quantitative sur la moelle humaine *in vivo* est détaillé dans l'article du **chapitre 4**.

Les méthodes d'IRM quantitative se heurtent cependant toutes à une difficulté : l'information obtenue est partielle et ne permet pas de donner une vision complète de l'intégrité du tissu. Pour reprendre l'exemple de l'IRM de diffusion, cette méthode est sensible uniquement aux protons des molécules d'eau libres, et est aveugle à la myéline et autres macromolécules. L'épaisseur de la gaine de myéline entourant les axones, une information pourtant cruciale pour diagnostiquer l'évolution de patient atteints de maladies neuro-dégénérative, n'est donc pas mesurable avec l'IRM de diffusion seule. L'idée proposée par nos collaborateurs de l'université McGill est donc de combiner plusieurs méthodes d'IRM quantitative afin d'obtenir cette information (Stikov et al., 2011). L'application de cette méthode sur l'humain *in vivo* est détaillé dans l'article du **chapitre 5**.

Un important défi lors de l'application de l'IRM quantitative *in vivo* consiste alors à corriger, ou à se prémunir de tout biais potentiel. Il y a ainsi l'effet du bruit des antennes de moyenne non-nulle (Aja-Fernández et al., 2011; Koay et al., 2009); du mouvement du patient (Mohammadi et al., 2013); de la courbure de sa moelle (Duval et al., 2015); du repliement potentiel de signal issue de la graisse du cou, de sa pulsation cardiaque (qui peut entraîner une perte de signal) (Piché et al., 2009; Summers et al., 2006), du flou lié aux inhomogénéités local du champ (T2*) et des effets de volume partielle (CSF et matière blanche combinés dans un pixel) (Lévy et al., 2015), ou encore des artefacts de Gibbs (Block et al., 2008). Des algorithmes prenant en compte ces biais ont été développés et intégrés à la librairie open-source Spinal Cord Toolbox[4] (SCT) développée au sein du laboratoire (De Leener et al., 2016). En plus de la correction des biais, cette librairie a été développée pour répondre à un important défi : traiter de façon systématique et reproductible les images IRM de la moelle épinière. Tout une chaîne de post-traitement incluant la création d'un atlas des tractus de la moelle, recalage de cet atlas sur la moelle de chaque sujet, et extraction des mesures a été mis en place. Cela a permis dès nos premiers essais à faire des analyses statistiques par tractus de la moelle, automatiquement. Le projet SCT a grandi aux côtés de nos essais d'IRM quantitative de la moelle, les deux projets s'abreuvant mutuellement. La bonne reproductibilité entre deux scans successifs du protocole et de la chaîne de traitement a été validée dans l'article 4 du **chapitre 6**.

Des solutions ont été proposées pour post-traiter ces images, les combiner et enfin les exploiter. Tous ces défis techniques surmontés, l'utilisation de l'IRM quantitative sur la moelle épinière humaine peut donc être envisagée.

[4] https://sourceforge.net/projects/spinalcordtoolbox/

Les problèmes de modélisation bio-physique du signal IRM ont été abordés dans l'article de revue du **chapitre 2** (Modeling White Matter Microstructure), et une bonne partie de cette thèse a été consacrée à la validation de ces modèles par la mise en place de l'histologie à grand champ de vue avec segmentation automatique de la myéline. Les résultats de cette validation sont détaillés dans les articles des **chapitres 7 et 8**.

Enfin, afin que cette recherche ait une réalité clinique, des études sur le transfert des méthodes d'IRM quantitative sur IRM clinique à gradients modéré, ainsi que l'applicabilité sur des patients atteint de sclérose en plaques, était nécessaire. Ces travaux, présentés en conférences (Duval et al., 2017, 2016), sont décrits au **chapitre 9**.

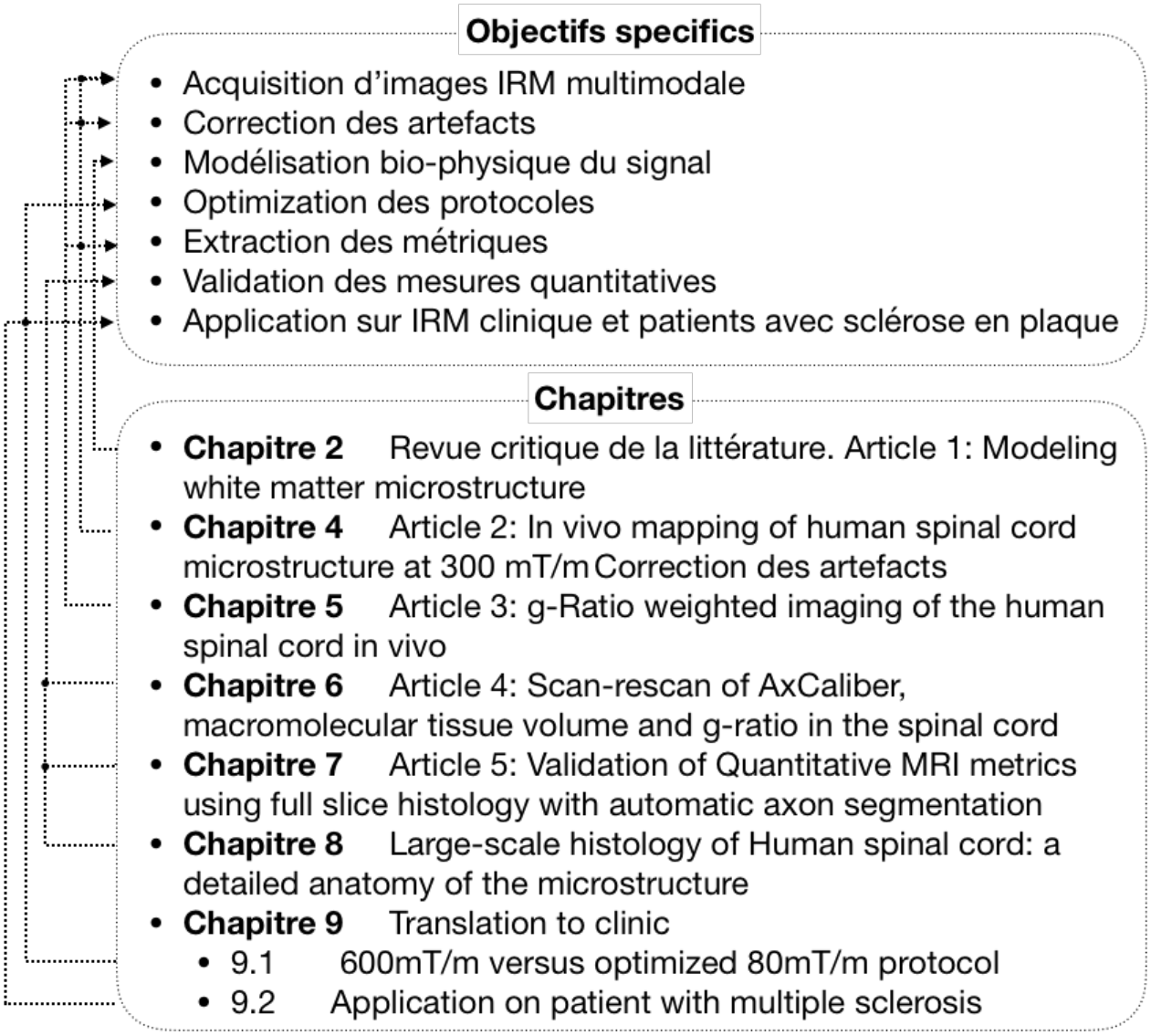

Figure 3.1: Structure de la thèse

CHAPITRE 4 ARTICLE 2: IN VIVO MAPPING OF HUMAN SPINAL CORD MICROSTRUCTURE AT 300 MT/M

Journal – NeuroImage - Elsevier

Tanguy Duval[1], Jennifer A. McNab[2], Kawin Setsompop[3], Thomas Witzel[3], Torben Schneider[4], Susie Yi Huang[3], Boris Keil[3], Eric C. Klawiter[5], Lawrence L. Wald[3], and Julien Cohen-Adad[1,6]

[1]*Institute of Biomedical Engineering, Polytechnique Montreal, Montreal, QC, Canada*

[2]*Department of Radiology, Stanford University, Stanford, CA, United States,*

[3]*A.A. Martinos Center for Biomedical Imaging, Massachusetts General Hospital, Harvard Medical School, Charlestown, MA, United States,*

[4]*NMR Research Unit, Department of Neuroinflammation, Queen Square MS Centre, UCL Institute of Neurology, London, London, United Kingdom*

[5]*Department of Neurology, Massachusetts General Hospital, Harvard Medical School, Boston, MA, United States*

[6]*Functional Neuroimaging Unit, CRIUGM, Université de Montréal, Montreal, QC, Canada*

The ability to characterize white matter microstructure non-invasively has important applications for the diagnosis and follow-up of several neurological diseases. There exists a family of diffusion MRI techniques, such as AxCaliber, that provide indices of axon microstructure, such as axon diameter and density. However, to obtain accurate measurements of axons with small diameters (<5 μm), these techniques require strong gradients, i.e. an order of magnitude higher than the 40-80 mT/m currently available in clinical systems. In this study we acquired AxCaliber diffusion data at a variety of different q-values and diffusion times in the spinal cord of five healthy subjects using a 300 mT/m whole body gradient system. Acquisition and processing were optimized using state-of-the-art methods (e.g., 64-channel coil, template-based analysis). Results consistently show an average axon diameter of 4.5 +/- 1.1 μm in the spinal cord white matter. Diameters ranged from 3.0 μm (gracilis) to 5.9 μm (spinocerebellar tracts). Values were similar across laterality (left-right), but statistically different across spinal cord pathways ($p<10^{-5}$). The observed trends are similar to those observed in animal histology. This study shows, for the first time, in vivo mapping of axon diameter in the spinal cord at 300 mT/m, thus creating opportunities for applications in spinal cord diseases.

Keywords*: diffusion MRI, AxCaliber, axon diameter, quantification, human, spinal cord*

Contribution: *Acquisition and analysis of the MRI data, redaction of the article and generation of the figures.*

Submitted: *3 December 2014*

Accepted: *11 June 2015*

4.1 Introduction

The spinal cord white matter is organized into bundles of myelinated and unmyelinated axons. Each bundle, or pathway, conveys ascending or descending electrical signals that are essential to ensure adequate synergy between the brain and the peripheral nervous system. Any damage to these axons can have a dramatic impact on a person's quality of life leading to motor (paralysis) and/or sensory deficits; and, in some cases, neuropathic pain (Dijkers et al., 2009). Axon damage can have various causes, such as spinal cord injury, autoimmune and neurodegenerative diseases (e.g., multiple sclerosis), cancers, and vascular diseases. Due to the highly specific roles of each spinal pathway in the regulation of the central nervous system, the prognosis of functional recovery, for a patient who has sustained an injury, strongly depends on the type of pathways damaged (Rossignol et al., 2006). Moreover, in some pathologies, specific populations of axons are preferentially targeted: multiple sclerosis affects smaller axons first (DeLuca et al., 2004), while motor-neuron diseases target larger axons (Cluskey and Ramsden, 2001). These observations motivate the development of non-invasive biomarkers of axon diameter sizes for a better understanding of the pathophysiology of those diseases, and to improve precision of diagnosis and validation of therapeutic strategies.

In the human spinal cord, the internal diameter of myelinated axons varies from 1 to 10µm (Peters et al., 1991; Waxman et al., 1995). Large axons are believed to have higher firing frequencies and conduction velocities, at the expense of more energy used (Perge et al., 2012). Histological studies reported large differences of axonal microstructure (e.g., mean axon diameter, density and myelin membrane thickness) across spinal pathways (Dula et al., 2010; Nieuwenhuys et al., 2007). For instance, dorsal column axons in the gracilis are generally smaller than that in the cuneatus (Nieuwenhuys et al., 2007). However, due to the need for sub-micrometric resolution and the difficulty in performing histology across the entire spinal cord with large throughput, there is poor documentation of spinal cord microstructure in humans.

Diffusion magnetic resonance imaging (MRI) measures the random microscopic motion (diffusion) of water protons (Le Bihan et al., 1986; Stejskal and Tanner, 1965). In white matter, water molecules diffuse preferentially along the coherently oriented myelinated axons (Beaulieu and Allen, 1994). This anisotropic diffusion is often modeled as a tensor (diffusion tensor imaging, DTI) (Basser and Pierpaoli, 1996) and was shown to correlate with demyelination and/or axonal loss (Klawiter et al., 2011; Song et al., 2005). However, the interpretation of water diffusion via a tensor is often challenging, as diffusion anisotropy can be affected by axon density, size and shape and other fibrous structure such as scar tissue (Schwartz et al., 2005; Wheeler-Kingshott and Cercignani, 2009). A family of advanced diffusion MRI, called q-space imaging, measures the full diffusion propagation profile of water molecules at a given diffusion time (Callaghan et al., 1988), providing metrics related to the microstructure (Lätt et al., 2008; Ong et al., 2008). Moreover, by introducing models of white matter, diffusion MRI can quantify the relative size of compartments where diffusion is restricted (within axons), hindered (between axons) and free (Gaussian) (Assaf and Basser, 2005). Based on these compartments, Assaf et al. introduced a method called "AxCaliber" which is sensitive to axon diameter distribution (Assaf et al., 2008). In practice, this is achieved by varying the strength of the diffusion-sensitizing gradients (G_{max}) and the duration between the applications of these two diffusion gradients (diffusion time, Δ). In recent years, several diffusion MRI experiments were performed in the animal ex vivo spinal cord showing (i) good contrast of microstructure parameters between the spinal cord pathways (Ong and Wehrli 2010; Shemesh et al. 2013) and (ii) better sensitivity to traumatic lesions compared to anatomical images (Nossin-Manor et al. 2002). Results from diffusion MRI in the in vivo human spinal cord also showed that metrics related to tissue microstructure could be extracted (Grussu et al. 2015).

However, model-free (Lätt et al., 2008; Ong et al., 2008) and model-based (Assaf et al., 2008) quantitative diffusion MRI methods require strong magnetic gradients (several hundreds of mT/m) in order to obtain accurate measures of axon diameters and are therefore not feasible in clinical scanners (40-80 mT/m) (Bar-Shir et al., 2008). Other

model-based diffusion MRI techniques like ActiveAx (Alexander, 2008) can yield robust estimate of axon diameters even at 60 mT/m (Alexander et al., 2010; Schneider et al., 2012) but come at the expense of adding more constraints to the model, which can introduce further bias in the estimation (Alexander et al., 2010). Furthermore, despite advances in the modeling approaches to axon diameter measurements there is an intrinsic limitation in the minimum axon diameters that can be disentangled (Huang et al., 2015; Nilsson and Alexander, 2012). For example, the minimal axon diameter is around 6μm at 60mT/m and 3μm at 300mT/m (Nilsson and Alexander, 2012). This justifies the use of strong gradients for advanced diffusion MRI experiments. A corollary advantage of using stronger gradients is the possibility to achieve lower echo times (TE) while keeping b-value constant, which offers significantly higher signal-to-noise ratio (Cohen-Adad et al., 2011). Recently, the first human scanner equipped with 300 mT/m gradients showed encouraging applications in humans including mapping axon diameter distributions in the in vivo human corpus callosum (McNab et al. 2013; Huang et al. 2015).

The goals of the current study were (i) to design an experimental setup and acquire q-space AxCaliber data in the *in vivo* human cervical spinal cord using 300 mT/m gradients and (ii) to estimate axon diameters and density within specific spinal pathways. Data acquisition and processing were optimized using state-of-the-art methods, including a 64-channel coil (Keil et al., 2013) and a newly-developed template and atlas of spinal cord (Benhamou et al., 2014; Fonov et al., 2014) for automatic and unbiased quantification of metrics within specific spinal pathways.

4.2 Methods

4.2.1 Acquisition

Five healthy subjects were recruited (mean age 28 +/- 11, three males). This study was approved by the institutional review board at Massachusetts General Hospital (MGH) and written informed consent was obtained from all subjects. MR experiments were performed on a 3T system (MAGNETOM, Siemens Healthcare, Germany), equipped with a Connectom Gradient (AS302) (Setsompop et al., 2013) capable of up to 300 mT/m along each axis and a maximum slew rate of 200 mT/m/ms (downgraded to 90 mT/m/ms for the diffusion gradients due to safety concerns). A custom-made 60-channel phased-array head/neck receive coil was used, in combination with the 4 more superior elements of the commercial spine matrix (Keil et al., 2013), yielding 64 channels. The isocenter was set at the level of the mouth.

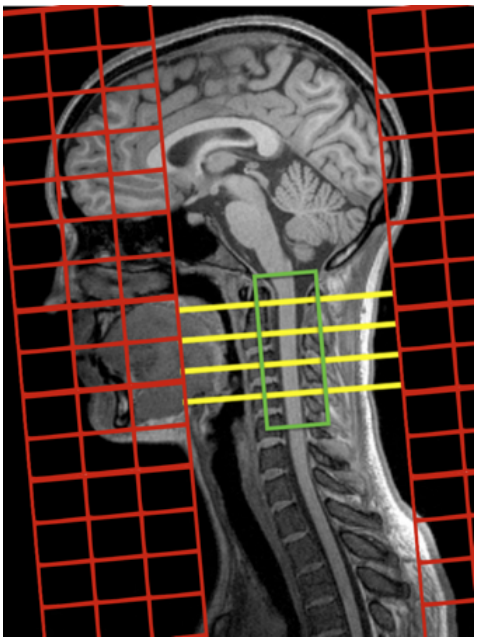

Figure 4.1: Placement of slices (yellow), saturation bands (red) and shimming volume (green). Four slices were placed in the middle of the vertebral body at levels C1, C2, C3 and C4, by adjusting the slice gap for each subject. Slices were orthogonal to the SC. Optimal shim coefficients (up to 2nd order) were calculated within a small box encompassing the spinal cord. To prevent aliasing associated with reduced FOV, two saturation bands were prescribed anteriorly and posteriorly.

Diffusion weighted (DW) data were acquired using a single shot spin echo EPI sequence with monopolar gradient scheme. Four axial slices (5 mm thick) were centered at C1, C2, C3 and C4 vertebral bodies to minimize B0 inhomogeneity (Cohen-Adad et al., 2011), as illustrated in **Figure 4.1**. Optimal shim coefficients of second order were calculated within a small box encompassing the spinal cord (green box in **Figure 4.1**). Two saturation bands were prescribed anterior and posterior to the spinal cord to prevent aliasing in the phase-encoding direction (A-P) (red grids in **Figure 4.1**).

Q-space was sampled in the plane orthogonal to the slice-select gradient (i.e., orthogonal to the main direction of spinal tracts) along four opposite directions: XY, -XY, X-Y and -X-

Y, as illustrated in **Figure 4.2**.a. These four directions were chosen in order to (i) correct eddy-current distortions using the reversed-gradient method (Bodammer et al., 2004), (ii) minimize the bias introduced by fibers that would be not perfectly aligned along Z and (iii) maximize gradient strength by a factor √2, given that 300 mT/m is available in each channel and can be summed up. Sampling density was increased quadratically towards high q-values to overcome the loss of SNR and be more sensitive to smaller axon diameters.

Sequence parameters were: pulse width δ= 8 ms, maximal gradient strength G_{max} = √2 * 300 = 410 mT/m, diffusion times Δ = {20, 35, 50} ms, TE = {65, 70, 85} ms (minimized for each diffusion time), TR ≈ 2 s (depends on cardiac rate), voxel size = 0.8×0.8×5 mm^3, matrix size = 128×128, bandwidth = 1185 Hz/pixel, R=2 acceleration with GRAPPA reconstruction, effective echo spacing (accounting for acceleration) = 0.49 ms. Acquisitions were cardiac-gated using pulse oximeter probe. Acquisition window for gating was set to 700 ms and started at 100 ms after the pulse oximeter peak to be in the quiescent regime (Summers et al., 2006). Acquisition time for the AxCaliber protocol was around 30 min for a total of 623 images.

In addition to the AxCaliber protocol, 43 volumes were acquired with diffusion gradients rotating about the spinal cord axis (see **Figure 4.2**.b), with b-value set to 8,770 s/mm^2 (δ=8 ms, Δ=50 ms, G_{max}=200 mT/m). This was done to quantify the contribution of axons that were not perfectly aligned along the Z axis, as they would create an angular dependence on the diffusion-weighted signal.

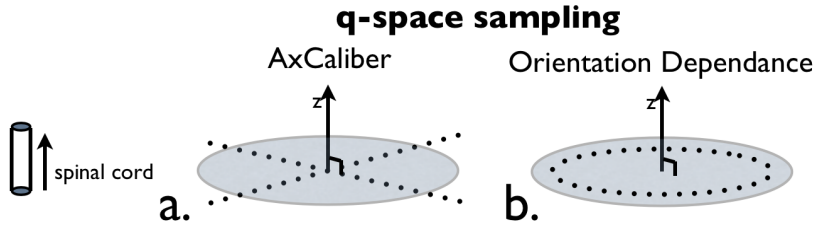

Figure 4.2: Illustration of the diffusion encoding gradients used in the AxCaliber protocol (**a**) and in the protocol for probing orientation dependence (**b**). The latter protocol aims at exploring fibers that are not oriented along Z (e.g., collateral fibers entering the dorsal aspect of the cord).

4.2.2 Preprocessing

4.2.2.1 Eddy-current correction

Reversed-gradients technique was used for correcting eddy-current artifacts (Bodammer et al., 2004). This technique consists of estimating the transformation between two images acquired with opposite diffusion gradient directions. To improve accuracy, each slice was corrected independently, assuming only rigid transformation (Tx, Ty). No scaling or shearing was estimated, which, to our preliminary data, was a satisfactory assumption, given that the spinal cord occupies a relatively small region (~1×1 cm^2), and hence is minimally affected by transformations that scales with X and Y. The slice-wise correction was preferred to the volume-based correction because the amplitude of eddy-current artifacts varied along Z, yielding non-rigid deformations. Transformations were estimated with FSL FLIRT (Jenkinson et al., 2002), using a custom-made schedule file[5]. A 2D Gaussian mask centered on the spinal cord was used as a weighting mask in order to register the spinal cord independently from the rest of the body (e.g., surrounding muscles, fat). All transformations were then saved (for final combination with motion correction transformations) and applied (for estimating motion correction, see below).

4.2.3 Motion Correction

After correcting for eddy-current distortions, subject motion was estimated on a slice-by-slice basis using the same schedule file as before (Tx, Ty) and the same Gaussian mask. Contrary to previous studies (Cohen-Adad et al., 2008), interspersed b=0 images were not used to estimate subject motion, because CSF flow affected some b=0 images differently and hence could have introduced spurious motion correction parameters. Instead, motion was estimated based on the diffusion-weighted images that ranged between b-values of 430 s/mm^2 and b-values of 4000 s/mm^2. These values were empirically chosen so that images

[5] https://github.com/neuropoly/spinalcordtoolbox/blob/master/flirtsch/schedule_TxTy.sch

presented sufficient SNR and no visible CSF contamination (see **Figure 4.3**). The first image was used as the reference image for registration (i.e., target image).

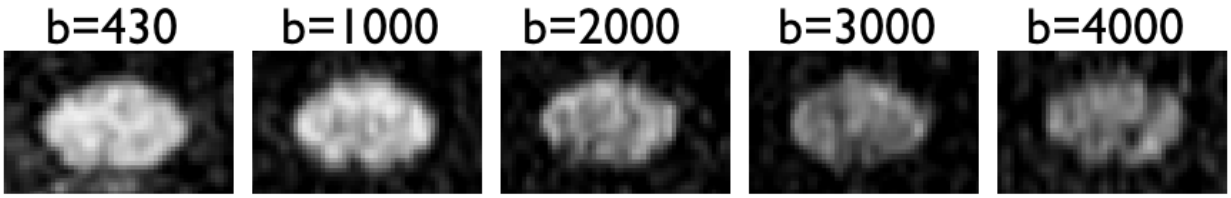

Figure 4.3: Examples of DW images with selected b-values in the lowest range ($430<b<4000$ s/mm^2) used for motion correction. These images offer sufficient SNR for robust estimation of motion parameters without CSF contamination.

To further improve the robustness of the motion correction, x-translations and y-translations were respectively approximated by a spline function (see **Figure 4.4**). This approach was chosen empirically, under the assumption that subject motion is slow with time (low frequency drifts). Images acquired at b<430 and b>4000 s/mm^2 were corrected using extrapolated transformation values from the spline function.

As a final step, in order to reduce the number of interpolations, transformation matrices from eddy-current and motion corrections were combined and applied only once using sinc interpolation.

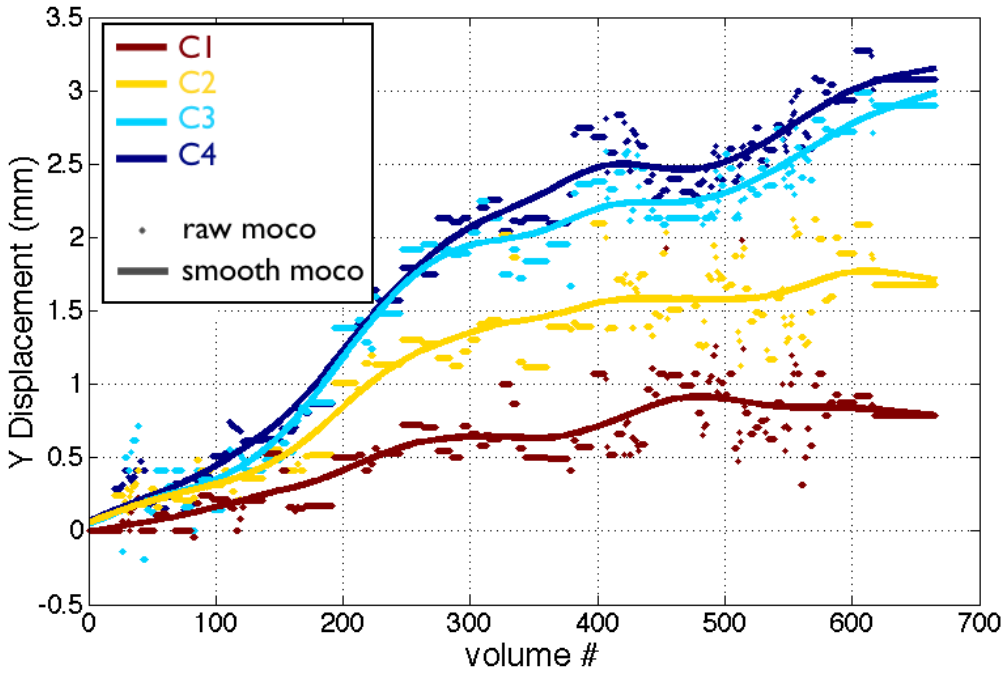

Figure 4.4: Estimated motion in anteroposterior direction (raw moco) and fitted spline functions (smooth moco) at each cervical level in one subject. All data with different Δ were concatenated. Here, "moco" stands for motion correction.

4.2.3.1 Normalization of DW data related to variable TE

All DW data were divided by the mean b=0 image of the corresponding TE to account for T2 relaxation. Here we assumed a single T2 compartment for normalization (see discussion about potential presence of multiple T2 compartments). An additional normalization step was set for each group of Δ during curve fitting (see model fitting below).

4.2.3.2 Bias correction and noise reduction

Magnitude data were bias-corrected assuming Rician noise using the method of (Gudbjartsson and Patz, 1995):

$$A = \sqrt{|M^2 - \sigma^2|} \quad (1)$$

Where A is the true voxel intensity, M is the measured voxel intensity and σ is the standard deviation of the Gaussian noise. The parameter σ was computed by calculating the standard deviation within a moving window (size = 15) along q-values, after detrending the data using the AxCaliber model. All the calculated standard deviations were then averaged within the spinal cord. Preliminary results showed similar sigma across the three Δ values, therefore the three calculated sigma were averaged. Noise was then reduced using the Local Principal Component Analysis (LPCA) algorithm using (Manjón et al., 2013). The reader is referred to the discussion for the potential impact of the LCPA filter for axon diameter estimation.

4.2.4 Model fitting

A modification of the AxCaliber model was implemented in Matlab (MathWorks, Natick, MA). The model was assumed to have two compartments (restricted and hindered) but only a single axon diameter, as proposed in the ActiveAx technique (Alexander et al., 2010). Throughout this manuscript we refer to the AxCaliber model for clarity. Also, fibers were assumed to be oriented along Z.

The model was fitted using a non-linear least square algorithm (using trust-model-reflective optimization), with a maximum of ten iterations for fast convergence (we empirically found that more iterations did not improve accuracy of fitting). Six parameters were estimated: fraction hindered (fh), diffusion hindered coefficient (Dh), mean diameter (d), and the intensities I_{b0}(TE=65 ms), I_{b0}(TE=70 ms) and I_{b0}(TE=85 ms). These parameters are related by the following equation: $I = I_{b0}(\Delta)[fh.Eh(Dh) + (1 - fh).Er(d)]$, where Eh and Er are the signal decay in the hindered and restricted compartment respectively and are defined as follow (Callaghan, 1995):

$$Eh = exp\ (-bD_h) \quad (2)$$

$$E_r = \sum_{k=0}^{\infty}\left[4\exp\left(-\frac{4\beta_{0k}{}^2 D_r \Delta}{d^2}\right)\times\left[\frac{\pi q d\times J_0'(\pi q d)}{(\pi q d)^2-\beta_{0k}{}^2}\right]^2 + \sum_{n=1}^{\infty} 8\exp\left(-\frac{4\beta_{nk}{}^2 D_r \Delta}{d^2}\right)\times\frac{\beta_{nk}{}^2}{\beta_{nk}{}^2-n^2}\times \left[\frac{\pi q d\times J_n'(\pi q d)}{(\pi q d)^2-\beta_{nk}{}^2}\right]^2\right] \quad (3)$$

Where $J_n{}'$ is the first derivative of the nth Bessel function of the first kind and β_{nk} its kth zero crossing. Dr represents the diffusion coefficient in the restricted compartment. See discussions concerning the violation of small pulse approximation.

The fraction of restricted compartment was deduced by complementarity: fr = 1 – fh. Diffusion coefficient for the restricted compartment (Dr) was set to 1.4 μm^2/ms (Barazany et al., 2009). No cerebrospinal fluid (CSF) compartment was included in the model (see Discussion).

The fitting procedure was run voxel-by-voxel using broad limits: fh [0 1]; Dh [0 3] μm2/ms; d [1 10] μm; $I_{b0}(TE)$ [0 2]. Results were plotted and visually inspected. The quality of the fit was assessed by computing the reduced chi-squared statistic for each voxel.

4.2.5 Post-processing

4.2.5.1 Registration to template

Data from all subjects were registered to the white matter template available from the MNI-Poly-AMU template (Fonov et al., 2014). The transformation was estimated from an average of high b-value DW images (>3000 s/mm^2), as these images exhibited the best white/gray matter contrast. A diffeomorphic transformation was estimated using the SyN method available in ANTs (Avants et al., 2008) (see **Figure 4.6**).

4.2.5.2 Extraction of metrics within spinal pathways using maximum likelihood

An atlas of spinal pathways (Benhamou et al., 2014) was used to extract model-based diffusion MRI metrics within specific tracts (see **Figure 4.6**d). Briefly, the atlas was constructed from an existing anatomical reference (Standring, 2008) and then merged within the MNI-Poly-AMU template. The atlas consists of 30 different pathways, each of them accounting for partial volume effect (values ranging from 0 to 1). In order to

disentangle voxels overlapping with adjacent pathways, model-based diffusion MRI metrics were estimated using the maximum likelihood estimation described in the following equation, which assumes homogeneous metric value within each tract:

$$M_{voxel_i} = \sum_{tracts} p_{voxel_i,tract_j} M_{tract_j} \quad (4)$$

Where M_{voxel_i} is the observed metric at voxel i, and M_{tract_j} is the metric to estimate for tract j(assuming homogeneous tracts). $p_{voxel_i,tract_j}$ is the volume fraction of tract j in voxel i, given by the atlas.

If we define the matrix $P = (p_{voxel_i,tract_j})_{i,j}$, we can recast the problem in the form:

$$\overrightarrow{M_{voxels}} = P\overrightarrow{M_{tracts}} \quad (5)$$

Then, the vector $\overrightarrow{M_{tracts}}$ is calculated by computing the pseudoinverse of matrix P:

$$\overrightarrow{M_{tracts}} = (P^t P)^{-1} P^t \overrightarrow{M_{voxels}} \quad (6)$$

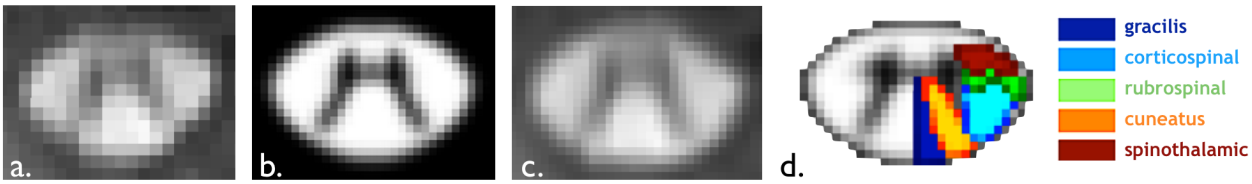

Figure 4.5: a: Mean high b-values images. **b:** image of the template used for registration. **c:** registered image after applying the deformation field. **d:** Five major axonal pathways with different morphological features were selected from the white matter atlas in order to extract model-based diffusion MRI metrics.

All scripts used for preprocessing, template registration and metrics extraction are freely available in the Spinal Cord Toolbox (http://sourceforge.net/projects/spinalcordtoolbox/).

4.2.6 Statistics

SNR was computed voxel-wise by dividing average values (extracted from fits) by the σ computed previously (see section: "Bias correction and noise reduction").

The reduced chi-squared statistic of the fitting curves was calculated voxel-by-voxel as follows:

$$\chi^2_{red} = \frac{\chi^2}{\nu} = \frac{1}{\nu}\sum\frac{(O-E)^2}{\sigma^2} \quad (7)$$

where O are the observed data, E are the theoretical data (i.e. from the AxCaliber model), σ is the Gaussian noise standard deviation and ν is the degree of freedom, given by $N - n - 1$, where N is the number of observations, and n is the number of fitted parameters. Here, N=623 and n=6. Based on previous studies validating the AxCaliber model (Panagiotaki et al. 2012), we anticipate χ^2_{red} values to be close to one.

The quantity $\chi^2 = \chi^2_{red} \cdot \nu$ follows a chi-squared distribution f using the degree of freedom ν. To assess whether the AxCaliber model correctly fitted our data, the area under the χ^2 distribution (α) was calculated as follows:

$$\alpha = \int_{\chi^2_{vox}}^{\infty} f(x)\, dx \quad (8)$$

Due to the large degree of freedom ν, a significant difference between the fitted model and the data is expected to be found, resulting in very small values of α.

A three-way ANOVA was performed to assess whether there are any significant differences (significance level set to p=0.05) of axon diameters between the pathways of each subject, between the right and the left pathways, and between the five subjects themselves.

4.2.6.1 Reproducibility tests

The reproducibility of extracted metrics over the direction of diffusion gradients was assessed by analyzing two sub-datasets of acquired q-space data (see **Figure 4.13**): one with diffusion-gradient along (-X,+Y; +X,-Y) and one along (-X,-Y; +X,+Y). Each sub-dataset was processed separately and then compared.

The reproducibility of extracted metrics over q-space sampling was assessed using a bootstrap analysis in one subject. Q-space data were randomly subsampled by 10% and 90% were kept for analysis. This procedure was run 200 times in order to derive standard deviations, related to q-space sampling, of extracted metrics in each voxel.

4.2.6.2 Orientation dependence

The rotational symmetry of water diffusion in the spinal cord was studied using the data from the protocol b (**Figure 4.2**.b). After normalizing with the b=0 images, the curve representing the MR signal as a function of gradient direction was low-pass filtered using sine and cosine functions. The peak-to-peak variation was used to indicate the orientation dependence. The angle at the minima (i.e., larger signal loss) corresponded to the direction of the crossing fibers.

4.3 Results

4.3.1 Quality of the data

Data were successfully acquired in all five subjects. **Figure 4.6** illustrates data acquired in a subject at four different b-values (0, 450, 5924 and 39011 s/mm2). Even at maximum b-value (39,011 s/mm^2, with δ=8 ms, Δ=50 ms and G=300*√2=424 mT/m), signal from the spinal cord white matter is visible. The majority of this signal likely comes from the restricted compartment, given that the signal from the hindered and free compartments was lost due to the strong dephasing.

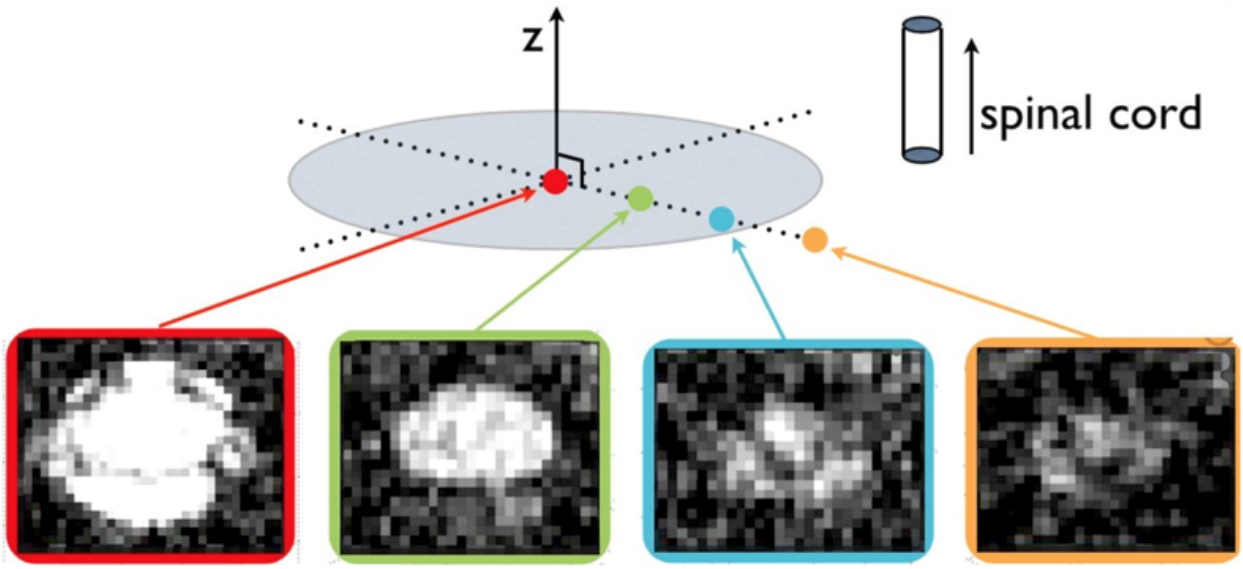

Figure 4.6: Example of images acquired at different q-vectors. Data are not interpolated. Contrast is kept the same for better comparison. Notice the low SNR at very-high q-value (orange), which was compensated by averaging over the four directions.

Figure 4.7 shows the data in one subject averaged across q, before and after applying eddy-current and motion correction. The corrected data shows sharper edges, suggesting that the preprocessing pipeline was effective. Notice the visible gray/white matter contrast, which was helpful in registering the spinal cord to the template while maintaining consistent anatomical topology during mapping spinal pathways from the template.

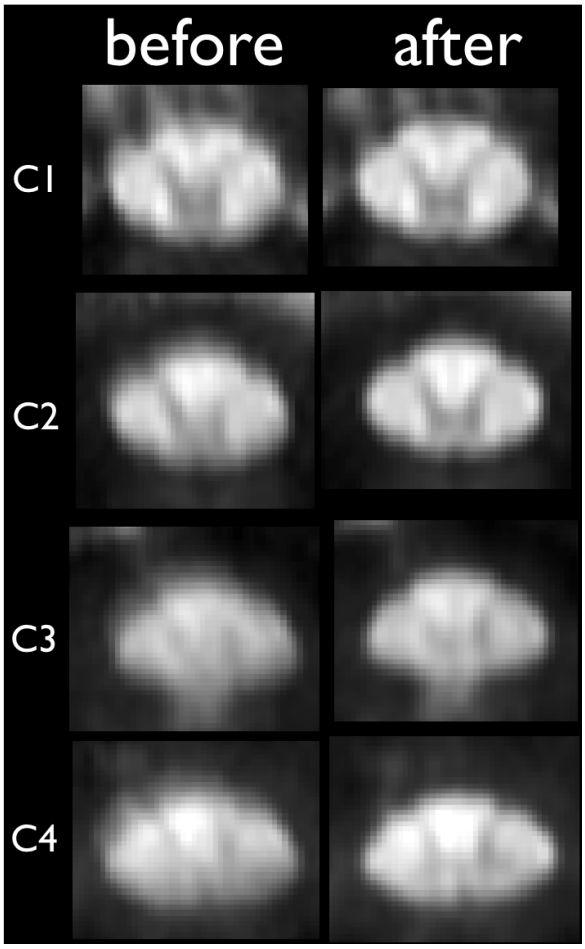

Figure 4.7: Data averaged along q-values in one subject (excluding images acquired at b < 430s/mm^2), before and after applying the correction for eddy-currents and subject motion.

Figure 4.8 shows the q-space data in one representative voxel in the white matter in one subject. There is a clear separation of q-space data across the three groups of Δ suggesting that the model adequately identified the hindered versus the restricted compartments. Notice that the data acquired with small diffusion time (Δ=20ms, blue) exhibit stronger signal with monotonic decay, due to the residual signal in the hindered compartment. Data acquired with large diffusion time (Δ=50ms, red) plateau for q-space values above 0.08 μm^{-1}, suggesting that the signal mostly originates from the restricted compartment given the near-complete attenuation of the hindered compartment. Assuming a diffusion coefficient Dh>0.5 $\mu m^2/ms$, the attenuation is over 98% at q>0.08 μm^{-1} (see Eq.2).

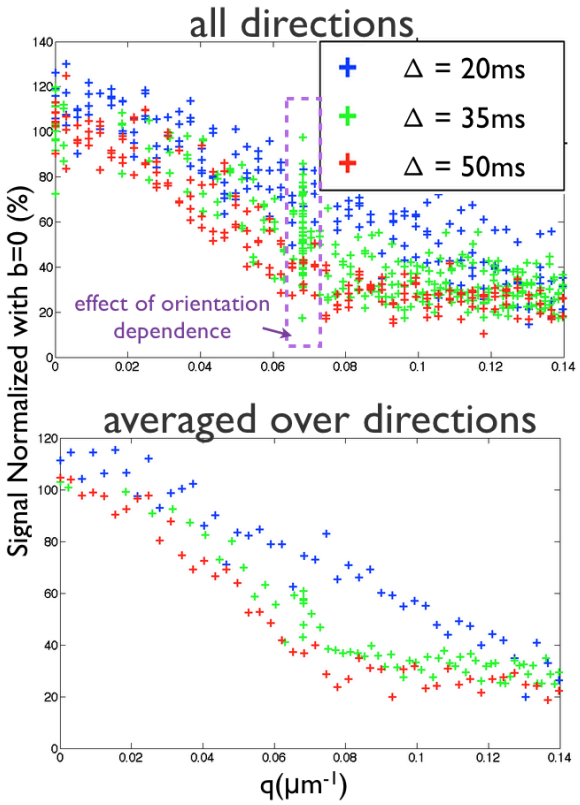

Figure 4.8: Top: Rician corrected q-space data in one voxel of the spinal cord white matter for one subject before LPCA correction (normalized by b=0). **Bottom:** same data averaged over the four directions. The purple dashed box shows the data collected for probing the orientation dependence (see Figure 2.b.).

4.3.2 SNR analysis

Figure 4.9 shows the standard deviation across q, calculated using a moving window (size = 15) after detrending the data with AxCaliber fits. In all subjects, the standard deviation ranged from 8% to 15% of the b=0 signal.

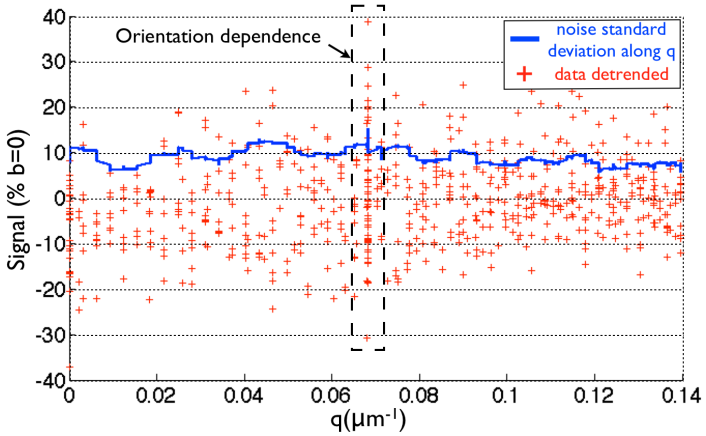

Figure 4.9: Standard deviation of noise along q (blue curve) in one voxel and one subject before LPCA correction. Values are shown as percentage of the b=0 signal. This estimated noise includes thermal and physiological noise. Notice that the standard deviation is fairly constant along q.

SNR (static + temporal) was computed voxel-wise by dividing average values (extracted from fits) by noise standard deviation. Table 4.1 shows SNR results per vertebral level in all subjects. SNR averaged across vertebral levels ranged between 1.4-2.0 in the b_{max}=39,011 s/mm^2 images and 9.0-11.7 in the b=0 images for all subjects. In two subjects, SNR was higher at C4 level, which could be attributed to (i) closer proximity of this region to the neck coil in these two subjects and/or (ii) lower amplitude of cardiac-related noise, as it was shown that this amplitude varies across subjects and vertebral levels (Piché et al., 2009).

Table 4.1: SNR computed per subject and per vertebral level at b=0 and b=39,011 s/mm^2 (b_{max})

	Subject #1		Subject #2		Subject #3		Subject #4		Subject #5	
Z	SNR b_{max}	SNR b0	SNR b_{max}	SNR b0	SNR b_{max}	SNR b0	SNR b_{max}	SNR b0	SNR b_{max}	SNR b0
C1	1.8	8.6	1.7	8.1	2.2	12.7	1.9	12.2	1.1	9.1
C2	1.7	8.1	1.6	8.5	1.9	11.5	1.6	10.8	1.5	10.5
C3	1.8	10.0	1.9	9.1	2.0	11.6	1.5	11.2	1.5	11.3
C4	1.7	9.1	1.6	8.9	2.1	10.9	1.3	9.6	1.5	10.4
Average	1.8	9.0	1.7	8.7	2.1	11.7	1.6	11.0	1.4	10.3

4.3.3 Quality of q-space Fitting

Table 4.2 shows the average χ^2_{red} for all subjects. Each value is the average of the χ^2 across voxels within the spinal cord. Here, values range between 1.09 and 1.23, suggesting a good fit. Supplementary material S1 shows the reduced chi-squared statistics of AxCaliber fitting in one subject. Values for α associated with the χ^2_{red} statistics were less than 5% (except for subject 3), meaning that the model did not fit the data appropriately (See discussion). Supplementary material S2 shows two q-space fitting in two different voxels, yielding in two different quality of fit (α=0.13 and α=9E-9).

Table 4.2: Goodness of fits using χ^2_{red} statistics. α represents the probability that our data are well described with the AxCaliber model (the higher the better).

Subject #	1	2	3	4	5
${\chi_{red}}^2$	1.23	1.21	1.09	1.15	1.18
α	5E-5	2E-4	5E-2	5E-3	1E-3

Figure 4.10 shows AxCaliber fitting in one subject in three different ROIs. The fitted curves exhibit different shapes between the three regions, which is expected because the underlying microstructure (axon size and density) is different across the three regions. Conversely, when comparing neighboring voxels within a given region however, the fitted curves exhibit a similar shape (not shown here). These observations suggest that the AxCaliber model is reproducible and sensitive to differences in microstructures. Note that the curve fitting for Δ=20ms is qualitatively not perfect and can partly be explained by the absence of time-dependence of the diffusion coefficient in the model equation.

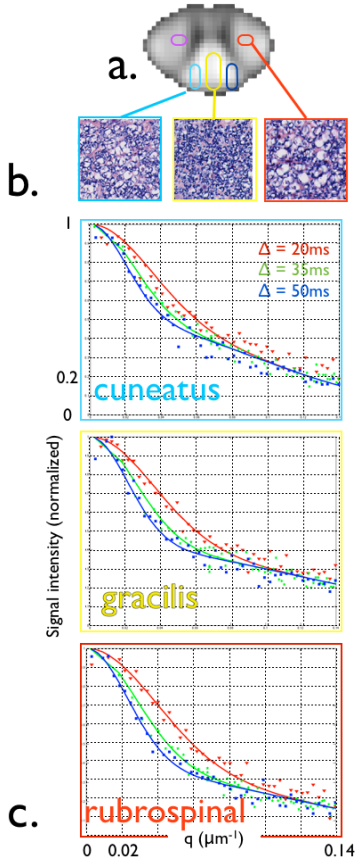

Figure 4.10: a: Cuneatus (blue), gracilis (yellow) and rubrospinal (red) tracts highlighted on the mean DWI in one subject. **b.** Histological images of axons stained for myelin (luxol fast blue cross) over corresponding pathways of a human spinal cord ("Histology at the University of Michigan," n.d.), reproduced with permission. **c.** Model fitting on signal decay acquired in one subject on a single voxel in the corresponding regions.

4.3.4 Mapping of axon diameter

The first two columns of **Figure 4.11** exhibit maps of the estimated hindered water volume fraction (fh) and the apparent diffusion coefficient of the hindered compartment (Dh). These maps were registered to the template and averaged across subjects (N=5). Since the model did not account for CSF compartment (in order to achieve higher precision), any partial voluming with CSF at the periphery of the cord translated into a more elevated Dh. The two last columns show the mean and standard deviations of axon diameters. Here, the single axon diameter model was used (Alexander et al., 2010). Results are consistent across slices and across subjects, as assessed by the relatively low standard deviation maps. Axon diameters ranged from 3.0μm in the gracilis at C4 to 5.9μm in the spinocerebellar tract at C2. In the posterior funiculus (black arrow), estimated axon diameters get smaller towards the inferior direction.

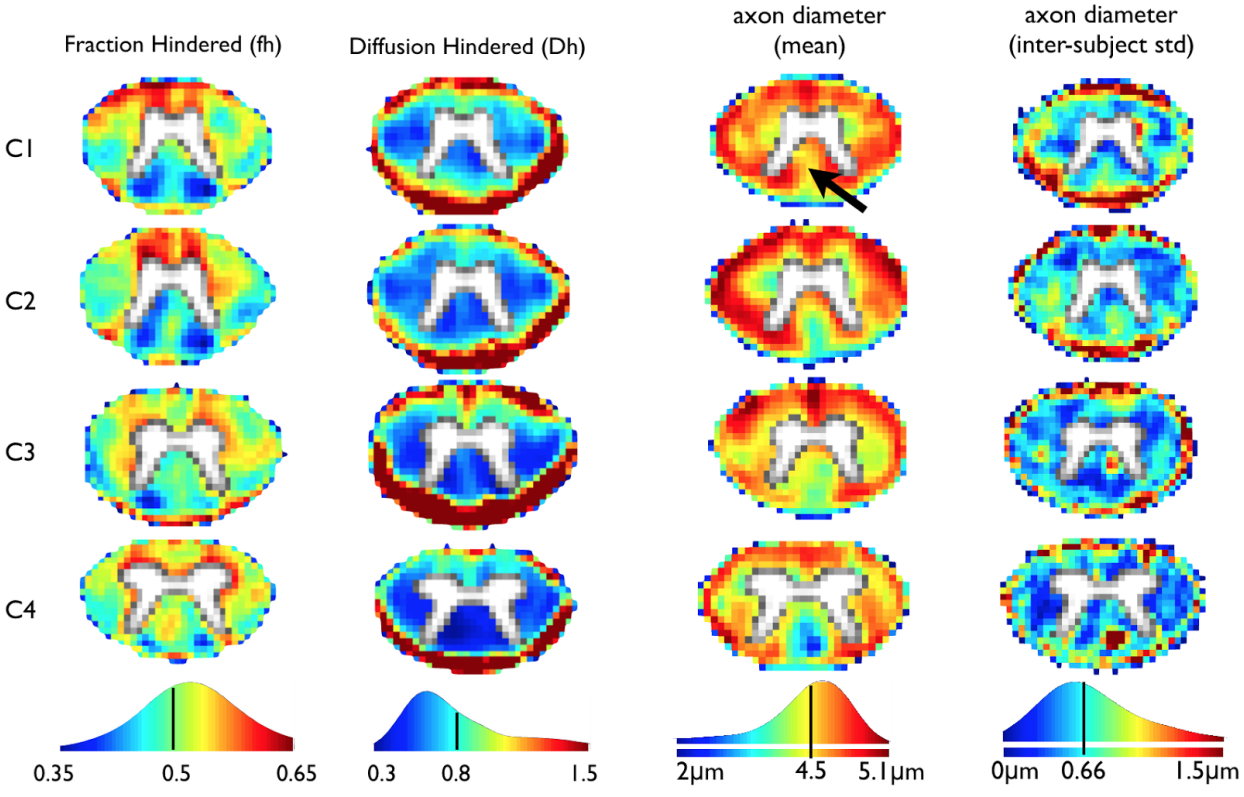

Figure 4.11: Maps of fitted parameters using single diameter model. Data histograms with range and mean value are shown at the bottom. The black arrows points to the posterior funiculus,

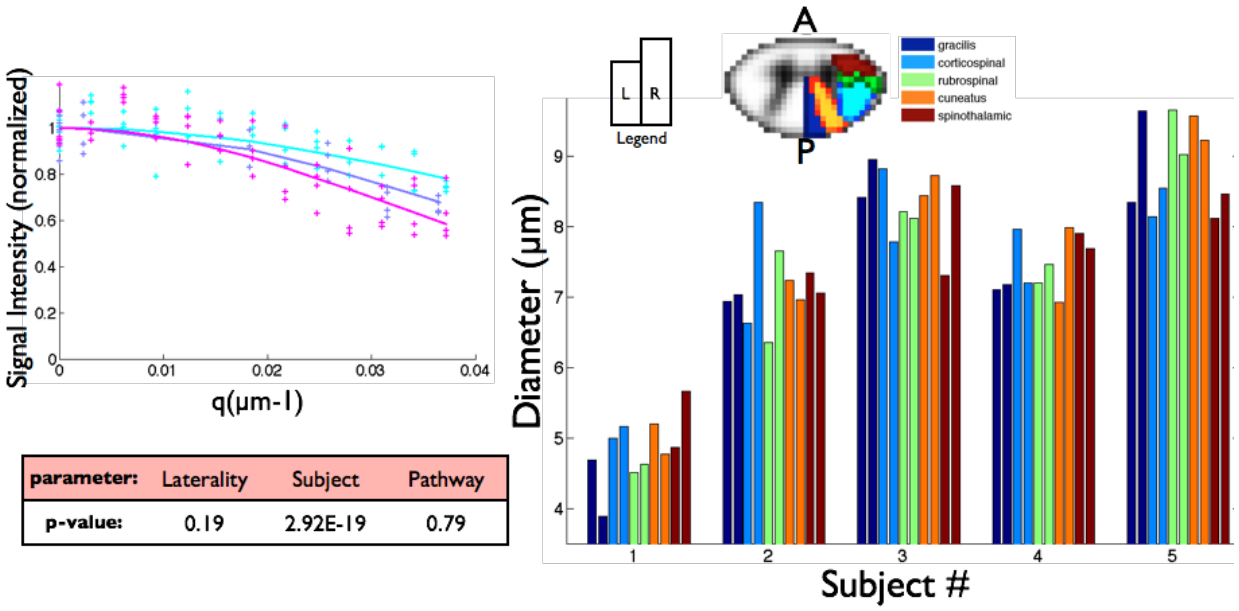

parameter:	Laterality	Subject	Pathway
p-value:	0.19	2.92E-19	0.79

Figure 4.12 reports numerical values of mean axon diameter, fh and Dh per subject, within specific pathways. The restricted water fraction (1-fh), which correlates with axon density (Alexander, 2008), was the highest in the cuneatus and the lowest in spinothalamic tract with 55% and 44% of intra-axonal water, respectively. Standard deviation of axon density across subjects was remarkably low (<0.02), suggesting good reproducibility of the technique and stability of this parameter across individuals. Mean axon diameters (across subjects and across vertebral levels) ranged from 3.51 μm (+/- 0.54) in the gracilis to 4.15 μm (+/- 0.46) in the cuneatus tract. In each subject taken individually, axon diameter and density were smaller in the gracilis than in the cuneatus. The same trends were reported in literature regarding the human spinal cord (Trobe, 2010). Dh was somewhat uniform (0.65 +/- 0.12 $\mu m^2/ms$) within the whole white matter. A three-way ANOVA tested the dependence towards laterality (left/right), pathways (five pathways were included in the ANOVA) and subjects. Results show an effect of pathway ($p<10^{-5}$) and subject ($p<10^{-7}$), but no effect for laterality (p=0.24). The interaction terms were not significant, i.e., Laterality*Subject (p=0.19), Laterality*Pathway (p=0.07) and Subject*Pathway (p=0.73). Supplementary material S3 shows axonal diameter histograms for each subject, computed in the entire white matter.

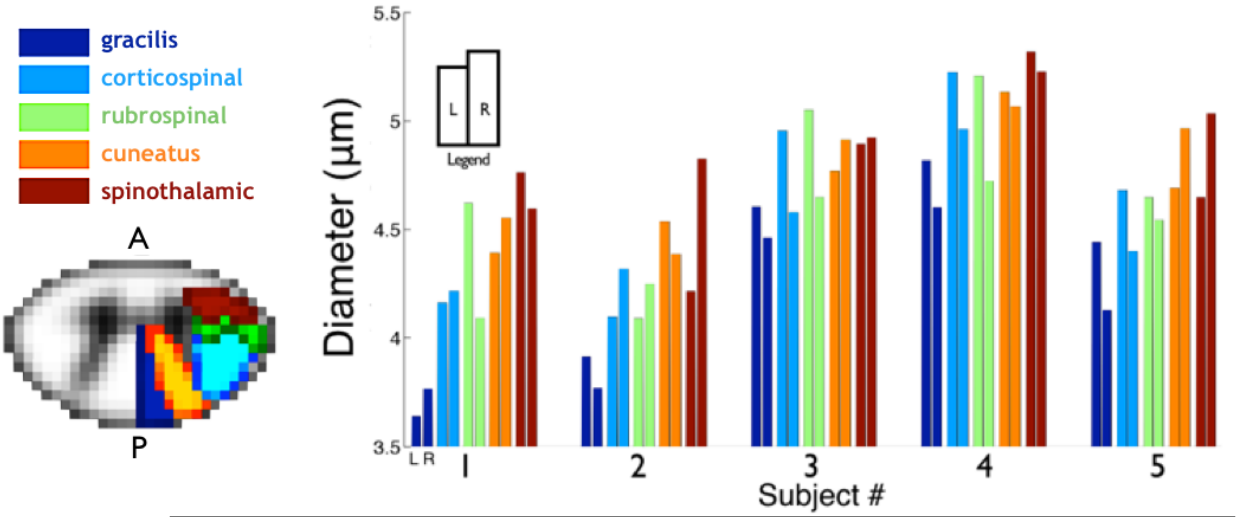

	Mean axon diameter (μm)				fh			
	right	left	mean	std across subjects	right	left	mean	std across subjects
gracilis	3.55	3.47	**3.51**	0.54	0.49	0.49	**0.49**	0.01
cuneatus	4.15	4.16	**4.15**	0.46	0.45	0.45	**0.45**	0.02
corticospinal	4.17	4.10	**4.14**	0.48	0.53	0.52	**0.52**	0.02
rubrospinal	3.81	4.03	**3.92**	0.35	0.56	0.51	**0.54**	0.01
spinothalamic	3.69	3.74	**3.71**	0.36	0.57	0.55	**0.56**	0.01

	Dh (μm²/ms)			
	right	left	mean	std across subjects
gracilis	1.01	1.06	**1.04**	0.21
cuneatus	0.75	0.85	**0.80**	0.24
corticospinal	0.66	0.77	**0.72**	0.18
rubrospinal	0.52	0.72	**0.62**	0.10
spinothalamic	0.60	0.57	**0.58**	0.07

Three-way ANOVA test

parameter:	Laterality	Subject	Pathway
p-value:	**0.244**	**3.42E-8**	**3.54E-6**

Figure 4.12: Top left: Mean DWI with overlay of ROIs for computing parameters within specific white matter tracts. **Top right:** Bar graph showing estimated axon diameter within tracts, laterality and subject. The estimated axon diameters range between 3.5 and 5.5 *μm*, suggesting fairly precise estimate of axon diameters on an individual basis. **Bottom table:** Estimated parameters averaged across subjects. Mean axon diameter was 3.51 (+/-0.54), 4.15 (+/-0.46) and 3.71 (+/- 0.36) μm in the gracilis, cuneatus and spinothalamic tracts, respectively. The restricted water fraction (1-fh), which correlates with axon density, was 55% and 44% (+/- 2%) in the cuneatus and spinothalamic tracts, respectively. Results of the three-way ANOVA show a significant effect of pathway and subjects but no effect for laterality.

4.3.5 Orientation dependence and reproducibility

4.3.5.1 Effect of gradient direction

The resulting mean difference between the two sub-datasets (within the white matter, across subjects and vertebral levels) was 1.1µm for axon diameter and 0.08 for hindered water fraction (fh). **Figure 4.13** (right panel) shows the resulting map of axon diameter difference between the two sub-datasets in one subject. Other subjects showed similar trends. Large differences between exp #1 and exp #2 are observed in the lateral and dorsal regions, and can be attributed to the presence of collateral fibers, as previously shown in monkeys (Lundell et al., 2011). The presence of collateral fibers violates the assumption of fibers being solely oriented along the spinal cord axis (as was assumed here), inducing orientation-dependence when applying diffusion gradients perpendicular to the spinal cord axis.

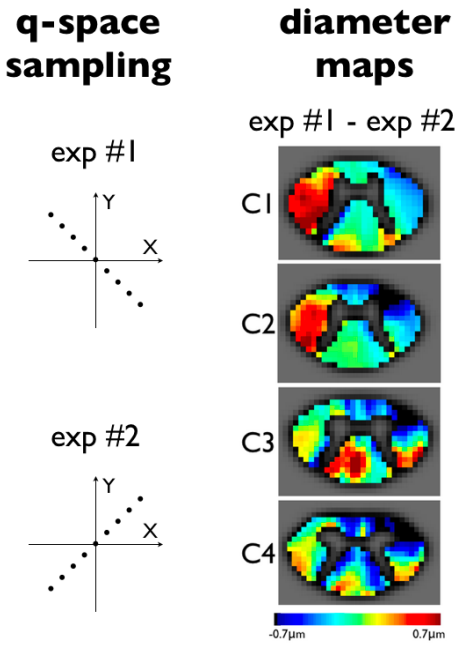

Figure 4.13: Difference in axon diameter estimated using two sub-sets of data with orthogonal diffusion gradient direction (X,Y;-X,-Y) and (-X,Y; X,-Y) in one subject. Symmetrical differences (red versus blue) are observed in the lateral region (especially at C1 and C2), which could be attributed to the presence of collateral fibers.

4.3.5.2 Orientation dependence

The change in signal amplitude as a function of gradient orientation was 22 % (averaged in the white matter across subjects), confirming the presence of an orientation dependence. **Figure 4.14**c. shows the principal direction of the collateral fibers computed from the highest diffusion peak. Notice that in the lateral portion of the spinal cord, collateral fibers have orthogonal directions between the left and the right side and are oriented diagonally, which corroborate the observations from **Figure 4.13**. **Figure 4.14**.d. shows a map of orientation dependence obtained from the peak-to-peak amplitude in the orientation dependence plot (averaged across subjects and located at C2). Higher angular dependence was found in dorsal roots regions at C1 and C2. This was expected, as this region encompasses longitudinal fibers as well as transverse, as shown in *ex vivo* monkey spinal cord with PAS-MRI (Lundell et al., 2011).

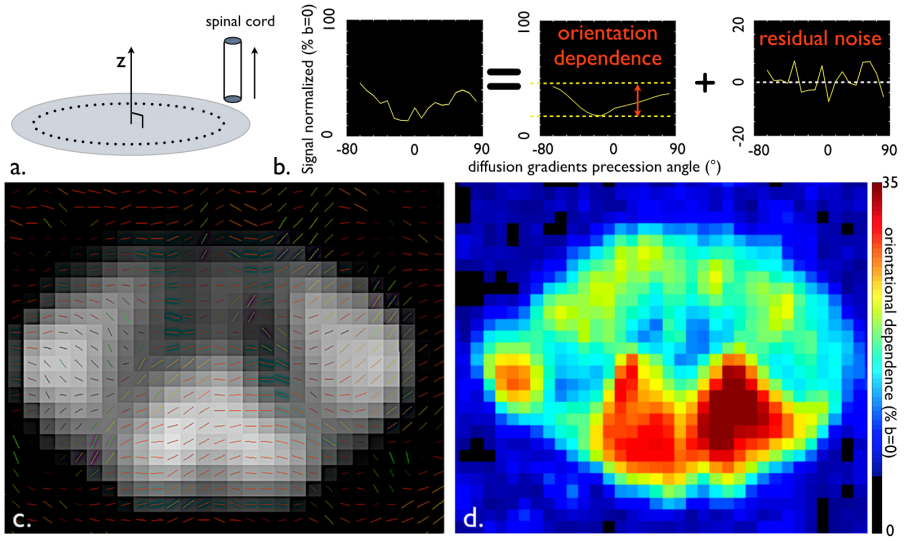

Figure 4.14: a. q-space sampling for orientation dependence study. **b.** Signal at different gradient orientations, which was detrended using cosines into a function representing the signal variation as a function of gradient orientation ("orientation dependence" plot). **c.** Directions of collateral fibers averaged across subjects at level C2. This map was obtained by extracting the angular value corresponding to the highest diffusion (i.e. lower signal). **d.** Corresponding map of orientation

dependence obtained using the peak-to-peak amplitude from the orientation dependence plot.

4.3.5.3 Bootstrap analysis

The average standard deviations of the fitting parameters were found to be 0.25μm for axon diameter and 0.02 for hindered water fraction (fh) in the white matter (95 percentile of the voxels).

4.4 Discussion

The purpose of this study was to demonstrate mapping of axon diameter in the *in vivo* human spinal cord using model-based q-space diffusion MRI at 300 mT/m. Model-estimated diameters fall within the range of those reported from previous histology work, opening the door to *in vivo* evaluation of specific features of spinal cord axons. The following discussion covers aspects related to the acquisition and preprocessing, diffusion model fitting (including discussions about noise) interpretation of axon diameter maps and future work.

4.4.1 Interpretation of axon diameter maps

4.4.1.1 Validation against histology

There is very little literature on axon diameter mapping in the human spinal cord. Histological data reporting quantitative values of axon diameters were found only for the pyramidal tracts. In this tract, 89.6% of axons were reported to range from 1 to 4μm, 8.7% from 5 to 10 μm, and 1.7% from 11 to 20 μm (Lassek, 1945). When accounting for the larger signal contribution from larger axons (Alexander et al. 2010), the volume-weighted average axon diameter is 7.82 μm. This value is larger than that from the corticospinal found in the present study (4.14 μm), which can be partly explained by the violation of the small pulse approximation. When using Gaussian Phase Distribution (GDP) approximation, the average axon diameter is 6.05μm (supplementary material S4). However, some discrepancies remain, which can come from a combination of fibre dispersion (not

modelled), permeability of unmyelinated axons (not modelled), and other oversimplifications of the model, as well as skewed sensitivity to large axons. **Figure 4.15** compares AxCaliber results with two histological resources: optical micrographs and maps of cytoarchitecture obtained from adult individuals with no records of neurological diseases (Nieuwenhuys et al., 2007). Trends were similar between histology and AxCaliber results: large axons in the spinocerebellar tract (4-5 μm), moderate axons in the rubrospinal tract (3-4 μm) and small axons in the gracilis (2-3 μm). In the posterior funiculus (black arrow in **Figure 4.11**), estimated axon diameters get smaller towards the inferior direction. This observation is in accordance with previous histology work (Nieuwenhuys et al., 2007). Notice that the gracilis, composed of small axons, has larger surface at C4 than at C1 levels due to incoming fibers from the cuneatus. Also notice the heterogeneity of axon diameter within tracts (as seen on the optical micrographs), suggesting that single-axon models are not appropriate. Future studies of histological validation in *ex vivo* human spinal cord are needed.

When comparing our results with those from studies on animals, the same trends are observed between tracts. For example, results in the gracilis, cuneatus and rubrospinal tracts (3.51, 4.14, 3.92 μm respectively) show the same trends in rats (1.1, 2.7, 1.1 μm) (Chin et al., 2004) and mice (0.99, 1.40, 1.16 μm) (Ong and Wehrli, 2010).

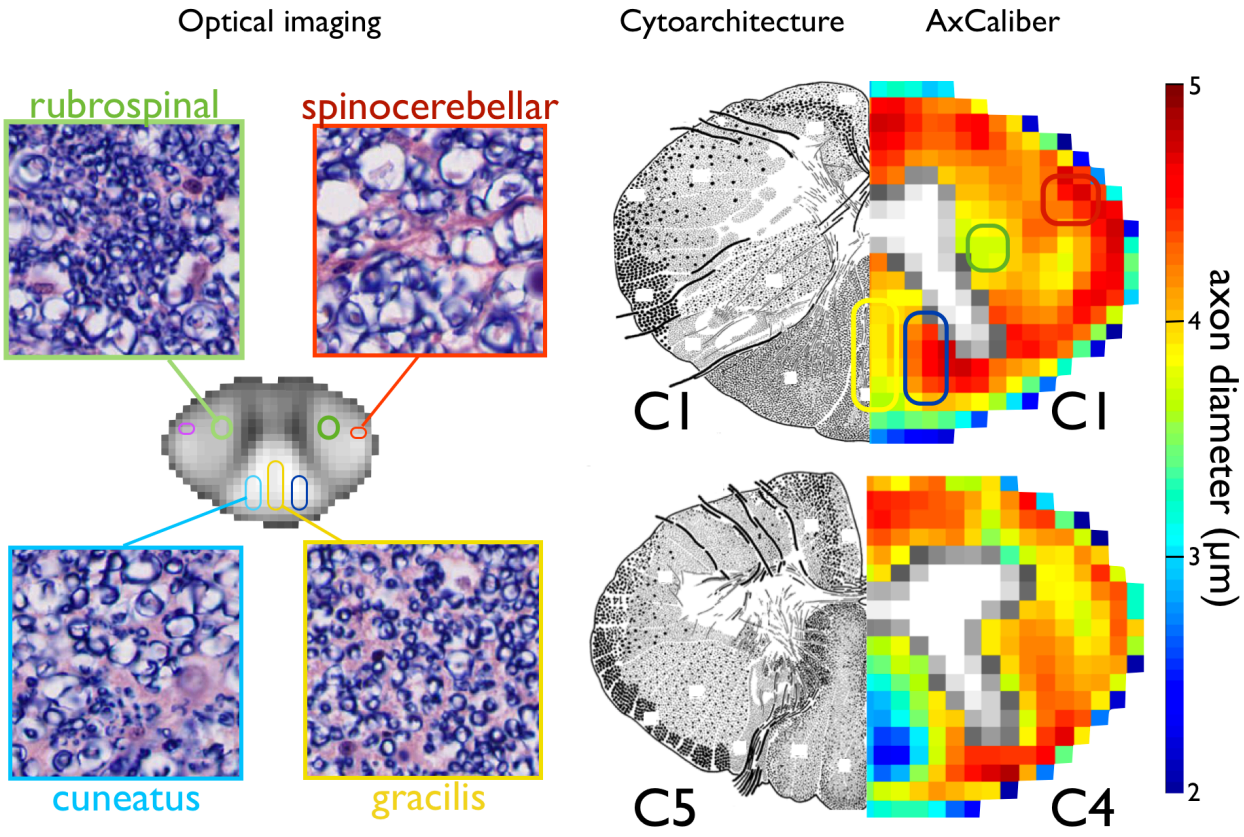

Figure 4.15: Comparison of AxCaliber results with two histological resources. **Left:** Optical images (50x50μm^2) of human thoracic spinal cord ("Histology at the University of Michigan," n.d.), reproduced with permission. **Middle**: Cytoarchitecture of human spinal cord white matter at vertebral levels C1 and C5 (Nieuwenhuys et al., 2007), reproduced with permission. Axon size is gray-level coded (the darker the bigger). Note that this representation of axon diameter is qualitative. Notice that some tracts have monodisperse axonal sizes (e.g. spinocerebellar and gracilis), while others present some super-axons surrounded by tiny axons (e.g. Pyramidal tracts). For direct comparison, AxCaliber results (averaged over five subjects) are overlaid on the right portion of the cytoarchitecture map at the corresponding levels (note: given that we did not acquire lower than C4, the C4 level is shown next to the C5 level from the cytoarchitecture map). Regions corresponding to the optical imaging panel are

circled on the AxCaliber maps: gracilis (yellow), cuneatus (blue), rubrospinal (green) and spinocerebellar (red).

4.4.1.2 Inter-subject variability

Results showed rather large inter-subject variability, relative to the within-subject inter-tract variability (see **Figure 4.12**). However, it is worth mentioning that the maps of axon diameter were consistent across subjects, i.e., gracilis smaller than the cuneatus, or corticospinal smaller than spinothalamic. Causes for the inter-subject variability can be anatomical and/or artifactual. Artifactual causes are related to noise (i.e., different noise levels owing to variable coil loading, inducing bias in the estimation) and to the variable subject motion. The hypothesis of a noise-related bias is supported by a strong correlation ($r=0.94$, $p=0.02$) between axon diameter (**Figure 4.15**) and SNR (Table 4.1), although this will have to be confirmed in a larger population. It is also possible that the fiber composition could vary between subjects, which could in turn induce bias in the estimation of axon diameters. Also, we cannot rule out the possibility of the curvature of the cord varying across subjects, which would result in a variable degree of orthogonality between the spinal cord centerline and the imaging slices. However, if present, this effect is presumed to be minimal given the relatively small longitudinal coverage (C1-C4) as well as the careful positioning of each subject performed to reduce cervical lordosis.

4.4.1.3 Tract by tract analysis

Microstructure was assumed to be homogeneous (i.e., single diameter) within each tract of the spinal cord atlas used for metrics extraction. Despite the advantages of atlas-based analysis for objectivity (free from user-bias) and accuracy (accounts for partial volume effect using Gaussian mixture model), there are limitations. Firstly, the transition between two neighboring tracts might be progressive, resulting in non-homogeneous microstructure around the interface. For example, the rubrospinal and corticospinal tracts are partially overlapped (Altman and Bayer, 2001). Secondly, the classical delimitation of tracts is not based on microstructure but on macroscopic observations. For example, the cuneatus is separated from the gracilis by a septum (Standring et al., 2005). However, this pathway is

a combination of thin fibers emerging from the sixth thoracic level and of thick fibers coming from the eighth cervical level (Carpenter, 1976; Nieuwenhuys et al., 2007). Thirdly, the delimitation of tracts in the present study was based on an atlas, which assumed the same spatial parcellation across individuals. However, the human spinal cord morphology was reported to vary across individuals (Kameyama et al., 1995). Fourthly, microstructure is not necessarily homogeneous along the spinal cord (e.g. the posterior funiculus as shown in **Figure 4.11**) and hence averaging microstructural features across slices might introduce further variability. Fifthly we assumed a linear relation between the axon diameter measured in a voxel and the combination of several axon diameters from each tract in that voxel. The potential biases associated with this approach (e.g. the measured axon diameters are weighted by the density and volume of axons within each tract) requires further investigations.

4.4.2 Acquisition and preprocessing

4.4.2.1 Eddy-currents

The switching of large gradient amplitude during diffusion encoding generated large eddy-currents, which manifested as translation, scaling and shearing in the phase-encoding direction (set to A-P). Although a twice-refocusing pulse sequence (Reese et al., 2003) could have been used to minimize this effect, these sequences are also subject to longer TE, thereby decreasing the SNR. Instead, an image-based eddy-current distortion correction was implemented, as proposed in (Bodammer et al., 2004). Here, given that the spinal cord was centered in the middle of the FOV (isocenter), no scaling or shearing was apparent. Hence the correction only addressed translations along the phase-encoding direction, leading to a more robust correction. Results indeed showed satisfactory eddy-current correction (see **Figure 4.7**).

4.4.2.2 Effect of TR

Due to gating, the TR varied with the cardiac rate, which had some consequences in the signal time series. In this study, two slices were acquired per cardiac pulse, resulting in a

TR of approximately 2 s. Moreover, TR was forced to be always greater than 1.6 s. The use of relatively short TR might have resulted in lower SNR due to only partial recovery of the spins given that the T1 in the spinal cord is about 800 ms at 3T (Smith et al. 2008). However, considering the SNR efficiency (i.e., SNR per unit time), the optimal TR was reported to be around 1 s at 3T in the white matter (Johansen-Berg and Behrens 2013). However, a drawback of cardiac gating with low TR is the introduction of additional variance in the diffusion time-series related to the variation of the heart rate throughout the acquisition, and therefore a variation in the recovery of the longitudinal magnetization. The impact of this additional variance for fitting diffusion models needs to be further investigated.

4.4.2.3 Different TE across Δ

The TE was minimized at each diffusion time in order to increase the SNR. To compensate for signal variation due to T2 relaxation, data were normalized using b=0 volumes, assuming the same T2 relaxation within the intra- and the extra-axonal water compartments. Although the assumption of a similar T2 in the intra- and extra-axonal compartment has been challenged (Does et al. 1998; Beaulieu et al. 1998; Whittall et al. 1997), a review by (Nilsson et al., 2013) reported that most in vivo studies have observed two components with short (10–50 ms) and long (70–130 ms) T2 relaxation times, that were respectively assigned to myelin water and to the combined intra- and extracellular water (Whittall et al. 1997; Laule et al. 2007; Deoni et al. 2008). Moreover, diffusion MRI studies based on fast- and slow diffusion components reported no dependence of the measured T2 as a function of diffusion encoding (Mulkern et al. 2000; Pfeuffer et al. 1999) (except at ultra-high field (Kunz et al. 2013)), and no detectable dependence of diffusion metrics on the TE (Huisman et al. 2006; Clark and Le Bihan 2000), again suggesting minimal T2 difference between the intra- and the extra-axonal compartments.

4.4.2.4 Effect of smoothing

The model fitting was done after eddy-current and motion correction. As a consequence, images were interpolated, which introduced spatial correlations between neighboring voxels. If neighboring voxels belonged to a different microstructure, this could have

introduced further partial volume effect across tracts of different underlying microstructures and hence less accuracy in the model. To minimize this effect, all transformations (eddy-current and motion correction) were concatenated into a single transformation in order to apply the sinc interpolation only once. Also note that the interpolation yielded an underestimation of the noise (σ) and hence a wrong correction of the magnitude bias. Nearest neighbor interpolation can overcome the alteration of the noise property, however this type of interpolation also yields inaccuracies in the motion correction and is therefore not recommended.

4.4.2.5 Noise

Even though the calculated SNR in b=0 (SNR=10.1) and b_{max}=39,011 (SNR=1.7) were low compared to previously published studies, where typical SNR in b=0 was ~20 (Bammer and Fazekas, 2003; Kim et al., 2010; Klawiter et al., 2011), it should be stressed that our calculation of SNR included both static (thermal) and temporal SNR. Static SNR could not accurately be calculated from the images using the standard background method (Koay et al., 2009) due to (i) the absence of 'pure' background caused by the use of reduced FOV, (ii) the presence of spatially-correlated noise related to GRAPPA reconstruction, and (iii) the use of a multi-channel coil (Dietrich et al., 2007). Hence, we reported the combination of both static and temporal SNR, which represents a more complete assessment of the data. Furthermore, physiological noise, which is known to be particularly significant in the spinal cord (Piché et al., 2009), was likely the dominant cause of the low SNR herein observed. While higher number of averaging (instead of higher number of q-values) would have yielded similar results than the one presented here, the rationale for sampling more densely was to qualitatively assess the goodness of fit to the chosen model. In particular, having a dense sampling towards high q-values enabled us to better assess the contribution of the Rician noise at low SNR regimes.Magnitude MR images were reconstructed from multiple channels (here 64). This procedure transforms the Gaussian distribution of complex noise in a non-symmetric and positively-defined distribution, inducing an upward bias in the magnitude signal. While signal from a single coil can be modeled with a Rician distribution, the distribution of noise from multi-channel coil using adaptive combine algorithm (Walsh

et al., 2000) presents a non-central chi distribution (Aja-Fernández et al., 2011). Moreover, the GRAPPA reconstruction introduces a non-uniformity of noise distribution throughout the volume (Aja-Fernández et al., 2011). Correcting the magnitude bias requires an exhaustive characterization of noise distribution for a specific coil and reconstruction method, which was beyond the scope of this study. Here we used a Rician noise correction, which is a particular case of the non-central chi noise. It is important to notice that magnitude bias can have particularly detrimental effect on the estimation of axon diameters using AxCaliber methods, because this residual signal would increase the apparent signal from restricted water at high q-values.

LPCA correction was used for reducing the noise on the data and might have had an impact on the estimation of AxCaliber parameters. To address this issue, AxCaliber was re-run on the data without applying the LCPA filter. The resulting coefficient of variation (diameter_withLCPA vs. diameter_withoutLCPA) in each voxel in one subject ranged from -7% to 4% at 95 percentile (mean -2%), suggesting minimal impact of the LCPA filter for estimating axon diameter.

4.4.3 Diffusion model

4.4.3.1 Small pulse approximation

In this study we used the small pulse approximation, which assumes no moving particles during the application of each diffusion gradient. Although the ratio Δ/δ was kept larger than 2.5 (as suggested by (Bar-Shir et al., 2008)), here we used comparatively long pulses (δ=8 ms) in contrast to the typical AxCaliber pulse length (δ~4 ms) (Assaf et al., 2008; Barazany et al., 2009). Despite the maximum gradient switching rate of 200 mT/m/ms, we had to set the limit to 90 mT/m/ms for safety purpose. This yielded a ramp-up time of about 3.3 ms to reach 300 mT/m. Assuming a Gaussian diffusion of $D_r = 1.4$ μm^2/ms (Barazany et al., 2009) in the intra-axonal compartment, during the application of the diffusion gradient the particles moved by an averaged distance of $l = \sqrt{4 * D_r * \delta} = 6.7$ μm, which is

on the order of axon diameters. The violation of the small pulse approximation might have resulted in underestimation of fiber diameters (Bar-Shir et al., 2008).

However, the choice of using a relatively large δ was motivated by the possibility to achieve higher q, increasing the diffusion encoding resolution and providing higher sensitivity to smaller axon diameters (Alexander et al., 2010; Dyrby et al., 2012). The Gaussian phase approximation (Stepišnik, 1993; Wang et al., 1995) was shown to correct this bias, but the sensitivity to small axons would still be affected. We have conducted a comparison between small pulse approximation and Gaussian phase approximation (see Supplementary Material S4). As expected, results show a global increase of axon diameter of 1.6μm (averaged across subjects) in the white matter and a more stable estimation of the fraction of hindered water. Notice however that $\delta = 7$ ms was shown to be appropriate for measuring axon diameter in the corpus callosum of monkeys (Alexander et al., 2010).

4.4.3.2 Considerations of gradient strength and axon resolution

By adding more constraints on the estimated parameters, other model-based quantitative diffusion MRI techniques like ActiveAx (Alexander et al., 2010) can yield accurate estimate of axon parameters, even at 60 mT/m (Nilsson and Alexander, 2012; Zhang et al., 2011), although axons smaller than 5 μm cannot be distinguished with this range of gradient strength (Alexander et al., 2010). The resolution limit at 300 mT/m is estimated to be slightly less than 3 μm using the minimal model of white matter based on simulations (Nilsson and Alexander, 2012). We performed a comparison of AxCaliber results with a maximal gradient strength of 80 mT/m versus 300 mT/m (Supplementary Materials S5 and S6). Results showed that the estimation of axon diameter is globally increased and that the contrast of axon diameter between pathways is lost (p=0.78). The fraction of hindered water is reduced but show similar trends between pathways, suggesting the reliability of this parameter on clinical systems.

4.4.3.3 Free water compartment

In this study we chose to remove the free water compartment. This compartment was originally proposed by Barazany (2009) to compensate for partial volume effect with the

CSF. The decision to not use the free water compartment was driven by preliminary data comparing AxCaliber results with and without an additional free water compartment (see Supplementary Material S7). These results showed that more than 10% of the free water compartment was wrongly estimated within the spinal cord, i.e., in regions not affected by partial volume with the CSF. These wrong estimations of the free water compartment size introduced larger instabilities when estimating axon diameter. On the other hand, when the free water compartment was not included, the diffusion hindered coefficient correctly compensated for the increase of free water fraction in voxels at the periphery of the spinal cord, with an estimated value of up to 3 $\mu m^2/ms$, and was thus a satisfactory replacement of the free water compartment. From the maps of axon diameter, one could notice a ring of large estimated axon diameter at the periphery. Although this estimate could partly be due to CSF contamination, it is also possible that the observed result is genuine, as previous histological studies of axon diameters in the spinal cord did report significantly larger axon diameter at the periphery of the cord (Nieuwenhuys et al., 2007). Moreover, the ring is also present in the maps when accounting for the free water compartment (see S7).

4.4.3.4 Diffusion coefficients

The model used in this study (composite hindered and restricted compartments) assumes (i) a fixed diffusion coefficient of Dr=1.4μm^2/ms in the restricted compartment and (ii) a Gaussian apparent diffusion coefficient Dh in the hindered compartment.

In order to validate the first assumption (Dr=1.4μm^2/ms), we compared AxCaliber results using two extreme fixed diffusion coefficients: Dr=0.3μm^2/ms and Dr=2μm^2/ms. The error on axon diameter estimation was below 1.3μm (99 percentile) and 0.1μm in average in all subjects. Also, the error on the fraction of restricted water was below 0.06 (99 percentile) and 0.006 in average in all subjects. Those results were expected since the water in the restricted compartment presents a permanent regime at the diffusion time Δ, pulse width δ, and axon diameters used in this study (model simulation not shown).

The second assumption (Gaussian apparent diffusion coefficient Dh) is not rigorously correct due to the time-dependence of the parameter Dh (Huang et al. 2015; Burcaw et al. 2015). This assumption might have biased our measurements, yielding over-estimation of axon diameter (Burcaw et al. 2015). However it should be mentioned that the use of very high b-value in this study (bmax=39,011 s/mm2) discriminated the signal from the hindered compartment, thus minimizing this effect. Note that the extracellular water is also affected by the size of the axons that hinder its diffusion.

4.4.3.5 Quality of q-space data fitting

The goodness-of-fit analysis suggested that the model used in this study did not describe the data within an acceptable level of significance (α<5%). However, it should be mentioned that this goodness-of-fit analysis strongly depends on the degree of freedom. Here, the degree of freedom was very large (ν=616), imposing a χ^2_{red} thresholds close to 1 (1.09 for $\alpha = 0.05$), which is difficult to achieve while maintaining a robust fit. Indeed, the simplicity of the AxCaliber model (6 parameters in our implementation) provides reproducible fitting results at the expense of accuracy. As illustrated in supplementary material S2, two voxels within the white matter can yield different qualities of fits. Poor fitting at high q-values could be caused by several factors. First, the applied Rician correction might be too

simplistic and a noise floor (magnitude bias) might be present. This hypothesis is supported by studies showing that GRAPPA reconstruction introduces higher spatially-variable magnitude bias (Aja-Fernández et al., 2011). Second, the presence of crossing fibers in the spinal cord (Cohen-Adad et al., 2008; Lundell et al., 2011) can violate the cylindrical assumption, because the attenuation of the signal would then be larger at high Δ if collateral fibers are present (i.e., orthogonal to longitudinal fibers). Third, a difference in T2 decay between the restricted and the hindered compartment would introduce a bias related to a different baseline signal (b=0) across Δ, given that the TE was different across Δ. This choice was made to minimize the TE for each Δ in order to maximize the SNR. Finally the non-negligible permeability of axon membranes might have introduced exchanges between the hindered and the restricted compartments, yielding biases when estimating the fraction in each of the compartments. This effect might be exacerbated in vivo, due to the presence of intra/extra-axonal flow triggered by active channels at the membrane surface related to the saltatory conduction of action potentials (Nilsson et al., 2013).

4.4.4 Applications and future work

Being able to non-invasively quantify axon diameter and density opens the door to understanding the pathophysiology of diseases targeting specific population of axons, such as multiple sclerosis and amyotrophic lateral sclerosis. The proposed method can therefore be used to improve the precision of the diagnosis and to validate therapeutic strategies. Amongst other possible applications is the combination of axon diameter and density with myelin density estimated from quantitative magnetization transfer (Sled and Pike, 2000) and/or macromolecular tissue volume methods (Mezer et al., 2013). Combining these quantities would enable in vivo estimation of the myelin g-ratio (Campbell et al., 2014; Stikov et al., 2011). The g-ratio is the ratio of the inner to the outer diameter of an axon. It was shown to be related to axon conduction (Pajevic and Basser, 2013) and can therefore provide a sensitive measure of pathology.

4.5 Conclusion

This paper reported *in vivo* mapping of axon diameter and density in the human spinal cord using 300 mT/m gradients. Results show similar trends with previous histology in humans and animals. Some potential biases (crossing fibers and noise) were identified and require further investigations. This method has the potential to provide relevant markers of spinal cord microstructure for diseases affecting specific fiber populations.

4.6 Bibliography

Aja-Fernández, S., Tristán-Vega, A., Hoge, W.S., 2011. Statistical noise analysis in GRAPPA using a parametrized noncentral Chi approximation model. Magn. Reson. Med. 65, 1195–1206.

Alexander, D.C., 2008. A general framework for experiment design in diffusion MRI and its application in measuring direct tissue-microstructure features. Magn. Reson. Med. 60, 439–448.

Alexander, D.C., Hubbard, P.L., Hall, M.G., Moore, E.A., Ptito, M., Parker, G.J.M., Dyrby, T.B., 2010. Orientationally invariant indices of axon diameter and density from diffusion MRI. Neuroimage 52, 1374–1389.

Altman, J., Bayer, S.A., 2001. Development of the Human Spinal Cord: An Interpretation Based on Experimental Studies in Animals. Oxford University Press.

Assaf, Y., Basser, P.J., 2005. Composite hindered and restricted model of diffusion (CHARMED) MR imaging of the human brain. Neuroimage 27, 48–58.

Assaf, Y., Blumenfeld-Katzir, T., Yovel, Y., Basser, P.J., 2008. AxCaliber: a method for measuring axon diameter distribution from diffusion MRI. Magn. Reson. Med. 59, 1347–1354.

Avants, B.B., Epstein, C.L., Grossman, M., Gee, J.C., 2008. Symmetric diffeomorphic image registration with cross-correlation: evaluating automated labeling of elderly and neurodegenerative brain. Med. Image Anal. 12, 26–41.

Bammer, R., Fazekas, F., 2003. Diffusion imaging of the human spinal cord and the vertebral column. Top. Magn. Reson. Imaging 14, 461–476.

Bar-Shir, A., Avram, L., Ozarslan, E., Basser, P.J., Cohen, Y., 2008. The effect of the diffusion time and pulse gradient duration ratio on the diffraction pattern and the structural information estimated from q-space diffusion MR: experiments and simulations. J. Magn. Reson. 194, 230–236.

Barazany, D., Basser, P.J., Assaf, Y., 2009. In vivo measurement of axon diameter distribution in the corpus callosum of rat brain. Brain 132, 1210–1220.

Basser, P.J., Pierpaoli, C., 1996. Microstructural and physiological features of tissues elucidated by quantitative-diffusion-tensor MRI. J. Magn. Reson. B 111, 209–219.

Beaulieu, C., Allen, P.S., 1994. Determinants of anisotropic water diffusion in nerves. Magn. Reson. Med. 31, 394–400.

Beaulieu, C., Fenrich, F.R., Allen, P.S., 1998. Multicomponent water proton transverse relaxation and T2-discriminated water diffusion in myelinated and nonmyelinated nerve. Magn. Reson. Imaging 16, 1201–1210.

Benhamou, M., Fonov, V., Taso, M., Le Troter, A., Sdika, M., Collins, L., Callot, V., Cohen-Adad, J., 2014. Atlas of white-matter tracts in the human spinal cord, in: Proceedings

of the 22th Annual Meeting of ISMRM, 13.

Bodammer, N., Kaufmann, J., Kanowski, M., Tempelmann, C., 2004. Eddy current correction in diffusion-weighted imaging using pairs of images acquired with opposite diffusion gradient polarity. Magn. Reson. Med. 51, 188–193.

Burcaw, L.M., Fieremans, E., Novikov, D.S., 2015. Mesoscopic structure of neuronal tracts from time-dependent diffusion. Neuroimage.

Callaghan, P.T., 1995. Pulsed-Gradient Spin-Echo NMR for Planar, Cylindrical, and Spherical Pores under Conditions of Wall Relaxation. J. Magn. Reson. A 113, 53–59.

Callaghan, P.T., Eccles, C.D., Xia, Y., 1988. NMR microscopy of dynamic displacements: k-space and q-space imaging. J. Phys. E 21, 820.

Campbell, J.S.W., Stikov, N., Dougherty, R.F., Bruce Pike, G., 2014. Combined NODDI and qMT for full-brain g-ratio mapping with complex subvoxel microstructure, in: Proceedings of the 22th Annual Meeting of ISMRM, Milan.

Carpenter, M.B., 1976. Human neuroanatomy, Williams and Wilkins Company, Baltimore, Maryland.

Chin, C.-L., Wehrli, F.W., Fan, Y., Hwang, S.N., Schwartz, E.D., Nissanov, J., Hackney, D.B., 2004. Assessment of axonal fiber tract architecture in excised rat spinal cord by localized NMR q-space imaging: simulations and experimental studies. Magn. Reson. Med. 52, 733–740.

Clark, C.A., Le Bihan, D., 2000. Water diffusion compartmentation and anisotropy at high b values in the human brain. Magn. Reson. Med. 44, 852–859.

Cluskey, S., Ramsden, D.B., 2001. Mechanisms of neurodegeneration in amyotrophic lateral sclerosis. Mol. Pathol. 54, 386–392.

Cohen-Adad, J., Descoteaux, M., Rossignol, S., Hoge, R.D., Deriche, R., Benali, H., 2008. Detection of multiple pathways in the spinal cord using q-ball imaging. Neuroimage 42, 739–749.

Cohen-Adad, J., El Mendili, M.-M., Lehéricy, S., Pradat, P.-F., Blancho, S., Rossignol, S., Benali, H., 2011. Demyelination and degeneration in the injured human spinal cord detected with diffusion and magnetization transfer MRI. Neuroimage 55, 1024–1033.

DeLuca, G.C., Ebers, G.C., Esiri, M.M., 2004. Axonal loss in multiple sclerosis: a pathological survey of the corticospinal and sensory tracts. Brain 127, 1009–1018.

Deoni, S.C.L., Rutt, B.K., Arun, T., Pierpaoli, C., Jones, D.K., 2008. Gleaning multicomponent T1 and T2 information from steady-state imaging data. Magn. Reson. Med. 60, 1372–1387.

Dietrich, O., Raya, J.G., Reeder, S.B., Reiser, M.F., Schoenberg, S.O., 2007. Measurement of signal-to-noise ratios in MR images: Influence of multichannel coils, parallel imaging, and reconstruction filters. J. Magn. Reson. Imaging 26, 375–385.

Dijkers, M., Bryce, T., Zanca, J., 2009. Prevalence of chronic pain after traumatic spinal

cord injury: a systematic review. J. Rehabil. Res. Dev. 46, 13–29.

Does, M.D., Beaulieu, C., Allen, P.S., Snyder, R.E., 1998. Multi-component T1 relaxation and magnetisation transfer in peripheral nerve. Magn. Reson. Imaging 16, 1033–1041.

Dula, A.N., Gochberg, D.F., Valentine, H.L., Valentine, W.M., Does, M.D., 2010. Multiexponential T2, magnetization transfer, and quantitative histology in white matter tracts of rat spinal cord. Magn. Reson. Med. 63, 902–909.

Dyrby, T.B., Søgaard, L.V., Hall, M.G., Ptito, M., Alexander, D.C., 2012. Contrast and stability of the axon diameter index from microstructure imaging with diffusion MRI. Magn. Reson. Med. 70, 711–721.

Fonov, V.S., Le Troter, A., Taso, M., De Leener, B., Lévêque, G., Benhamou, M., Sdika, M., Benali, H., Pradat, P.-F., Collins, D.L., Callot, V., Cohen-Adad, J., 2014. Framework for integrated MRI average of the spinal cord white and gray matter: The MNI-Poly-AMU template. Neuroimage 102P2, 817–827.

Grussu, F., Schneider, T., Zhang, H., Alexander, D.C., Wheeler-Kingshott, C.A.M., 2015. Neurite orientation dispersion and density imaging of the healthy cervical spinal cord in vivo. Neuroimage 111, 590–601.

Gudbjartsson, H., Patz, S., 1995. The Rician distribution of noisy MRI data. Magn. Reson. Med. 34, 910–914.

Histology at the University of Michigan [WWW Document], n.d. URL http://histology.med.umich.edu/medical/central-nervous-system (accessed 8.24.14).

Huang, S.Y., Nummenmaa, A., Witzel, T., Duval, T., Cohen-Adad, J., Wald, L.L., McNab, J.A., 2015. The impact of gradient strength on in vivo diffusion MRI estimates of axon diameter. Neuroimage 106, 464–472.

Huisman, T.A.G.M., Loenneker, T., Barta, G., Bellemann, M.E., Hennig, J., Fischer, J.E., Il'yasov, K.A., 2006. Quantitative diffusion tensor MR imaging of the brain: field strength related variance of apparent diffusion coefficient (ADC) and fractional anisotropy (FA) scalars. Eur. Radiol. 16, 1651–1658.

Jenkinson, M., Bannister, P., Brady, M., Smith, S., 2002. Improved optimization for the robust and accurate linear registration and motion correction of brain images. Neuroimage 17, 825–841.

Johansen-Berg, H., Behrens, T.E.J., 2013. Diffusion MRI: From Quantitative Measurement to In vivo Neuroanatomy. Elsevier Science.

Kameyama, T., Hashizume, Y., Ando, T., Takahashi, A., Yanagi, T., Mizuno, J., 1995. Spinal cord morphology and pathology in ossification of the posterior longitudinal ligament. Brain 118 (Pt 1), 263–278.

Keil, B., Cohen-Adad, J., Porter, D.A., Biber, S., Heberlein, K., 2013. Simultaneous diffusion-weighted MRI of brain and cervical spinal cord using a 64-channel head-neck array coil at 3T. Proceedings of the 21th Annual Meeting of ISMRM, 1210.

Kim, T.H., Zollinger, L., Shi, X.F., Kim, S.E., Rose, J., Patel, A.A., Jeong, E.K., 2010. Quantification of diffusivities of the human cervical spinal cord using a 2D single-shot interleaved multisection inner volume diffusion-weighted echo-planar imaging technique. AJNR Am. J. Neuroradiol. 31, 682–687.

Klawiter, E.C., Schmidt, R.E., Trinkaus, K., Liang, H.-F., Budde, M.D., Naismith, R.T., Song, S.-K., Cross, A.H., Benzinger, T.L., 2011. Radial diffusivity predicts demyelination in ex vivo multiple sclerosis spinal cords. Neuroimage 55, 1454–1460.

Koay, C.G., Ozarslan, E., Pierpaoli, C., 2009. Probabilistic Identification and Estimation of Noise (PIESNO): a self-consistent approach and its applications in MRI. J. Magn. Reson. 199, 94–103.

Kunz, N., Sizonenko, S.V., Hüppi, P.S., Gruetter, R., van de Looij, Y., 2013. Investigation of field and diffusion time dependence of the diffusion-weighted signal at ultrahigh magnetic fields. NMR Biomed. 26, 1251–1257.

Laule, C., Vavasour, I.M., Kolind, S.H., Li, D.K.B., Traboulsee, T.L., Moore, G.R.W., MacKay, A.L., 2007. Magnetic resonance imaging of myelin. Neurotherapeutics 4, 460–484.

Le Bihan, D., Breton, E., Lallemand, D., Grenier, P., Cabanis, E., Laval-Jeantet, M., 1986. MR imaging of intravoxel incoherent motions: application to diffusion and perfusion in neurologic disorders. Radiology 161, 401–407.

Lundell, H., Nielsen, J.B., Ptito, M., Dyrby, T.B., 2011. Distribution of collateral fibers in the monkey cervical spinal cord detected with diffusion-weighted magnetic resonance imaging. Neuroimage 56, 923–929.

Lätt, J., Nilsson, M., Wirestam, R., Johansson, E., Larsson, E.-M., Stahlberg, F., Brockstedt, S., 2008. In vivo visualization of displacement-distribution-derived parameters in q-space imaging. Magn. Reson. Imaging 26, 77–87.

Manjón, J.V., Coupé, P., Concha, L., Buades, A., Collins, D.L., Robles, M., 2013. Diffusion Weighted Image Denoising Using Overcomplete Local PCA. PLoS One 8, e73021.

McNab, J.A., Edlow, B.L., Witzel, T., Huang, S.Y., Bhat, H., Heberlein, K., Feiweier, T., Liu, K., Keil, B., Cohen-Adad, J., Tisdall, M.D., Folkerth, R.D., Kinney, H.C., Wald, L.L., 2013. The Human Connectome Project and beyond: Initial applications of 300 mT/m gradients. Neuroimage 80, 234–245.

Mezer, A., Yeatman, J.D., Stikov, N., Kay, K.N., Cho, N.-J., Dougherty, R.F., Perry, M.L., Parvizi, J., Le H, H., Butts-Pauly, K., Wandell, B.A., 2013. Quantifying the local tissue volume and composition in individual brains with magnetic resonance imaging. Nat. Med. 19, 1667–1672.

Mulkern, R.V., Zengingonul, H.P., Robertson, R.L., Bogner, P., Zou, K.H., Gudbjartsson, H., Guttmann, C.R., Holtzman, D., Kyriakos, W., Jolesz, F.A., Maier, S.E., 2000. Multi-component apparent diffusion coefficients in human brain: relationship to spin-lattice relaxation. Magn. Reson. Med. 44, 292–300.

Nieuwenhuys, R., Voogd, J., van Huijzen, C., 2007. The Human Central Nervous System: A Synopsis and Atlas. Springer.

Nilsson, M., Alexander, D., 2012. Investigating tissue microstructure using diffusion MRI: How does the resolution limit of the axon diameter relate to the maximal gradient strength? Proceedings of the 20th Annual Meeting of ISMRM 3567.

Nilsson, M., van Westen, D., Ståhlberg, F., Sundgren, P.C., Lätt, J., 2013. The role of tissue microstructure and water exchange in biophysical modelling of diffusion in white matter. Magn. Reson. Mater. Phys. Biol. Med. 26, 345–370.

Nossin-Manor, R., Duvdevani, R., Cohen, Y., 2002. q-Space high b value diffusion MRI of hemi-crush in rat spinal cord: evidence for spontaneous regeneration. Magn. Reson. Imaging 20, 231–241.

Ong, H.H., Wehrli, F.W., 2010. Quantifying axon diameter and intra-cellular volume fraction in excised mouse spinal cord with q-space imaging. Neuroimage 51, 1360–1366.

Ong, H.H., Wright, A.C., Wehrli, S.L., Souza, A., Schwartz, E.D., Hwang, S.N., Wehrli, F.W., 2008. Indirect measurement of regional axon diameter in excised mouse spinal cord with q-space imaging: simulation and experimental studies. Neuroimage 40, 1619–1632.

Pajevic, S., Basser, P.J., 2013. An optimum principle predicts the distribution of axon diameters in normal white matter. PLoS One 8, e54095.

Panagiotaki, E., Schneider, T., Siow, B., Hall, M.G., Lythgoe, M.F., Alexander, D.C., 2012. Compartment models of the diffusion MR signal in brain white matter: a taxonomy and comparison. Neuroimage 59, 2241–2254.

Perge, J.A., Niven, J.E., Mugnaini, E., Balasubramanian, V., Sterling, P., 2012. Why do axons differ in caliber? J. Neurosci. 32, 626–638.

Peters, A., Palay, S.L., Webster, H.F., 1991. The fine structure of the nervous system: neurons and their supporting cells. Oxford University Press.

Pfeuffer, J., Provencher, S.W., Gruetter, R., 1999. Water diffusion in rat brain in vivo as detected at very large b values is multicompartmental. MAGMA 8, 98–108.

Piché, M., Cohen-Adad, J., Nejad, M.K., Perlbarg, V., Xie, G., Beaudoin, G., Benali, H., Rainville, P., 2009. Characterization of cardiac-related noise in fMRI of the cervical spinal cord. Magn. Reson. Imaging 27, 300–310.

Reese, T.G., Heid, O., Weisskoff, R.M., 2003. Reduction of eddy-current-induced distortion in diffusion MRI using a twice-refocused spin echo. Magn. Reson. Insights.

Rossignol, S., Dubuc, R., Gossard, J.-P., 2006. Dynamic sensorimotor interactions in locomotion. Physiol. Rev. 86, 89–154.

Schneider, T., Wheeler-Kingshott, C.A.M., Alexander, D.C., 2012. MAPPING THE AXON DIAMETER INDEX IN THE CORPUS CALLOSUM IS CLINICALLY FEASIBLE.

Proceedings of the 20th Annual Meeting of ISMRM 350.

Schwartz, E.D., Duda, J., Shumsky, J.S., Cooper, E.T., Gee, J., 2005. Spinal cord diffusion tensor imaging and fiber tracking can identify white matter tract disruption and glial scar orientation following lateral funiculotomy. J. Neurotrauma 22, 1388–1398.

Setsompop, K., Kimmlingen, R., Eberlein, E., Witzel, T., Cohen-Adad, J., McNab, J.A., Keil, B., Tisdall, M.D., Hoecht, P., Dietz, P., Cauley, S.F., Tountcheva, V., Matschl, V., Lenz, V.H., Heberlein, K., Potthast, A., Thein, H., Van Horn, J., Toga, A., Schmitt, F., Lehne, D., Rosen, B.R., Wedeen, V., Wald, L.L., 2013. Pushing the limits of in vivo diffusion MRI for the Human Connectome Project. Neuroimage 80, 220–233.

Shemesh, N., Alvarez, G.A., Frydman, L., 2013. Measuring small compartment dimensions by probing diffusion dynamics via Non-uniform Oscillating-Gradient Spin-Echo (NOGSE) NMR. J. Magn. Reson. 237, 49–62.

4.7 Supplementary Material

Supplementary material S1 shows the reduced chi-squared statistics of AxCaliber fitting in one subject. A χ^2_{red} value of 1 means that the fitting error equals the noise variance (i.e., perfect fit). If χ^2_{red} is superior to one, it means that the fitting error is larger than the noise variance. In this subject, the average χ^2_{red} value ranges between 1 and 1.5 (across slices). The fits are better in the white matter (χ^2_{red} ~1) when compared to voxels at the periphery (CSF contamination) or within the gray matter (χ^2_{red} ~1.5).

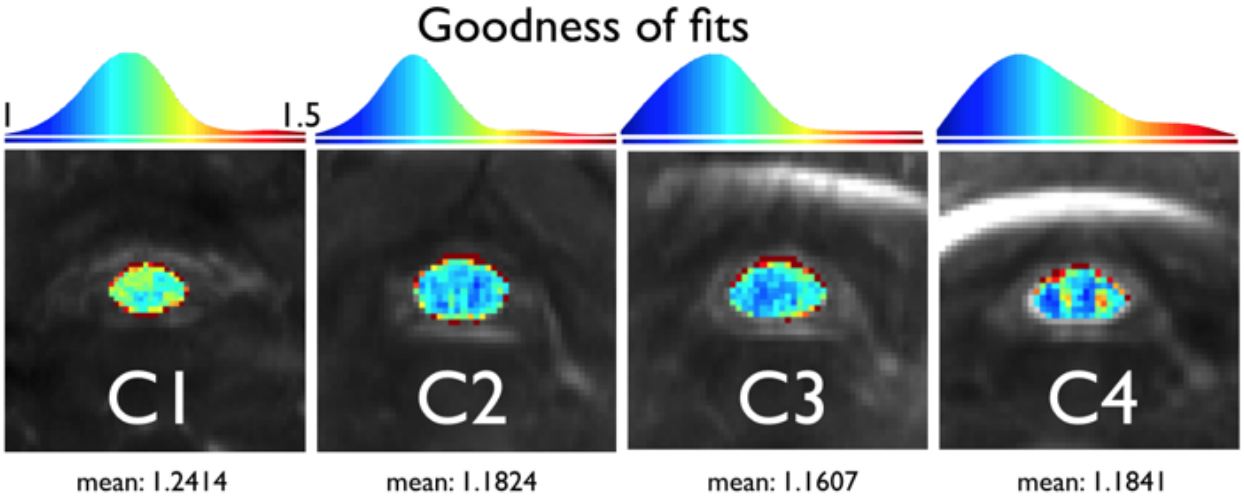

Figure 4.16: χ_{red}^2 histograms (top) and maps (bottom) in one subject per vertebral level. Values close to 1 (blue) represent the best fits. Values are smaller than 1.5 (red), which shows that all fitting errors were close to the noise standard deviation.

Supplementary material S2 shows two voxels in the white matter yielding different qualities of fits. The plot on the left ($\alpha = 0.13$) shows acceptable fit for all Δ, while the plot on the right ($\alpha = 9.10^{-9}$) shows overfitting at $\Delta = 50ms$ and underfitting at $\Delta = 20ms$ for high q-values ($> 0.8\mu m^{-1}$). Poor fitting can be caused by (i) the presence of crossing fibers, which violates the cylindrical model assumption, (ii) inadequate correction for Rician noise at large q-values, which overestimated the fitting curves, (iii) different T2 between the restricted and hindered compartment, given that TE was different across Δ and (iv) the non-negligible permeability of myelin membranes.

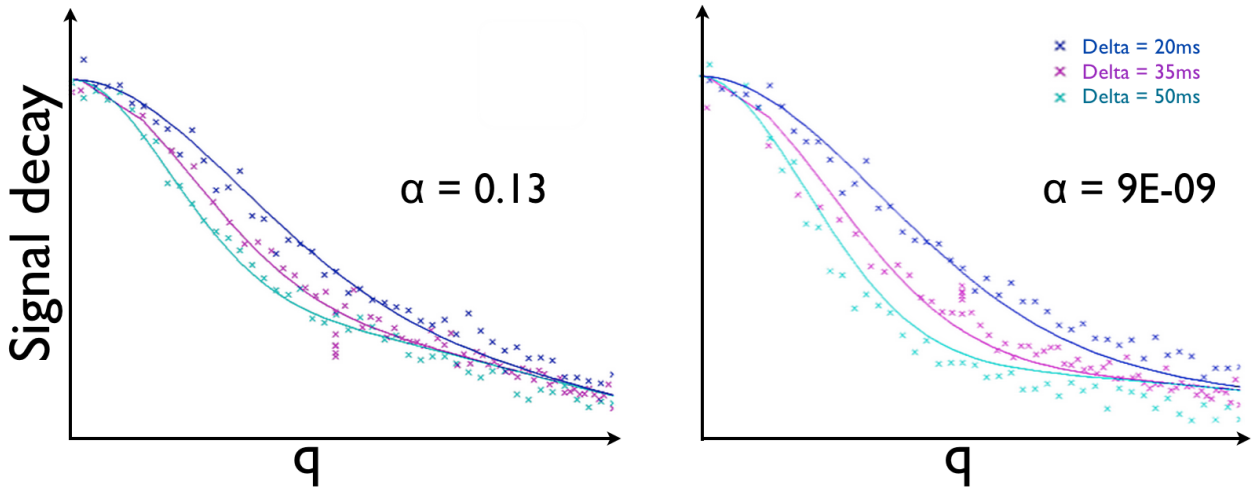

Figure 4.17: Example of fits at extreme **α**-values for two voxels in the white matter (each plot corresponds to one voxel). The right plot shows overfitting at Δ=50ms and underfitting at Δ=20ms for high q-values (>0.08μm^{-1})

Supplementary material S3 shows axonal diameter histograms for each subject, computed in the entire white matter. Histograms are remarkably similar across subjects, in terms of shape and median (ranging from 3.5 to 4.2 µm). All histograms present a dominant peak, which is centered at around 4µm. This suggests that the most representative axon diameter across individuals is 4µm in the spinal cord white matter. Lower values (1-2µm) are located at the boundary of the spinal cord and hence are likely related to partial volume effect with the CSF. We notice that large diameters (>5µm) are more present in subjects 3, 4 and 5, which highlights potential anatomical variations across individuals.

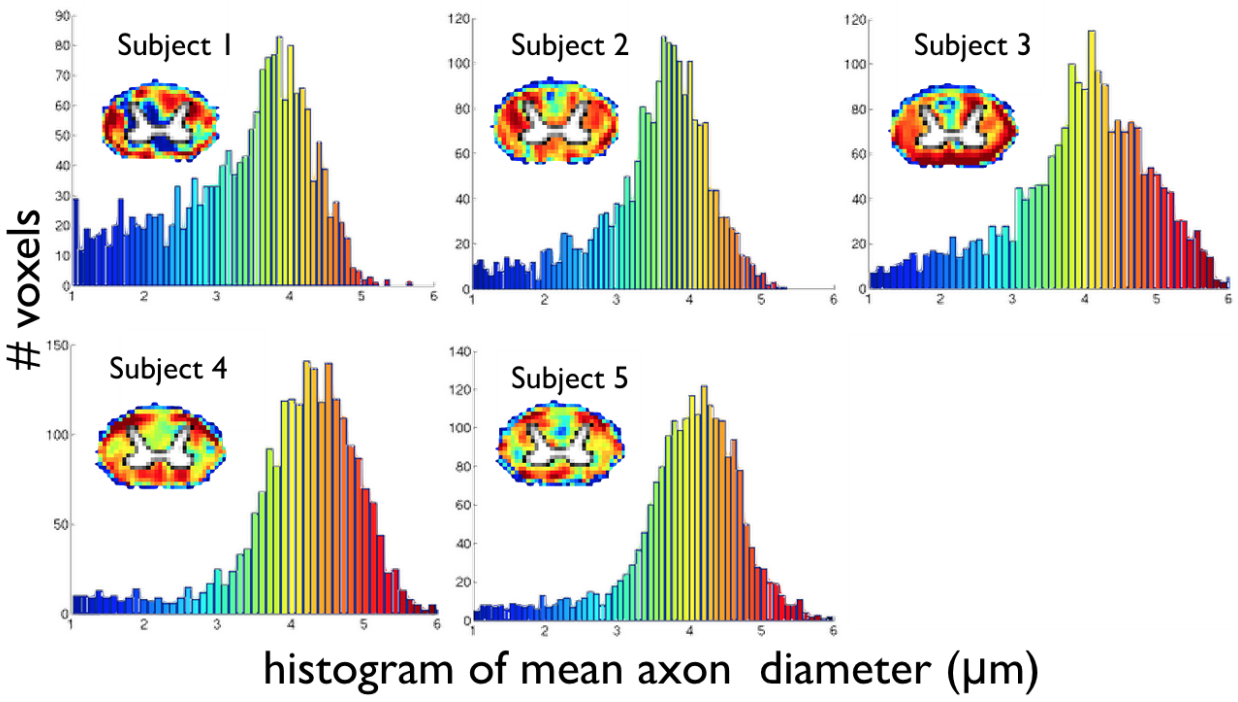

Figure 4.18: Histograms of mean axon diameter in spinal cord white matter for each subjects with m. Bottom right: Maps of estimated axon diameter at vertebral level C4 for each subject. All histograms present a dominant peak centered at around 4µm.

Supplementary material S4 shows the results of the AxCaliber analysis using Gaussian Phase distribution (GPD) model for cylinders (Stepišnik, 1993; Wang et al., 1995). As expected (Bar-Shir et al., 2008), larger axon diameters were estimated with this model (6.14 +/- 0.9µm versus 4.5 +/- 1.1 µm without GPD). Yet, maps of axon diameter presented very similar trends across tracts (e.g., smaller diameter in the gracilis versus in the rubrospinal tracts). Fraction of hindered water was also similar (0.53 in average in the white matter with and without GPD), but the hindered diffusion coefficient calculated in the white matter was higher with the GPD model (0.80µm^2/ms versus 0.73µm^2/ms). The significant difference of axon diameter between pathways was preserved (p=1.60e-5, versus p=3.54e-6).

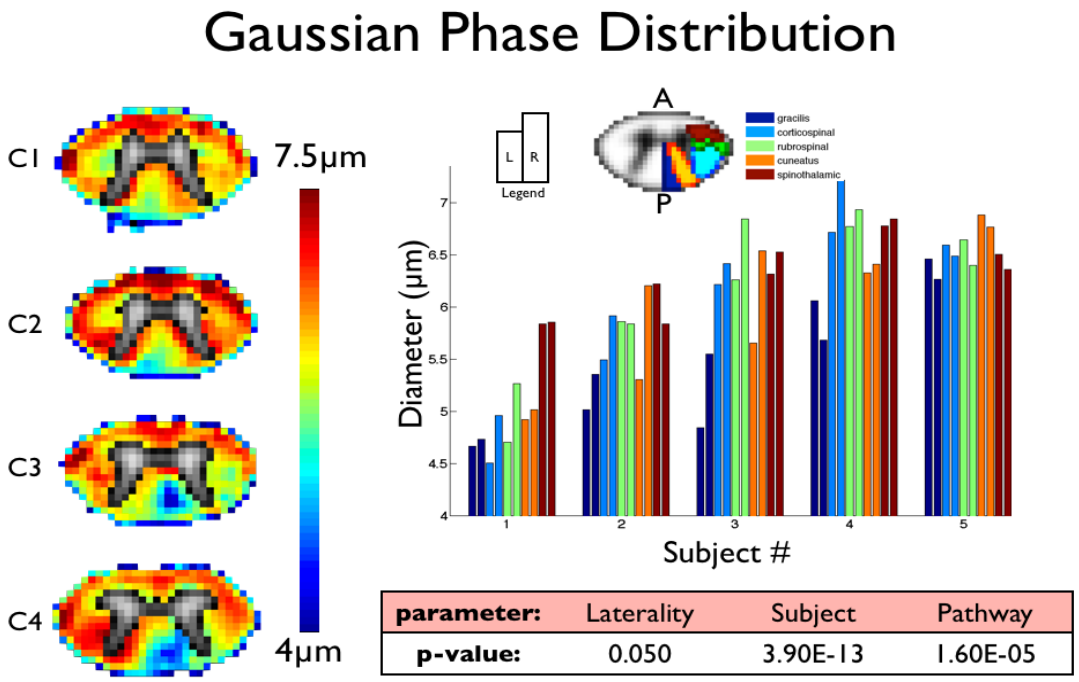

parameter:	Laterality	Subject	Pathway
p-value:	0.050	3.90E-13	1.60E-05

	Mean axon diameter (μm)				fh			
	left	right	**mean**	std	left	right	**mean**	std
fasciculus gracilis	5.41	5.52	**5.46**	0.68	0.50	0.50	**0.50**	0.08
fasciculus cuneatus	5.82	6.19	**6.00**	0.74	0.50	0.50	**0.50**	0.08
Corticospinal tract	5.91	6.20	**6.05**	0.88	0.51	0.51	**0.51**	0.08
rubrospinal tract	6.05	6.26	**6.15**	0.77	0.50	0.51	**0.50**	0.08
spinal lemniscus (spinothalamic and spinoreticular tracts)	6.33	6.29	**6.31**	0.39	0.51	0.51	**0.51**	0.08

	Dh(μm^2/ms)			
	left	right	**mean**	std
fasciculus gracilis	1.00	1.01	**1.00**	0.09
fasciculus cuneatus	0.84	0.90	**0.87**	0.08
Corticospinal tract	0.85	0.86	**0.85**	0.08
rubrospinal tract	0.91	0.94	**0.93**	0.09
spinal lemniscus (spinothalamic and spinoreticular tracts)	0.81	0.82	**0.81**	0.09

Figure 4.19: Results of the analysis using Gaussian Phase Distribution (GPD) approximation. Top left: Mean DWI with overlay of ROIs for computing parameters within specific white matter tracts. Top right: Bar graph showing estimated axon diameter within tracts, laterality and subject. Bottom table: Estimated parameters averaged across subjects. Overall, axon diameters estimated with GPD approximation were greater than that with the short pulse approximation (6.00μm versus 3.89μm in average between subjects and tracts). Fraction of hindered compartment was similar between models although the standard deviation was higher using the GPD model (0.08 versus 0.01).

Supplementary material S5 shows the effect of maximal gradient strength on AxCaliber results with maximal gradient strength of 300mT/m versus 80mT/m. For this comparison, q-space data were truncated so as to only keep data acquired with $|G|<\sqrt{2}*80mT/m$. The new data subset contained 142 q-space volumes (versus 623 for the whole dataset). Maps obtained at 80 mT/m show a global increase in axon diameter estimation (7.5µm versus 6.3µm in average in white matter) and a decrease in fraction of hindered water (0.4 versus 0.5 in average in white matter). While the estimation of axon diameter produced more noisy maps at 80mT/m, notably because this dataset had fewer data, the fraction of hindered water showed similar trends at 80mT/m and 300mT/m when qualitatively comparing its distribution across the spinal cord (e.g., lower fh in the dorsal column versus in the ventral aspect). More information about the impact of strong gradients for AxCaliber measurements can be found in (Huang et al., 2015).

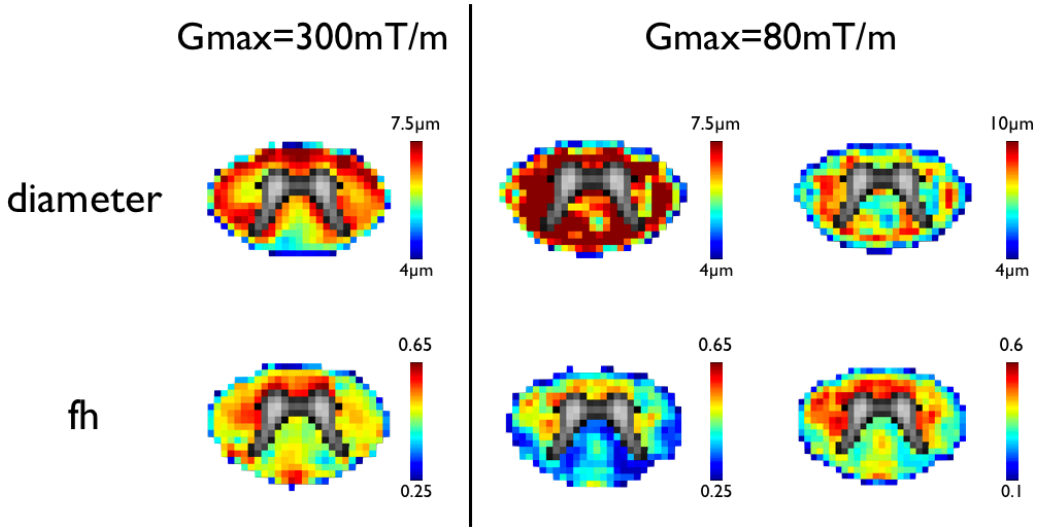

Figure 4.20: Effect of maximal gradient strength on AxCaliber results with maximal gradient strength of 300mT/m (first column) versus 80mT/m (second and third column). Column three is equivalent to column two except that colorbars were rescale for more clarity. Top row: Axon diameter maps at C2 vertebral level. Bottom row: Fraction of hindered water maps.

Supplementary material S6 shows the results of tract-by-tract analysis using the subset q-space data with $|G|<\sqrt{2}*80mT/m$. On this subset, the model used in this study correctly fitted our data. No significant differences in axon diameter were found between tracts using this subset ($p=0.79$). It should be stressed out that this dataset had fewer data (142 versus 623 for the entire dataset) and therefore less statistical power.

Figure 4.21: Results of axon diameter estimation at Gmax = 80 mT/m. Top left: example of q-space fitting in the spinal cord white matter in one subject. right: Estimated axon diameter in five different tracts for each subject. Bottom left: Table showing the 3-way Anova results for estimated axon diameter. No significant differences between tracts were found at 80 mT/m ($p=0.79$, versus $p=3.5x10^{-6}$ at 300mT/m).

Supplementary material S7 shows AxCaliber results using an additional free water compartment with the following signal contribution : $E_{free} = exp\,(-b * 3\mu m^2/ms)$. This model has an additional parameter f_{free} in order to fit the water fraction of the free compartment. When adding this compartment, Dh was decreased (0.45 versus 0.73µm^2/ms), fh was decreased (0.47 versus 0.53), axon diameter was decreased (3.11 versus 4.5µm) and the fraction of free water (f_{free}) was estimated at 0.15. Note that all values were averaged across subjects. Axon diameter in the gracilis tract was lower than in other tracts, as been observed without the free water compartment. Again the three-way anova analysis shows significant difference of axon diameter between pathways ($p<10^{-5}$) and subjects ($p<10^{-9}$), but no differences between left and right sides (p=0.20).

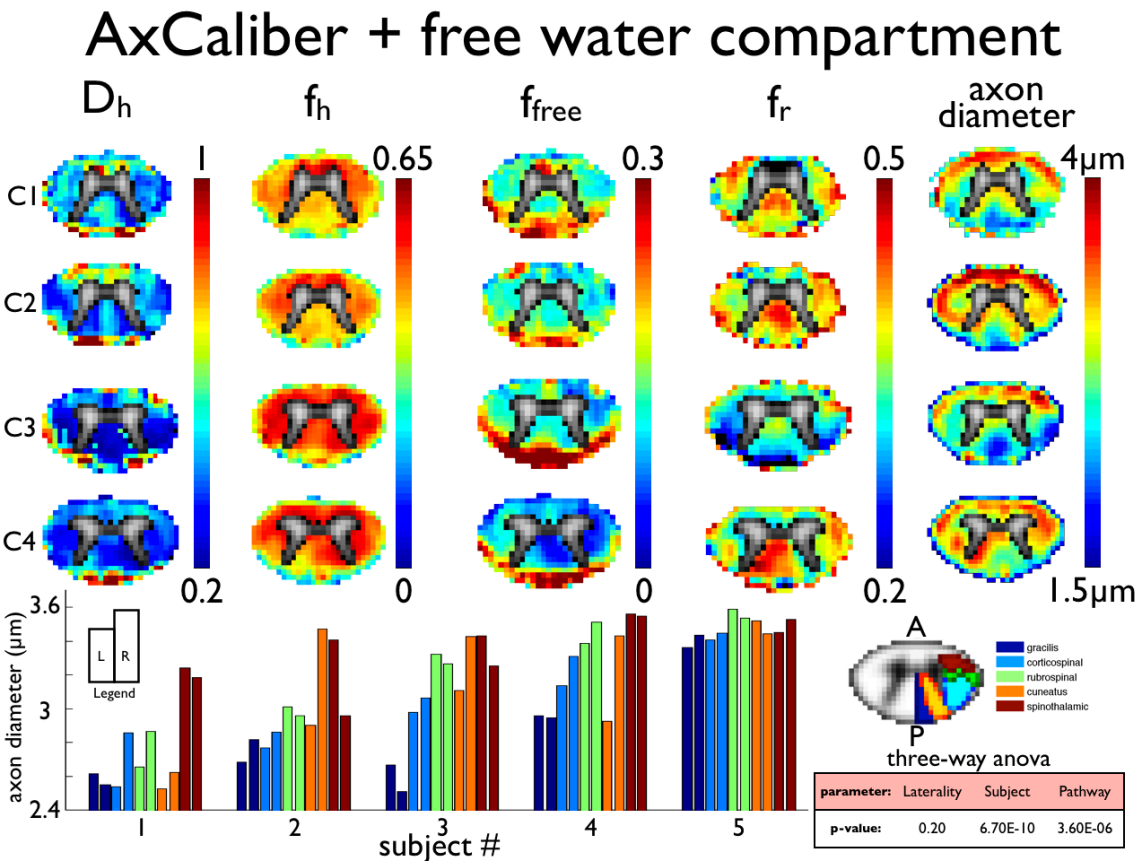

Figure 4.22: Results of AxCaliber analysis using an additional free water compartment in the model. Top: Maps of estimated parameters averaged across the five subjects. Bottom: bar plot showing estimated axon diameter per tract in each subject and results from the three-way ANOVA analysis.

References

Bar-Shir, A., Avram, L., Ozarslan, E., Basser, P.J., Cohen, Y., 2008. The effect of the diffusion time and pulse gradient duration ratio on the diffraction pattern and the structural information estimated from q-space diffusion MR: experiments and simulations. J. Magn. Reson. 194, 230–236.

Huang, S.Y., Nummenmaa, A., Witzel, T., Duval, T., Cohen-Adad, J., Wald, L.L., McNab, J.A., 2015. The impact of gradient strength on in vivo diffusion MRI estimates of axon diameter. Neuroimage 106, 464–472.

Stepišnik, J., 1993. Time-dependent self-diffusion by NMR spin-echo. Physica B Condens. Matter 183, 343–350.

Wang, L.Z., Caprihan, A., Fukushima, E., 1995. The Narrow-Pulse Criterion for Pulsed-Spin-Echo Diffusion Measurements. J. Magn. Reson. A 117, 209–219.

CHAPITRE 5 ARTICLE 3: G-RATIO WEIGHTED IMAGING OF THE HUMAN SPINAL CORD IN VIVO

Journal – NeuroImage - Elsevier

T. Duval[1], S. Lévy[1,6], N. Stikov[1,2], J. Campbell[3], A. Mezer[4], T. Witzel[5], B. Keil[5], V. Smith[5], L. L. Wald[5], E. Klawiter[5], and J. Cohen-Adad[1,6]

[1]*NeuroPoly Lab, Institute of Biomedical Engineering, Polytechnique Montreal, Montreal, QC, Canada*

[2]*Montreal Heart Institute, Montreal, QC, Canada*

[3]*Montreal Neurological Institute, McGill University, Montreal, QC, Canada*

[4]*Edmond and Lily Safra Center for Brain Sciences (ELSC), The Hebrew University, Jerusalem, Israel,*

[5]*A.A. Martinos Center for Biomedical Imaging, Massachusetts General Hospital, Harvard Medical School, Charlestown, Massachusetts, United States,*

[6]*Functional Neuroimaging Unit, CRIUGM, Université de Montréal, Montréal, QC, Canada*

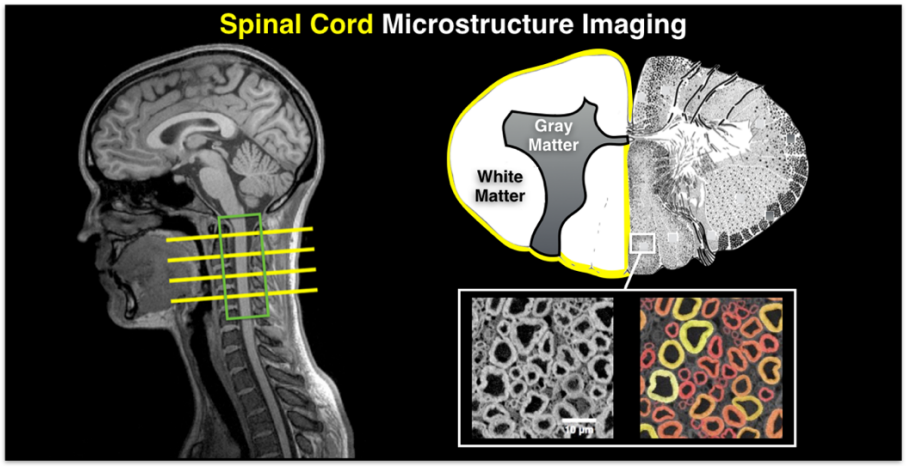

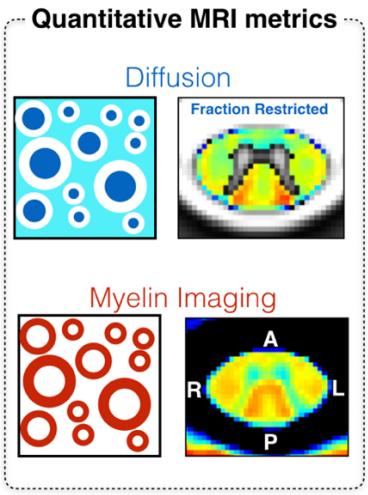

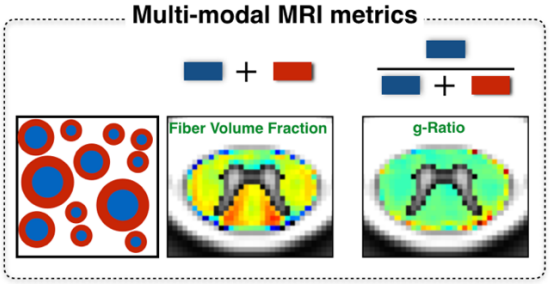

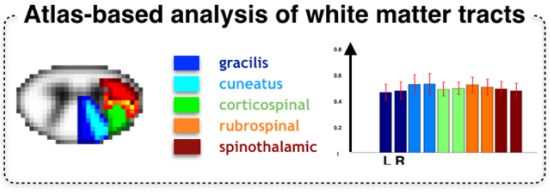

The fiber g-ratio is defined as the ratio of the inner to the outer diameter of the myelin sheath. This ratio provides a measure of the myelin thickness that complements axon morphology (diameter and density) with high specificity for assessment of demyelination in diseases such as multiple sclerosis. Previous work has shown that an aggregate g-ratio map can be computed using a formula that combines axon and myelin density measured with quantitative MRI.

In this work, we computed g-ratio weighted maps in the cervical spinal cord of nine healthy subjects. We utilized the 300 mT/m gradients from the CONNECTOM scanner for estimating the fraction of restricted water (*fr*) with high accuracy using the CHARMED model. Myelin density was estimated using the lipid and macromolecular tissue volume (MTV) method, derived from normalized proton density (PD) mapping. The variability across spinal level, laterality and subject were assessed using a three-way ANOVA.

The average g-ratio value obtained in the white matter was 0.76 +/- 0.03, consistent with previous histology work. Coefficients of variation of *fr* and MTV were respectively 4.3% and 13.7%**.** *fr* and myelin density were significantly different across spinal tracts ($p = 3x10^{-7}$ and 0.004 respectively) and were positively correlated in the white matter ($r = 0.42$), suggesting shared microstructural information. The g-ratio did not show significant differences across tracts ($p=0.6$).

This study suggests that *fr* and myelin density can be measured *in vivo* with high precision and that they can be combined to produce a map robust to free water pool contamination such as cerebrospinal fluid or veins and weighted by the fiber g-ratio. Potential applications include the study of early demyelination in multiple sclerosis and the quantitative assessment of remyelination drugs.

Keywords*: g-ratio, MRI, diffusion, axcaliber, myelin mapping, spinal cord*

Contribution: *Design of the study (50%), acquisition and analysis of the MRI data, redaction of the article and generation of the figures.*

Submitted: *12 February 2016*

Accepted: *8 Septembre 2016*

5.1 Introduction

The white matter of the central nervous system is composed of axons that transmit neuronal information. Most of these axons have a myelin sheath (Hildebrand et al., 1993) that enables faster propagation of action potentials (Rushton, 1951), notably via saltatory conduction (Huxley and Stämpfli, 1949), and higher firing frequency (Perge et al., 2012). Changes in the integrity of the myelin sheath can have dramatic consequences such as paralysis, loss of sensation or chronic pain (Dijkers et al., 2009) depending on the localization of dysfunction in the neuroaxis. Demyelination and/or axonal damage can be induced by neurodegenerative diseases such as amyotrophic lateral sclerosis or after traumatic injury through the process of Wallerian degeneration of the disrupted axons (Raff et al., 2002; Waller, 1850).

Magnetic Resonance Imaging (MRI) is the most widely used imaging modality to diagnose neuropathology (Saba, 2015). Conventional MRI contrasts (T_2- or T_1-weighted) can reveal pathologies such as focal MS lesions or edema and ischemia in spinal cord injury. However, conventional MRI lacks sensitivity to subtle white matter demyelination and degeneration. To overcome these limitations, several novels MRI techniques such as diffusion-weighted imaging or magnetization transfer have been developed to improve our ability to assess microstructure integrity (Saba, 2015). While these advanced techniques increase sensitivity and specificity to white matter microstructure, they are still not entirely specific to particular cellular properties. For instance, reduction of fractional anisotropy from diffusion tensor imaging can be caused by demyelination, axon degeneration, gliosis, edema, lower axon density or cerebrospinal fluid (CSF) contamination (Alexander et al., 2007; Metwalli et al., 2010; Saba, 2015). More advanced diffusion MRI techniques such as diffusion kurtosis imaging (Jensen et al., 2005; Lätt et al., 2008), AxCaliber (Assaf et al., 2008), ActiveAx (Alexander et al., 2010) or NODDI (Zhang et al., 2012), try to disentangle these different pathologic entities by introducing more complex models. Such models can quantify in particular the fraction of restricted water (*fr*), assumed to be the relative fraction of intra-axonal water in the white matter. This metric appears to be more specific to microstructural changes such as axon degeneration (Adluru et al., 2014; Zhang et al., 2012). However,

diffusion-based techniques alone cannot easily distinguish between different sources of axon pathology. For example, an increase of extracellular-space can be caused by edema or axon degeneration, and the ratio of intra- to extracellular diffusion-visible water is independent of absolute myelin content. Complementary measures of myelin density or myelin volume fraction (MVF) can help characterize the integrity of white matter axons. These can be estimated with MRI, using for example quantitative magnetization transfer (Sled and Pike, 2000), myelin water fraction (Mackay et al., 1994) or lipid and macromolecular tissue volume (Aviv Mezer et al., 2013).

By combining MVF with *fr* it is possible to calculate a map weighted by the fiber g-ratio, which is defined as the ratio of the inner to the outer diameter of the myelin sheath and thus provide a specific marker of demyelination (Stikov et al., 2011). For example, in a case of axonal loss or edema, *fr* and MVF would decrease, but the g-ratio would remain constant. However, in the case of pure demyelination, axon density (obtained using the formula (1-MVF)**fr*) would remain relatively constant while MVF would decrease, resulting in higher g-ratio.

The fiber g-ratio is known to vary between 0.6 and 0.8 in the central nervous system (Chomiak and Hu, 2009; Rushton, 1951), with an optimal value around 0.77 (Chomiak and Hu, 2009). Bigger axons are known to have a relatively thinner myelin sheath, and thus a higher g-ratio (Ikeda and Oka, 2012; Paus and Toro, 2009; West et al., 2015). For a given diameter, however, the fiber g-ratio is relatively constant in the central nervous system and across species (Chomiak and Hu, 2009). It is also associated with sex differences in brain development (Paus and Toro, 2009; Pesaresi et al., 2015), and pathologies such as schizophrenia (Uranova et al., 2001). Measurement of fiber g-ratio using MRI has been demonstrated in the corpus callosum of a macaque and the sensitivity to the g-ratio has been shown using comparison with histology (Stikov et al., 2015b). The feasibility *in vivo* has been shown in the brain of healthy subjects (Campbell et al., 2014; Mohammadi et al., 2015), as well as in an MS patient (Stikov et al., 2015b).

The goal of this study was to map the fiber g-ratio in the *in vivo* human cervical spinal cord and study the distribution of the resulting map across different spinal pathways using atlas-based analysis.

5.2 Methods

Experiments were performed in nine healthy subjects (29 +/- 14 years old, five males), in agreement with the institutional review board of Massachusetts General Hospital (MGH). A written consent was obtained from all subjects. For each subject, two successive protocols were used: a diffusion MRI AxCaliber protocol (Assaf et al., 2008), and a lipid and macromolecular tissue volume (MTV) protocol similar to the one used by Mezer et al. (Aviv Mezer et al., 2013). The total duration of the acquisition was about 30 min.

5.2.1 Acquisition

MR scans were performed using a dedicated high-gradient (AS302) (Setsompop et al., 2013), 3T MRI scanner (MAGNETOM Skyra CONNECTOM, Siemens Healthcare). The gradients are capable of 300mT/m in each direction (x, y, z) and a maximal slew rate of 200T/m/s (downgraded to 90T/m/s for the diffusion gradients for safety reasons). A custom-made 60-channel phased-array head/neck receive coil was used (Keil et al., 2013). The body coil was used for excitation. The isocenter was set at the level of the mouth.

5.2.1.1 Diffusion

Four axial slices were acquired in an interleaved spatial order, covering C2, C3, C4 and C5 (the gap was adjusted per subject). Slices were placed at the level of the mid-vertebral body, where B0 field is the most homogeneous (Cohen-Adad et al., 2011). Slice thickness was 5mm and matrix size 128x128. The field of view (FOV) was adjusted for each subject in order to have the slice-selection direction oriented along the spinal cord main axis. Second-order shimming was done in a small box encompassing the cervical cord. Field of view in the phase encoding direction (antero-posterior) was reduced using two saturation bands, resulting in an in-plane resolution of $0.8x0.8mm^2$. A single-shot spin-echo echo-planar imaging with monopolar diffusion-encoding was used. Parameters were: TE = 70ms, acceleration of R=2 using GRAPPA reconstruction (Griswold et al., 2002), bandwidth = 1185

Hz/pixel. Effective echo-spacing was 0.49ms. The acquisition was cardiac-gated using an oximeter probe. Two slices were acquired per cardiac cycle, resulting in a repetition time of approximately 2s (forced to be higher than 1.6s to maximize T1 recovery). Effect of T1-weighting caused by partial longitudinal recovery was discussed in (Duval et al., 2015).

Q-space was sampled linearly (from G = 0 to G = √2*300 = 424 mT/m) in four directions perpendicular to the spinal cord XY, X-Y,-XY,-X-Y as in (Duval et al., 2015). In addition, 32 b=0 images were acquired. Diffusion parameters were: gradient pulse duration δ = {3, 6, 6, 10} ms and diffusion time Δ = {20, 20, 40, 36} ms. In total 460 q-space images were acquired per subject. Image acquisition was randomized in order to intersperse high SNR data (used for motion correction) throughout the acquisition.

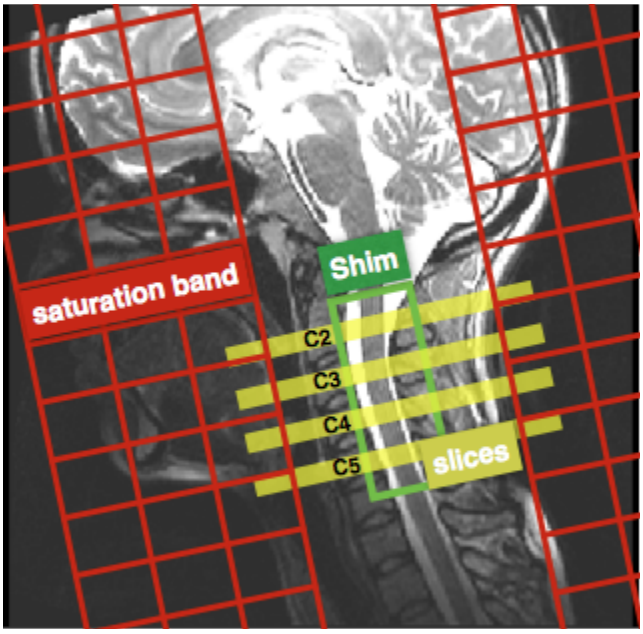

Figure 5.1: Slices, shim box and saturation bands position on subject #4.

5.2.1.2 MTV

Multiple flip angle spoiled gradient echo 3D FLASH images were acquired to measure MTV. Parameters were: TR/TE = 20/2.74 ms, flip angle = {4°, 10°, 20°, 30°}, 20 slices covering C2 to C5, matrix size = 192×192, resolution = 0.8x0.8x5mm^3, R=2 acceleration using GRAPPA reconstruction, bandwidth=400 Hz/pixel.

In order to correct for B_1+ inhomogeneity, a B_1 map was estimated using the double angle method (Insko and Bolinger, 1993). A segmented spin-echo EPI sequence was used with the following parameters: TR/TE=3000/19ms, flip angle = {60°, 120°}, 4 slices covering C2 to C5, voxel size = 3×3×5 mm^3, matrix size = 64x64.

5.2.2 Preprocessing

5.2.2.1 Diffusion

5.2.2.1.1 Estimation of noise standard deviation

For each subject, noise histogram was estimated on the raw diffusion data within a manually drawn mask showing no signal at high b-value (> 5000 s/mm^2) and close to the spinal cord (see **Figure 5.2**). The noise was estimated at b-value > 5000 s/mm^2 where signal from fat, muscles or CSF was mostly non-existent. This resulted in clean "background voxels" that were not affected by chemical shift, ghosting or aliasing artifact. This noise mask was chosen very close (<1cm) to the spinal cord in order to solve the smooth spatially-dependent noise distribution when using GRAPPA reconstruction (Aja-Fernández et al., 2011).

The noise was assumed to follow a non-central χ distribution (Aja-Fernández et al., 2011), which has three parameters: the standard deviation of the noise σ, the degree of liberty L (representing the effective number of coils) and the non-centrality parameter η (representing the underlying signal). Histogram fitting was done using Matlab[6].

[6] http://www.mathworks.com/matlabcentral/fileexchange/54244-histfit-noncentralchi

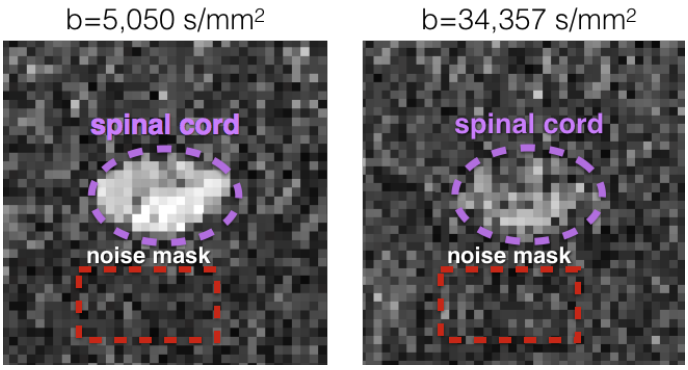

Figure 5.2: Illustration of the noise mask manually drawn on a slice of subject #5 at b = 5,050 s/mm^2 and b = bmax = 34,357 s/mm^2. Note that the high diffusion-weighting suppresses signal from CSF and fat, and thus allows to estimate the noise distribution close to the spinal cord.

5.2.2.1.2 Eddy-current and subject motion correction

Eddy-current distortions were corrected using the reversed gradient method (Bodammer et al., 2004). Subject motion was corrected by using a slice-by-slice registration method regularized along the superior-inferior direction (*SliceReg*) (Cohen-Adad et al., 2015). Images acquired with b-values ranging between 429 and 4000 s/mm^2 were used to estimate transformations as other images were not reliable (CSF contamination at low b-value and poor SNR on high b-value). The first of these images was used as a reference. Then, a spline regularization along the time dimension was used to correct images acquired at b-value < 429 and b-value > 4000 s/mm^2 (Duval et al., 2015).

5.2.2.2 MTV

FLASH images with flip angle 4°, 10° and 30° were registered to the FLASH image with flip angle 20° using *SliceReg* (Cohen-Adad et al., 2015) and mutual information metric. The B_1+ map obtained using the double-angle method was smoothed using 3D polynomial functions of order 6 and resampled to the FLASH space.

5.2.2.3 Registration of MTV metrics to diffusion data

The spinal cord was segmented on the MTV and mean diffusion image using *PropSeg* (De Leener et al., 2014). MTV data were then registered on the diffusion data based on spinal cord segmentations using slice-by-slice affine transformation.

5.2.3 Metric quantification

5.2.3.1 Diffusion

Q-space data were analyzed using the two-compartment model CHARMED (Assaf and Basser, 2005). This model assumes two compartments, intra- and extra-axonal, where water molecules present restricted (r) or hindered (h) diffusion. The MRI signal in each voxel is then expressed as:

$$S = S_0(TE, TR) \cdot [(1 - fr) \cdot S_h(q, \delta, \Delta, Dh) + fr \cdot S_r(q, \delta, \Delta, d)] \quad (1)$$

with q, δ and Δ the diffusion parameters of the MRI acquisition; Dh, fr and d quantitative metrics describing the tissue; S_h and S_r the signal models of the hindered and restricted compartments.

Dh represents the apparent diffusion coefficient of the hindered diffusion compartment, (1-fr) the fraction of hindered (or extra-axonal) water, Dr the diffusion coefficient of the restricted compartment, fr the fraction of restricted (or intra-axonal) water and d the axon diameter index (Alexander et al., 2010). Axon diameter index is the average axon diameter in a voxel, weighted by the volume of each axon. Throughout the manuscript, we refer to it as axon diameter for simplicity.

S_h was modeled assuming Gaussian diffusion using the Stejskal and Tanner equation (Stejskal and Tanner, 1965) and S_r was modeled using Gaussian phase distribution equation in a cylinder (Wang et al., 1995). The diffusion coefficient in cylinders was set to Dr = 1.4μm^2/ms as in (Barazany et al., 2009).

Model fitting was done voxel-by-voxel using the interior-point optimization algorithm (Byrd et al., 2000) included in the Matlab Optimization Toolbox Release 2014a (MathWorks, Inc.). Table 5.1 shows the fitting parameters with initialization and constraints. Rician likelihood was used in the objective function f in order to account for noise bias during the fitting:

$$f = -\sum \quad log\left(\frac{S_{data}}{\sigma} exp\left(-\frac{{S_{data}}^2 + {S_{model}}^2}{2\sigma^2}\right) I_0\left(\frac{S_{data}S_{model}}{\sigma^2}\right)\right) \qquad (2)$$

with S_{data} the experimental data, S_{model} the signal computed using equation 1 and σ the standard deviation of the noise evaluated using the method describe in the previous section.

Table 5.1: Fitting parameters used in the interior-point algorithm, with initialization and boundaries

fitting parameter	S_0	fr	Dh (μm^2/ms)	d (μm)
initialization	1	0.3	1	2
boundaries [min, max]	[0, 2]	[0, 1]	[0, 3]	[0, 10]

5.2.3.2 MTV

Voxel-wise estimation of *M0* (product of the coil reception profile and proton density) and T1 were done according to (Fram et al., 1987). B_1+ map was used to estimate the effective flip angle in each voxel (Venkatesan et al., 1998). Reception profile was estimated using the method described in (Mezer et al., 2015; Volz et al., 2012) that uses the linear relationship between T1 and PD to estimate a smooth field in the cord. We assumed no contribution from T_2* relaxation due to the fairly short TE (2.74 ms).

A cerebrospinal fluid mask was computed using (i) estimated T_1 values > 3 s and < 7 s and (ii) a 4mm dilation of the spinal cord segmentation. PD of cerebrospinal fluid (PDCSF) was then averaged in that mask. Finally, MTV was computed as in (Aviv Mezer et al., 2013):

$$MTV = 1 - (PD/PDCSF) \quad (3)$$

5.2.3.3 g-Ratio

The g-ratio weighted metric was computed as in Campbell et al. 2014 (Campbell et al., 2014; Stikov et al., 2015b), assuming that the Myelin Volume Fraction (MVF) is directly related to the Macromolecular Tissue Volume (MTV): MVF = MTV (see discussion). First, Fiber Volume Fraction (FVF) was calculated by combining Diffusion and MTV metrics: FVF = MVF+(1- MTV)*fr. Then, the g-ratio was computed as in (Stikov et al., 2011):

$$g = \sqrt{1 - MTV/FVF} \quad (4)$$

5.2.4 Effect of spinal cord curvature

The diffusion protocol assumed that the diffusion-encoding gradients were applied orthogonally to the main running spinal tracts, i.e., orthogonally to the spinal cord axis. Although we made sure that slices were positioned orthogonally to the cord (see **Figure 5.1**), some subjects exhibited a curved spinal cord and hence a bias on the estimated diffusion metrics might have been present. This bias was assessed by computing the Pearson's coefficient correlation between the error angle (defined as the angle between the slice encoding direction and the cord axis at the C2-C3 disc location) and the diffusion metrics, averaged in the white matter at C2 and C3 levels.

5.2.5 Template registration and atlas-based analysis

Registration of Diffusion and MTV metrics to the MNI-Poly-AMU template (Fonov et al., 2014), as well as the extraction of metrics per tract were done using the Spinal Cord Toolbox (SCT)[7] .

In order for the registration procedure to account for the inter-subject variability of gray matter shape, a highly contrasted white/gray matter image was generated from the diffusion data by averaging diffusion-weighted images acquired at b-values between 2,000 s/mm^2 and 20,000 s/mm^2 (see **Figure 5.5**). Throughout the manuscript, the term "mean DWI" will be used to define this image. This mean DWI image was then registered to the white matter template of the MNI-Poly-AMU template. Registration was performed slice-by-slice in two steps: (i) initial affine transformation and (ii) diffeomorphic SyN transform (Avants et al., 2008).

Quantification of metrics within the white matter and specific spinal pathways was done in the template space using the atlas of white matter tracts (Lévy et al., 2015). Maximum a posteriori method was used to correct for partial volume effect between tracts and between the white matter, the gray matter and the CSF. The following tracts were studied: gracilis, cuneatus, corticospinal, rubrospinal and spinothalamic.

In order to assess the reproducibility of g-ratio, MTV, T_1, *Dh*, *fr* and axon diameter a three-way ANOVA analysis was done using the following categories: subject, pathway and laterality (left/right). Significance level was set at $p = 0.01$.

[7] http://sourceforge.net/projects/spinalcordtoolbox/

5.3 Results

5.3.1 SNR and noise analysis

Table 5.2 shows the average SNR in the spinal cord for each subject at b=0 and bmax, along with fitted parameter L (effective number of coils) of the non-central χ distribution. Average SNR was 12.7 on b=0 images and 2.1 on images acquired at bmax. Note that this measure of SNR includes both the thermal noise and the physiological noise, hence the relatively low values. The effective number of coils L was always lower than 1.05, which is very close to a Rician distribution (L=1). Fitting results of noise histograms are shown in **Figure 5.3**. Fitting was very good for all subjects, suggesting a good modeling of the noise.

Table 5.2: SNR and L (non-central χ parameter) values for each subject

Subject #	1	2	3	4	5	6	7	8	9
SNR b=0	12.5	10.9	13.8	12.7	18.0	12.4	10.9	9.8	13.2
SNR bmax	1.9	2.3	2.5	2.0	2.8	2.4	2.0	1.7	1.8
L (Effective number of coils)	1.02	1.01	1.05	1.04	1.00	1.00	1.00	1.00	1.03

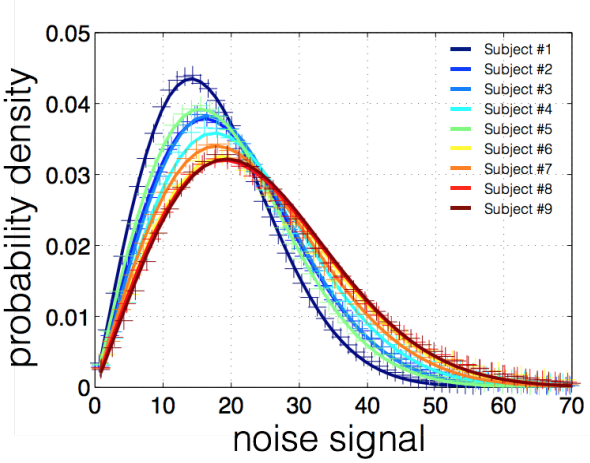

Figure 5.3: Non-central χ fitting of noise histogram for each subject. Noise was assessed on images acquired at b > 5,000 s/mm^2. Noise distribution was found to be Rician (L < 1.05 for all subjects).

5.3.2 Effect of spinal cord curvature

Figure 5.4 shows the effect of spinal cord's angle with respect to the slice encoding direction on diffusion metrics. The error angle was measured at the C3 disc for each subject. Diffusion metrics were averaged in the white matter of vertebral levels C2 and C3. *fr* was significantly decreased (r=-0.78, p=0.01) for angles over 20°. Axon diameter was significantly correlated with the error angle (r=0.67, p=0.05). The average error angle at C3, C4 and C5 discs was 17°, 12° and 23° respectively.

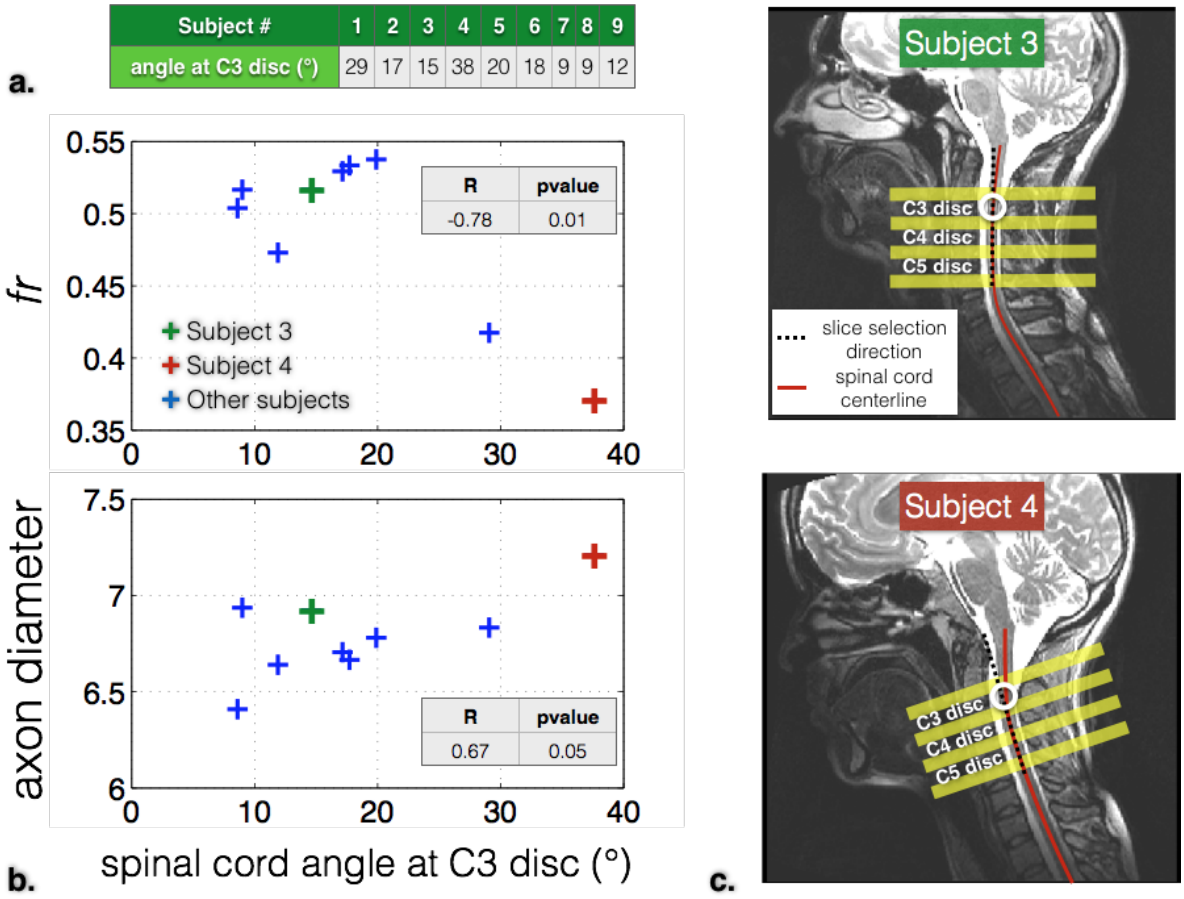

Figure 5.4. Effect of the spinal cord's angle with respect to the slice-selection direction on diffusion metrics. **a.** angle values (in degree) for each subject (here, extracted at C3 for illustration purpose). **b.** Diffusion metrics fr and axon diameter averaged in the white matter (at levels C2 and C3) as a function of spinal cord angle (at C2-C3 disc). **c.** Illustration of two subjects (#3 and #4) with different spinal cord angle at the C3 disc location.

5.3.3 Registration

Figure 5.5 shows the registration result for two different subjects. Although the initial shape of the spinal cord differed significantly between subjects, the SyN transform was able to register both the white and gray matter correctly on the MNI-Poly-AMU template.

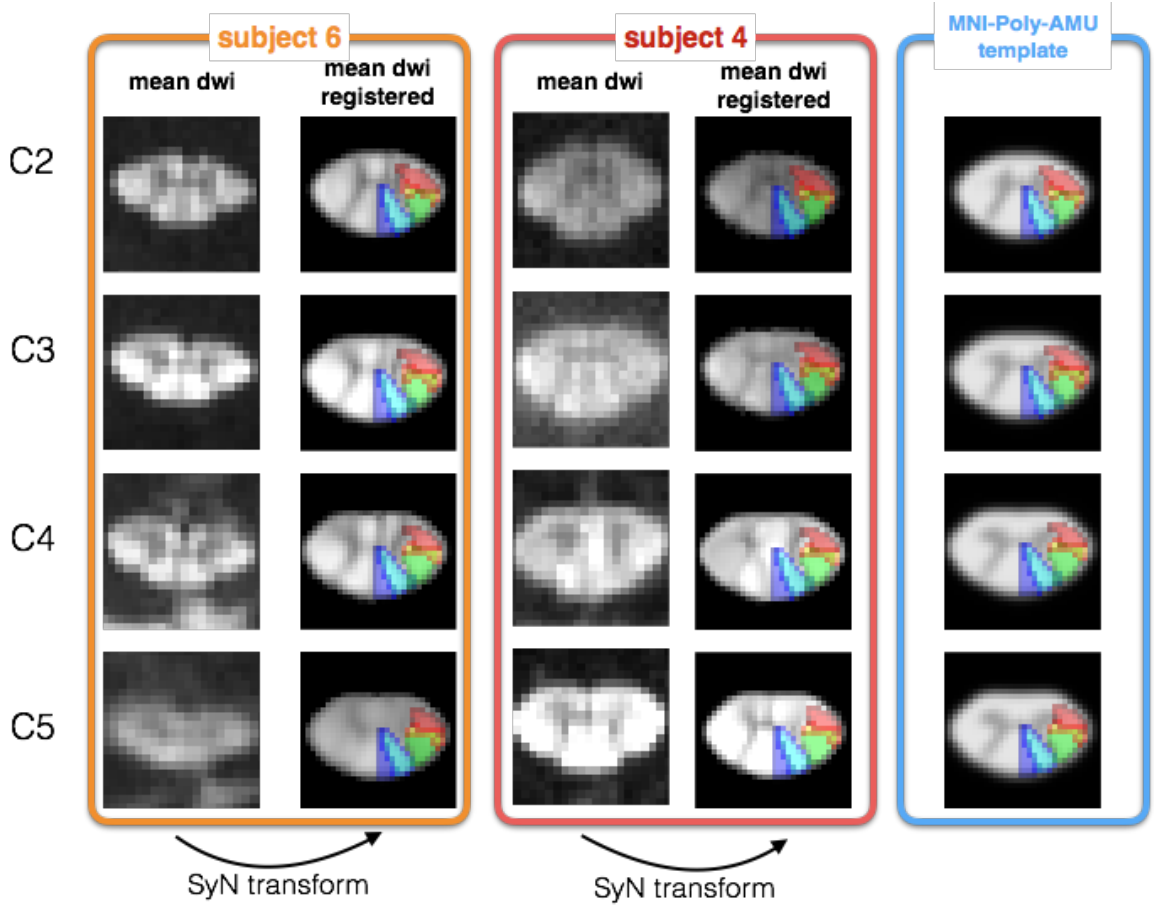

Figure 5.5: Registration result of the mean DWI to the template space. Subjects #6 (orange panel) and #4 (red panel) are presented here for illustration purpose. For each subject, the mean DWI was registered to the MNI-Poly-AMU white matter template (Blue panel) using a combination of affine and SyN transformations. Gracilis (blue), cuneatus (cyan), corticospinal (green), rubrospinal (orange) and spinothalamic (red) tracts are overlaid on the registered data for visualization purpose. Note that the mean DWIs shown here were generated using data acquired at b-values between 2,000 s/mm^2 and 20,000 s/mm^2 (also see the Methods section).

5.3.4 Quantitative MRI metric mapping

Figure 5.6 shows the quantitative maps of MTV, T_1, *fr*, axon diameter, *Dh*, FVF and g-ratio averaged across all nine subjects. We observe similar trends across slices and across left-right laterality for all metrics. Axon diameter in the gracilis tract was found to increase towards the upper cervical level (pink arrow). *fr* was similar across slices except at C5 where values were significantly lower (*fr* = 0.41 at C5 vs *fr* = 0.48 at C4, T-test gave p-value of $3x10^{-41}$). This is partly due to the larger curvature of the spinal cord at this level (23° at C4-C5 disc vs 12° at C3-C4 disc, see previous results). Lower *fr* at C5 resulted in lower FVF and lower g-ratio at this level. T_1 and MTV were negatively correlated (r = -0.81), consistent with a previous study (Aviv Mezer et al., 2013). *fr* and MTV were positively correlated (r = 0.42). As expected due to CSF contamination, apparent diffusion coefficient of the hindered compartment (*Dh*) increased at the periphery of the spinal cord, at the location of the anterior white commissure and at the thin posterior medial sulcus (black arrows on **Figure 5.6**). All metrics except the g-ratio weighted metric were sensitive to the characteristic variation of microstructure in the posterior column between cuneatus and gracilis tracts. The g-ratio weighted metric was fairly homogeneous within the spinal cord white matter except at the periphery of the spinal cord. The average g-ratio in the white matter was 0.75 +/- 0.03.

Figure 5.7 illustrate quality of *fr* and MTV metrics on an individual basis at slice C3. Even though subjects #5 and #7 present large differences in term of spinal cord shape and cross sectional area, the same pattern can be recognized in the white matter and grey matter. Some discrepancies can be observed between the two subjects, notably in the dorsal part, that we attribute to higher CSF contamination in the smaller spinal cord (subject #5). The high sensitivity of both metrics to microstructure is assessed by the strong contrast between spinal cord tracts, and their high precision by the low level of noise. Note again the apparent positive correlation between *fr* and MTV metrics in the white matter, this time on individual basis.

In order to prevent the report of biased values due to excessive spinal cord curvature, subjects #1 and #4 as well as slices acquired at C4 and C5 vertebral levels were discarded for all subsequent results.

Table 5.3 lists normative values of the different quantitative metrics extracted in the white matter (thresholding the probabilistic white matter template by 0.7). For each metric, we extracted the mean value, the standard deviation within the white matter (averaged across subjects), the standard deviation across subjects of the mean white matter values and the resulting coefficients of variation across subjects. Diffusion metrics *fr* and axon diameter were highly reproducible across subjects (COV = 4% and 3% respectively). A particularly significant variation of MTV, and thus g-ratio, was found between subjects (COV = 14%). Finally, the B1+ variation within the cord averaged across subjects was 1.02 +/- 0.06. The reader is referred to the Discussion section where possible sources of bias are listed.

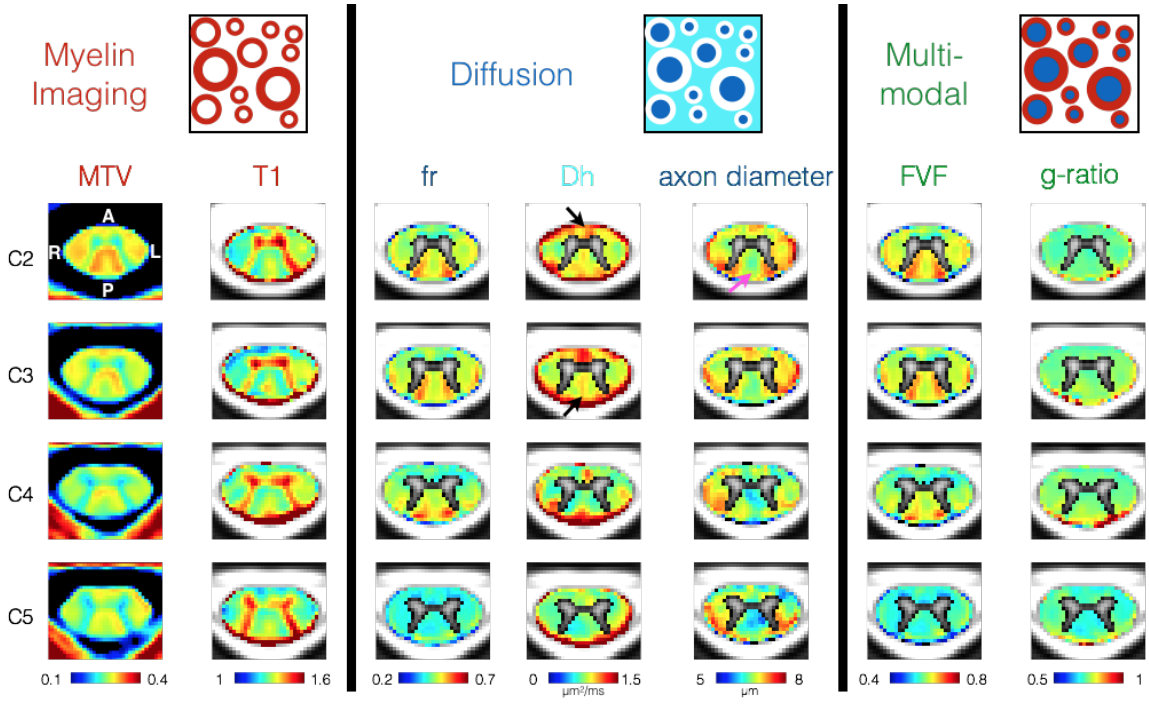

Figure 5.6: Maps of quantitative MRI metric averaged over nine subjects. **Top**: schematic cross-section of axons. **Left**: metrics obtained using MTV protocol. **Middle**: metrics obtained using diffusion MRI. **Right**: multimodal metrics

combining myelin and diffusion measures. The gray matter was masked using the probabilistic template on metrics where the model isn't adapted (mainly due to the orientation dispersion of the fibers).

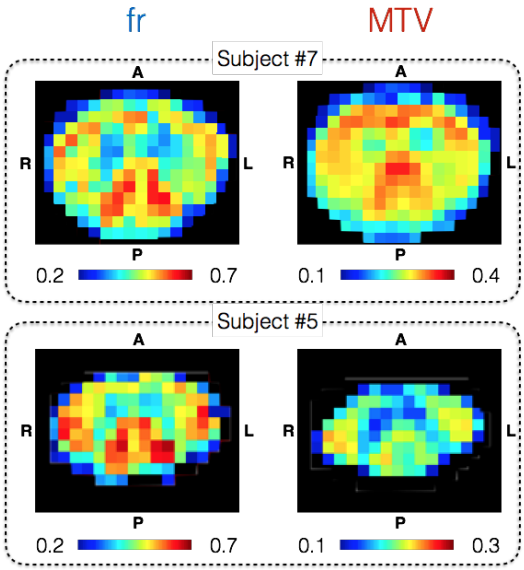

Figure 5.7: Illustration of the quality of *fr* (left column) and MTV (right column) at C3 level on two representative subjects: one with a large (subject #7) and another with a small spinal cord (subject #5). The relatively high precision and good sensitivity of these two metrics is suggested by the low level of noise and strong contrast in the white matter, allowing us to distinguish the fasciculus cuneatus and lateral corticospinal tracts, even on a single-subject basis.

Table 5.3: White matter normative values. Mean value, standard deviation within the white matter (computed per subject and then averaged), the standard deviation across subjects (of the mean white matter values obtained per subject) and the resulting coefficient of variation (COV) across subjects (STD across subjects divided by the mean).

	MTV	T1 (s)	fr	Dh ($\mu m^2/ms$)	axon diameter (μm)	FVF	g-ratio
mean	0.28	1.29	0.52	1.05	6.72	0.66	0.76
STD in white matter	0.02	0.13	0.04	0.24	0.32	0.04	0.03
STD across subjects	0.04	0.11	0.02	0.13	0.18	0.01	0.04
COV across subjects (%)	13.7	8.3	4.3	12.7	2.7	1.4	5.0

5.3.5 Tract-by-tract analysis

Figure 5.8 shows the results of the tract-by-tract analysis for each metric. The three-way ANOVA (tracts, laterality and subjects) showed no significant difference of g-ratio between tracts ($p = 0.6$). However, both myelin imaging and diffusion imaging metrics showed significant differences between tracts ($p < 4x10^{-3}$ for all metrics). Significant left-right differences were found only for the axon diameter metric, particularly in the rubrospinal and the lateral spinothalamic tracts (further work will assess if this is artefactual or not). Variation of axon diameter between tracts ($p = 4x10^{-10}$) was more significant than the variation between subjects ($p = 2x10^{-4}$), suggesting a particularly good reproducibility of axon diameter measurement across subjects. The same conclusion applies for the metrics *fr* and *Dh* with similar variation between tracts and between subjects. Results per tract can be found in supplementary material.

Based on the resulting F-scores, a post-hoc power analysis was performed in order to have more insights about the population size needed to detect changes across tracts and/or laterality, assuming a statistical power over 99%. To detect changes across tracts for g-ratio, axon diameter, *fr*, MTV and *Dh*, the required sample size is respectively 70, 2, 2, 3 and 2. To detect changes across laterality (also for the same metrics), the required sample size is 8, 2, 200, 2 and 4.

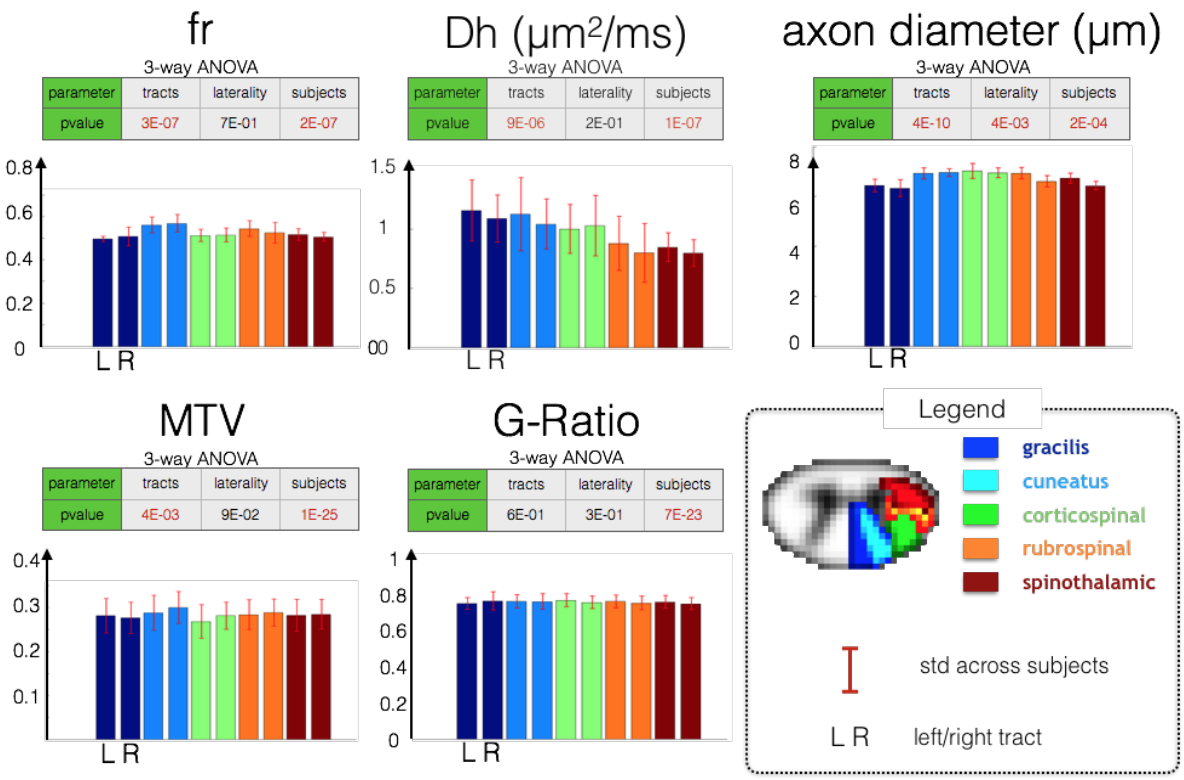

Figure 5.8: Tract-by-tract analysis of quantitative metrics. Metrics were extracted in five different tracts (color-coded) in the left and right hemispheres of the spinal cord. A three-way ANOVA analysis was done to assess reproducibility across tracts, laterality and subjects.

5.4 Discussion

In this work we combined axon and myelin density measures in the spinal cord of nine healthy subjects to derive a metric weighted by the fiber g-ratio. We believe this is the first attempt to measure the g-ratio *in vivo* in the spinal cord. Although results showed good reproducibility across tracts, slices and laterality left-right, the interpretation of these quantitative metrics needs to be discussed.

5.4.1 Comparison with histology

To our knowledge, there is very little literature reporting average values of g-ratio in the spinal cord. In their paper, Chomiak and Hu (Chomiak and Hu, 2009) presented an extensive literature review of the measured g-ratio in the CNS: a value of 0.79 has been reported in the spinal cord of mice (Benninger et al., 2006), and values ranging between 0.72 and 0.81 in different part of the CNS (corpus callosum, optic nerve, superior cerebellar peduncle, anterior commissure, internal capsule and brainstem) of a variety of small animals (mouse, rat, murine, guinea pig and rabbit). They also proposed a theoretical optimal g-ratio value of 0.77 in the CNS. (Remahl and Hildebrand, 1982) observed a higher myelination of axons, and thus a lower g-ratio, in the spinal cord compared to the corpus callosum in rodents. This observation is also corroborated by significantly higher myelin water fraction measured with MRI (Kolind and Deoni, 2011). In another study performed in the ventral root of cat spinal cord, g-ratio ranged between 0.6 and 0.7 (Berthold et al., 1983). The g-ratio measured in the present study (0.75 +/- 0.03) is in the same range as that reported by previous histological studies (between 0.6 and 0.81). Abnormal values (g-ratio > 0.85 or < 0.6) were found at the periphery of the spinal cord and are likely caused by low MTV and FVF values due to CSF contamination, and thus unstable values of g-ratio (see equation 4).

As also observed in (Duval et al., 2015), maps of axons diameter are particularly consistent with histology, but should be interpreted with caution. Indeed, values reported in the current paper are known to overestimate the real mean axon diameter because (i) the use of a single diameter model prevented us from correcting for the effect of larger signal

contribution from larger axons (Alexander et al., 2010), (ii) axons smaller than ~3µm hit the resolution limit for axon diameter at 300 mT/m (Nilsson and Alexander, 2012) and could be interpreted as axons of ~3µm diameter in the fitting procedure and (iii) the diffusion metrics might be biased by time-dependency of hindered diffusion coefficient *Dh* (Burcaw et al., 2015; De Santis et al., 2016; Novikov et al., 2014). Note that this last effect could also disturb the *fr* metric in this study due to the use of variable diffusion time, as it does in models that use the tortuosity approximation (De Santis et al., 2016).

MTV is the complement of the water volume fraction. Due to the use of short TE (2.74ms) the water volume fraction also includes myelin water or any free proton in the tissue (Tofts, 2003). As reviewed by (Tofts, 2003), evaporation or gravimetric technique of post-mortem or biopsy, as well as other MRI proton density studies, show that human white matter is composed of 72.5% water in the brain. A similar value was measured in the spinal cord (Lajtha, 2013, p. 308) and is consistent with the present study: PD = 1 - MTV = 72% in average. The relation between MTV and myelin content is discussed in the next section (4.2).

fr measures the ratio of the intra-axonal water over the MRI visible water content (assuming restriction in axons only). A range of 45 to 60% was proposed in the review paper (Nilsson et al., 2013). By fixing the g-ratio to 0.75, we came across the same range of *fr* based on the previous literature reporting an intra-axonal volume fraction of 33% estimated from osmium staining histology of the brain (Perge et al., 2009; Stikov et al., 2015c) and spinal cord (Ong and Wehrli, 2010). Those values are in agreement with the values of *fr* found in this study (0.52 +/- 0.04).

It should be noted that using histology as ground truth has limitations, given the numerous tissue alterations during preparation (tissue shrinkage after fixation, slicing, staining, microscopy resolution, etc.). For instance, histological studies based on optical imaging in the spinal cord (Chin et al., 2004, 2002; Ong et al., 2008) usually overestimate the myelin fraction compared to the axoplasm volume, leading to abnormal values of g-ratio (~0.3), which is likely due to the insufficient spatial resolution of optical imaging. Alternative histology techniques, such as in vivo microscopy of myelin using coherent anti-Stokes

Raman scattering (Bégin et al., 2009; Fu et al., 2008), might prove useful in addressing those limitations.

5.4.2 Myelin versus macromolecular volume fraction

The sensitivity of MTV to myelin has been demonstrated through the relationship of MTV with other quantitative myelin mapping techniques (Aviv Mezer et al., 2013). In particular, MTV correlates with myelin content (r=0.52 in a single subject and r=0.9 using literature data), as measured with quantitative magnetization transfer qMT (Sled and Pike, 2000). Note that qMT has been used to measure myelin content in different g-ratio applications (Stikov et al., 2015b, 2011). The sensitivity of MTV to myelin is also confirmed by (i) lower values in the grey matter (see **Figure 5.6**), (ii) its sensitivity to demyelination in the spinal cord (Bot et al., 2004; Chong et al., 2016), (iii) its high correlation with myelin stained histology (r^2 = 0.52) in multiple sclerosis (Mottershead et al., 2003), and (iv) its relation with brain development (Saito et al., 2012).

Like other MRI myelin mapping techniques, MTV has to be calibrated to retrieve the absolute myelin volume fraction from the myelin (or macromolecular)-specific metric. This could be done assuming a linear relationship MVF = a*MTV+b. Interestingly MTV values found in the present study are very close to the volume of the myelin sheath (MVF) in white matter tissue estimated using histology: 25 to 30% in the brain (Mottershead et al., 2003; Perge et al., 2009; Stikov et al., 2015c) and the spinal cord (Ong and Wehrli, 2010) (computed from extra-axonal volume assuming a g-ratio of 0.75). In addition, the relatively small variation of MTV (STD in the white matter = 0.02) measured in the present study is consistent with the small variation of myelin content measured with myelin segmented histology of rat spinal cord (STD across tracts = 0.03) (Harkins et al., 2016), or assessed with myelin stained human spinal cord (Bot et al., 2004; Nijeholt et al., 2001). These observations motivated the assumption MVF = MTV used in the present manuscript. This result is somewhat unexpected because MTV includes macromolecules and lipids present not only in the myelin, but also in glial cells membranes and organelles. MTV however

doesn't include the myelin water while MVF does. Similar values between myelin and MTV suggest that the non-myelin macromolecules compensate approximately the myelin water.

Note that the proton density (PD = 1 - MTV) is required in order to measure FVF accurately: FVF = MVF + PD*fr. So far, MRI g-ratio studies that use compartmental diffusion models assumed that PD is the opposite of myelin (1-MVF) (Campbell et al., 2014; Dean et al., 2016; Stikov et al., 2015b), without considering the fraction of macromolecules that are outside the myelin (11 to 14% in healthy tissue). In particular, this assumption could be critical in pathology where the extra-axonal compartment is modified due to glial cell proliferation, in particular microglia, or astrocyte scarring. The acquisition of both PD and myelin content might be an interesting means to increase the specificity of the g-ratio metric. While we considered additional myelin biomarkers, hardware constraints on the body coil of the CONNECTOM scanner prevented us from using magnetization transfer pulse. Further investigations using other myelin-specific techniques, such as multicomponent T_2, are needed.

5.4.3 Reproducibility of quantitative metrics

Axon diameter and *fr* were remarkably reproducible across subjects without significant spinal cord curvature with coefficients of variation of 2.7 and 4.3% respectively. Variation between tracts were larger than or similar to the variation between subjects. These findings suggest that axon diameter is very similar between subjects and that these metrics do not depend much on factors such as the coil sensitivity profile, the level of noise, the curvature of the spinal cord within reasonable range (< 20°) and other imaging artifacts that can affect the reproducibility of other metrics. This particularly good reproducibility could be attributed to the use of large diffusion gradient up to √2*300 = 424 mT/m, high SNR thanks to the custom-made tight fitting 64ch coil, and also to the 2D q-space sampling (orthogonal to the spinal cord axis) that simplifies the white matter modeling with fewer parameters to fit and fewer assumptions. Indeed, the tortuosity model designed for 3D sampling (Alexander et al., 2010) also has some bias (De Santis et al., 2016) and reduced sensitivity to the restricted diffusion coefficient *Dr* (see discussion in (Duval et al., 2015)). The

dependency of axon diameter and *fr* to the protocol scheme (diffusion parameters G, δ and Δ) will be investigated in future studies. Finally, we can note that comparison with our previous dataset (Duval et al., 2015), acquired with a different scheme, suggests relatively small variation for *fr* (see discussion "Comparison with previous work").

Two subjects exhibited large spinal cord curvature (>20° at C2/C3), which introduced biases in the estimation of diffusion metrics. Although the spinal cord curvature can be accounted for in the diffusion model, large curvature can also lead to a total loss of signal at high b-value due to higher diffusion and lower restriction. This issue could be solved with the development of sequences that enable the acquisition of non-parallel slices, or minimized using specially designed head supports that would enable easier antero-posterior tilting of the head.

Here we used cardiac gating to minimize the effect of CSF flow and cord motion on diffusion scans. While cardiac gating with a relatively short TR (here, TR was set to two cardiac cycles, hence about 2s) was previously shown to have minimum impact on the estimation of *fr* and *fh*, it should be mentioned that the CSF having a much longer T_1 than the tissue (0.85 vs. 3.5 s at 3T in the CSF, according to (Clare and Jezzard, 2001; Smith et al., 2008)), its partial recovery might have introduced a bias that needs to be further investigated (Pasternak et al., 2009).

MTV showed a reproducible contrast across tracts (three-way ANOVA, $p = 0.004$), but also a significant bias across subjects ($p = 1x10^{-25}$) and some inconsistency along the spinal cord (see **Figure 5.6**) that might be artifactual. This inconsistency along the spinal cord is different from the relative consistency of MTV values in different brain pathways (Aviv Mezer et al., 2013). Several causes could explain these discrepancies. Firstly, flip angle correction using B1+ mapping might have lacked accuracy (see **Figure 5.6**). Incorrect B1+ mapping could be due to an insufficiently long TR (5s) that led to incomplete longitudinal relaxation of spins (especially in the CSF). Alternative B1+ mapping techniques could be explored, such as actual flip angle (Yarnykh, 2007) or Bloch-Siegert technique (Sacolick et al., 2010). Secondly, the measure of PD in the CSF (PDCSF) used to normalize PD in the

spinal cord (see equation 3) might have been affected by flow artifacts (Lisanti et al., 2007) and partial volume effects (e.g., with spinal nerves and epidural fat).

5.4.4 Comparison with previous work

The diffusion protocol used here was slightly modified compared to our previous study (Duval et al., 2015): the echo time was kept fixed at 70 ms in order to prevent T_2 relaxation effects, gradient pulse duration δ was varied between 3 ms (necessary for the acquisition at short diffusion time Δ, as suggested by (Huang et al., 2015)) and 10 ms (necessary for large diffusion encoding (qmax = 0.18 μm^{-1})). Gaussian Phase Distribution was used here to model the restricted compartment as in the supplementary material S4 of (Duval et al., 2015). Correction of noise bias was improved in the present paper by (i) fitting a non-central χ distribution on noise histogram and (ii) using Rician likelihood in the objective function of the fitting procedure, which could partly explain why axon diameter measurements were more reproducible across subjects in the present study.

Figure 5.9 compares the results of axon diameter and *fr* mapping between (Duval et al., 2015) and the present study. The metric *fr* was reproducible between both studies (0.52 vs 0.5 in average). Axon diameter mapping however was slightly larger in the present paper (6.72 μm +/- 0.18 μm) than in (Duval et al., 2015) (6.14 +/ 0.9μm). While fairly small, these differences might be explained by differences between the two studies regarding (i) noise correction algorithm (ii) acquisition protocols or (iii) subject demography (effects of aging, spinal cord area or sex), although the small variation of axon diameter across subjects in the present study (STD = 0.18 μm) suggest a small effect of the subject phenotype. A similar contrast between the different tracts can be observed in both studies. For example, the gracilis tract exhibited small and dense axons with increasing diameter towards the rostral direction. Also, both studies show largest axons in the spinocerebellar tract.

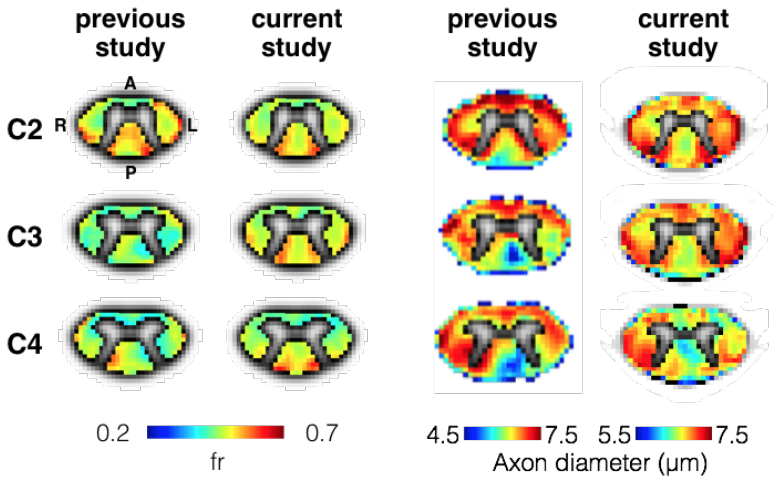

Figure 5.9: Comparison of axon diameter (left) and fr (right) between (Duval et al., 2015) and the current study (2016). Note that these maps were averaged across five subjects in the previous study (Duval et al., 2015) and seven other subjects in the current study.

The fraction of restricted water measured in the present study (0.52 +/- 0.04) agrees well with NODDI in the human spinal cord white matter (0.57 +/- 0.09) (Grussu et al., 2015). This result shows the consistency of the models between 3D and 2D q-space sampling, as was expected due to the relatively low dispersion of fibers in the spinal cord white matter as measured with NODDI (0.027 +/- 0.003) (Grussu et al., 2015). Values are also in agreement with studies using diffusion data acquired perpendicular to the fibers ($fr \approx 0.5$) as explained in (Nilsson et al., 2013). However it should be noted that intracellular volume fraction is often underestimated and can largely differ across methods (Ferezi et al, NIMG, 2015).

MTV values reported in the present paper (0.28 +/- 0.02 in the white matter) are consistent with previous brain studies (between 0.23 and 0.31) (Aviv Mezer et al., 2013; Tofts, 2003). MTV showed very little differences between the spinal cord tracts with a standard deviation in the white matter of only 0.02 (see Table 5.3 and MTV values in supplementary material). This small variation (less than 2% variation between white matter ROIs) was also reported using myelin mapping techniques on rat spinal cord white matter using both histology and

quantitative magnetization transfer methods (Dula et al., 2010), and on the *in vivo* human spinal cord using mcDESPOT (Kolind and Deoni, 2011) and inhomogeneous magnetization transfer (Taso et al., 2016).

We notice a negative correlation between the T1 map and the mean axon diameter map (see **Figure 5.6**) as previously demonstrated in the rodent spinal cord (Harkins et al., 2016). Although the contrast of T1 maps on **Figure 5.6** is qualitatively consistent with cervical spinal cord T1 maps found in the literature (Smith et al., 2008), the T1 values were overestimated (1290 +/- 130 ms versus 876 +/- 27 ms). A bias is expected with the variable flip angle T1 mapping method in vivo as shown in (Stikov et al., 2015a). The effect on the MTV metric is unclear: although MTV is normalized with the CSF, the slope of MTV might have been affected by biased T1 values. Future work will address this question by comparing results with MTV values obtained using calibrated T1 from inversion recovery sequence as done in (A. Mezer et al., 2013).

5.4.5 Interpretation of g-ratio measurements

Based on metric mapping (**Figure 5.6**) and tract-by-tract analysis (**Figure 5.8**), both *fr* and MTV are sensitive to the microstructural differences across spinal tracts. Theoretically however, both metrics present a lack of specificity. Indeed, a decrease of their value can be caused by axonal loss, edema, CSF contamination or demyelination. Combining both metrics via the g-ratio equation (equation 4) aims at disentangling the contributions of confounding factors and extracting only the degree of axon myelination. This would help for instance to understand the complex evolution of multiple sclerosis (MS) lesions: inflammatory cell swelling, demyelination, axon atrophy, astrocyte scarring; all these processes can increase both the intra- and extra-cellular spaces or reduce myelin content (Franklin, 2002; Frohman et al., 2006), making interpretation of single modality MRI metrics difficult and producing discrepancies between the lesion activity observed with MRI and the patient clinical score (Guttmann et al., 1995; Rovira et al., 2013). The robustness of the g-ratio weighted metric to these different case scenarios will be investigated in future studies. Some assumptions that are necessary for computing the g-ratio might not hold in

pathology. For instance, the hindered compartment might become restricted in case of aquaporin-4 deficiency (Badaut et al., 2011) or glial scar formation. Also, the macromolecular content might increase independently from (and not proportionally with, as assumed in "4.2. Myelin versus macromolecular volume fraction") myelin content due to the proliferation of microglia, migration of astrocytes or by the presence of axonal debris. Additional information, such as Myelin Water Fraction (MWF), might be required to resolve all these case scenarios. Yet, the g-ratio metric computed in the present manuscript is robust to the CSF contamination at the periphery of the spinal cord, suggesting that it can discriminate a pure oedema scenario from inflammation with demyelination, and thus is expected to bring a gain in specificity compared to the quantitative metrics *fr* and MTV taken independently.

The g-ratio is known to be fairly homogeneous in the white matter (Chomiak and Hu, 2009; Rushton, 1951), which has been confirmed in the current experiment with fairly low STD of g-ratio across the entire white matter (0.75 +/- 0.03). The underlying source of a homogeneous g-ratio measured with MRI is the correlation found between *fr* and MTV (r = 0.42, see results section "Quantitative MRI metric mapping"), which will be detailed in the following paragraph.

If we assume a perfectly constant g-ratio, equation 4 can be rewritten in order to express MTV as a function of *fr*:

$$MTV(fr) = \frac{k * fr}{(1 - k * (1 - fr))} \; with \; k = 1 - g^2 \qquad (5)$$

For g $\in$ [0,1], this function is increasing monotonically. A homogeneous g-ratio should then be associated with a correlation between MTV and *fr* metrics, as observed on metrics mapping of **Figure 5.6** and **Figure 5.7**. **Figure 5.10** shows the voxel-wise comparison of the subject-averaged metrics MTV and *fr* in the white matter, along with the line of constant g-ratio computed from equation 5, suggesting that both metrics tend to a homogeneous g-ratio for each subject. Note that this figure also gives information on the range of MTV and

fr values that would produce abnormal g-ratio values, as well as the precision of g-ratio measurement via the distance separating g-ratio level sets.

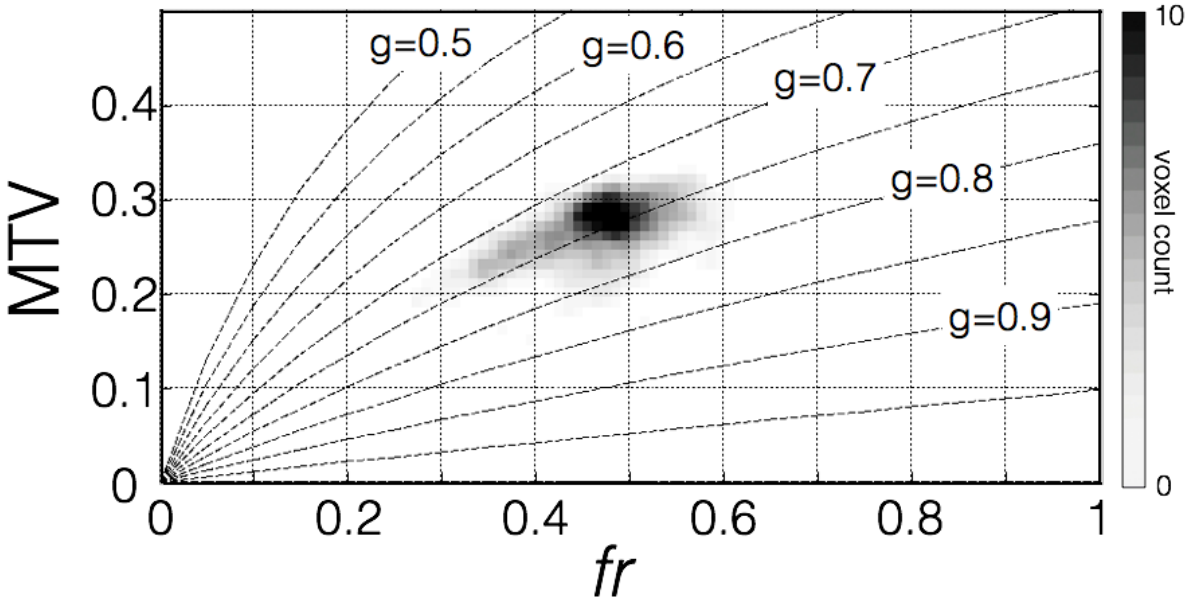

Figure 5.10: Voxel-wise comparison of subject-averaged MTV and fr metrics in the white matter with lines of constant g-ratio. The grayscale encodes for voxel count. The two different MRI metrics seem to tend toward a constant g-ratio.

g-Ratio values in the gray matter has been masked out voluntarily on **Figure 5.6** to prevent misinterpretation. Indeed, the large orientation dispersion of fibers, as well as the presence of numerous somas and dendrites, limit the interpretation of diffusion metrics acquired with 2D q-space sampling. Note however that the g-ratio appeared homogeneous on the entire cord (data not shown, STD within the cord = 0.03) due to the high correlation between MTV and *fr* in the entire cord ($r = 0.70$, $p = 10^{-80}$, 548 voxels).

The computation of the fiber g-ratio using equation 4 presents two main limitations. First, it provides an "aggregate" g-ratio instead of the average g-ratio in a voxel (Stikov et al., 2011). This metric has been shown experimentally (Stikov et al., 2015c; West et al., 2016) to correlate strongly with the average g-ratio ($r = 0.85$, $p = 0.007$) with moderate

overestimation ($g_{aggregate} \cong g_{mean} + 0.03$). Second, we assume a good specificity and accuracy of quantitative MRI metrics *fr* and MTV. As shown in (Campbell et al., 2016) and discussed in (Dean et al., 2016), this assumption is particularly critical because a lack of accuracy in one of these metrics would imply a poor decoupling of both metrics and thus wrong estimation of g-ratio. A good knowledge of the bias of the quantitative metrics would be required to use g-ratio as a direct measure of the degree of myelination, especially in the pathological white matter. Yet, the accuracy shouldn't be considered at the expense of the precision. Indeed, the quantitative metrics that we aim to develop are expected to measure subtle changes and should be sensitive to the diversity of microstructure in the white matter tissue.

Results from this study suggest that MTV and *fr* are particularly precise and sensitive to white matter characteristics, allowing us to detect microstructure differences between white matter tracts on an individual basis (see **Figure 5.7** and results of the three-way ANOVA on **Figure 5.8**). Regarding accuracy, the average *fr* measured in the present in vivo study are in good accordance with previous *ex vivo* histological studies, as discussed in section "4.1. Comparison with histology". The use of MTV as a surrogate for myelin provided an accurate approximation on healthy tissue with a 1:1 relation, although one has to keep in mind that this might not hold true in the pathological white matter, as discussed in section "4.2. Myelin versus macromolecular volume fraction".

All these evidences suggest that the technique used in this study provides a metric weighted by the fiber g-ratio that is expected to have higher sensitivity and specificity to the integrity of the myelin sheath. The specificity of this metric and its robustness in pathology will be investigated in the future.

5.5 Conclusion

A metric weighted by the fiber g-ratio can be measured in the *in vivo* human spinal cord using MRI. Indirect correlation with known histological features, as well as the good reproducibility across tracts of the metrics that are used to compute the g-ratio, suggest a good specificity of these quantitative metrics for the underlying microstructure. These new biomarkers might prove useful for the early diagnosis of demyelination and for assessing the efficiency of new remyelinating drugs.

5.6 Acknowledgements

We would like to thank the participants of this study and M. Brun-Cosme-Bruny and M. De Leener for their help with the processing of the data. We also thank the anonymous reviewers for their valuable comments. This study was founded by the National Institutes of Health, the NIH Blueprint Initiative for Neuroscience Research grant U01MH093765, the National Institutes of Health grant P41EB015896, the MS Society of Canada [EGID 2370], the Canada Research Chair in Quantitative Magnetic Resonance Imaging (JCA), the Canadian Institute of Health Research [CIHR FDN-143263], the Fonds de Recherche du Québec - Santé [28826], the Fonds de Recherche du Québec - Nature et Technologies [2015-PR-182754], the Natural Sciences and Engineering Research Council of Canada [435897-2013] and the Quebec BioImaging Network.

5.7 Bibliography

Adluru, G., Gur, Y., Anderson, J.S., Richards, L.G., Adluru, N., DiBella, E.V.R., 2014. Assessment of white matter microstructure in stroke patients using NODDI. Conf. Proc. IEEE Eng. Med. Biol. Soc. 2014, 742–745.

Aja-Fernández, S., Tristán-Vega, A., Hoge, W.S., 2011. Statistical noise analysis in GRAPPA using a parametrized noncentral Chi approximation model. Magn. Reson. Med. 65, 1195–1206.

Alexander, A.L., Lee, J.E., Lazar, M., Field, A.S., 2007. Diffusion tensor imaging of the brain. Neurotherapeutics 4, 316–329.

Alexander, D.C., Hubbard, P.L., Hall, M.G., Moore, E.A., Ptito, M., Parker, G.J.M., Dyrby, T.B., 2010. Orientationally invariant indices of axon diameter and density from diffusion MRI. Neuroimage 52, 1374–1389.

Assaf, Y., Basser, P.J., 2005. Composite hindered and restricted model of diffusion (CHARMED) MR imaging of the human brain. Neuroimage 27, 48–58.

Assaf, Y., Blumenfeld-Katzir, T., Yovel, Y., Basser, P.J., 2008. AxCaliber: a method for measuring axon diameter distribution from diffusion MRI. Magn. Reson. Med. 59, 1347–1354.

Avants, B.B., Epstein, C.L., Grossman, M., Gee, J.C., 2008. Symmetric diffeomorphic image registration with cross-correlation: evaluating automated labeling of elderly and neurodegenerative brain. Med. Image Anal. 12, 26–41.

Badaut, J., Ashwal, S., Adami, A., Tone, B., Recker, R., Spagnoli, D., Ternon, B., Obenaus, A., 2011. Brain water mobility decreases after astrocytic aquaporin-4 inhibition using RNA interference. J. Cereb. Blood Flow Metab. 31, 819–831.

Barazany, D., Basser, P.J., Assaf, Y., 2009. In vivo measurement of axon diameter distribution in the corpus callosum of rat brain. Brain 132, 1210–1220.

Bégin, S., Bélanger, E., Laffray, S., Vallée, R., Côté, D., 2009. In vivo optical monitoring of tissue pathologies and diseases with vibrational contrast. J. Biophotonics 2, 632–642.

Benninger, Y., Colognato, H., Thurnherr, T., Franklin, R.J.M., Leone, D.P., Atanasoski, S., Nave, K.-A., Ffrench-Constant, C., Suter, U., Relvas, J.B., 2006. Beta1-integrin signaling mediates premyelinating oligodendrocyte survival but is not required for CNS myelination and remyelination. J. Neurosci. 26, 7665–7673.

Berthold, C.H., Nilsson, I., Rydmark, M., 1983. Axon diameter and myelin sheath thickness in nerve fibres of the ventral root of the seventh lumbar nerve in the adult and developing cat. J. Anat. 3).

Bodammer, N., Kaufmann, J., Kanowski, M., Tempelmann, C., 2004. Eddy current correction in diffusion-weighted imaging using pairs of images acquired with opposite diffusion gradient polarity. Magn. Reson. Med. 51, 188–193.

Bot, J.C.J., Blezer, E.L.A., Kamphorst, W., Lycklama A Nijeholt, G.J., Ader, H.J., Castelijns, J.A., Ig, K.N., Bergers, E., Ravid, R., Polman, C., Barkhof, F., 2004. The spinal cord in multiple sclerosis: relationship of high-spatial-resolution quantitative MR imaging findings to histopathologic results. Radiology 233, 531–540.

Burcaw, L.M., Fieremans, E., Novikov, D.S., 2015. Mesoscopic structure of neuronal tracts from time-dependent diffusion. Neuroimage 114, 18–37.

Byrd, R.H., Gilbert, J.C., Nocedal, J., 2000. A trust region method based on interior point techniques for nonlinear programming. Math. Program. 89, 149–185.

Campbell, J.S.W., Leppert, I.R., Boudreau, M., Narayanan, S., Cohen-Adad, J., Pike, G.B., Stikov, N., 2016. Mapping the myelin g-ratio: promises and pitfalls, in: Proceedings of the 24th Annual Meeting of ISMRM. p. 1501.

Campbell, J.S.W., Stikov, N., Dougherty, R.F., Bruce Pike, G., 2014. Combined NODDI and qMT for full-brain g-ratio mapping with complex subvoxel microstructure, in: Proceedings of the 22th Annual Meeting of ISMRM, Milan. p. 393.

Chin, C.-L., Wehrli, F.W., Fan, Y., Hwang, S.N., Schwartz, E.D., Nissanov, J., Hackney, D.B., 2004. Assessment of axonal fiber tract architecture in excised rat spinal cord by localized NMR q-space imaging: simulations and experimental studies. Magn. Reson. Med. 52, 733–740.

Chin, C.-L., Wehrli, F.W., Hwang, S.N., Takahashi, M., Hackney, D.B., 2002. Biexponential diffusion attenuation in the rat spinal cord: computer simulations based on anatomic images of axonal architecture. Magn. Reson. Med. 47, 455–460.

Chomiak, T., Hu, B., 2009. What is the optimal value of the g-ratio for myelinated fibers in the rat CNS? A theoretical approach. PLoS One 4, e7754.

Chong, A.L., Chandra, R.V., Chuah, K.C., Roberts, E.L., Stuckey, S.L., 2016. Proton Density MRI Increases Detection of Cervical Spinal Cord Multiple Sclerosis Lesions Compared with T2-Weighted Fast Spin-Echo. AJNR Am. J. Neuroradiol. 37, 180–184.

Clare, S., Jezzard, P., 2001. Rapid T1 mapping using multislice echo planar imaging. Magn. Reson. Med. 45, 630–634.

Cohen-Adad, J., El Mendili, M.-M., Lehéricy, S., Pradat, P.-F., Blancho, S., Rossignol, S., Benali, H., 2011. Demyelination and degeneration in the injured human spinal cord detected with diffusion and magnetization transfer MRI. Neuroimage 55, 1024–1033.

Cohen-Adad, J., Lévy, S., Avants, B., 2015. Slice-by-slice regularized registration for spinal cord MRI: SliceReg, in: Proceedings of the 23th Annual Meeting of ISMRM. Toronto, p. 4428.

Dean, D.C., O'Muircheartaigh, J., Dirks, H., Travers, B.G., Adluru, N., Alexander, A.L., Deoni, S.C.L., 2016. Mapping an index of the myelin g-ratio in infants using magnetic resonance imaging. Neuroimage 132, 225–237.

De Leener, B., Kadoury, S., Cohen-Adad, J., 2014. Robust, accurate and fast automatic segmentation of the spinal cord. Neuroimage 98, 528–536.

De Santis, S., Jones, D.K., Roebroeck, A., 2016. Including diffusion time dependence in the extra-axonal space improves in vivo estimates of axonal diameter and density in human white matter. Neuroimage 130, 91–103.

Dijkers, M., Bryce, T., Zanca, J., 2009. Prevalence of chronic pain after traumatic spinal cord injury: a systematic review. J. Rehabil. Res. Dev. 46, 13–29.

Dula, A.N., Gochberg, D.F., Valentine, H.L., Valentine, W.M., Does, M.D., 2010. Multiexponential T2, magnetization transfer, and quantitative histology in white matter tracts of rat spinal cord. Magn. Reson. Med. 63, 902–909.

Duval, T., McNab, J.A., Setsompop, K., Witzel, T., Schneider, T., Huang, S.Y., Keil, B., Klawiter, E.C., Wald, L.L., Cohen-Adad, J., 2015. In vivo mapping of human spinal cord microstructure at 300mT/m. Neuroimage 118, 494–507.

Fonov, V.S., Le Troter, A., Taso, M., De Leener, B., Lévêque, G., Benhamou, M., Sdika, M., Benali, H., Pradat, P.-F., Collins, D.L., Callot, V., Cohen-Adad, J., 2014. Framework for integrated MRI average of the spinal cord white and gray matter: The MNI-Poly-AMU template. Neuroimage 102P2, 817–827.

Fram, E.K., Herfkens, R.J., Johnson, G.A., Glover, G.H., Karis, J.P., Shimakawa, A., Perkins, T.G., Pelc, N.J., 1987. Rapid calculation of T1 using variable flip angle gradient refocused imaging. Magn. Reson. Imaging 5, 201–208.

Franklin, R.J.M., 2002. Why does remyelination fail in multiple sclerosis? Nat. Rev. Neurosci. 3, 705–714.

Frohman, E.M., Racke, M.K., Raine, C.S., 2006. Multiple Sclerosis — The Plaque and Its Pathogenesis. N. Engl. J. Med. 354, 942–955.

Fu, Y., Huff, T.B., Wang, H.-W., Wang, H., Cheng, J.-X., 2008. Ex vivo and in vivo imaging of myelin fibers in mouse brain by coherent anti-Stokes Raman scattering microscopy. Opt. Express 16, 19396–19409.

Griswold, M.A., Jakob, P.M., Heidemann, R.M., Nittka, M., Jellus, V., Wang, J., Kiefer, B., Haase, A., 2002. Generalized autocalibrating partially parallel acquisitions (GRAPPA). Magn. Reson. Med. 47, 1202–1210.

Grussu, F., Schneider, T., Zhang, H., Alexander, D.C., Wheeler-Kingshott, C.A.M., 2015. Neurite orientation dispersion and density imaging of the healthy cervical spinal cord in vivo. Neuroimage 111, 590–601.

Guttmann, C.R., Ahn, S.S., Hsu, L., Kikinis, R., Jolesz, F.A., 1995. The evolution of multiple sclerosis lesions on serial MR. AJNR Am. J. Neuroradiol. 16, 1481–1491.

Harkins, K.D., Xu, J., Dula, A.N., Li, K., Valentine, W.M., Gochberg, D.F., Gore, J.C., Does, M.D., 2016. The microstructural correlates of T1 in white matter. Magn. Reson. Med. 75, 1341–1345.

Hildebrand, C., Remahl, S., Persson, H., Bjartmar, C., 1993. Myelinated nerve fibres in the CNS. Prog. Neurobiol. 40, 319–384.

Huang, S.Y., Nummenmaa, A., Witzel, T., Duval, T., Cohen-Adad, J., Wald, L.L., McNab, J.A., 2015. The impact of gradient strength on in vivo diffusion MRI estimates of axon diameter. Neuroimage 106, 464–472.

Huxley, A.F., Stämpfli, R., 1949. Evidence for saltatory conduction in peripheral myelinated nerve fibres. J. Physiol. 108, 315–339.

Ikeda, M., Oka, Y., 2012. The relationship between nerve conduction velocity and fiber morphology during peripheral nerve regeneration. Brain Behav. 2, 382–390.

Insko, E.K., Bolinger, L., 1993. Mapping of the Radiofrequency Field. J. Magn. Reson. A 103, 82–85.

Jensen, J.H., Helpern, J.A., Ramani, A., Lu, H., Kaczynski, K., 2005. Diffusional kurtosis imaging: The quantification of non-gaussian water diffusion by means of magnetic resonance imaging. Magn. Reson. Med. 53, 1432–1440.

Keil, B., Blau, J.N., Biber, S., Hoecht, P., Tountcheva, V., Setsompop, K., Triantafyllou, C., Wald, L.L., 2013. A 64-channel 3T array coil for accelerated brain MRI. Magn. Reson. Med. 70, 248–258.

Kolind, S.H., Deoni, S.C., 2011. Rapid three-dimensional multicomponent relaxation imaging of the cervical spinal cord. Magn. Reson. Med. 65, 551–556.

Lajtha, A., 2013. Pathological Neurochemistry. Springer US.

Lätt, J., Nilsson, M., Wirestam, R., Johansson, E., Larsson, E.-M., Stahlberg, F., Brockstedt, S., 2008. In vivo visualization of displacement-distribution-derived parameters in q-space imaging. Magn. Reson. Imaging 26, 77–87.

Lévy, S., Benhamou, M., Naaman, C., Rainville, P., Callot, V., Cohen-Adad, J., 2015. White matter atlas of the human spinal cord with estimation of partial volume effect. Neuroimage 119, 262–271.

Lisanti, C., Carlin, C., Banks, K.P., Wang, D., 2007. Normal MRI appearance and motion-related phenomena of CSF. AJR Am. J. Roentgenol. 188, 716–725.

Mackay, A., Whittall, K., Adler, J., Li, D., Paty, D., Graeb, D., 1994. In vivo visualization of myelin water in brain by magnetic resonance. Magn. Reson. Med. 31, 673–677.

Metwalli, N.S., Benatar, M., Nair, G., Usher, S., Hu, X., Carew, J.D., 2010. Utility of axial and radial diffusivity from diffusion tensor MRI as markers of neurodegeneration in amyotrophic lateral sclerosis. Brain Res. 1348, 156–164.

Mezer, A., Rokem, A., Hastie, T., Wandell, B., 2015. Proton density mapping: Removing receive-inhomogeneity using multi-coil information and T1 regularization, in: Proceedings of the 23th Annual Meeting of ISMRM. Toronto, p. 1684.

Mezer, A., Yeatman, J.D., Stikov, N., Kay, K.N., Cho, N.J., Dougherty, R.F., Perry, M.L., Parvizi, J., Hua le, H., Butts-Pauly, K., Wandell, B.A., 2013. Quantifying the local tissue volume and composition in individual brains with magnetic resonance imaging. Nat. Med. 19, 1667–1672.

Mezer, A., Yeatman, J.D., Stikov, N., Kay, K.N., Cho, N.-J., Dougherty, R.F., Perry, M.L., Parvizi, J., Hua, L.H., Butts-Pauly, K., Wandell, B.A., 2013. Quantifying the local tissue volume and composition in individual brains with magnetic resonance imaging. Nat. Med. 19, 1667–1672.

Mohammadi, S., Carey, D., Dick, F., Diedrichsen, J., Sereno, M.I., Reisert, M., Callaghan, M.F., Weiskopf, N., 2015. Whole-Brain In-vivo Measurements of the Axonal G-Ratio in a Group of 37 Healthy Volunteers. Front. Neurosci. 9, 441.

Mottershead, J.P., Schmierer, K., Clemence, M., Thornton, J.S., Scaravilli, F., Barker, G.J., Tofts, P.S., Newcombe, J., Cuzner, M.L., Ordidge, R.J., McDonald, W.I., Miller, D.H., 2003. High field MRI correlates of myelin content and axonal density in multiple sclerosis--a post-mortem study of the spinal cord. J. Neurol. 250, 1293–1301.

Nijeholt, G.J., Bergers, E., Kamphorst, W., Bot, J., Nicolay, K., Castelijns, J.A., van Waesberghe, J.H., Ravid, R., Polman, C.H., Barkhof, F., 2001. Post-mortem high-resolution MRI of the spinal cord in multiple sclerosis: a correlative study with conventional MRI, histopathology and clinical phenotype. Brain 124, 154–166.

Nilsson, M., Alexander, D., 2012. Investigating tissue microstructure using diffusion MRI: How does the resolution limit of the axon diameter relate to the maximal gradient strength? Proc. Intl. Soc. Mag. Reson. Med. 20, 3567.

Nilsson, M., van Westen, D., Ståhlberg, F., Sundgren, P.C., Lätt, J., 2013. The role of tissue microstructure and water exchange in biophysical modelling of diffusion in white matter. Magn. Reson. Mater. Phys. Biol. Med. 26, 345–370.

Novikov, D.S., Jensen, J.H., Helpern, J.A., Fieremans, E., 2014. Revealing mesoscopic structural universality with diffusion. Proc. Natl. Acad. Sci. U. S. A. 111, 5088–5093.

Ong, H.H., Wehrli, F.W., 2010. Quantifying axon diameter and intra-cellular volume fraction in excised mouse spinal cord with q-space imaging. Neuroimage 51, 1360–1366.

Ong, H.H., Wright, A.C., Wehrli, S.L., Souza, A., Schwartz, E.D., Hwang, S.N., Wehrli, F.W., 2008. Indirect measurement of regional axon diameter in excised mouse spinal cord with q-space imaging: simulation and experimental studies. Neuroimage 40, 1619–1632.

Pasternak, O., Sochen, N., Gur, Y., Intrator, N., Assaf, Y., 2009. Free water elimination and mapping from diffusion MRI. Magn. Reson. Med. 62, 717–730.

Paus, T., Toro, R., 2009. Could Sex Differences in White Matter be Explained by g ratio? Front. Neuroanat. 3, 14.

Perge, J.A., Koch, K., Miller, R., Sterling, P., Balasubramanian, V., 2009. How the optic nerve allocates space, energy capacity, and information. J. Neurosci. 29, 7917–7928.

Perge, J.A., Niven, J.E., Mugnaini, E., Balasubramanian, V., Sterling, P., 2012. Why do axons differ in caliber? J. Neurosci. 32, 626–638.

Pesaresi, M., Soon-Shiong, R., French, L., Kaplan, D.R., Miller, F.D., Paus, T., 2015. Axon

diameter and axonal transport: In vivo and in vitro effects of androgens. Neuroimage 115, 191–201.

Raff, M.C., Whitmore, A.V., Finn, J.T., 2002. Axonal self-destruction and neurodegeneration. Science 296, 868–871.

Remahl, S., Hildebrand, C., 1982. Changing relation between onset of myelination and axon diameter range in developing feline white matter. J. Neurol. Sci. 54, 33–45.

Rovira, A., Auger, C., Alonso, J., 2013. Magnetic resonance monitoring of lesion evolution in multiple sclerosis. Ther. Adv. Neurol. Disord. 6, 298–310.

Rushton, W.A.H., 1951. A theory of the effects of fibre size in medullated nerve. J. Physiol. 115, 101–122.

Saba, L., 2015. Imaging in Neurodegenerative Disorders. OUP Oxford.

Sacolick, L.I., Wiesinger, F., Hancu, I., Vogel, M.W., 2010. B1 mapping by Bloch-Siegert shift. Magn. Reson. Med. 63, 1315–1322.

Saito, N., Watanabe, M., Sakai, O., Jara, H., 2012. Human lifespan age-related changes of the brain proton density by quantitative MRI, in: Proceedings of the 20th Annual Meeting of ISMRM. p. 780.

Setsompop, K., Kimmlingen, R., Eberlein, E., Witzel, T., Cohen-Adad, J., McNab, J.A., Keil, B., Tisdall, M.D., Hoecht, P., Dietz, P., Cauley, S.F., Tountcheva, V., Matschl, V., Lenz, V.H., Heberlein, K., Potthast, A., Thein, H., Van Horn, J., Toga, A., Schmitt, F., Lehne, D., Rosen, B.R., Wedeen, V., Wald, L.L., 2013. Pushing the limits of in vivo diffusion MRI for the Human Connectome Project. Neuroimage 80, 220–233.

Sled, J.G., Pike, G.B., 2000. Quantitative interpretation of magnetization transfer in spoiled gradient echo MRI sequences. J. Magn. Reson. 145, 24–36.

Smith, S.A., Edden, R.A.E., Farrell, J.A.D., Barker, P.B., Van Zijl, P.C.M., 2008. Measurement of T1 and T2 in the cervical spinal cord at 3 tesla. Magn. Reson. Med. 60, 213–219.

Stejskal, E.O., Tanner, J.E., 1965. Spin Diffusion Measurements: Spin Echoes in the Presence of a Time-Dependent Field Gradient. J. Chem. Phys. 42, 288–292.

Stikov, N., Boudreau, M., Levesque, I.R., Tardif, C.L., Barral, J.K., Pike, G.B., 2015a. On the accuracy of T1 mapping: searching for common ground. Magn. Reson. Med. 73, 514–522.

Stikov, N., Campbell, J.S.W., Stroh, T., Lavelée, M., Frey, S., Novek, J., Nuara, S., Ho, M.-K., Bedell, B.J., Dougherty, R.F., Leppert, I.R., Boudreau, M., Narayanan, S., Duval, T., Cohen-Adad, J., Picard, P.-A., Gasecka, A., Côté, D., Pike, G.B., 2015b. In vivo histology of the myelin g-ratio with magnetic resonance imaging. Neuroimage 118, 397–405.

Stikov, N., Campbell, J.S.W., Stroh, T., Lavelée, M., Frey, S., Novek, J., Nuara, S., Ho, M.-K., Bedell, B.J., Dougherty, R.F., Leppert, I.R., Boudreau, M., Narayanan, S., Duval, T.,

Cohen-Adad, J., Picard, P.-A., Gasecka, A., Côté, D., Pike, G.B., 2015c. Quantitative analysis of the myelin g-ratio from electron microscopy images of the macaque corpus callosum. Data Brief 4, 368–373.

Stikov, N., Perry, L.M., Mezer, A., Rykhlevskaia, E., Wandell, B.A., Pauly, J.M., Dougherty, R.F., 2011. Bound pool fractions complement diffusion measures to describe white matter micro and macrostructure. Neuroimage 54, 1112–1121.

Taso, M., Girard, O.M., Duhamel, G., Le Troter, A., Feiweier, T., Guye, M., Ranjeva, J.-P., Callot, V., 2016. Tract-specific and age-related variations of the spinal cord microstructure: a multi-parametric MRI study using diffusion tensor imaging (DTI) and inhomogeneous magnetization transfer (ihMT). NMR Biomed.

Tofts, P.S., 2003. PD: proton density of tissue water. Quantitative MRI of the brain. Wiley, England 85–109.

Uranova, N., Orlovskaya, D., Vikhreva, O., Zimina, I., Kolomeets, N., Vostrikov, V., Rachmanova, V., 2001. Electron microscopy of oligodendroglia in severe mental illness. Brain Res. Bull. 55, 597–610.

Venkatesan, R., Lin, W., Haacke, E.M., 1998. Accurate determination of spin-density and T1 in the presence of RF-field inhomogeneities and flip-angle miscalibration. Magn. Reson. Med. 40, 592–602.

Volz, S., Nöth, U., Deichmann, R., 2012. Correction of systematic errors in quantitative proton density mapping. Magn. Reson. Med. 68, 74–85.

Waller, A., 1850. Experiments on the Section of the Glossopharyngeal and Hypoglossal Nerves of the Frog, and Observations of the Alterations Produced Thereby in the Structure of Their Primitive Fibres. Philosophical Transactions of the Royal Society of London Series I 140, 423–429.

Wang, L.Z., Caprihan, A., Fukushima, E., 1995. The Narrow-Pulse Criterion for Pulsed-Gradient Spin-Echo Diffusion Measurements. J. Magn. Reson. A 117, 209–219.

West, K.L., Kelm, N.D., Carson, R.P., Does, M.D., 2016. A revised model for estimating g-ratio from MRI. Neuroimage 125, 1155–1158.

West, K.L., Kelm, N.D., Carson, R.P., Does, M.D., 2015. Quantitative analysis of mouse corpus callosum from electron microscopy images. Data Brief 5, 124–128.

Yarnykh, V.L., 2007. Actual flip-angle imaging in the pulsed steady state: a method for rapid three-dimensional mapping of the transmitted radiofrequency field. Magn. Reson. Med. 57, 192–200.

Zhang, H., Schneider, T., Wheeler-Kingshott, C.A., Alexander, D.C., 2012. NODDI: practical in vivo neurite orientation dispersion and density imaging of the human brain. Neuroimage 61, 1000–1016.

5.8 Supplementary Material

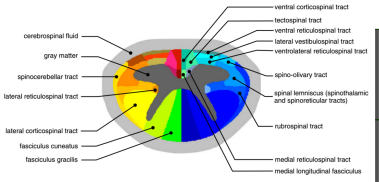

	T1 (s)		MTV		*fr*		*Dh* (μm²/ms)		axon diameter (μm)		g-ratio	
	mean across subjects	std across subjects	mean across subjects	std across subjects	mean across subjects	std across subjects	mean across subjects	std across subjects	mean across subjects	std across subjects	mean across subjects	std across subjects
fasciculus gracilis	1.27	0.12	0.28	0.04	0.47	0.06	1.12	0.25	6.4	0.32	0.76	0.05
fasciculus cuneatus	1.20	0.14	0.29	0.04	0.53	0.07	1.08	0.28	6.9	0.20	0.76	0.04
lateral corticospinal tract	1.30	0.17	0.27	0.04	0.49	0.06	1.01	0.25	7.0	0.27	0.76	0.04
spinocerebellar tract	0.53	0.48	0.27	0.06	0.35	0.13	1.81	0.33	8.3	0.41	0.72	0.06
rubrospinal tract	1.31	0.11	0.29	0.04	0.51	0.08	0.84	0.26	6.8	0.25	0.76	0.04
lateral reticulospinal tract	1.22	0.09	0.28	0.04	0.47	0.07	0.96	0.12	6.9	0.32	0.77	0.04
spinal lemniscus (spinothalamic and spinoreticular tracts)	1.31	0.12	0.28	0.04	0.48	0.05	0.82	0.13	6.6	0.20	0.76	0.04
spino-olivary tract	0.83	0.20	0.30	0.05	0.42	0.07	1.28	0.28	7.1	0.80	0.72	0.05
ventrolateral reticulospinal tract	1.28	0.14	0.26	0.04	0.40	0.12	1.07	0.20	6.7	0.34	0.74	0.03
lateral vestibulospinal tract	1.36	0.09	0.28	0.04	0.48	0.07	0.99	0.14	6.6	0.31	0.75	0.04
ventral reticulospinal tract	-0.06	0.60	0.34	0.05	0.32	0.17	1.33	0.42	8.1	1.81	0.64	0.06
ventral corticospinal tract	1.21	0.11	0.29	0.04	0.46	0.08	1.20	0.34	7.0	0.38	0.74	0.04
tectospinal tract	1.29	0.11	0.28	0.04	0.46	0.12	1.10	0.18	6.7	0.27	0.75	0.04
medial reticulospinal tract	1.31	0.12	0.27	0.04	0.44	0.15	1.21	0.20	6.8	0.19	0.76	0.04
medial longitudinal fasciculus	1.32	0.09	0.27	0.04	0.44	0.16	1.19	0.15	6.7	0.24	0.76	0.05

Figure 5.11: Results per tract of quantitative metrics (T1, MTV, *fr*, Dh, axon diameter, g-ratio). For each metric, the mean and the standard deviation across subjects were highlighted in red. Sensory tracts are highlight in blue and motor tracts in red.

CHAPITRE 6 ARTICLE 4: SCAN-RESCAN OF AXCALIBER, MACROMOLECULAR TISSUE VOLUME AND G-RATIO IN THE SPINAL CORD

Journal – Magnetic Resonance in Medicine - Wiley

Tanguy Duval[1], Victoria Smith[2], Nikola Stikov[1,3], Eric C. Klawiter[2], and Julien Cohen-Adad[1,4]

[1]*NeuroPoly Lab, Institute of Biomedical Engineering, Polytechnique Montreal, Montreal, QC, Canada*

[2]*Department of Neurology, Massachusetts General Hospital, Harvard Medical School, Boston, MA, United States*

[3]*Montreal Heart Institute, Montreal, QC, Canada*

[4]*Functional Neuroimaging Unit, CRIUGM, Université de Montréal, Montréal, QC, Canada*

Purpose—Recent MRI techniques have been introduced that can extract microstructural information in the white matter, such as the density or macromolecular content. Translating quantitative MRI to the clinic raises many challenges in terms of acquisition strategy, modeling of the MRI signal, artifact corrections and metric extraction (template registration and partial volume effects). In this work, we investigated the scan-rescan repeatability of several quantitative MRI techniques in the human spinal cord.

Methods—AxCaliber metrics, macromolecular tissue volume (MTV) and the fiber g-ratio were estimated in the spinal cord of eight healthy subjects, scanned and rescanned the same day in two different sessions.

Results—Scan-rescan repeatability deviation was less than 5%. Intraclass correlation coefficient was up to 0.95. A three-way ANOVA showed significant effects of white matter pathway, laterality and subject.

Conclusion—The present study suggests that quantitative MRI gives stable measurements of white matter microstructure in the spinal cord of healthy subjects. Our findings remain to be evaluated in diseased populations.

***Keywords*:** *AxCaliber, Diffusion, MRI, Myelin mapping, Spinal cord, g-Ratio*

Contribution: *Design of the study (50%), acquisition and analysis of the MRI data, redaction of the article and generation of the figures.*

Submitted: *26 April 2017* ***Accepted:*** *3 Septembre 2017*

6.1 Introduction

QUANTITATIVE magnetic resonance imaging (qMRI) aims at providing quantitative biomarkers that are insensitive to the protocol parameters, coil excitation and reception profiles. Combined with models of the white matter tissue, quantitative information characterizing microstructure (e.g. the size or density of neuronal fibers) can be inferred from the MRI signal. Using these metrics, investigators would ultimately be able to monitor tissue properties over time in the same individuals, compare subjects, detect lesions based on the biomarker value (as opposed to a detection based on the contrast with the surrounding tissue), and interpret the underlying damage of a tissue, e.g. axonal loss vs. inflammation vs. proliferation of astrocytes.

Quantitative metrics can be obtained from nearly any MRI contrast; diffusion MRI methods such as AxCaliber (1) provide metrics sensitive to the axon diameter and density (metric *fr*) while T1-weighted images and Macromolecular Tissue Volume (MTV) provide information on myelin content (2). By combining *fr* and MTV, a quantitative metric sensitive to the fiber g-ratio (defined as the ratio between the inner to the outer diameter of the myelin sheath) can be obtained (3,4).

These techniques, however, are hampered by many challenges in term of acquisition strategy, modeling of the MRI signal, artifact corrections, segmentation, and metric extraction, especially when applied to the spinal cord (5,6). In order to apprehend the repeatability of these pipelines, a common method is to acquire qMRI data on a couple of subjects at different time points and compute the variation of the metrics across time, assuming that the intra-subject variability is zero. Table 6.1 lists some scan-rescan studies, with an emphasis on spinal cord and qMRI methods. Note that a distinction needs to be made between *repeatability* and *reproducibility*: while both are types of measurement precision, *repeatability* studies use unchanged acquisition conditions whereas *reproducibility* studies report the impact of varying conditions on the precision (7). The additional sources of variance between scan and rescan in reproducibility studies can be the time delay between the scans, the repositioning of the subject, different MR tech,

different centers with potentially different scanners, coils, etc. A particular attention on the post-processing is also necessary in order to compare scan/rescan experiments. For example, a scan/rescan experiment will likely exhibit more variability if metrics are averaged within a small region (e.g., dorsal column between C2 and C4 levels) versus the entire cervical white matter, because of the presence of noise and potential mis-registration. From Table 6.1 we can conclude that qMRI metrics in the spinal cord have a scan-rescan deviation of 5-10%.

In this work, we investigated the repeatability of quantitative MRI of spinal cord microstructure (AxCaliber and MTV metrics) on the same MRI system, with subject repositioning.

Table 6.1: Review of the scan-rescan studies in the spinal cord and brain white matter.

	Region	voxel-wise correlation (R)	ICC (IntraClass Correlation Coefficient)	COV (Within-subject coefficient of variance)	REFERENCE
NODDI fraction of restricted water (*fr* or v_r)	**Spinal cord white matter**		0.84	7%	(8)
	Brain white matter	0.82			(9)
FA (fractional anisotropy)	**Spinal cord white matter**			<5%	(10)
	Brain white matter	0.90	0.79	COV across **13 scanners**: <5% (Global) 2-8% (per fasciculus)	(11) (9) (12)
$\lambda_\perp$ (radial diffusion coefficient)	**Spinal cord white matter**			<9%	(10)
	Brain white matter		.89	COV across **13 scanners**: <3% (Global) 3-10% (per fasciculus)	(11)
$\lambda_{//}$ (axial diffusion coefficient)	**Spinal cord white matter**			<4%	(10)
	Brain white matter		0.82	<4% (COV across **13 scanners**)	(11,12)
MTR (Magnetization Transfer Ratio)	**Spinal cord white matter**			<10%	(10)
MWF (Myelin Water Fraction)	**Spinal cord**			3-10%	(13)
	Brain white matter			2-20%	(14)
qMT (quantitative Magnetization Transfer)	brain white matter			5%	(15)
normalized PD (MTV)	Brain white matter	0.92 (different coils)		<2% (**different coils**)	(2)

6.2 Methods

Experiments were performed in 8 healthy subjects (28+/-10, 3 males), scanned and rescanned the same day (with subject repositioning between session 1 and 2). The protocol and processing of the data are detailed in (4).

6.2.1 Acquisition

Data were obtained using a high-gradient (Gmax=300mT/m per axis) 3T MRI scanner (Skyra CONNECTOM, Siemens) (16) equipped with a 64-channel head/spine coil (17). AxCaliber and MTV protocols were acquired in about 30min (depending on the cardiac rate) with the following parameters.

Diffusion: A cardiac-gated 2D single-shot spin-echo EPI with reduced field of view using two saturation bands placed anterior and posterior to the spinal cord was used with the following parameters: matrix 70x70, voxel size 0.8x0.8x5mm; 4 slices centered at intervertebral disks C1 to C4; 575 diffusion-weighted images (40 b=0, δ=3/3/6/8/10ms, Δ=20/40/20/36/30ms, TE=57/73/67/76/75ms, Gmax=√2*300=424mT/m, and diffusion encoding gradients applied in four directions perpendicular to the spinal cord (XY, -XY, -X-Y, X-Y).

MTV: Proton Density mapping was obtained using three 3D FLASH acquisitions (FA=4,10,20°, TE=2.74ms, TR=30ms, matrix 192x192x22, spacing 0.8x0.8x5mm, GRAPPA R=2). B1+ mapping was acquired using the double-angle method (18) (spin-echo EPI, FA=60/120°, TE=13ms, TR=7s, matrix 64x64x20).

6.2.2 Processing

Preprocessing, metric extraction and registration was done as in (4). Briefly, raw diffusion and FLASH volumes were motion-corrected using the Spinal Cord Toolbox[8] (SCT) version

[8] https://sourceforge.net/p/spinalcordtoolbox/

2.2.3 (19); MTV was computed as in (2) and registered to the mean DWI; AxCaliber was computed using qMRLab[9] and g-ratio was computed as in (20). Lastly, mean DWI volumes were registered slice-by-slice to the MNI-Poly-AMU template using SCT. This processing resulted in four slices located at each intervertebral body C1/C2/C3/C4. An atlas of white matter tracts (21) was used to extract metrics in each spinal cord pathway while accounting for partial volume effect using the maximum a posteriori estimation. Images for scan and rescan were processed independently (i.e., images of scan and rescan were not co-registered) in order to report the repeatability of the entire processing pipeline (i.e., including registration to the template).

6.2.3 Statistics

Repeatability of metric estimation was assessed in the template space by computing the scan-rescan correlation of white matter voxels. Gray-matter voxels were excluded to prevent artificially high correlations that result when two distinct clusters are fitted by a line and a Pearson's correlation is reported. Note that scan-rescan correlations were computed globally, without averaging the maps across subjects.

Precision was assessed using the absolute scan-rescan deviation in white matter computed per subject, then averaged across subjects:

$$Error = 1/M \sum_{subject_i=1}^{M} \left| 1/N \sum_{voxel_j=1}^{N} (m_{vox_j,sub_i,scan} - m_{vox_j,sub_i,rescan}) \right|$$

with $m_{vox_j,sub_i,scan}$ the metric value in the voxel j of the white matter, for subject i and session #1 (scan).

In order to assess the capability of these metrics to detect reliable differences between subjects, the intraclass correlation coefficient (ICC) was computed in each spinal cord

[9] https://github.com/neuropoly/qMRLab

tract. The formula for ICC was: $ICC = \frac{{\sigma_{inter}}^2}{{\sigma_{intra}}^2 + {\sigma_{inter}}^2}$ $with$ $\sigma_{intra} =$

$mean_i\left(\sqrt{1/2 \cdot (m_{i,scan} - \underline{m_i})^2 + (m_{i,rescan} - \underline{m_i})^2)}\right)$ and $\sigma_{inter} = std_i(\underline{m_i})$.

$m_{i,scan}$ is the metric value measured in a specific tract for subject i, and $\underline{m_i}$ is the average value between scan and rescan. From this formula, it appears that an ICC close to 1 reveals a much greater inter-subject variation than the scan-rescan error. Note that $\sigma_{intra} < \sigma_{inter}$, and ICC should always be larger than 0.5.

Finally, a three-way ANOVA was done to assess the capability of these metrics to detect significant differences between tracts, subjects and laterality (left/right).

6.3 Results

The quality of the scan-rescan and registration to the template can be qualitatively assessed on a GIF animation[10] showing in turn the quantitative maps from session #1 (scan), from session #2 (rescan) and the template. This animation shows a consistency across slices and subjects of all metrics in term of contrast (between white matter tracts) and accuracy. Similarly, raw maps at C3 in subject space were visually assessed[11]. Subject #3 was discarded from the rest of the study due to particularly strong movements during the scan.

Figure 6.1 shows the voxel-wise comparison of scan-rescan from all subjects and for each metric. *fr* and MTV showed a good correlation (r>0.74) and low deviation between scan and rescan (<2%).

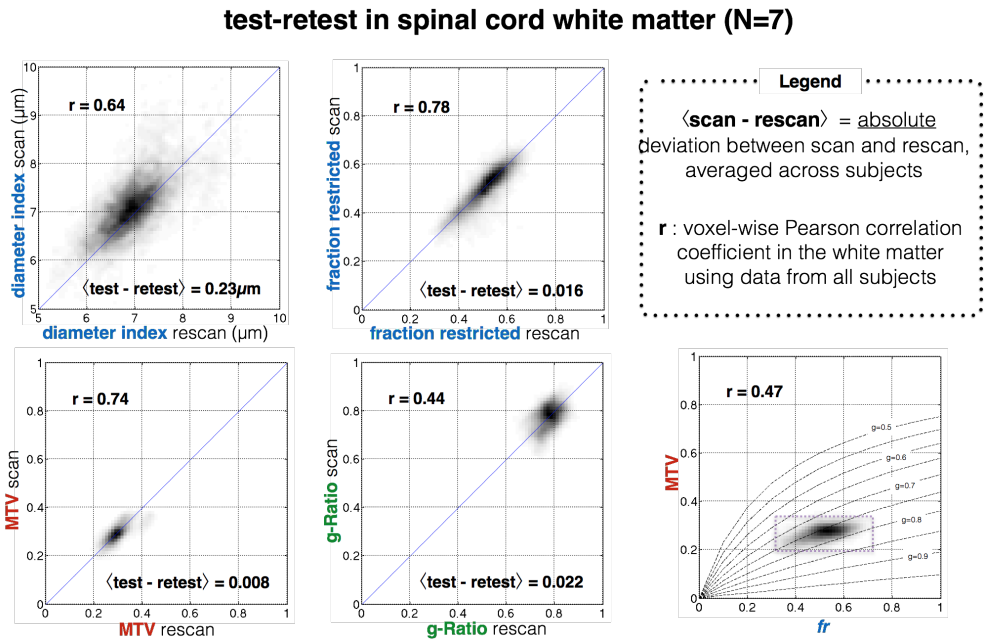

Figure 6.1: Scan-rescan repeatability of the different quantitative metrics, assessed voxel-wise, in the template space, in the white matter. Bottom right. the

[10] https://osf.io/yebwd/

[11] https://osf.io/xgsn9/

correlation between MTV and fr seems to follow the line of iso-g-ratio g=0.75, thus reducing the dynamic of the g-ratio metric (achievable values are emphasized by the dashed box).

Figure 6.2 shows the ICC obtained per tract for all subjects (excluding subject #3). Metric *fr* was particularly sensitive to differences between subjects (ICC>0.9) in the gray matter, ventral and lateral tracts. The axon diameter index detected differences between subjects in the motor tract, and the left cuneatus (ICC>0.8).

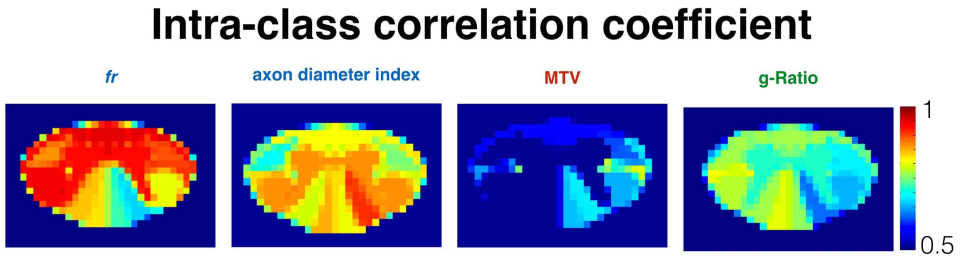

Figure 6.2: Intra-class correlation coefficient (ICC) assessed per tract using the atlas of spinal cord tracts. An ICC close to 1 shows the capability of the metric to detect differences between subjects.

Figure 6.3 shows the results of the ANOVA. *fr*, axon diameter and MTV could detect reproducible differences between tracts and subjects. Axon diameter, MTV and g-ratio could detect significant differences between right and left tracts, with inverse trends between axon diameter and MTV.

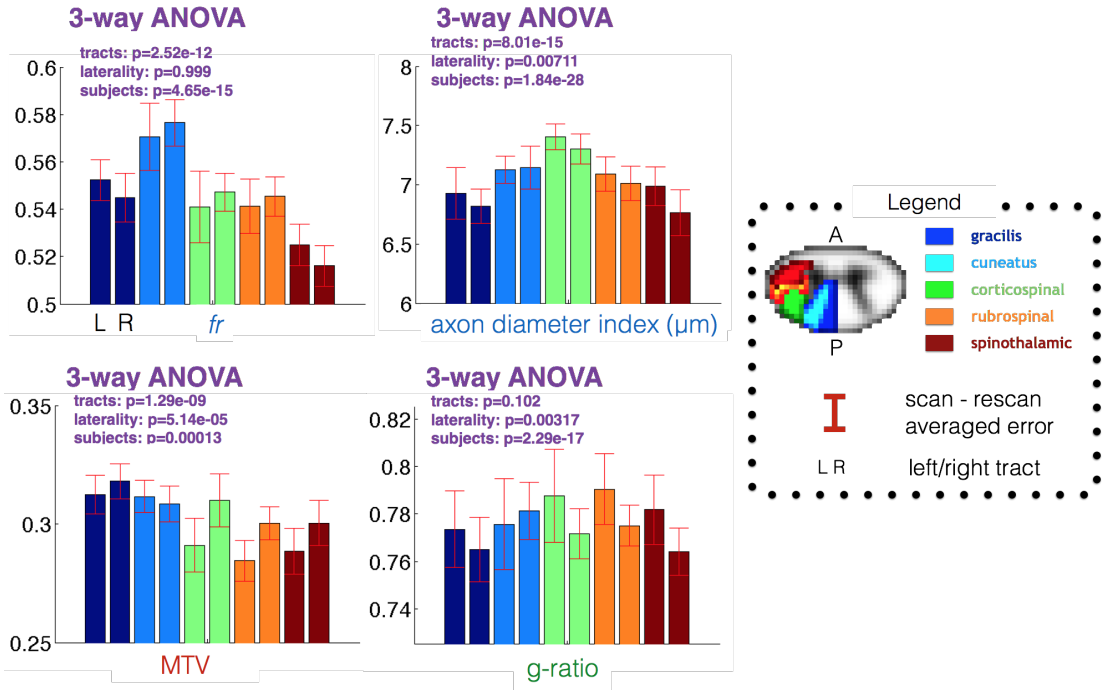

Figure 6.3: Result of the three-way ANOVA (tracts, subjects, and laterality) for each metric along with the bar plot of metric values in each tract, and scan-rescan error.

6.4 Discussion

In previous studies from our group (4,22), we reported the consistency across slices and across subjects, as well as the sensitivity of these metrics to microstructural differences between tracts and between the left and right sides.

In this study, eight new subjects were scanned twice in order to study the performance of the microstructural biomarkers in term of sensitivity to subject variation (ICC), precision (voxel-wise correlation) and repeatability (deviation between scan and rescan).

Results of the tract-by-tract analysis (**Figure 6.3**) are consistent with (4,22), in terms of contrast between tracts (higher axonal density, higher macromolecular content, and smaller fibers in the dorsal column than in the lateral tracts) and statistical results (ANOVA).

6.4.1 Voxel-wise correlation

fr and MTV showed good precision and sensitivity to the microstructure based on the voxel-wise correlation and the ANOVA analysis. A worse correlation coefficient was found for g-ratio (r=0.44), that we attribute to (i) unstable g-ratio due to the indeterminate form (0/0) of the equation $\left(g = \sqrt{\frac{(1-MTV)fr}{MTV+(1-MTV)fr}}\right)$ when both *fr* and MTV are close to 0 (at the periphery of the spinal cord) and (ii) to the small dynamic range of this metric in healthy tissue due to the correlation between MTV and *fr* (r=0.47) that follows the line of iso-gratio (g=0.75) (**Figure 6.1**).

6.4.2 Intra-Class Correlation Coefficient

The large ICC found in ventral and peripheral tracts for the *fr* metric can be explained by the significant ($p<0.05$) correlation of *fr* with the cross-sectional area (CSA) of the spinal cord (r=-0.6 in average in these tracts). This negative correlation shows that smaller spinal cords have higher *fr* values, which can be explained by higher spatial constraints in smaller spinal cords if we assume approximately the same number of fibers between individuals. Histological studies are necessary to validate this hypothesis. Note that partial volume effect, with CSF or gray matter, would result in a positive correlation between *fr* and the CSA because *fr* in the CSF and in the gray matter is very low.

A relatively small ICC was found for MTV (about 0.5), which can be explained by (i) the small dynamic range of this metric in healthy tissue (STD<0.1 in white matter) as shown by histology (23,24), and simulations (25), and (ii) the difficulty to normalize proton density robustly using the CSF in the spinal cord due to CSF pulsation and the presence of spinal roots. The use of an external calibration phantom, or other tissues with known water content could be considered for the normalization of the proton density. Although MTV

might not be capable of detecting the subtle variations between healthy subjects, this metric is highly sensitive to demyelination in neurodegenerative diseases (30% contrast in multiple sclerosis lesions) (26,27), and higher ICC is expected if patients are included.

6.4.3 Laterality difference

A significant laterality (left/right) difference was found for MTV ($P<10^{-4}$), axon diameter index ($P<10^{-2}$) and g-ratio ($p<10^{-2}$). We notice an inverse trend between axon diameter and MTV (**Figure 6.3**), which is confirmed by simulations (25) (large fibers have proportionally less myelin). Although such microstructure differences could be genuine, other potential confounds should be considered, such as partial voluming. For instance, different thickness between the two gray matter posterior horns would bias the estimated metrics differently between the left and right columns. This effect is suspected on the ICC maps with larger values (i.e. large inter-subject variation) close to one of the two horns. Although the metric extraction procedure minimizes the effect of partial voluming thanks to a maximum a posteriori approach (21), this requires a good segmentation and registration of the atlas of tracts. Future studies will include gray matter segmentation to further reduce this potential bias (28).

6.4.4 Model assumptions

The assumptions (notably the relationship between myelin and MTV) of the biomarkers used in this study were already discussed in these previously published studies (4,22). In this study, the diffusion model assumes a fixed intra-axonal diffusion coefficient; no time-dependence of the extra-axonal perpendicular diffusivity (Fieremans NIMG 2016); and no free water compartment. However, in pathology, one could expect a different intra-axonal diffusion coefficient, an increased effect of time-dependence due to axonal loss, and presence of a free water compartment due to inflammation and/or oedema. We investigated the impact of these effects on the repeatability and accuracy using simulations in supplementary material S1.

6.4.5 Data quality

While we acknowledge that the repeatability study is expected to include all possible sources of variation (including subject motion), the motion of subject #3 was particularly large (see **Figure 7.1**). We decided to remove this subject because it would have strongly affected the repeatability measures without being relevant for the study. The present study assumes that a certain level of data quality is achieved before being considered for the analysis. We would like to stress that quality control is a necessary step in all research and clinical studies, and discarding subject on the basis of large motion is a common routine.

Strong motion results in blurry and distorted spoiled gradient echo images (see **Figure 7.1**.a). This acquisition is particularly sensitive to motion due to the long duration of the 3D scan. Sensitivity to motion could be reduced by using simultaneous multi-slice, reduced field of view or higher bandwidth (at the expense of lower SNR). Navigator-based or camera-based methods to track motion and correct the phase can also be considered but the non-rigid motion of the spinal cord in relation to the rest of the body will limit their performance. Diffusion-weighted EPI images, combined with the motion correction algorithm, are less affected by such strong motion, although we note more blurry borders on the mean DWI of subject #3 (see **Figure 7.1**.c). Note that in this study, we tried to minimize subject motion by informing subject of the issues of motion (before MRI session and between runs), and by using pads to ensure subject comfort and to minimize head rotation. More restrictive designs could be considered.

6.4.6 Applicability of the results

In all repeatability studies the infrastructure and acquisition parameters are a major source of variability, so our results might not be readily applicable to other configurations. Here we used a 300mT/m system with a 64ch head/neck coil. While the strong gradients definitely helped for the diffusion-weighted scans, they had negligible influence for the MTV/T1 protocol we used for quantifying myelin. Therefore, the presented results for the myelin protocol are applicable to clinical systems equipped with similar coils and pulse sequences.

Regarding the diffusion-weighted scans, the present study is still relevant to the community at large, as it sets a lower limit to the variability that can be expected with systems equipped with lower gradients. In a previous ex vivo study, we showed that the restricted water fraction can be measured robustly even at lower b-values (b=4,000mm2/ms), but the lower gradient strength prevents the measurement of the axon diameter index (Duval et al. 2017). Stimulated echo sequences could also be considered to increase the b-value on clinical systems (Alexander and Dyrby 2013), but the experimenter should be aware of (i) the stronger time-dependence effect (Fieremans et al. 2016), (ii) the much higher sensitivity to non-rigid motion of the spinal cord, and (iii) the different T1- and T2- weighting when compared to the PGSE sequence.

It is also important to note that the presented results are bound to a specific acquisition and analysis protocol. For example, lowering spatial resolution or using models with fewer degrees of freedom (compared to AxCaliber) would likely produce better reproducibility results.

6.5 Conclusion

It is possible to robustly extract AxCaliber, MTV and g-ratio metrics in the different spinal cord tracts and to detect significant differences between healthy subjects and spinal cord tracts. The proposed acquisition and processing framework could be useful for assessing spinal cord demyelination in diseases such as multiple sclerosis.

6.6 References

1. Assaf Y, Blumenfeld-Katzir T, Yovel Y, Basser PJ. AxCaliber: a method for measuring axon diameter distribution from diffusion MRI. Magn. Reson. Med. 2008;59:1347–1354.

2. Mezer A, Yeatman JD, Stikov N, et al. Quantifying the local tissue volume and composition in individual brains with magnetic resonance imaging. Nat. Med. 2013;19:1667–1672.

3. Stikov N, Campbell JSW, Stroh T, et al. In vivo histology of the myelin g-ratio with magnetic resonance imaging. Neuroimage 2015;118:397–405.

4. Duval T, Le Vy S, Stikov N, et al. g-Ratio weighted imaging of the human spinal cord in vivo. Neuroimage 2017;145:11–23.

5. Wheeler-Kingshott CA, Stroman PW, Schwab JM, et al. The current state-of-the-art of spinal cord imaging: applications. Neuroimage 2014;84:1082–1093.

6. Stroman PW, Wheeler-Kingshott C, Bacon M, et al. The current state-of-the-art of spinal cord imaging: methods. Neuroimage 2014;84:1070–1081.

7. Sullivan DC, Obuchowski NA, Kessler LG, et al. Metrology Standards for Quantitative Imaging Biomarkers. Radiology 2015;277:813–825.

8. Grussu F, Schneider T, Zhang H, Alexander DC, Wheeler-Kingshott CAM. Neurite orientation dispersion and density imaging of the healthy cervical spinal cord in vivo. Neuroimage 2015;111:590–601.

9. Tariq M, Schneider T, Alexander DC, Wheeler-Kingshot C, Zhang H. Scan-rescan reproducibility of neurite microstructure estimates using NODDI. In: Xie X, editor. Medical Image Understanding and Analysis 2012: Proceedings of the 16th Conference on Medical Image Understanding and Analysis. Vol. 16. Swansea, UK: The British Machine Vision Association and Society for Pattern Recognition; 2012. pp. 255–261.

10. Smith SA, Jones CK, Gifford A, et al. Reproducibility of tract-specific magnetization transfer and diffusion tensor imaging in the cervical spinal cord at 3 tesla. NMR Biomed. 2010;23:207–217.

11. Palacios EM, Martin AJ, Boss MA, et al. Toward Precision and Reproducibility of Diffusion Tensor Imaging: A Multicenter Diffusion Phantom and Traveling Volunteer Study. AJNR Am. J. Neuroradiol. [Internet] 2016. doi: 10.3174/ajnr.A5025.

12. Veenith TV, Carter E, Grossac J, Newcombe VFJ, Outtrim JG, Lupson V, Williams GB, Menon DK, Coles JP. Inter subject variability and reproducibility of diffusion tensor imaging within and between different imaging sessions. PLoS One 2013;8:e65941.

13. Wu Y, Alexander AL, Fleming JO, Duncan ID, Field AS. Myelin water fraction in human cervical spinal cord in vivo. J. Comput. Assist. Tomogr. 2006;30:304–306.

14. Meyers SM, Vavasour IM, Mädler B, Harris T, Fu E, Li DKB, Traboulsee AL, MacKay AL, Laule C. Multicenter measurements of myelin water fraction and geometric mean T2 : intra- and intersite reproducibility. J. Magn. Reson. Imaging 2013;38:1445–1453.

15. Levesque IR, Sled JG, Narayanan S, Giacomini PS, Ribeiro LT, Arnold DL, Pike GB. Reproducibility of quantitative magnetization-transfer imaging parameters from repeated measurements. Magn. Reson. Med. 2010;64:391–400.

16. Setsompop K, Kimmlingen R, Eberlein E, et al. Pushing the limits of in vivo diffusion MRI for the Human Connectome Project. Neuroimage 2013;80:220–233.

17. Keil B, Blau JN, Biber S, Hoecht P, Tountcheva V, Setsompop K, Triantafyllou C, Wald LL. A 64-channel 3T array coil for accelerated brain MRI. Magn. Reson. Med. 2013;70:248–258.

18. Insko EK, Bolinger L. Mapping of the Radiofrequency Field. J. Magn. Reson. A 1993;103:82–85.

19. De Leener B, Lévy S, Dupont SM, Fonov VS, Stikov N, Louis Collins D, Callot V, Cohen-Adad J. SCT: Spinal Cord Toolbox, an open-source software for processing spinal cord MRI data. Neuroimage [Internet] 2016. doi: 10.1016/j.neuroimage.2016.10.009.

20. Stikov N, Perry LM, Mezer A, Rykhlevskaia E, Wandell BA, Pauly JM, Dougherty RF. Bound pool fractions complement diffusion measures to describe white matter micro and macrostructure. Neuroimage 2011;54:1112–1121.

21. Lévy S, Benhamou M, Naaman C, Rainville P, Callot V, Cohen-Adad J. White matter atlas of the human spinal cord with estimation of partial volume effect. Neuroimage 2015;119:262–271.

22. Duval T, McNab JA, Setsompop K, Witzel T, Schneider T, Huang SY, Keil B, Klawiter EC, Wald LL, Cohen-Adad J. In vivo mapping of human spinal cord microstructure at 300mT/m. Neuroimage 2015;118:494–507.

23. Harkins KD, Xu J, Dula AN, Li K, Valentine WM, Gochberg DF, Gore JC, Does MD. The microstructural correlates of T1 in white matter. Magn. Reson. Med. 2016;75:1341–1345.

24. Duval T, Mingasson T, Klawiter E, Stikov N, Cohen-Adad J. Translating AxCaliber on a Clinical System : 600mT/m Versus Optimized 80mT/m Protocol. In: Proceedings of the 25th Annual Meeting of ISMRM. ; 2017. p. 1760.

25. Mingasson T, Duval T, Stikov N, Cohen-Adad J. AxonPacking: An Open-Source Software to Simulate Arrangements of Axons in White Matter. Front. Neuroinform.

2017;11:5.

26. Chong AL, Chandra RV, Chuah KC, Roberts EL, Stuckey SL. Proton Density MRI Increases Detection of Cervical Spinal Cord Multiple Sclerosis Lesions Compared with T2-Weighted Fast Spin-Echo. AJNR Am. J. Neuroradiol. 2016;37:180–184.

27. Nijeholt GJ, Bergers E, Kamphorst W, Bot J, Nicolay K, Castelijns JA, van Waesberghe JH, Ravid R, Polman CH, Barkhof F. Post-mortem high-resolution MRI of the spinal cord in multiple sclerosis: a correlative study with conventional MRI, histopathology and clinical phenotype. Brain 2001;124:154–166.

28. Dupont SM, De Leener B, Taso M, Le Troter A, Stikov N, Callot V, Cohen-Adad J. Fully-integrated framework for the segmentation and registration of the spinal cord white and gray matter. Neuroimage [Internet] 2016. doi: 10.1016/j.neuroimage.2016.09.026.

6.7 Supplementary Material

6.7.1 Supporting Information S1: ANOVA

As in (Duval et al. 2015, 2017), an ANOVA 3 was used to test if qMRI metrics are sensitive to laterality differences (left versus right tracts), tracts differences and subjects differences.

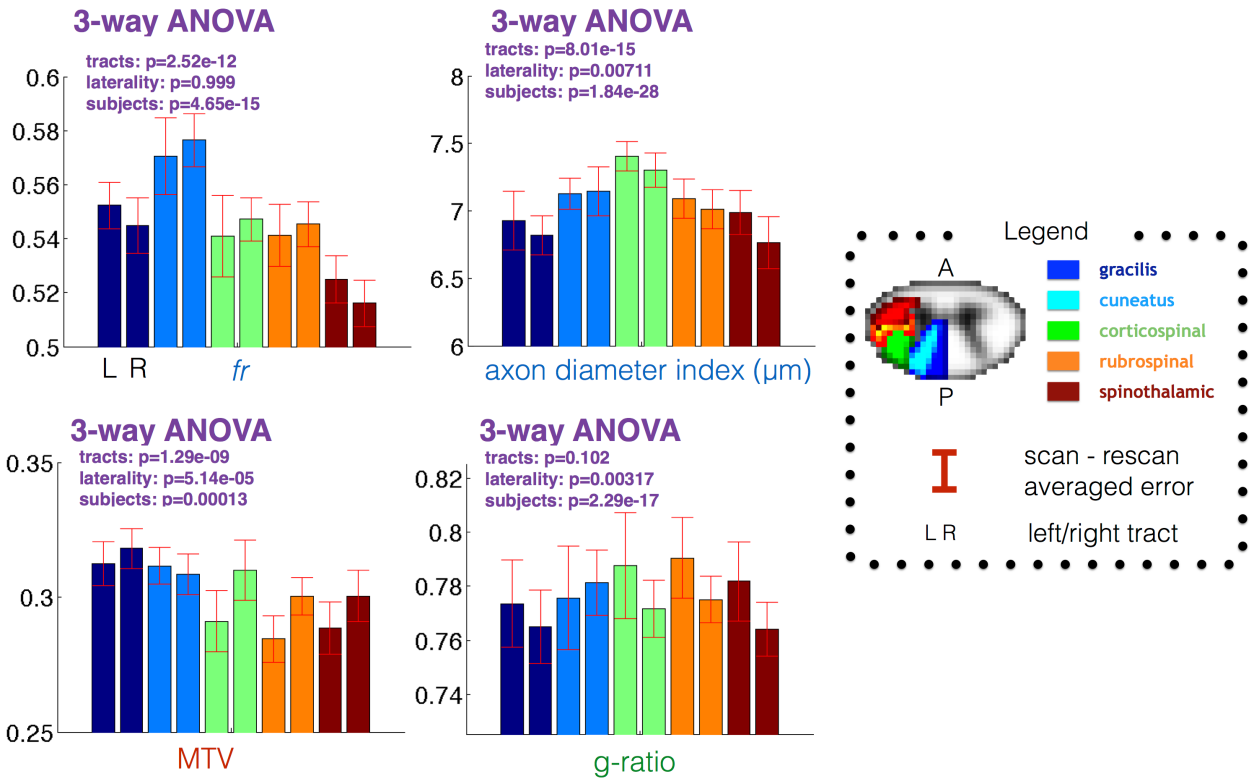

Figure 6.4: *Result of the three-way ANOVA (tracts, subjects, and laterality) for each metric along with the bar plot of metric values in each tract, and scan-rescan error.*

6.7.2 Supporting Information S2: Simulation of the impact of diffusion model assumptions on repeatability and accuracy

In this section, we simulated the impact of model assumptions on the accuracy and stability of the fits for a particular signal-to-noise level. The following assumptions were challenged: (i) time-dependence of the diffusion coefficient in the extra-axonal (hindered) compartment, (ii) presence of a free water compartment and (iii) fixed intra-axonal diffusivity.

Method. The assumptions were added to the model equation (see next paragraph) in order to simulate a realistic MR signal. For each assumption, the parameter in question (i.e. length of coherence, free water compartment fraction or intra-axonal diffusion coefficient) was varied in 10 steps, while all other parameters were fixed (see "Nominal" values in table of **Figure 6.5**). MR data were simulated with the same protocol used in the manuscript. Rician noise (SNR = 50 at b=0) was then added, and equation (1) was used to fit the simulated data. This procedure was run 20 times in order to compute a mean and standard deviation for all fitted parameters. This entire procedure can be reproduced using the Sensitivity Analysis add-on of qMRLab (https://github.com/neuropoly/qMRLab).

Equation. Diffusion MRI data were simulated using the following equation:

$$S_{\perp} = S_0(TE, TR) \cdot \left[(1 - fr - fcsf) \cdot S_h(b, D_{ha}, lc) + fr \cdot S_r(q, \delta, \Delta, D_{intra}, d) + fcsf \cdot S_{csf}(b, Dcsf)\right] \quad (1)$$

with q, δ and Δ the diffusion parameters and $b = (2\pi q)^2(\Delta - \delta/3)$.

S_h, the signal in the hindered compartment, is modeled by a time-dependent Gaussian Diffusion (Fieremans et al., 2016, equation (9)):

$$D_{ha} = D_h - mean(D_{adjustment}(lc)) + D_{adjustment}(lc)$$

with D_h the mean (across acquisition parameters) diffusion coefficient adjusted by:

$$D_{adjustment} = \frac{0.2 \cdot lc^2}{2\delta^2(\Delta - \delta/3)}\left[\Delta^2 \cdot ln\frac{\Delta^2 - \delta^2}{\Delta^2} + \delta^2 \cdot ln\frac{\Delta^2 - \delta^2}{\delta^2} + 2\Delta\delta \cdot ln\frac{\Delta + \delta}{\Delta - \delta}\right]$$

S_r, the intra-axonal signal, is modeled by the Gaussian phase distribution in a cylinder (Wang et al., 1995). D_{intra} is the intra-axonal real diffusion coefficient, and d is the axonal diameter index (Alexander et al., 2010). S_{csf}, the signal in the free compartment (e.g. CSF contamination or inflammation), is modeled with a Gaussian diffusion. Dcsf is the diffusion coefficient.

Results. Violation of model assumptions (i.e. fcsf>0, lc>0 or Dintra ≠ 1.4 μm2/ms) has little impact on the stability of the fitted parameters with respect to noise, as shown by the stable standard deviations of the fitted metrics Dh, axon diameter index and *fr* in **Figure 6.5**. However, the following bias can be observed:

- fcsf ∈ [0 0.5]: up to 10% overestimation for axon diameter index and fr, with a peak for fcsf=0.25. Dh tends to compensate for the free compartment contamination.
- lc > 3μm: overestimation of all parameters by more than 5%
- Dintra: Axon diameter index is inversely proportional (slope -0.8) with the true Dintra value. No major impact on fr and Dh

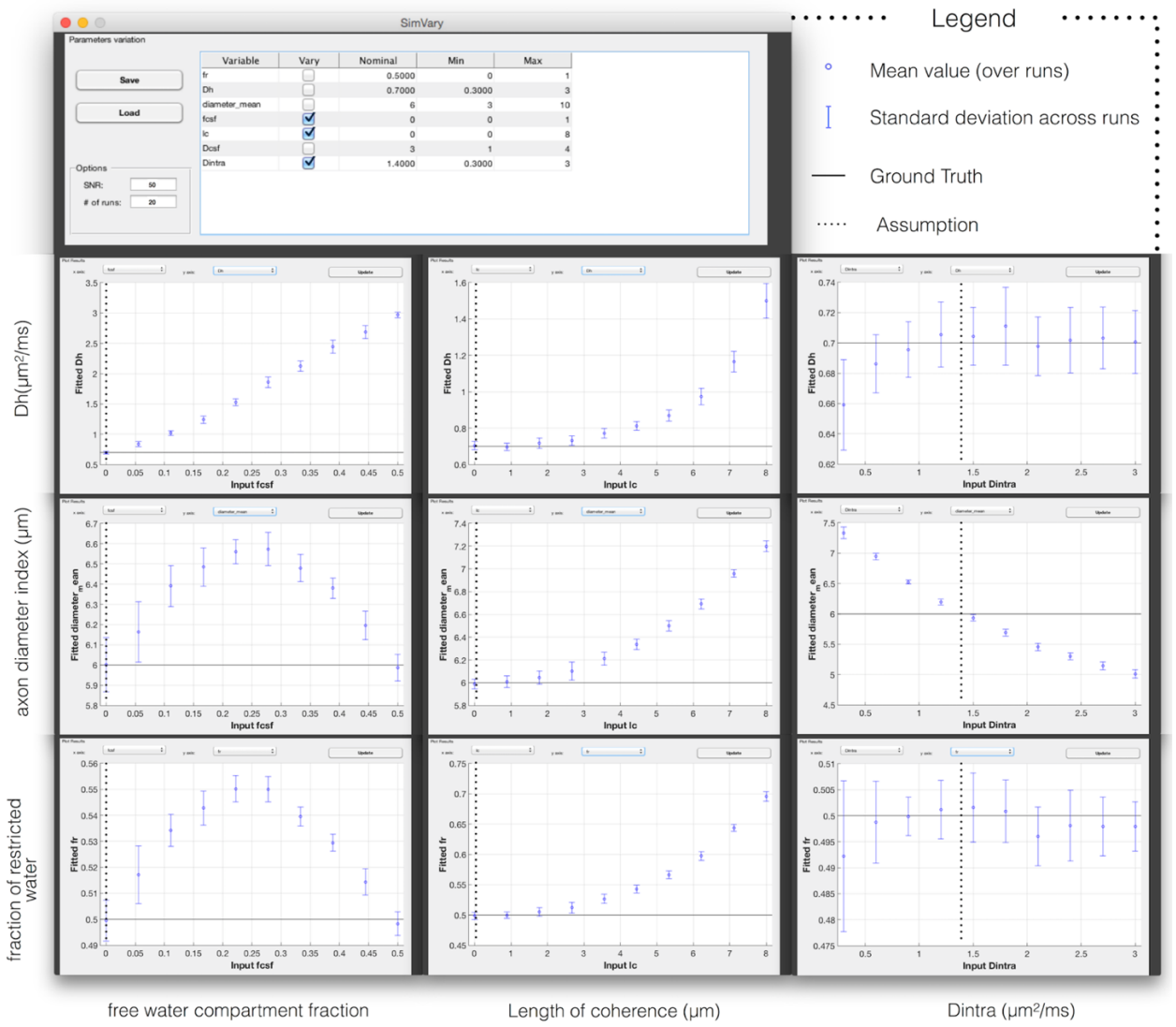

Figure 6.5: Simulation of the impact of model assumptions (X-axis) on the fitted parameters (Y-axis) using qMRLab. In order to improve the precision of fitting parameters, the number of parameters is reduced by fixing some of them to a particular value (vertical dotted lines). Violation of these assumptions can introduce biases, illustrated by the deviation of the average fitted values (blue circles) from the ground truth (horizontal black lines), or reduce precision of the fitted values (blue error bars).

Note that the assumptions were made to improve the precision of the measurements, at the expense of accuracy. In pathology, it could be of interest to relax an assumption and fit the associated parameter. Similar simulations could be used in the future to study the impact of additional fitting parameters on the repeatability.

References.

Alexander, D.C., Hubbard, P.L., Hall, M.G., Moore, E.A., Ptito, M., Parker, G.J.M., Dyrby, T.B., 2010. Orientationally invariant indices of axon diameter and density from diffusion MRI. Neuroimage 52, 1374–1389.

Duval, T., Lévy, S., Stikov, N., Campbell, J., Mezer, A., Witzel, T., Keil, B., Smith, V., Wald, L.L., Klawiter, E., Cohen-Adad, J., 2017. g-Ratio weighted imaging of the human spinal cord in vivo. Neuroimage 145, 11–23.

Duval, T., McNab, J.A., Setsompop, K., Witzel, T., Schneider, T., Huang, S.Y., Keil, B., Klawiter, E.C., Wald, L.L., Cohen-Adad, J., 2015. In vivo mapping of human spinal cord microstructure at 300mT/m. Neuroimage 118, 494–507.

Fieremans, E., Burcaw, L.M., Lee, H.-H., Lemberskiy, G., Veraart, J., Novikov, D.S., 2016. In vivo observation and biophysical interpretation of time-dependent diffusion in human white matter. Neuroimage 129, 414–427.

CHAPITRE 7 ARTICLE 5:
VALIDATION OF QUANTITATIVE MRI METRICS USING FULL SLICE HISTOLOGY WITH AUTOMATIC AXON SEGMENTATION

Conference – Proceedings of the 24th Annual Meeting of ISMRM

Tanguy Duval[1], Blanche Perraud[1], Manh-Tung Vuong[1], Nibardo Lopez Rios[1], Nikola Stikov, Julien Cohen-Adad

[1]NeuroPoly Lab, Institute of Biomedical Engineering, Polytechnique Montreal, Montreal, QC, Canada

[2]Montreal Heart Institute, Montreal, QC, Canada

[3]Functional Neuroimaging Unit, CRIUGM, Université de Montréal, Montréal, QC, Canada

Modeling the biophysical processes that produce the MRI contrast is a challenging problem. Many models have been proposed to solve the inverse problem and retrieve quantitative microstructural information based on the MRI contrast, but this procedure needs validation.

In this work, we propose to validate the measurement of myelin content, axonal diameter and density with MRI by comparing the results with full slice histology of the neuronal fibers with axon and myelin segmentation. High resolution MRI data (150µm/px) were acquired on an ex vivo spinal cord and compared voxel by voxel with histology. We found that q-space metrics were precise enough to distinguish between various fiber distributions. A correlation coefficient of r=0.62 was found between AxCaliber and histology for axon diameter metric. Also, good agreement was found between the different q-space models and with MTV.

Keywords**:** *histology, MRI, spinal cord, osmium, axon, whole-slide, microstructure, tissue modeling*

Contribution: *Design of the study, acquisition and analysis of the MRI and histology data, redaction of the article and generation of the figures.*

Submitted: *11 November 2015*

Accepted*: 1 February 2016*

7.1 Introduction

Model-based quantitative magnetic resonance imaging (MRI) technique allows the extraction of meaningful values associated to a microstructural feature such as the myelin content or the axon density within a voxel. This technique presents many advantages over conventional MRI. Firstly, it brings a gain in sensitivity and specificity because it combines multiple MRI images acquired with different parameters and correct for confounding effects (e.g. coil sensitivity and excitation profiles, T1/T2 relaxation). Secondly it provides reproducible values that enables to trace a lesion activity, to perform inter-subject comparison studies and generate reference atlases of healthy tissue. Thirdly it is expected to help the interpretation of tissue microstructure and tissue integrity in lesions: for instance to discriminate between demyelination, axon loss or inflammation only.

In practice, this is done by acquiring many MRI images sensitive to a particular feature (myelin in magnetization transfer, axonal density in diffusion MRI) and by interpreting signal change via models and equations. These models, however, make some assumptions and simplifications, that might produce false interpretation of the underlying microstructure, and thus need to be validated. Although a lot of effort has been put to validate each of these models, none of these validations is totally satisfying and the exact modeling of white matter is still under debate (Burcaw et al., 2015; Ferizi et al., 2014; Nilsson et al., 2013).

Three main approaches have been used. The first method is to look at how models predict MRI signal change in the white matter for different acquisition parameters (Ferizi et al., 2014; Lee et al., 2016). This approach is particularly useful to develop models and to reveal their limits and incoherences. However, this verification is a necessary but not a sufficient condition for having a realistic modeling. In fact, there is not a unique model that can predict correctly the MRI signal (Ferizi et al., 2014), partly because the MRI signal presents a relatively simple behavior (e.g. biexponential) in the achievable range of acquisition parameter (b-value in diffusion MRI, flip angle and offset in magnetization transfer). The second approach is to use numerical (Burcaw et al., 2015; Hall and Alexander, 2009; Nilsson

et al., 2012) or synthetic (Fieremans et al., 2008; Shemesh et al., 2010) phantoms where each microstructural parameter can be controlled independently. While necessary for the calibration of the methods and the validation of the equations, these phantoms aren't perfectly realistic and can't be considered as an irrefutable validation. The last complementary approach consists on comparing the quantitative MRI metrics with histology. Thanks to the diversity of microstructure in the white matter, as observed between the different region of the corpus callosum (Aboitiz et al., 1992) or between the different pathways of the spinal cord (Nieuwenhuys et al., 2007), histology can show the high sensitivity of these measurements to the desired microstructural feature and can assess their accuracy (Barazany et al., 2009; Chin et al., 2004; Farrell et al., 2010; Golabchi et al., 2010; Harkins et al., 2012; Kolasinski et al., 2012; Ong et al., 2008; Stikov et al., 2015). Histology requires to fix, stain, the image at high resolution (fraction of micrometers), and segment correctly the axons, myelin sheath and other components of the white matter, a task that is technically complex. Due to these challenges, histological validation studies have been performed using a couple (around ten) of small images (around 20 x 20 μm^2) that are united in regions of interest presenting similar microstructure (e.g. genu, body, and splenium of the corpus callosum). This small number of data limit the statistical power of these studies, which is necessary for (i) validating the sensitivity to subtle changes of microstructure throughout the white matter such as changes myelin content, (ii) comparing and ranking models and (iii) assessing the specificity of a particular metric.

Indeed, assessing the specificity is particularly challenging because many microstructural and physical parameters correlate with each other in the white matter (e.g. axon diameter, axon density, myelin/iron/water content, CSF contamination, T1 and T2 relaxation): how to be sure, for instance, that axon diameter index from MRI is not biased by axon density or T2 relaxation? In previous histological validation studies, only a couple of points was opposing the quantitative metric (M_{MRI}) to the desire microstructural feature (M_{histo}), making it tricky to validate a 1:1 relationship (only the correlation was assessed). We expect that a large amount of data presenting a large spectrum of axon diameter and density, in healthy and damaged tissue, will help to answer this question.

In this work, we focus on the variety of diameter distribution and densities present in the spinal tracts to validate and compare in a same study the quantitative metrics from the following models and techniques: AxCaliber (Assaf et al., 2008), NODDI (Zhang et al., 2012), ActiveAx (Alexander et al., 2010) and MTV (Mezer et al., 2013). All protocols were acquired on an ex vivo cat spinal cord and the sensitivity and precision of the extracted metrics were assessed using full slice histology with automatic axon segmentation. Data from this study are made publicly available as a basis for future comparisons (http://www.neuro.polymtl.ca/downloads).

7.2 Methods

7.2.1 Tissue preparation

The spinal cord of an healthy adult cat was supplied by the SensoriMotor Rehabilitation Research Team and approved by the local ethic committee. Just after sacrifice, the animal was perfused, first with 500 mL of saline 0.9% to wash blood and improve fixative penetration, and then with 1L 4% paraformaldehyde (PFA) in Phosphate buffer 0.1M. Immediately after perfusion, a cervical segment of spinal cord was extracted and post-fixed overnight in PFA 4% at 4°C. Two contiguous pieces of one-centimeter-long were cut, one piece was sent for histology, the other was used for MRI.

7.2.2 MRI acquisition

The first piece was scanned on a Agilent 7T animal scanner equipped with 600 mT/m gradients and a slew rate of 1 T/m/ms. The tissue was washed in phosphate buffered saline (PBS 1x) five days at 4°C before scanning and inserted into a small glass tube filled with buffered water. A custom-made solenoid coil was used for transmission and reception (S11 ~ -40dB). One axial slice of spinal cord was acquired with a matrix size of 64x64 and a resolution of 0.16x0.16x0.20 mm^3.

7.2.2.1 Diffusion

A single shot echo planar imaging sequence was used with following acquisition settings: bandwidth of 250kHz, TR=2s.

Figure 7.1 shows the qspace sampling for the AxCaliber protocol (2D sampling perpendicular to the spinal cord). Diffusion parameters were δ=3/8/8/8 ms, Δ = 7/12/25/40 ms, G = [0 .. 849] mT/m (199 increments), echo time (TE) was minimized (TE = 36 - 62 ms). A total of 796 increments were acquired. The CHARMED model (Assaf et al., 2004) was used to analyse the data. This model assumes perfectly parallel fibers with a single axon diameter and present the following fitting parameters: (i) axon diameter index (Alexander et al., 2010) (ii) fraction of restricted water (*fr*), and (iii) apparent hindered diffusion coefficient (Dh). The restricted compartment was modeled using the Gaussian phase distribution approximation (Murday and Cotts, 1968).

Figure 7.1.b. shows the qspace sampling used for NODDI and ActiveAx. Diffusion parameters were δ=3ms, Δ=30ms, TE=47ms. Four shells were acquired with bvalue=40/189/1680/6720 $s.mm^{-2}$. 796 diffusion weighted images were acquired in 27 min in each protocol.

For NODDI, the WatsonSHStickTortIsoVIsoDot_B0 model was used.

Both ActiveAx and NODDI were fitted using (1) AMICO framework (Daducci et al., 2015). ActiveAx results were obtained using a two compartment model (ZeppelinCylinder) and NODDI used a four compartment model WatsonSHStickTortIsoVIsoDot_B0.

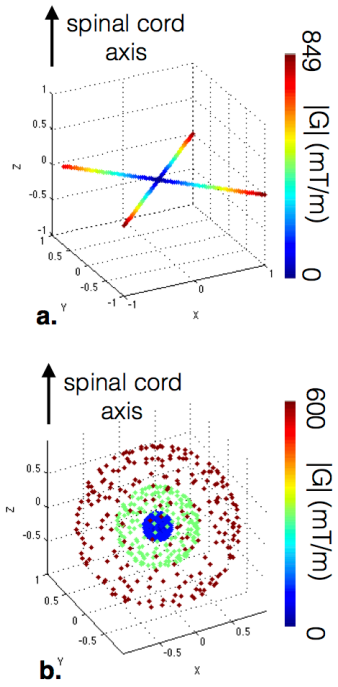

Figure 7.1. qspace sampling of the diffusion protocols. a. AxCaliber b. NODDI and ActiveAx

7.2.2.2 Macromolecular Tissue Volume (MTV)

MTV was measured using the procedure described in (Mezer et al., 2013). First a T1 map was produced using an Inversion Recovery Fast Spin Echo (Barral et al., 2010) with 38 inversion times exponentially distributed between 3ms and 2s (hard-inversion pulse, TR=14s, ESP=6.18ms). Spoiled Gradient-Echo images (2 dummy scan, 16 average, TE=2.4ms, TR=24ms) were acquired using flip angles of 2,4,6,10,15,20,25 and 30°.

7.2.3 Histology

The second piece of spinal cord was stained with osmium 2% for 2 hours, dehydrated, embedded in paraffin, cut in 4 µm slices and imaged using an optical 20x whole slice microscope (Hamamatsu NanoZoomer 2.0-HT). Resolution was 230 nm/px and allowed us to segment the axons automatically using AxonSeg. **Figure 7.2** shows the histological image before and after myelin segmentation.

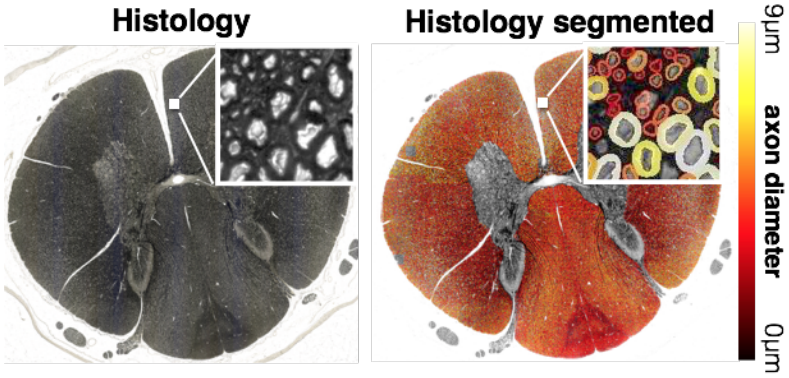

Figure 7.2: Optical image of the full spinal cord before (left) and after (right) myelin segmentation (color-coded for axon diameter).

7.2.4 Voxel-wise comparison

Figure 7.3 describes the procedure used to perform voxel-wise comparison between MRI and histology. The axon-segmented image was first downsampled by averaging the axon morphological properties (axon diameter (mean and std), myelin volume fraction, fiber volume fraction, number of axons per mm^2) on 150x150 μm^2 windows. Then the downsampled histology was registered to MRI using affine transformation supervised by control points (image processing Toolbox, MATLAB, R2014a). Correlation (Pearson coefficient) was computed voxel-wise between MRI and histological metrics.

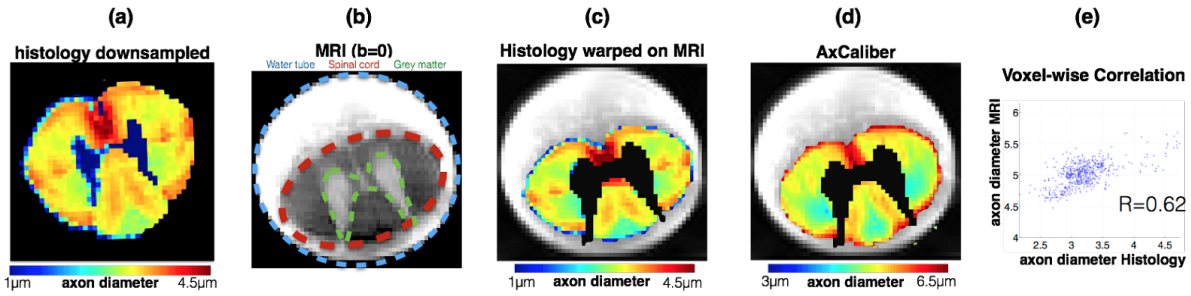

Figure 7.3: Framework for the comparison of MRI quantitative metrics with histology. Histology was downsampled (a) by computing the average axonal metrics in 150x150µm2 pixels. Metrics were then registered on the MRI (b) using affine transform. MRI quantitative metrics (c) were compared with histology (d) voxel by voxel using Pearson correlation coefficient (e).

7.3 Results

Figure 7.4 shows the MRI metrics and histological results. Both histology and MRI show a strong contrast in the white matter. A good agreement can be seen between MRI metrics and between histology and MRI.

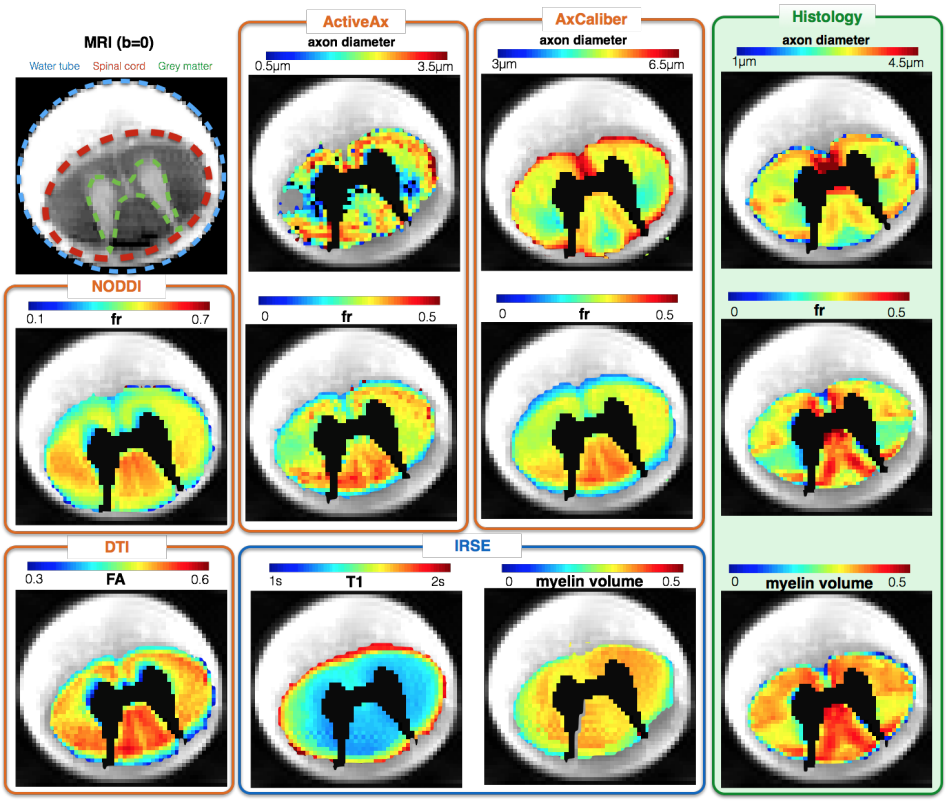

Figure 7.4: Quantitative MRI metrics mapping (left 2 columns) and histology mapping (right column). **Top row**: Axon diameter metrics. **Middle row**: Fraction of restricted water. **Bottom row**: FA and myelin volume fraction metrics.

Figure 7.5 shows the correlation matrix of MRI and histological metrics. We found a high correlation between AxCaliber and histology for axon diameter (r=0.62) (box 1) and a moderate correlation for the fraction of restricted water (r=0.38) (box 2). A good correlation for the measurement of the restricted water fraction between AxCaliber and NODDI (r=0.59) (box 3), ActiveAx (0.86), FA (0.83) and MTV (0.76) (box 4). Interestingly most MRI metrics do not correlate significantly with histology (see black boxes on the top right corner "histology *versus* MRI"), suggesting a good specificity of the metrics that do correlate with histology. No particular correlation was found between MTV and myelin volume fraction obtained from histology, probably due to the difficulty to measure myelin volume fraction with optical microscopy (see discussions).

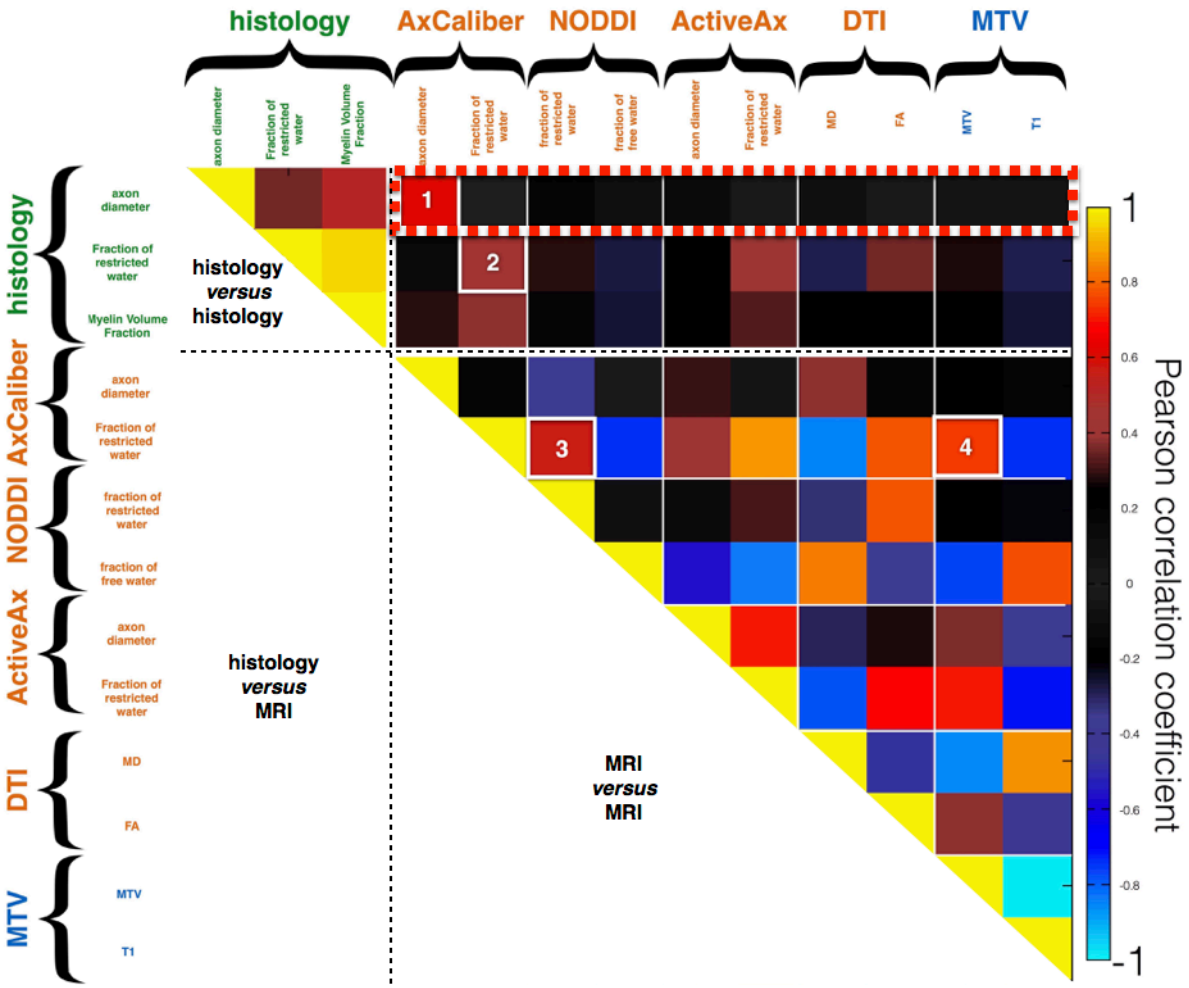

Figure 7.5: Correlation matrix comparing histology (green) quantitative diffusion MRI metrics (orange) and quantitative myelin imaging (blue). Note the numbered cases. **Box 1** exhibits a high correlation (0.62) between histology and MRI for axon diameter. **Box 2** presents a moderate correlation (0.48) between histology and MRI for the restricted fraction. **Box 3** highlights the agreement between 2D and 3D sampled q-pace metrics. **Box 4** highlights the link between diffusion and myelin imaging.

7.4 Discussion

In this work, we used for the first time a fully axon-segmented slice of spinal cord and we compared it with different diffusion and myelin imaging quantitative metrics. We showed, through a correlation analysis, that AxCaliber was precise enough to distinguish between various fiber distributions present in the spinal cord white matter.

Due to the relatively large size of the axons in the spinal cord (up to 9µm in this cat sample), the axons could clearly be distinguished in our image, even using optical microscopy. Optical microscopy presents the advantage of being particularly fast (entire slices can be acquired in a minute with a slide scanner) and multiple staining can be used easily to reveal other microstructural features (e.g. luxol fast blue, H&E). While optical images are sufficient to get a precise and accurate mapping of the mean axon diameter throughout the spinal cord, the inherent blur tends to bias the measures of myelin thickness (underestimation of g-ratio), and limits the detection of the smallest axons. We believe that this limitation greatly explains the poor correlation between MTV and myelin volume fraction obtain with histology. This is especially problematic because the dynamic of the myelin volume fraction in the spinal cord is particularly small (5-10%) (Harkins et al., 2016), and thus needs to be measure with high precision for both MRI and histology in order to obtain good correlation.

In addition to the physical limitation of optical microscopy, the broad point spread function (blur) can also be explained by the thickness of the slice (tenth of microns) that is larger than the depth of field (6µm at 20x and 1µm at 40x). Cutting thinner such a large sample would have resulted in holes and thus could not be obtained. As a result, we were limited to 20x magnification (NA=0.41, effective resolution = 1µm). Better (but slower and monomodale) microscopy, such as electron microscopy or CARS (Duval et al., 2015), would overcome this issue and allow accurate measurement of the myelin thickness and axonal density.

In addition, axon segmentation error might bias our reported results and limit the validation of the accuracy of the MRI metrics. Quantification of these bias are, however,

possible by training on manual correction of the axon segmentation using online crowd contribution (Guttmann, n.d.).

Finally, tissue deterioration during preparation is an additional bias that would be overcome with preservative histological methods such as CARS (Duval et al., 2015).

7.5 Acknowledgments

We would like to thanks Serge Rossignol, Hugo Delivet-Mongrain and all the members of the SensoriMotor Rehabilitation Research Team (SMRRT) for providing us with the cat spinal cord. Also we would like to thanks the histology unit of the Institute for Research in Immunology and Cancer.

References.

Aboitiz, F., Scheibel, A.B., Fisher, R.S., Zaidel, E., 1992. Fiber composition of the human corpus callosum. Brain Res. 598, 143–153.

Alexander, D.C., Hubbard, P.L., Hall, M.G., Moore, E.A., Ptito, M., Parker, G.J.M., Dyrby, T.B., 2010. Orientationally invariant indices of axon diameter and density from diffusion MRI. Neuroimage 52, 1374–1389.

Assaf, Y., Blumenfeld-Katzir, T., Yovel, Y., Basser, P.J., 2008. AxCaliber: a method for measuring axon diameter distribution from diffusion MRI. Magn. Reson. Med. 59, 1347–1354.

Assaf, Y., Freidlin, R.Z., Rohde, G.K., Basser, P.J., 2004. New modeling and experimental framework to characterize hindered and restricted water diffusion in brain white matter. Magn. Reson. Med. 52, 965–978.

Barazany, D., Basser, P.J., Assaf, Y., 2009. In vivo measurement of axon diameter distribution in the corpus callosum of rat brain. Brain 132, 1210–1220.

Barral, J.K., Gudmundson, E., Stikov, N., Etezadi-Amoli, M., Stoica, P., Nishimura, D.G., 2010. A robust methodology for in vivo T1 mapping. Magn. Reson. Med. 64, 1057–1067.

Bégin, S., Dupont-Therrien, O., Bélanger, E., Daradich, A., Laffray, S., De Koninck, Y., Côté, D.C., 2014. Automated method for the segmentation and morphometry of nerve fibers in large-scale CARS images of spinal cord tissue. Biomed. Opt. Express, BOE 5, 4145–4161.

Burcaw, L.M., Fieremans, E., Novikov, D.S., 2015. Mesoscopic structure of neuronal tracts from time-dependent diffusion. Neuroimage 114, 18–37.

Chin, C.-L., Wehrli, F.W., Fan, Y., Hwang, S.N., Schwartz, E.D., Nissanov, J., Hackney, D.B., 2004. Assessment of axonal fiber tract architecture in excised rat spinal cord by

localized NMR q-space imaging: simulations and experimental studies. Magn. Reson. Med. 52, 733–740.

Daducci, A., Canales-Rodríguez, E.J., Zhang, H., Dyrby, T.B., Alexander, D.C., Thiran, J.-P., 2015. Accelerated Microstructure Imaging via Convex Optimization (AMICO) from diffusion MRI data. Neuroimage 105, 32–44.

Duval, T., Gasecka, A., Pouliot, P., Côté, D., Stikov, N., Cohen-Adad, J., 2015. Validation of MRI microstructure measurements with Coherent Anti-Stokes Raman Scattering (CARS), in: Proceedings of the 23th Annual Meeting of ISMRM. Toronto, p. 682.

Farrell, J.A.D., Zhang, J., Jones, M.V., Deboy, C.A., Hoffman, P.N., Landman, B.A., Smith, S.A., Reich, D.S., Calabresi, P.A., van Zijl, P.C.M., 2010. q-space and conventional diffusion imaging of axon and myelin damage in the rat spinal cord after axotomy. Magn. Reson. Med. 63, 1323–1335.

Ferizi, U., Schneider, T., Panagiotaki, E., Nedjati-Gilani, G., Zhang, H., Wheeler-Kingshott, C.A.M., Alexander, D.C., 2014. A ranking of diffusion MRI compartment models with in vivo human brain data. Magn. Reson. Med. 72, 1785–1792.

Fieremans, E., De Deene, Y., Delputte, S., Ozdemir, M.S., D'Asseler, Y., Vlassenbroeck, J., Deblaere, K., Achten, E., Lemahieu, I., 2008. Simulation and experimental verification of the diffusion in an anisotropic fiber phantom. J. Magn. Reson. 190, 189–199.

Golabchi, F.N., Brooks, D.H., Hoge, W.S., De Girolami, U., Maier, S.E., 2010. Pixel-based comparison of spinal cord MR diffusion anisotropy with axon packing parameters. Magn. Reson. Med. 63, 1510–1519.

Guttmann, C.R.G., n.d. Spine [WWW Document]. spinevirtuallab.org. URL https://spinevirtuallab.org/public/#/index

Hall, M.G., Alexander, D.C., 2009. Convergence and parameter choice for Monte-Carlo simulations of diffusion MRI. IEEE Trans. Med. Imaging 28, 1354–1364.

Harkins, K.D., Dula, A.N., Does, M.D., 2012. Effect of intercompartmental water exchange on the apparent myelin water fraction in multiexponential T2 measurements of rat spinal cord. Magn. Reson. Med. 67, 793–800.

Harkins, K.D., Xu, J., Dula, A.N., Li, K., Valentine, W.M., Gochberg, D.F., Gore, J.C., Does, M.D., 2016. The microstructural correlates of T1 in white matter. Magn. Reson. Med. 75, 1341–1345.

Kolasinski, J., Stagg, C.J., Chance, S.A., Deluca, G.C., Esiri, M.M., Chang, E.-H., Palace, J.A., McNab, J.A., Jenkinson, M., Miller, K.L., Johansen-Berg, H., 2012. A combined post-mortem magnetic resonance imaging and quantitative histological study of multiple sclerosis pathology. Brain 135, 2938–2951.

Lee, H.-H., Veraart, J., Novikov, D.S., Fieremans, E., 2016. What dominates the diffusivity time dependence transverse to axons: Intra- or extra-axonal water?, in: Proceedings of the 24th Annual Meeting of ISMRM. p. 656.

Mezer, A., Yeatman, J.D., Stikov, N., Kay, K.N., Cho, N.-J., Dougherty, R.F., Perry, M.L., Parvizi, J., Hua, L.H., Butts-Pauly, K., Wandell, B.A., 2013. Quantifying the local tissue volume and composition in individual brains with magnetic resonance imaging. Nat. Med. 19, 1667–1672.

Murday, J.S., Cotts, R.M., 1968. Self-Diffusion Coefficient of Liquid Lithium. J. Chem. Phys. 48, 4938–4945.

Nieuwenhuys, R., Voogd, J., van Huijzen, C., 2007. The Human Central Nervous System: A Synopsis and Atlas. Springer.

Nilsson, M., Lätt, J., Ståhlberg, F., van Westen, D., Hagslätt, H., 2012. The importance of axonal undulation in diffusion MR measurements: a Monte Carlo simulation study. NMR Biomed. 25, 795–805.

Nilsson, M., van Westen, D., Ståhlberg, F., Sundgren, P.C., Lätt, J., 2013. The role of tissue

microstructure and water exchange in biophysical modelling of diffusion in white matter. Magn. Reson. Mater. Phys. Biol. Med. 26, 345–370.

Ong, H.H., Wright, A.C., Wehrli, S.L., Souza, A., Schwartz, E.D., Hwang, S.N., Wehrli, F.W., 2008. Indirect measurement of regional axon diameter in excised mouse spinal cord with q-space imaging: simulation and experimental studies. Neuroimage 40, 1619–1632.

Shemesh, N., Ozarslan, E., Basser, P.J., Cohen, Y., 2010. Detecting diffusion-diffraction patterns in size distribution phantoms using double-pulsed field gradient NMR: Theory and experiments. J. Chem. Phys. 132, 034703.

Stikov, N., Campbell, J.S.W., Stroh, T., Lavelée, M., Frey, S., Novek, J., Nuara, S., Ho, M.-K., Bedell, B.J., Dougherty, R.F., Leppert, I.R., Boudreau, M., Narayanan, S., Duval, T., Cohen-Adad, J., Picard, P.-A., Gasecka, A., Côté, D., Pike, G.B., 2015. Quantitative analysis of the myelin g-ratio from electron microscopy images of the macaque corpus callosum. Data Brief 4, 368–373.

Zhang, H., Schneider, T., Wheeler-Kingshott, C.A., Alexander, D.C., 2012. NODDI: practical in vivo neurite orientation dispersion and density imaging of the human brain. Neuroimage 61, 1000–1016.

CHAPITRE 8 HISTOLOGIE A GRANDE ECHELLE DE LA MOELLE EPINIERE HUMAINE : UNE ANATOMIE DETAILLEE DE LA MICROSTRUCTURE

Objectif. Les axones dans la matière blanche du cerveau sont les cables d'information de notre système nerveux central. Entourés par la myéline, membrane lipidique qui permet une conduction plus rapide des signaux, ces cellules allongées assurent la communication neuronale chez tous les mammifères. Les lésions traumatiques ou les maladies neurodégénératives telles que la sclérose en plaques peuvent endommager les axones myélinisés, conduisant éventuellement à la douleur chronique et des déficits fonctionnels tels que la paraplégie. Pour comprendre l'impact spécifique de ces pathologies sur la microstructure de la matière blanche, une première étape nécessaire est de caractériser les axones de la moelle épinière en bonne santé. A ce jour, seules des connaissances limitées sont disponibles sur la morphologie de ces axones, sur comment les axones varient entre les populations humaines et ce qui se passe au niveau micro- et macroscopiques dans des conditions pathologiques. A cet effet, nous avons construit le premier atlas complet de microstructure de la matière blanche d'une moelle épinière humaine ex vivo, avec des mesures quantitatives telles que le diamètre de l'axone, la densité des axones et l'épaisseur de la myéline.

Méthode. Une moelle épinière humaine a été disséqué et 24 coupes axiales ont été extraits à chaque niveau de la colonne vertébrale, entre L5 et C1. Après fixation et coloration à l'osmium, un microscope électronique à balayage a été utilisée pour imager la totalité de chaque tranche à une résolution variant de 130 à 260 nm / px, donnant des images composées d'environ 10 gigapixels. À cette résolution, les axones myélinisés, ainsi que leurs gaines de myéline, se distinguent clairement à cette résolution, permettant d'effectuer une segmentation automatique. Des cartes de morphologie axonale (forme, diamètre, épaisseur de la myéline, la densité) ont été obtenus à partir de ces segmentations et recallées sur un modèle d'imagerie par résonance magnétique de la moelle épinière (IRM) (PAM50) pour créer le premier atlas 3D de la microstructure de la moelle épinière.

Résultats. Entre 500 000 (lombaire) et 1 million (cervical) d'axones myélinisés ont été segmentés dans la moelle épinière humaine. Une grande variabilité du diamètre des axones a été observée dans la substance blanche : au niveau du niveau cervical, le diamètre moyen des axones varie entre 2,5 µm (gracilis) et 3,5 µm (spino-cérébellar), et la fraction volumique de fibres myélinisées varie de 30% (gracilis) à 50% (cunéatus et spino-cérébellar). Nous avons également observé que la moelle épinière est très symétrique. En moyenne, la différence entre les voies gauche et droite pour le diamètre est de 0,01 µm axonale, 1% pour la densité axonale et 0,4% pour le volume de myéline. Par conséquent, le fait d'être droitier ou gaucher a très peu d'impact sur la morphologie axonale. Le premier modèle de microstructure de la moelle épinière humaine a été rendu public pour le téléchargement : https://osf.io/8k7jr/

8.1 Introduction

la substance blanche de la moelle épinière est composé de fibres neuronales, regroupés en faisceaux, qui relient les différentes régions du cerveau avec le système nerveux périphérique. Les fibres myélinisées et non-myélinisées occupent ensemble environ 60% du volume de la substance blanche (Mottershead et al., 2003;. Perge et al, 2009), et le reste est occupé par les cellules gliales, les vaisseaux sanguins, le collagène, et quelques corps cellulaires. La morphologie de ces fibres est remarquablement hétérogène: tandis que la matière blanche pourrait être considéré comme un réseau de câbles identiques transmettant des potentiels d'action, en réalité la taille de ces fibres varie entre 0,1 et 10 microns (Perge et al, 2012.). Les différentes voies de la matière blanche sont caractérisées par des microstructures différentes (Nieuwenhuys et al., 2007), mais cette observation est surtout qualitative, et il existe peu de données qui décrivent clairement et quantifient ces différences (Watson et al., 2009). L'absence d'information claire sur la microstructure de la matière blanche de la moelle épinière est également problématique pour la validation des méthodes d'imagerie par résonance magnétique quantitatives qui sont sensibles, voire spécifique, à la microstructure (Cohen-Adad et Wheeler-Kingshott, 2014; Dula et al., 2010; Duval et al., 2017).

Comme on peut observer dans les livres d'anatomie relativement récents (Gray et al., 2005; Nieuwenhuys et al, 2007;.. Watson et al, 2009), les connaissances sur l'organisation des fibres dans la matière blanche est une accumulation de décennies de recherche par des experts neuroanatomistes et il n'est pas rare d'utiliser des études de références qui ont plus de cinquante ans (Demyer, 1959; Gray, 1867; Lassek, 1945, Verhaart, 1962). En effet, la cartographie et la classification de la connexion et la morphologie des millions de fibres nécessite des études particulièrement minutieux qui ne peuvent être reproduites facilement. Dans le paragraphe suivant, nous allons donner un aperçu de l'état de l'art de la microstructure de la matière blanche dans la moelle épinière.

Les cartes générales de la cytoarchitecture se trouvent dans (Nieuwenhuys et al., 2007), mais les descriptions sont qualitatives. Pour les valeurs quantitatives, les études se

concentrent généralement sur une seule voie spinale. Parce que chaque voie a souvent été étudié par un auteur différent, une comparaison quantitative entre les voies est délicate. Seules les principales voies ont été largement étudiées, à savoir corticospinal, spinothalamique, spinocérébellar et la colonne dorsale. **Corticospinal**. Cette grande voie de fibres moteur a été la plus étudiée. Chez l'homme, les principales voies corticospinal (anciennement appelées faisceaux pyramidale) sont situés dans les colonnes latérales et le diamètre de leurs fibres myélinisées varie de 1 à 20 um (Lassek, 1945; Verhaart, 1947), avec 90% des fibres compris entre 1 et 4 um (Lassek, 1945). A noter que, chez les rongeurs, ce tube se trouve dans la colonne dorsale et il est composé de petites uniformément axones (~1µm) (Verhaart, 1962). La présence de quelques très grands axones chez l'homme est attribuée au développement de la dextérité (Nudo et Frost, 2007). Nous comptons environ 60,000 axones myélinisées dans l'ensemble des voies cortico pour l'humain, ce qui équivaut à 7.000 axones / mm^2 (Wada, 2001). **Spino-thalamique**. Le faisceau spino-thalamique est composé d'environ 18 000 fibres chez les singes (Apkarian et Hodge, 1989), avec la plus grande densité au niveau du cervical (C1-C3). La structure est stratifiée, avec des fibres afférentes s'accumulant sur la partie latérale. En direction rostrale, les voies spinothalamique migrent progressivement vers le ventral, en particulier avant l'élargissement cervical (Zhang et al., 2000). Chez le singe, le chat et l'écureuil, ce tube est connu pour être hétérogène avec de grands axones situés sur la partie ventrale du tube et des axones plus fins situés dorsalement (Stevens et al., 1991). **Spinocerebellar.** Cette organisation stratifiée est également observée pour les voies spinocerebellar. Les axones les plus internes viennent des segments inférieurs de la moelle épinière. Ces tracts contiennent des axones particulièrement grands, mais quelques petits axones sont également présents dans les parties ventrales (Watson et al., 2009, p. 155). **Colonne dorsale.** La colonne dorsale se compose de deux voies sensorielles: gracilis et cunéatus. Alors que la plupart des axones dans ces voies sont de petite taille, la plupart du temps non-myélinisés et court (2-3 segments), la majorité du volume est occupé par des axones grandes et longues (Burgess et Horch, 1978). Chez le chat, la majorité des fibres du gracilis sont 2-5µm large (Hwang et al., 1975). Le cuneatus contient des axones beaucoup plus grands que la gracilis avec un

diamètre moyen de 1 um et 1.4µm respectivement chez le rat (Ong et al., 2008). Un examen plus approfondi de la morphologie axonale dans la moelle épinière peut se trouver dans l'article de revue (Saliani et al. 2017).

Récemment, grâce à la puissance de calcul de plus en plus importante, qui permet l'acquisition et le stockage de plus en plus de données, l'imagerie à grand champ de vue et à la résolution suffisante pour distinguer les plus petits axones est désormais possible (par exemple cerveau complet de la souris) (Hua et al, 2015;. Mikula et al ., 2012; Mikula et Denk, 2015). De plus, des logiciels automatique pour segmenter ces ensembles de données ont été mis au point (et al Bégin, 2014;.. Sommer et al, 2011;. Zaimi et al, 2016).

Dans ce travail, nous avons acquis 24 images entières d'une tranche de moelle épinière humaine à l'aide de la microscopie électronique à balayage à une résolution 130-260 nm, du niveaux cervical au niveaux lombaire. Les axones et leurs gaines de myéline sont automatiquement segmentés en vue de mesurer leur diamètre individuel, leur forme (par l'excentricité), et le g-ratio (le rapport du diamètre interne sur externe de la gaine de myéline). Le diamètre moyen des axones, la densité des axones, et de la myéline ont été mesurées dans chaque échantillon. Enfin, des statistiques ont été réalisées pour étudier les différences entre les niveaux, entre la gauche et la droite et entre fibres ascendantes et descendantes (voies sensorielles ou moteur). Les cartes de morphologie axonale ont été combinés et recallées à un modèle de la moelle épinière pour créer le premier atlas des microstructures de la moelle épinière.

8.2 Méthodes

8.2.1 Préparation du tissue

Ethique. La moelle épinière a été extraite d'un cadavre frais de femme (1,60m, 55 kg, 71 ans), léguée au laboratoire d'anatomie à l'Université du Québec à Trois-Rivières par un consentement éclairé. Toutes les procédures ont été approuvées par le Comité d'éthique local (scelera-15-03-PR01).

Dissection. Deux heures après la mort, la moelle épinière a été disséqué et coupé en sections transversales 5-10mm d'épaisseur (voir **Figure 8.1**). La position rostro-caudal a été estimée par comptage des racines nerveuses cervicales (8, 12 thoraciques et lombaires 5). Le côté droit de la colonne vertébrale a été marquée à l'aide des cordes attachées aux racines nerveuses.

Figure 8.1. dissection de la moelle épinière. La moelle épinière a été entièrement exposée (à gauche) et une 24 tranches de un centimètre de moelle épinière ont été extraites et post-fixées (à droite).

Fixation. Juste après dissection, les échantillons ont été immergés dans des flacons séparés de 50 ml contenant une solution de paraformaldehyde à 4% et 0 à 2% de glutaraldéhyde (Ga) (voir tableau 1), et stockés à 4 ° C. La solution tampon est une solution PBS 1x, ajusté pour un pH de 7,4 avec HCl. Les différentes concentrations de glutaraldéhyde ont été utilisées afin d'évaluer le biais de contraction des tissus (qui dépend de la concentration en Ga) et empêcher le rapport des conclusions erronées (voir la discussion). Après une semaine, des échantillons ont été transférés dans du PBS 1x pour empêcher une fixation. Le tableau 1 énumère les sections extraites de la moelle épinière, le niveau de la colonne vertébrale, et les concentrations exactes de glutaraldéhyde.

Tableau 8.1: Liste des échantillons. C: niveau cervical, T: niveau thoracique et L: niveau lombaire. Lorsque plusieurs tranches ont été extraites au même niveau, les lettres A, B et C ont été utilisés avec A la tranche la plus rostrale.

spinal level	PFA	Glutaraldehyde	SEM resolution (nm)
C1A	4%	0%	260
C1B	4%	0%	260
C2A	4%	2%	*130*
C2B	4%	0%	260
C2C	4%	0.5%	130
C3A	4%	2%	130
C3B	4%	0.5%	130
C3C	4%	0%	260
C4A	4%	2%	130
C5B	4%	0.5%	130
C5B	4%	0.5%	130
C5B	4%	2%	130
C6A	4%	0.5%	130
C6B	4%	2%	130
C7B	4%	0.5%	130
T12	4%	0%	260
T4	4%	0%	130
T9	4%	0.5%	130
T6	4%	2%	130
L1	4%	0.5%	130
L2A	4%	2%	130
L2B	4%	0%	260
L3A	4%	0.5%	130
L4A	4%	0%	260
L5	4%	0%	260

Préparation pour la microscopie. Des échantillons ont été colorés avec osmium 2% pendant 10 heures dans des flacons 10 ml. Un dispositif de rotation bidirectionnel a été utilisé pour empêcher le dépôt de l'osmium au fond du flacon. Les échantillons ont ensuite été lavées dans de l'eau distillée et déshydraté à 10, 25, 50, 75 et 100% des bains d'acétone pendant 30 minutes chacune. L'acétone a ensuite été progressivement remplacée par 50 et 100% Epon 812 (Mecalab, Canada) pendant 12 heures chacun. L'enrobage final a été effectué à 60 ° C pendant 24 heures. Au cours de l'enrobage final, chaque tranche axiale a été

soigneusement positionné au fond du moule, et maintenu à l'aide d'une grille en plastique, ceci afin d'avoir la surface la plus plane possible. Une fois la procédure d'incorporation terminée, un microtome (Reichert-Jung) a été utilisé pour éliminer les premières couches de résine (épaisseur de 15 um) et exposer l'ensemble de la tranche de la moelle épinière (voir **Figure 8.2**). La grande lame en carbure de tungstène du microtome a permit de couper la totalité du bloc par des coupes de 15 µm. Lorsque la surface était légèrement courbé, la découpe a été effectuée à différents angles. 50 à 100µm du tissu a été retiré avant d'obtenir des tranches entièrement exposées de la moelle épinière. Cette procédure a été nécessaire parce que l'osmium a une profondeur de pénétration de seulement 200 µm (Hua et al., 2015). Les tranches exposées de la moelle épinière ont ensuite été polies à l'aide d'une solution de polissage d'aluminium en suspension de 0,05 µm, et la conduction électrique est assurée par dépôt en phase vapeur d'or (couche de 600 Â).

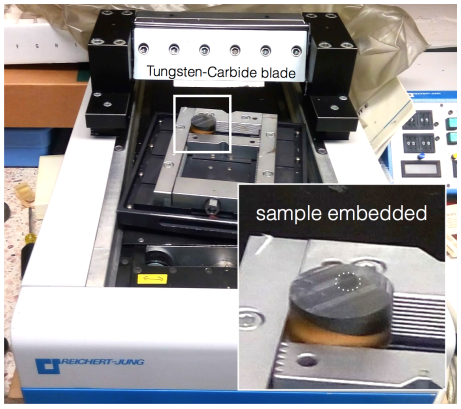

Figure 8.2: Microtomie. Une lame en carbure de tungstène a été utilisé pour exposer la surface de la moelle épinière. L'angle de découpe a été ajusté afin d'éviter de couper plus profond que 100 microns.

8.2.2 Microscopie

Les images ont été obtenues à l'aide d'un microscope électronique à balayage (MEB) (JEOL JSM7600F) contrôlé par le logiciel Aztec 3.2 (Oxford Instruments, Royaume-Uni). Chaque échantillon a été soigneusement positionné sur le porte-échantillon pour assurer une surface parallèle et une bonne conduction avec le porte-échantillon en utilisant du ruban de carbone. La fonction de mappage de zone du logiciel Aztec a été utilisé pour acquérir entre 150 et 300 mosaïques (en fonction du niveau spinal de la moelle) de 8192x5632 pixels et une zone de 1060x729 µm2. Les paramètres suivants ont été utilisés pour l'analyse : le mode de faible grossissement, à faible angle détecteur d'électrons rétrodiffusés (LABE), 15 kV, la sonde à courant de 140 µA, grossissement à 110x, distance 15 mm, temps de pause de 2µs. Le mode faible grossissement a été choisi pour augmenter le champ de vision et la profondeur de champ. Le focus a été ajusté au niveau des nerfs périphériques afin d'éviter la dégradation de la surface, et le contraste / luminosité est réglé manuellement. Si le rapport signal-bruit n'était pas satisfaisant, la distance de balayage était réduite à 10 mm et le courant de sonde augmenté à 16.

8.2.3 Traitement d'image

Collage. Les mosaïques ont été automatiquement collées en utilisant le plugin collage d'une collection en grille (Preibisch et al., 2009) du programme de traitement d'image Fidji (Schindelin et al., 2012). Étant donné que le collage a été défaillant dans certaines régions (généralement à la périphérie de la moelle épinière, où le fond noir est très présent), une détection des valeurs aberrantes a été mis en œuvre en supposant un déplacement constant du support (voir matériel supplémentaire S1).

Segmentation. Les axones et la myéline de chaque image en mosaïque sont automatiquement segmentés en utilisant AxonSeg (Zaimi et al., 2016) sur un ordinateur équipé d'un processeur 12 cœurs Xeon Phi. La segmentation d'une tranche complète de la moelle épinière a été obtenue en environ 12h (en utilisant la boîte à outils de calcul parallèle Matlab). Pour chaque axone, les propriétés suivantes ont été mesurées:

- Diamètre équivalent de l'axone : $d = 2\sqrt{A_{axon}/\pi}$
  (A_{axon} = aire de l'axone segmenté)
- Diamètre équivalent de la fibre : $D = 2\sqrt{A_{fiber}/\pi}$
  ($A_{fiber} = A_{myelin} + A_{axon}$)
- g-Ratio : $g = d/D$
- excentricité : $e = \frac{\sqrt{a^2-b^2}}{a}$
  (avec a la longueur du grand axe et b la longueur du petit axe de l'ellipse qui a les mêmes deuxièmes moments centraux normalisés que l'axone segmentée) (Haralick and Shapiro, 1992, Appendix A)

Afin d'éviter une sur- ou sous-segmentation, les biais de segmentation ont été compensées en comparant segmentations manuelles (vérité terrain) et segmentations automatiques sur une région de 1x0.5mm2. Nous avons constaté que la majorité des axones plus petit que 1 µm étaient faux positifs, et cette valeur a déterminé notre limite de résolution. Voir matériel supplémentaire S2 pour plus de détails.

Sous-échantillonnage. Les images assemblées ont ensuite été sous-échantillonnés à une résolution de 50, 100 et 200 µm (donnant différents rapport signal sur bruit) pour produire des cartes du (i) diamètre axonal équivalent moyen, (ii) le nombre d'axones allant de 1 à 4 µm par pixel, (iii) le nombre d'axones allant de 4 à 8 µm par pixel, (iv) le nombre total d'axones par pixel, (v) la fraction volumique de la myéline, (vi) la fraction volumique de l'axone, et (vii) des fibres (= myéline, plus axone) volume fraction. Notez que l'on extrapole le volume de la myéline ou des axones de la région en assumant la cohérence de ces zones le long de l'axe de la moelle épinière. Donc,

$$Myelin\ Volume\ Fraction = N_{myelin}/N_{total}$$
$$Axonal\ Volume\ Fraction = N_{axon}/N_{total}$$
$$Fiber\ Volume\ Fraction = (N_{axon} + N_{myelin})/N_{total}$$

avec Nj le nombre de pixels attribués à la classe j dans les blocs de sous-échantillonnage (par exemple, pour un sous-échantillonnage de 0,130 à 50 µm, Ntotal = $(50 / 0{,}13)^2$ = 150 000 pixels).

Recalage de l'atlas. Afin d'identifier les différentes voies de la moelle épinière, la version numérique (80x80x500µm3) de l'atlas de l'anatomie de Gray (Gray et al., 2005) qui fait partie de la boîte à outils de la moelle épinière (SCT) (De Leener et al, 2016;. Lévy et al. , 2015) a été recalée en utilisant une déformation élastique vers la version à 50 µm sous-échantillonné de l'histologie. Pour chaque échantillon, le niveau spinal correspondant (ou légèrement décalé lors de multiples tranches ont été extraites au même niveau) de l'atlas a été extraite et recalée en deux étapes: une première transformation affine basée sur des points de contrôle sélectionnés manuellement (cpselect et fitgeotrans fonctions disponibles dans la boîte à outils de traitement d'image Matlab), et une transformation élastique difféomorphes (SYN) estimées sur les masques tirés manuellement de la moelle épinière avec trois valeurs pour la matière grise, blanche et le fond noir (commande sct_register_multimodal de la boîte à outils de la moelle épinière SCT, métriques « moindres carrés ») (Avants et al, 2011;. De Leener et al, 2016). La transformation élastique (régularisé avec B-splines, BsplineSyN) a été divisée en deux étapes : une première transformation des déformations « douces » (à savoir globaux) et une seconde transformation permettant des déformations plus locales. La **Figure 8.3** montre un exemple de recalage.

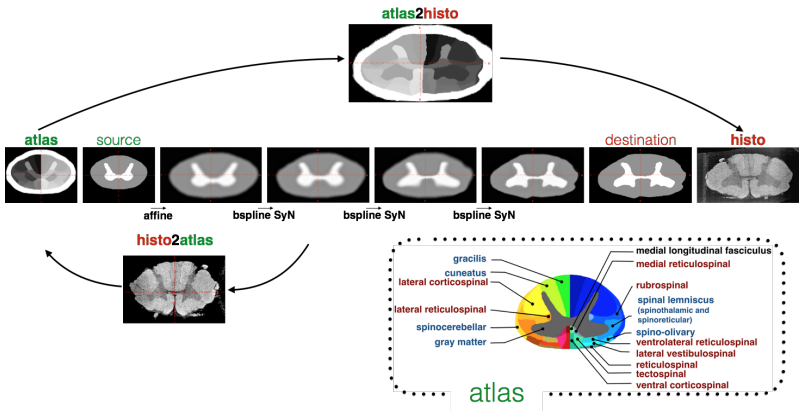

Figure 8.3: Recalage de l'atlas (en bas à droite) vers l'histologie (« histo »). Le recalage a été estimé sur la base des masques de la matière blanche et grise de l'atlas (source) et histologie (destination). Plusieurs étapes ont été utilisées: affines, et de multiples déformations non linéaires régularisés avec BSplines (bspline-syn).

La transformation inverse (de histo2atlas) utilise uniquement la déformation douce afin de maintenir la forme de la structure interne intacte.

Création du modèle. Les cartes sous-échantillonnées ont été ensuite recalées au modèle PAM50 de la moelle épinière (modèle IRM) (De Leener et al., 2017). Pour cette transformation (histologie à l'espace de modèle), l'étape de déformation locale n'a pas été inclus dans le but de préserver la forme des structures internes (par exemple de la matière grise). Les niveaux manquants ont été remplis par recalage et interpolation des plus proches tranches disponibles. Les tranches supérieures et inférieures les plus proches ont d'abord été recalées aux niveaux manquants en utilisant les masques de la substance blanche, la moyenne pondérée par la distance a été utilisé. En raison du petit nombre de tranches au niveau thoracique, le modèle a été généré pour la partie cervicale complète seulement.

8.2.4 Statistiques

L'atlas de la moelle épinière, recalées dans l'espace histologie sous-échantillonnée, a été utilisé pour mesurer la morphologie des axones dans chaque voie spinale. La corrélation entre les tranches a été calculé en utilisant la corrélation de Pearson. La différence maximale de latéralité a été évaluée en utilisant le coefficient de reproductibilité (1,96 fois l'écart-type des différences), et un test t apparié a permit de tester les différences significatives.

Résultats

8.2.5 Imagerie de la moelle entière

Tous les niveaux du cervicaux (sauf C8), quatre thoraciques et six parties lombaires ont été imagées en mosaïque, recollées et segmentés (voir **Figure 8.4**). Quelques échantillons ont souffert d'une mauvaise pénétration de l'osmium (points noirs indiqués par une flèche blanche). Qualitativement, la segmentation est apparue symétrique et cohérente entre les différentes tranches. L'intensité du signal est uniforme pour la plupart des niveaux, à l'exception L2A et L3A, probablement en raison d'une mauvaise calibration de la position

du faisceau d'électrons. La forme de la matière grise a montré une bonne correspondance avec l'atlas anatomique de Gray (**Figure 8.4**, à gauche).

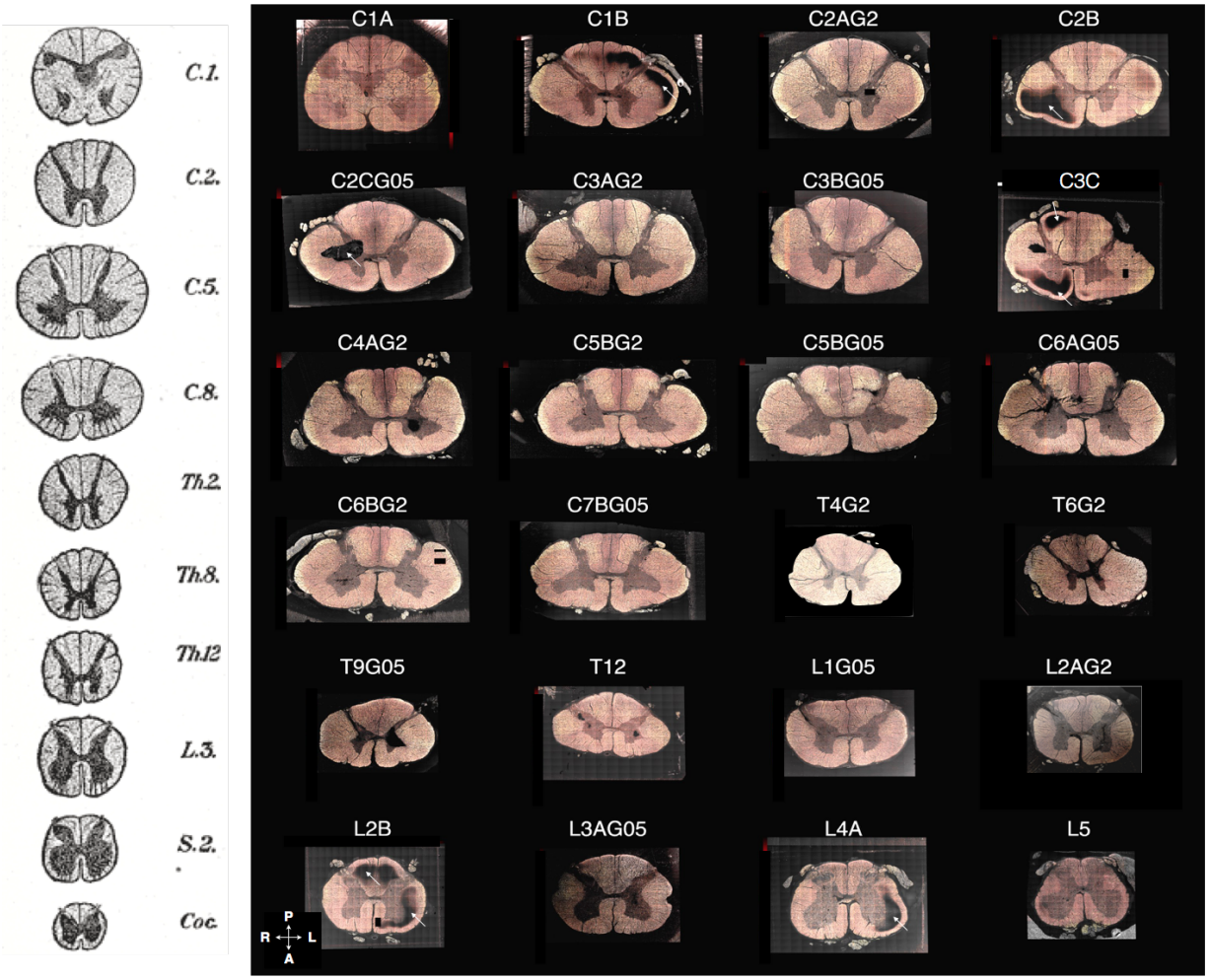

Figure 8.4: Images MEB de moelle entières (recollées), acquises à une résolution allant jusqu'à 129 nm (à droite), et segmentées (code couleur pour diamètre axonal) en utilisant AxonSeg. La forme de la moelle épinière et de la matière grise correspond correctement à l'anatomie du Grays (Gray et al., 2005).

8.2.6 Morphologie axonale dans des petites régions

La qualité de l'image et la segmentation a également été évaluée qualitativement dans quelques régions de 200x200 μm^2 à haute résolution. Les gaines de myéline étaient clairement identifiables avec des frontières nettes (**Figure 8.5**.b). La grande majorité des axones ont été détectés (**Figure 8.5**.c). En utilisant la segmentation manuelle comme vérité terrain, nous avons évalué les performances de segmentation automatique. Nous avons trouvé une sensibilité de 87% et une précision de 78%. La segmentation de la myéline était qualitativement précise.

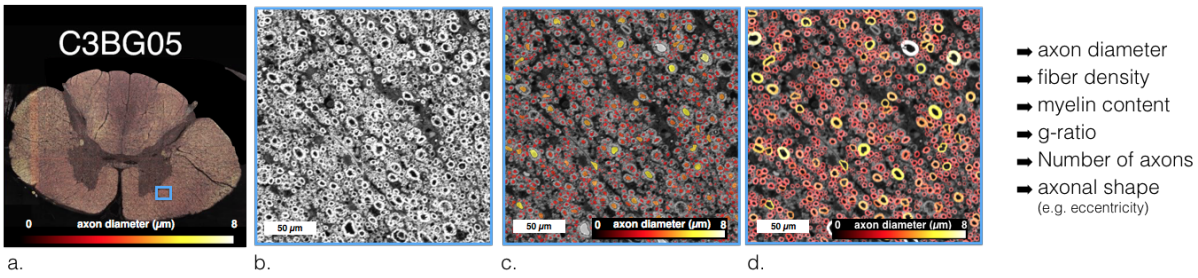

Figure 8.5: Extraction de l'information microstructurale. Suite à la détection de l'axone (c) et de la segmentation de la myéline (d) des images MEB (b), les coupes complètes (a) sont sous-échantillonnées en petits pixels de 100x100μm^2, où l'information morphologique est extraite (indiquée sur la droite).

Nous avons observé une densité axonale beaucoup plus grande dans le proprius fasciculus (boîtes bleues dans la **Figure 8.6**) que dans les régions graciles (boîtes vertes). De nombreux axones plus grands étaient présents dans le tractus corticospinale (boîtes rouges) que dans le gracile.

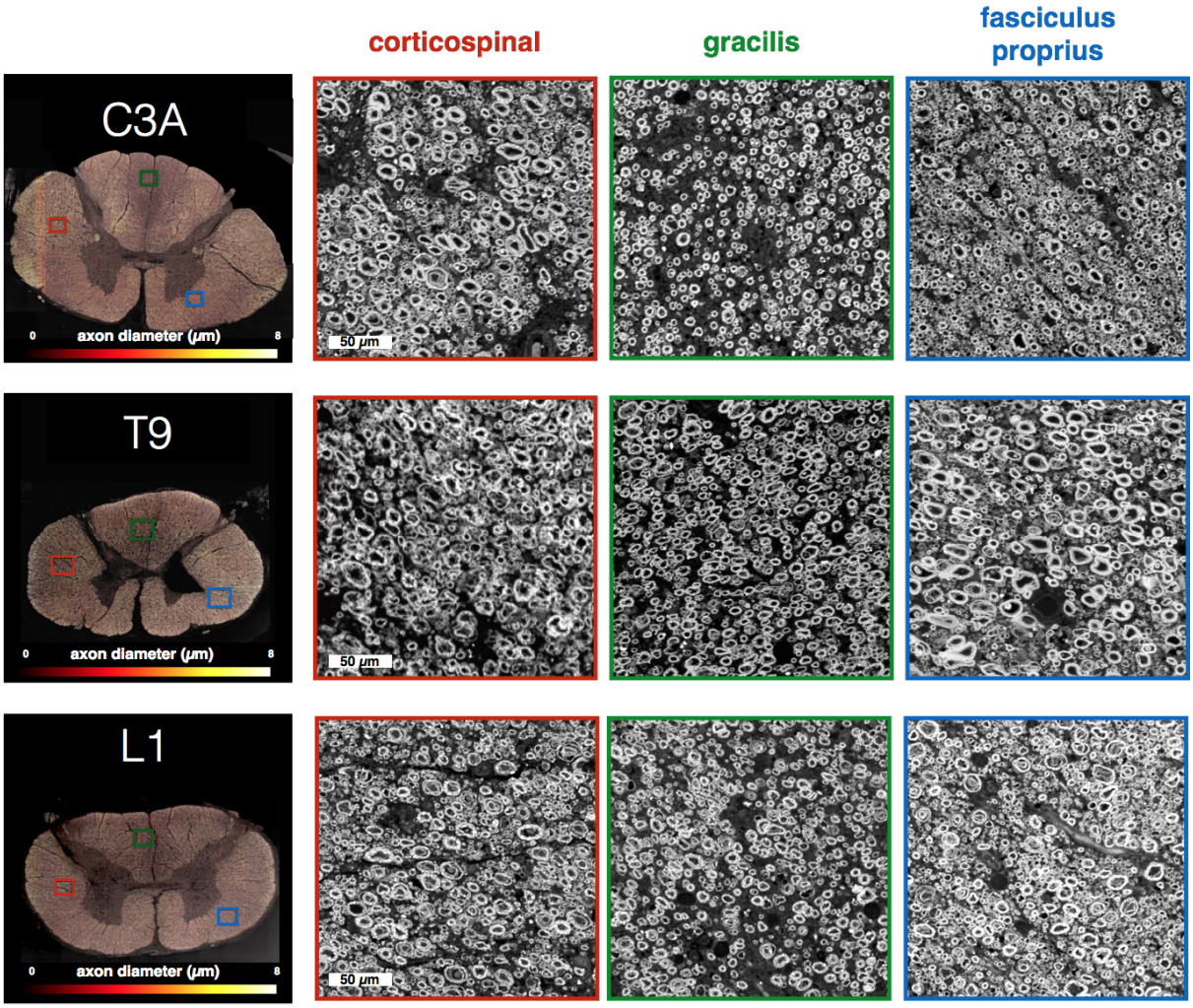

Figure 8.6: images MEB de la moelle épinière dans trois régions différentes (rouge, vert et bleu), à trois niveaux différents de la colonne vertébrale (C3, T9 et L1). Les axones myélinisés peuvent être facilement distingués sur les images MEB.

La distribution de la morphologie axonale a été analysé dans de petites régions (**Figure 8.7**). Plusieurs fonctions de probabilité ont été ajustées sur l'histogramme des diamètres en utilisant la fonction allfitdist[12]. La distribution de probabilité "valeur extrême généralisée" a été trouvée comme étant celle qui décrit le mieux l'histogramme avec trois paramètres (forme k, emplacement μ et mise à l'échelle σ). Avec seulement deux paramètres (emplacement μ et mise à l'échelle σ), la distribution lognormale était la meilleur. La fonction de densité de probabilité du diamètre de l'axone (pdf) a ensuite été pondérée par la surface de l'axone (π (d / 2) 2) afin d'obtenir la fonction de densité volumique de fibres (**Figure 8.7**, tracés du milieu). Dans toutes les régions étudiées (spinocérébellar, gracilis et faisceau cortico-spinal dans la tranche C5B), la densité volumique de fibres la plus élevée est atteinte à 2.2μm (à savoir cette population de fibres occupent un grand espace). Le g-ratio augmente en fonction du diamètre, avec un comportement similaire dans les différentes régions. Fait intéressant, la g-ratio révèle deux groupes de fibres : les petits axones à gaine mince de myéline et des axones de taille variable avec une large gamme d'épaisseur de la myéline. Les valeurs de rapport de g-ratio moyen étaient particulièrement faible (environ 0,5) et uniforme dans l'espace, ce qui indique une surestimation constante de l'épaisseur de la myéline (voir la discussion pour plus de détails).

[12]https://www.mathworks.com/matlabcentral/fileexchange/34943-fit-all-valid-parametric-probability-distributions-to-data?focused=5228686&tab=function

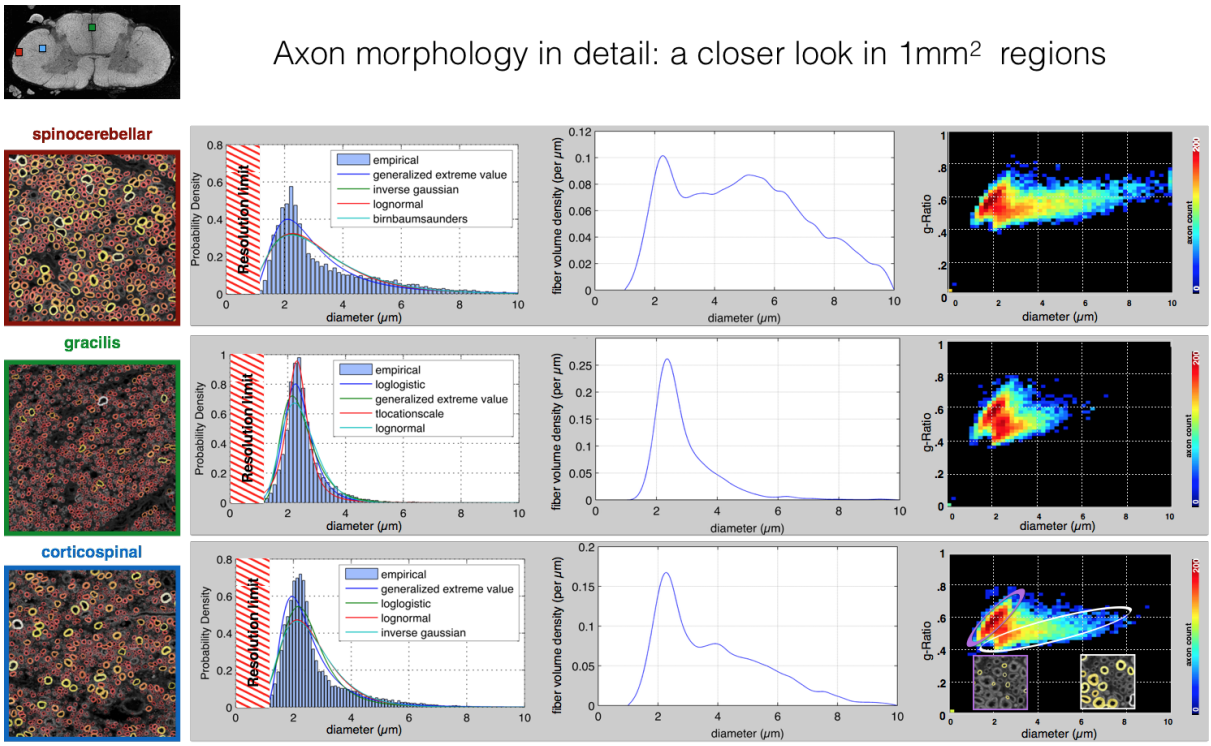

Figure 8.7: Morphologie axonale en fonction du diamètre axonal dans trois régions de 1mm2 (code couleur en rouge pour spinocérébellar, vert et bleu pour gracilis pour faisceau cortico-spinal) de l'échantillon C5B. Tracés de gauche. La distribution des diamètres axonal ajustées en utilisant de multiples fonctions de probabilité (limite de résolution a été estimée à environ 1 µm, voir **Figure 8.17**). Milieu. Tracés de la densité volumique de fibres en fonction du diamètre axonal. Tracés de droite. g-Ratio en fonction du diamètre axonal.

8.2.7 Cartes de la microstructure

Les cartes de microstructures (voir la **Figure 8.8**) ont été obtenus par sous-échantillonnage de l'histologie segmentée à une résolution de 100x100µm2. Les cartes obtenues sont cohérentes entre les différentes tranches et étaient symétriques. Bien que certaines corrélations ont pu être observées entre les différentes cartes (par exemple le diamètre et la densité des axones axonal corrélation dans la région dorsale), la corrélation a été limitée à quelques secteurs, ce qui suggère fortement que les informations sont complémentaires.

La mesure du diamètre de l'axone a été divisé en trois cartes de densité (1-4µm, 4-8µm et 8-12µm, et rapportée en nombre d'axones dans une fenêtre 100x100µm2). Cette subdivision révèle clairement la présence des grands axones proprioceptives du cunéatus (Niu et al. 2013) et les voies spinocerebellar. Les axones de plus de 8 um n'ont été détectés que dans la voie spinocerebellar.

Les cartes d'excentricité axonal représentent une combinaison de deux effets : coupe non parfaitement perpendiculaire par rapport à l'orientation de l'axone (et donc une informations sur la troisième dimension) et compression axonale. Les carte d'excentricités des axones étaient très symétriques, ce qui suggère que le contraste à l'intérieur de la moelle épinière est le plus souvent entraînée par de véritables caractéristiques microstructurales (à savoir pas de compression ou d'artefacts de coupe). Dans certaines voies (par exemple celles des colonnes dorsales), les axones sont plus près de la forme d'un cercle, ce qui indique que les axones sont bien droits et parallèle le long de la moelle épinière. Au contraire, les axones dans le tractus corticospinal sont plus obliques.

La matière grise présente une microstructure très différente de la matière blanche en termes de densité et d'orientation axonale. Parce que le logiciel de segmentation et la méthode de correction ont été entraînés sur les régions de la matière blanche, l'exactitude des mesures est dégradée. Cependant, une comparaison avec une segmentation manuelle révèle un échec non catastrophique de la segmentation dans la matière grise avec une sensibilité de 66%, une précision de 64%, et une erreur moyenne inférieure à 25% pour la plupart des

mesures, mais 70-80% surévaluation pour la carte de densité 4-8µm et la carte de densité de fibres. Voir un exemple de segmentation dans la matière grise dans la **Figure 8.15**.

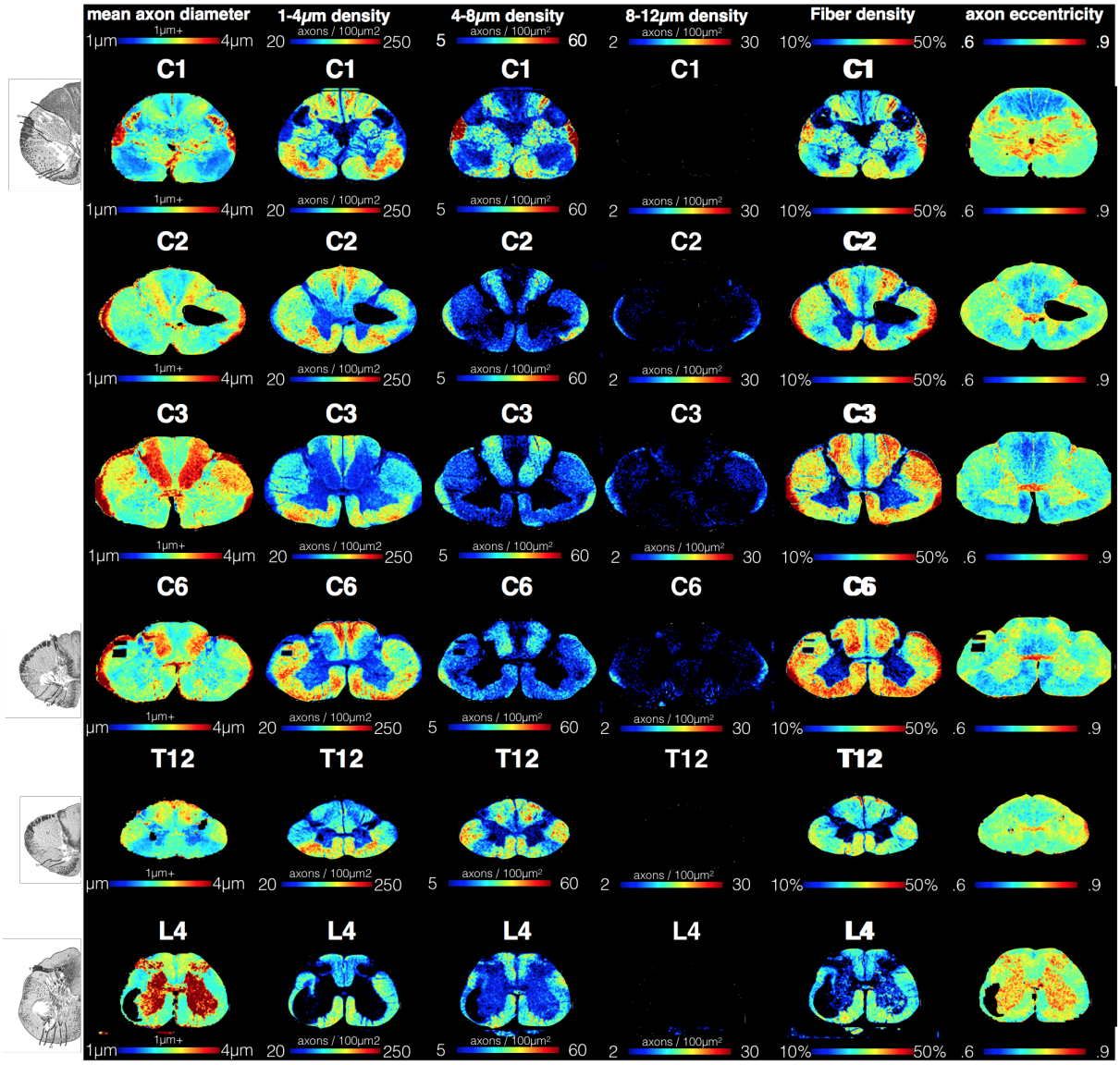

Figure 8.8: Les cartes de microstructure axonale. Le diamètre moyen des axones (première colonne), la densité de 1-4µm (nombre d'axones par pixel de 100µm2) (deuxième colonne), de 4-8µm (troisième colonne), de 8-12µm (quatrième colonne), la densité des fibres (axones plus myéline) (cinquième colonne), et l'excentricité moyenne axonale (sixième colonne) dans des pixels de 100x100µm à différents niveaux de la colonne vertébrale (lignes). Ces cartes peuvent être

comparés avec le dessin manuel de cytoarchitecture extrait de (Nieuwenhuys et al., 2007) (à gauche).

8.2.8 Analyse basée sur l'atlas

La morphologie axonale a ensuite été extraite par voies en utilisant un procédé de recalage d'atlas (**Figure 8.3**). Nous avons étudié la variation de la morphologie des axones par rapport aux voies de la moelle épinière, par rapport au niveau de la colonne vertébrale et par rapport au côté droite ou gauche.

8.2.8.1 Variation inter-voie spinale

Dans la section de la matière blanche du niveau C5B (**Figure 8.9**), le diamètre moyen des axones variait de 2,5 μm dans le tube gracile à 3.4 μm dans le tractus spinocerebellar. La densité axonale se situait entre 40% dans le tube gracile et 50% dans le tractus spino-olivaire.

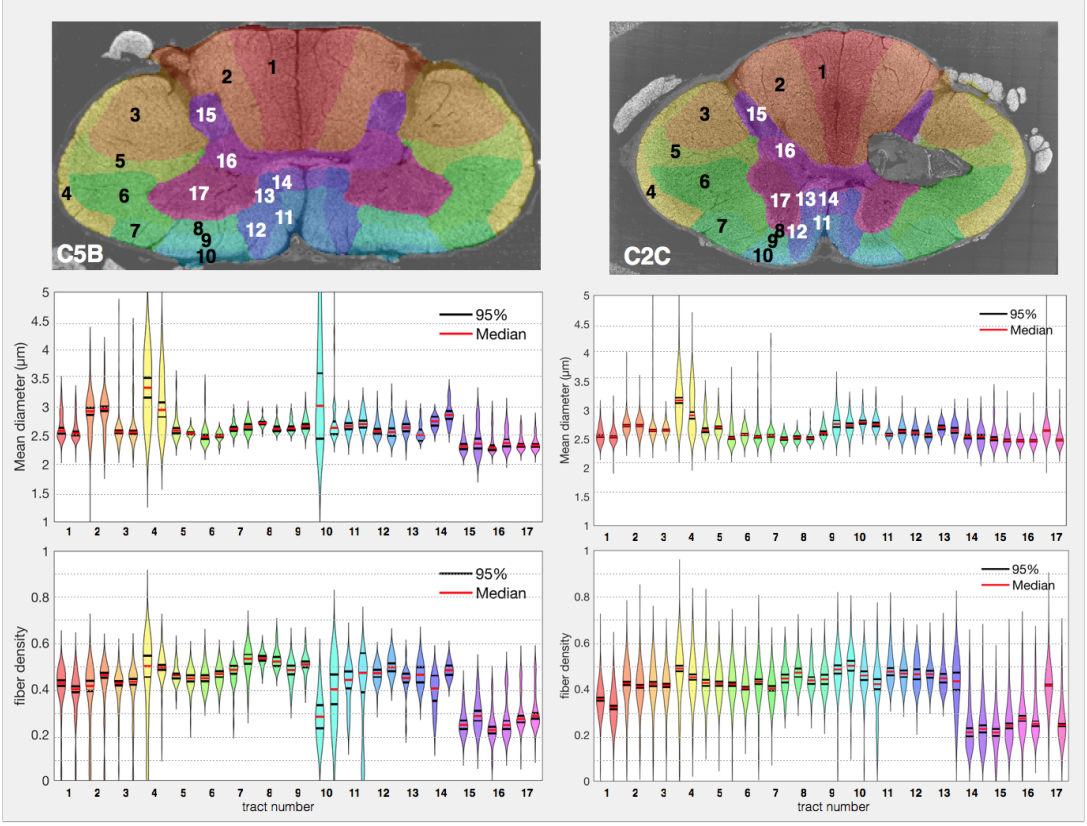

Figure 8.9: analyse basée sur l'atlas de la **Figure 8.3** (s'y référer pour le nom des voies spinales). L'atlas de la substance blanche de la moelle épinière, construit à partir de l'anatomie de Gray (Gray et al., 2005) et disponible dans la boîte à outils de la moelle épinière SCT (Lévy et al., 2015), a été recallé sur les coupes histologiques afin d'extraire la morphologie axonale dans les différentes voies spinales. La répartition des diamètres moyen des axones (rangée du milieu) et la fraction volumique des fibres (rangée du bas) au sein du même voie spinale (code couleur) a été tracée. Les médianes (lignes rouges), avec l'intervalle de confiance de 95% (lignes noires) montrent que chaque tube présente des microstructures caractéristiques. La plupart des régions présentes des microstructures assez homogènes comme le montrent leur distribution étroite.

Les valeurs extraites dans les plus grands tractus (numérotés de 1 à 6 sur la **Figure 8.9**) sont consistantes entre les différents niveaux cervicaux C2 à C7. Dans ces tranches, la matrice de corrélation de Pearson était de 0,86, 0,68, 0,72, en moyenne pour le diamètre de l'axone, la fraction volumique de la myéline et la densité des axones respectivement. Les autres sections de moelles sont moins consistantes, ce qui est dû soit à des modifications de microstructure, soit à des déformations de l'atlas plus grandes (la forme de la matière grise change rapidement à C1). La **Figure 8.10** illustre la cohérence entre les tranches.

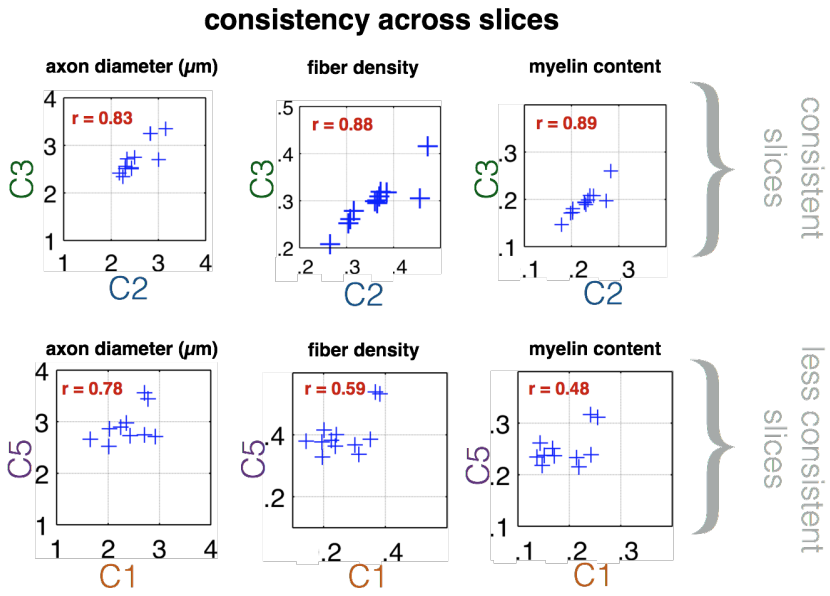

Figure 8.10: Cohérence de l'analyse basée sur un atlas à travers les différentes coupes de moelles (en utilisant les plus grands tractus, numérotés de 1 à 6 sur la **Figure 8.9**). La plupart des tranches du cervical sont fortement cohérents (r> 0,8) entre eux (par exemple C3 versus C2 à la ligne du haut). Cependant, C1 et les niveaux thoraciques étaient moins consistants (par exemple C5 versus C1 à la rangée du bas), notamment en raison de la déformation de l'atlas particulièrement forte.

8.2.8.2 Effet du niveau de la colonne vertébrale

La position de la tranche a été définie dans les coordonnées du modèle de la moelle épinière. Les mesures morphologiques ont été moyennées dans la matière blanche et tracés en fonction de la position de la tranche (voir **Figure 8.11**). Les valeurs étaient consistantes entre les tranches et une spline de lissage a été ajustée pour mettre en évidence les tendances. Le nombre d'axones augmente de façon monotone à mesure que nous montons rostralement jusqu'à environ C3, ce qui correspond à l'arrivée de nouveaux axones afférents à chaque niveau de la colonne vertébrale. Cette augmentation du nombre de fibres (**Figure 8.11**, e.) est en corrélation avec l'élargissement (a.) de la moelle épinière ($r = 0,9$, $p = 10\text{-}7$), plus qu'il est en corrélation avec la densité des fibres (b.). ($r = 0,5$, $p = 10\text{-}2$). La surface en coupe transversale de la moelle épinière (1) est également corrélé de manière significative avec le diamètre moyen (c.) Des fibres ($r = 0,7$, $p = 10\text{-}4$). Le contenu de la myéline (d.) Le long de la moelle épinière a été relativement constant, avec une différence de seulement 3% entre la partie lombaire (moyenne de 20%) et la parties cervicale (23%). Le diamètre des axones, la densité des fibres et la teneur en myéline présentent des valeurs maximales entre C4 et T7. T4 est une valeur aberrante en raison de la mauvaise mise au point lors de l'acquisition MEB (voir la discussion).

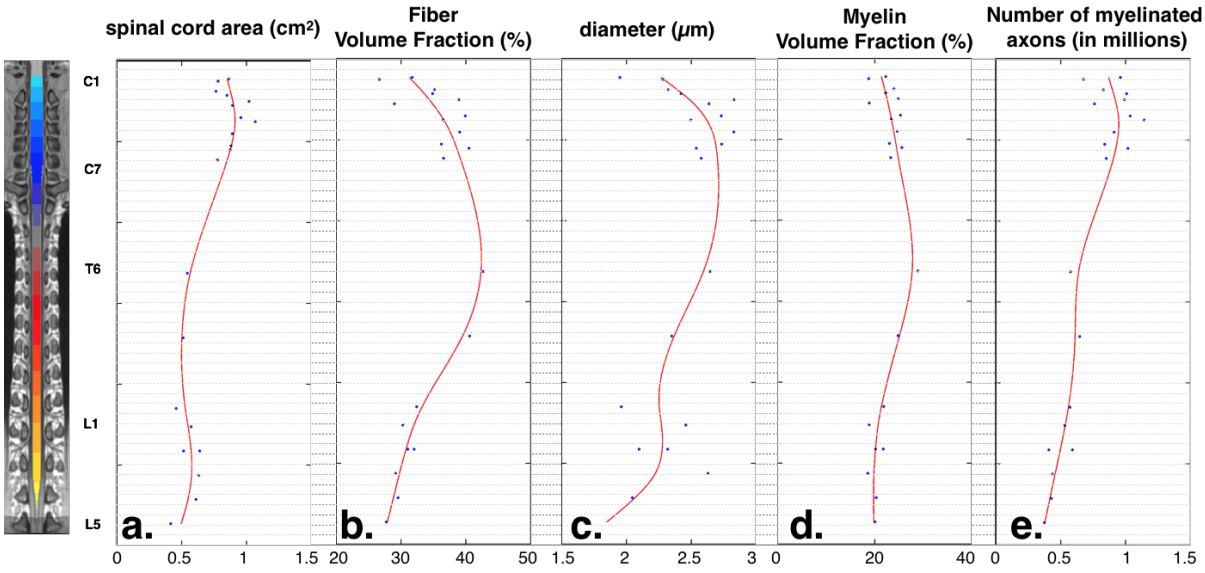

Figure 8.11: Evolution de la morphologie axonale le long de la moelle épinière. Les propriétés morphologiques ont été moyennées dans la matière blanche pour chaque échantillon (points bleus), et une fonction de lissage (ligne rouge) a été ajustée pour la visualisation des tendances.

8.2.8.3 Effet de latéralité

La microstructure de la moelle épinière a été jugée remarquablement symétrique (voir **Figure 8.12**). Nous avons trouvé une différence moyenne entre les voies gauche et droite de la moelle épinière de 0,01 µm pour le diamètre axonale, 1% pour la densité axonale et 0,4% pour le contenu de la myéline. Par conséquent, le fait d'être droitier ou gaucher a très peu d'impact sur la morphologie axonale.

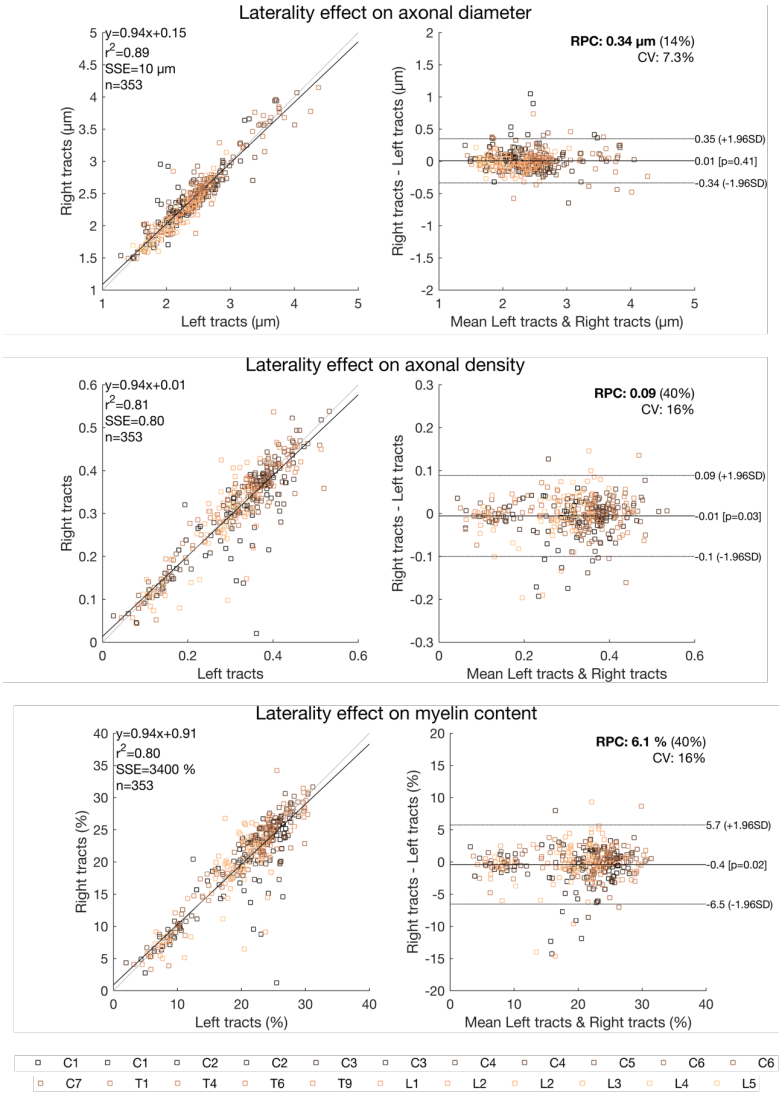

Figure 8.12: Comparaison de la morphologie axonale dans la partie gauche et droite. Les différences de morphologie axonale entre voies gauche et droite sont très limitées : pour le diamètre axonale 0,01 um, 1% pour la densité axonale, et 0,4% pour le contenu de la myéline.

8.3.1 Modèle de microstructure

Les cartes de microstructure ont été enregistrées dans le modèle de la moelle épinière afin de générer le premier modèle de microstructure de la moelle épinière cervicale humaine (voir **Figure 8.13**). La combinaison du recalage et de l'interpolation non élastique a conduit à des transitions relativement douces entre les tranches adjacentes. Bien que visuellement pas parfait, le recalage a réussi à déplacer la fissure médiane des différentes tranches vers le centre. Le modèle couvre en C1 à C8.

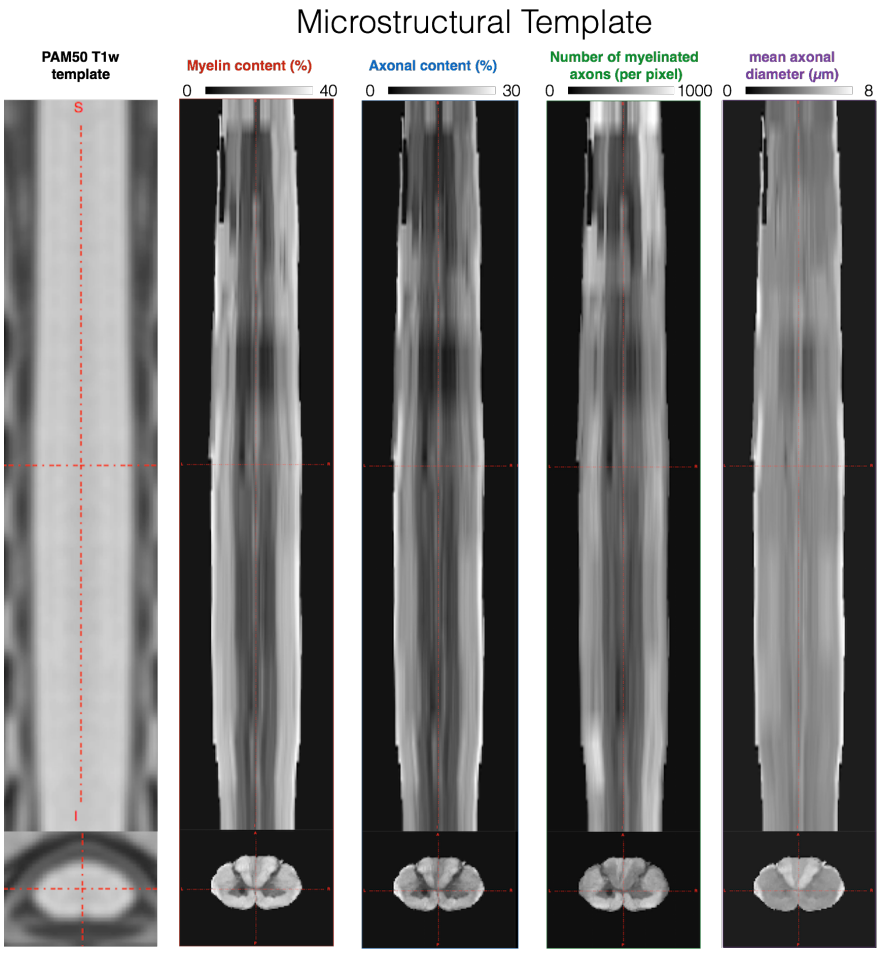

Figure 8.13: Modèle de la microstructure de la moelle épinière. Coronale (en haut) et vue axiale (en bas) du modèle généré. Les coupes histologiques ont été recalées au niveau des vertèbres correspondantes, puis interpolées entre des coupes à l'aide de déformations non-linéaires. Le modèle résultant présente des transitions en douceur entre les tranches.

8.4 Discussion

Dans ce travail, nous avons combiné l'histologie entier de coupe de moelle à haute résolution et un logiciel de segmentation automatique pour produire les premières cartes microstructurales de la moelle épinière humaine. Alors que la moelle épinière est très symétrique, les différentes voies spinales présentent des caractéristiques distinctes de microstructures.

8.4.1 Interprétation

Pourquoi est-ce que nous observons une grande variation du diamètre de l'axone ?

Une question qui se pose immédiatement est de savoir pourquoi on observe de telles variations de microstructure entre les différentes régions de la moelle épinière ? Par exemple, les diamètres des axones ont été observés à varier entre 0,1 et 10 um (Perge et al., 2012). En utilisant des modèles bioélectriques et des montages expérimentaux, il peut être démontré que, dans les axones myélinisés, la vitesse de propagation et la fréquence de décharge est proportionnelle au diamètre de l'axone (d) (Plonsey et Barr, 2007); tandis que la consommation d'énergie et le volume de la fibre est proportionnelle à d^2 (Perge et al., 2012). La présence de grands axones dans le système nerveux central se fait au détriment de l'efficacité énergétique et de l'espace, et doit être compensé par des avantages importants. La nécessité d'une plus rapide propagation dans le système nerveux périphérique peut être apprécié en termes de l'avantage acquis par des réflexes plus rapides (par exemple axone géant de calmar), ou pour assurer la synchronisation des impulsions nerveuses qui proviennent d'organes situés à différentes distances du cerveau. Cependant, la nécessité d'une propagation plus rapide ne peut pas expliquer en général la présence de grandes axones myélinisés dans le système nerveux central (SNC) pour plusieurs raisons: (i) le diamètre des axones n'est pas proportionnel avec la taille des animaux (Lassek et Rasmussen, 1940, Plus et al. , 2010), (ii) il n'existe aucune corrélation entre la longueur et le diamètre axonal dans le nerf optique (Perge et al., 2009), (iii) le diamètre de l'axone dans la moelle épinière augmente rostralement (voir **Figure 8.11**). Par conséquent, la seconde hypothèse, qui considère la fréquence des impulsions comme la principale raison de la

présence d'axones de plus grande taille dans le système nerveux central, semble plus probable (Perge et al., 2012). Des études de électromyographie des axones reliés à la moelle épinière montrent une variété de fréquences et de comportements des impulsions nerveuses (soit en brefs éclats ou en feu continu) (Evarts, 1965;. Rossignol et al, 2002), et donc des informations très diverses. Les informations les plus complexes qui nécessite une bande passante plus élevée sont transmise « non filtrée » à travers les plus grands axones. A l'inverse, les informations simples sont transmises par les petits axones pour plus d'efficacité. Cette relation entre le calibre et la complexité de l'information est magnifiquement illustrée par la comparaison des axones proprioceptives et mécanorécepteurs de la colonne dorsale (Niu et al., 2013). En effet, ces axones sensoriels afférents possèdent un calibre différent, ce qui crée le contraste entre le gracile et le cunéatus (voir les cartes de diamètre axone de la **Figure 8.8**): les axones mécanoréceptifs qui transmettent de simple mais nombreuses informations au cerveau ont une surface en coupe transversale inférieure à 5µm2 (90ème percentile); tandis que les axones proprioceptives qui intègrent des informations globales et complexes sont plus grandes que 5µm2 (5e percentile). Sur la base de cette hypothèse, les cartes de diamètres présentées dans ce manuscrit révèlent une organisation fonctionnelle des axones.

8.4.2 Limitations de la méthode

La méthode proposée dans le présent document fait face à de nombreux défis dont les lecteurs doivent être conscients pour éviter une sur-interprétation des résultats. Les sections suivantes sont donc consacrées aux limites de la méthode.

8.4.2.1 Préparation du tissue

Le premier défi dans toutes les études histologiques sur les tissus post-mortem est la préservation du tissu et notamment l'intégrité de la myéline. Dans ce travail, une procédure de fixation relativement standard a été utilisé (post-fixation par immersion en utilisant un mélange de glutaraldéhyde et le paraformaldehyde). Divers concentration de glutaraldéhyde (0,5-4%) peuvent être trouvées dans la littérature (Biedenbach et al, 1986;. Firmin et al, 2014;. Ralston et al., 1987). En raison de l'incertitude sur l'impact de cette

concentration sur la morphologie axonale, nous avons décidé d'utiliser trois concentrations (0, 0,5 et 2%). Aucune différence n'a pu être trouvée notamment entre les trois fixateurs à la résolution de l'imagerie, comme le montre la **Figure 8.11**.

En ce qui concerne la procédure de coloration, quelques tranches présentent quelques points avec une mauvaise coloration de l'osmium (voir la **Figure 8.4**, les flèches blanches). En effet, l'osmium pénètre par seulement quelques centaines de microns (Hua et al., 2015) ce qui rend difficile d'assurer une bonne coloration uniforme sur ces grands échantillons. Ces taches sont le résultat de la présence, dans certains cas, des bulles d'air dans la résine époxy et par le fait que la surface n'a pas été parfaitement aplatie. Afin d'éviter le polissage aller plus loin que quelques centaines de microns, la surface a été exposée en coupant à différents angles. Une autre stratégie serait d'améliorer la pénétration de l'osmium en utilisant des protocoles récemment publiés (Hua et al, 2015;. Mikula et Denk, 2015).

8.4.2.2 Limitation de l'imagerie

8.4.2.2.1 Imagerie 2D

Dans ce travail, des images 2D de la moelle épinière ont été obtenus, et nous avons supposé les axones relativement droites et parallèles à la moelle épinière. Les images 2D ont été interpolées afin de produire le modèle 3D. Bien que quelques informations sur la troisième dimension puissent être obtenue en se basant sur la forme des axones en supposant que les formes elliptiques obliques correspondent à des axones, la compression axonale est un facteur de confusion qui ne peuvent pas être séparés. La carte excentricité des axones étaient très symétriques, ce qui suggère que le contraste à l'intérieur de la moelle épinière révèle des informations microstructurale (par opposition à la compression, au cisaillement ou aux artefacts de découpage qui se traduiraient par des contrastes locaux ou asymétriques). Cependant, la compression axonale ne peut être négligée.

En ce qui concerne la surestimation du diamètre de l'axone pour les axones obliques, ce biais peut être formulé (en supposant que les axones sont des cylindres parfaits) comme suit. Tout d'abord, l'excentricité e de l'ellipse obtenue par la coupe de l'axone est une

fonction de l'angle θ de l'axone (Kenna, 1959), et en fonction du demi-axe majeur (a) et mineur (b) de l'ellipse :

$$e = sin(\theta) = \sqrt{1 - \frac{b^2}{a^2}}$$

D'autre part, le diamètre équivalent d (métrique rapporté dans ce manuscrit) d'une ellipse est :

$$d = 2\sqrt{A_{axon}/\pi} = 2\sqrt{ab}$$

Enfin, le diamètre équivalent d 'un axone oblique surestime le véritable diamètre de l'axone (= 2b) par : $error(\%) = 100.\frac{d-2b}{2b} = \frac{1}{(1-sin^2(\theta))^{1/4}} - 1$. On peut observer sur la **Figure 8.14** que cette surestimation est supérieure à 50% pour les axones ayant un angle de 60 ° ou plus avec l'axe de la moelle. Notez que AxonSeg filtre les axones fortement obliques (> 73 ° en supposant que l'axone est parfaitement cylindrique) en utilisant le rapport du petit sur le grand axe de l'ellipse.

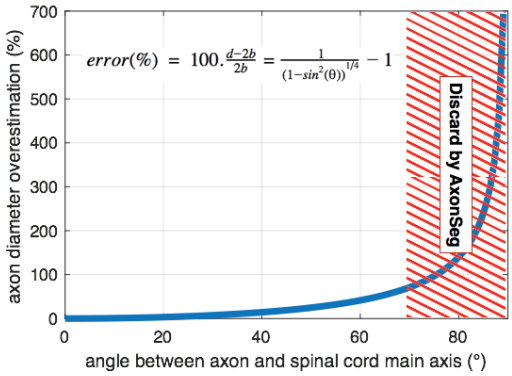

Figure 8.14: Axon equivalent diameter overestimates the true axon diameter for axons that are not running along the spinal cord main axis. Oblique axons are filtered by AxonSeg based on the minor over major axis ratio of the axon to prevent dramatic failure.

8.4.2.2.2 Coloration

La méthode présentée se limitait à la coloration par osmium de la myéline. Les axones non myélinisés et les cellules gliales ne pouvaient donc pas être distingués dans nos images. Ces

structures peuvent être vues à basse tension (Mikula et Denk, 2015), mais ceci aurait donné lieu à un signal plus faible rapport de bruit et des logiciels de segmentation plus avancés devraient être mis au point.

8.4.2.3 Matière grise

Bien que AxonSeg a été entraîné et conçu pour les régions de la matière blanche, on ne constate pas une défaillance catastrophique par rapport à la segmentation manuelle (voir **Figure 8.15**). Dans la matière grise, nous avons trouvé une sensibilité de 66%, une précision de 64%, et moins de 30% d'erreur pour la plupart des métriques (diamètre axonale, l'excentricité, le nombre d'axones), mais aussi une surévaluation de 70-80% des grands (4-8µm) axones et de la densité des fibres. Notez que AxonSeg est aveugle aux fibres perpendiculaires à la moelle, mais ces fibres sont qualitativement très peu nombreuses.

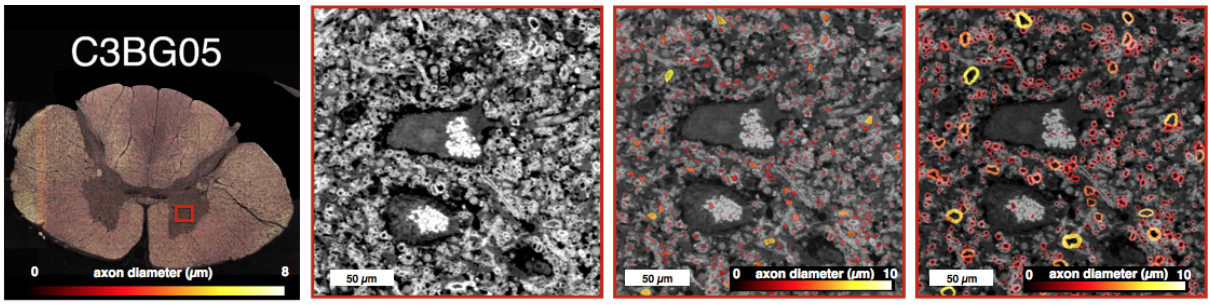

Figure 8.15: la performance AxonSeg dans la matière grise. Similaire à la Figure 8.5, mais dans une région de la matière grise.

8.5 Conclusion

Nous présentons le premier modèle microstructural de la moelle épinière humaine basée sur l'histologie, recalée sur le modèle IRM de la moelle épinière PAM50. Pour générer ce modèle, nous avons développé une méthode qui comprend la microscopie électronique à large champ de vue, la segmentation automatique des axones et le recalage des coupes histologiques. Le modèle peut être utilisé pour valider les modèles biophysiques ou des modalités d'imagerie qui décrivent la microstructure.

8.6 Remerciements

Nous tenons à remercier Micheline Fortin et les autres employés du département d'histologie de l'Institut de recherche en immunologie et en cancérologie (Université de Montréal, QC, Canada), Diane Gingras du service de microscopie électronique de l'Université de Montréal, ainsi que Irène Londono, Monica Nelea et Anik Chevrier. Leur aide et leurs conseils pour la préparation des échantillons ont grandement contribué au succès de ce travail. Enfin, nous tenons à remercier le membre du Centre de caractérisation microscopique des matériaux (CM) ², notamment Nicole MacDonald, Philippe Plamondon et Jean-Philippe Masse, pour leurs rétroactions dans le polissage et la numérisation des moelles épinières en utilisant la microscopie électronique.

8.7 Matériel supplémentaire

8.7.1 S1 : Correction des valeurs aberrantes de l'algorithme de collage

Bien que puissant, l'algorithme de collage a échoué dans quelques cas, notamment pour les images contenant un fond sombre. Ce problème a été corrigé par la modélisation du déplacement de phase en tant que deux décalages constants :

$$\begin{cases} X_{staqe} = a \times row + b \times col = [row \quad col] \begin{bmatrix} a \\ b \end{bmatrix} \\ Y_{staqe} = a \times row + b \times col = [row \quad col] \begin{bmatrix} c \\ d \end{bmatrix} \end{cases}$$

avec *row=[1 2 ... Nrow]*^{T} et *col=[1 2 ... Ncol]*^{T} l'indice de mosaïques; Xstage et Ystage les coordonnées spatiales (en pixels) du coin supérieur gauche de chaque image; a, b, c et d des constantes inconnues.

Sur la base des valeurs de Xstage et Ystage fournies par l'algorithme de collage, a, b, c et d ont été estimées (solution de pseudo-inverse). Les valeurs aberrantes ont été définies comme les coordonnées qui diffèrent de plus de 3 fois l'écart médian absolu. **Figure 8.16** illustre l'algorithme de détection d'observations aberrantes.

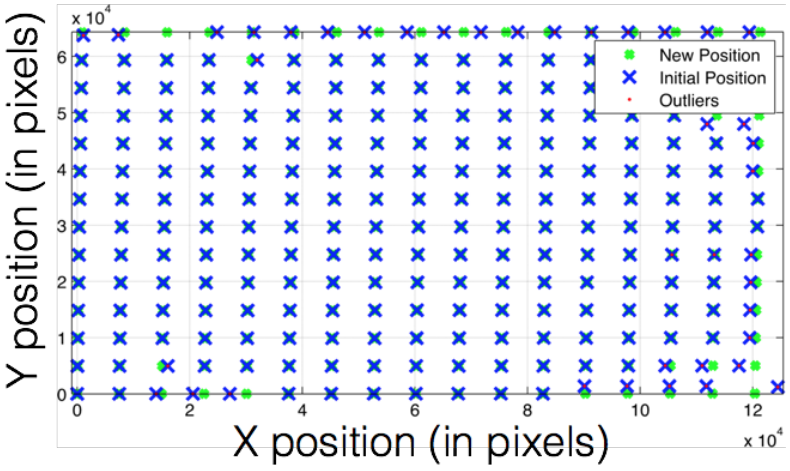

Figure 8.16: Correction d'outliers de l'algorithme de collage de mosaïques. Mosaïque poste (des croix bleues), estimée à l'aide de l'algorithme de couture, a été trouvé pour être disposé dans une grille oblique (polarisation constante dans X et

Y). Sur la base de cette hypothèse, les valeurs aberrantes peuvent être détectés (points rouges) et corrigés (croix verte).

8.7.2 S2 : Correction de AxonSeg

Deux méthodes ont été utilisées afin de corriger le biais des mesures morphométriques. La première méthode a été utilisée pour corriger la densité des axones et le contenu de la myéline par un ajustement linéaire. La deuxième méthode a été utilisée pour corriger le diamètre de l'axone et le numéro axone en utilisant une correction d'histogramme. La correction a été effectuée en faisant la formation de a4 sur une région segmentée manuellement (région 1) et la compare à l'image AxonSeg au même endroit. Les statistiques corrigées obtenues ont été montées, puis cet ajustement a été ensuite appliqué à une seconde région sur l'image AxonSeg (région 2). Cela a été ensuite validé par le Groundtruth de cette région pour faire en sorte que les résultats étaient corrects. Ce champ de la région de vue était 1x0.5mm2 et contenait 5133 axones. Le pipeline utilisé pour chaque procédé peut être vu dans la figure ci-dessous S2.

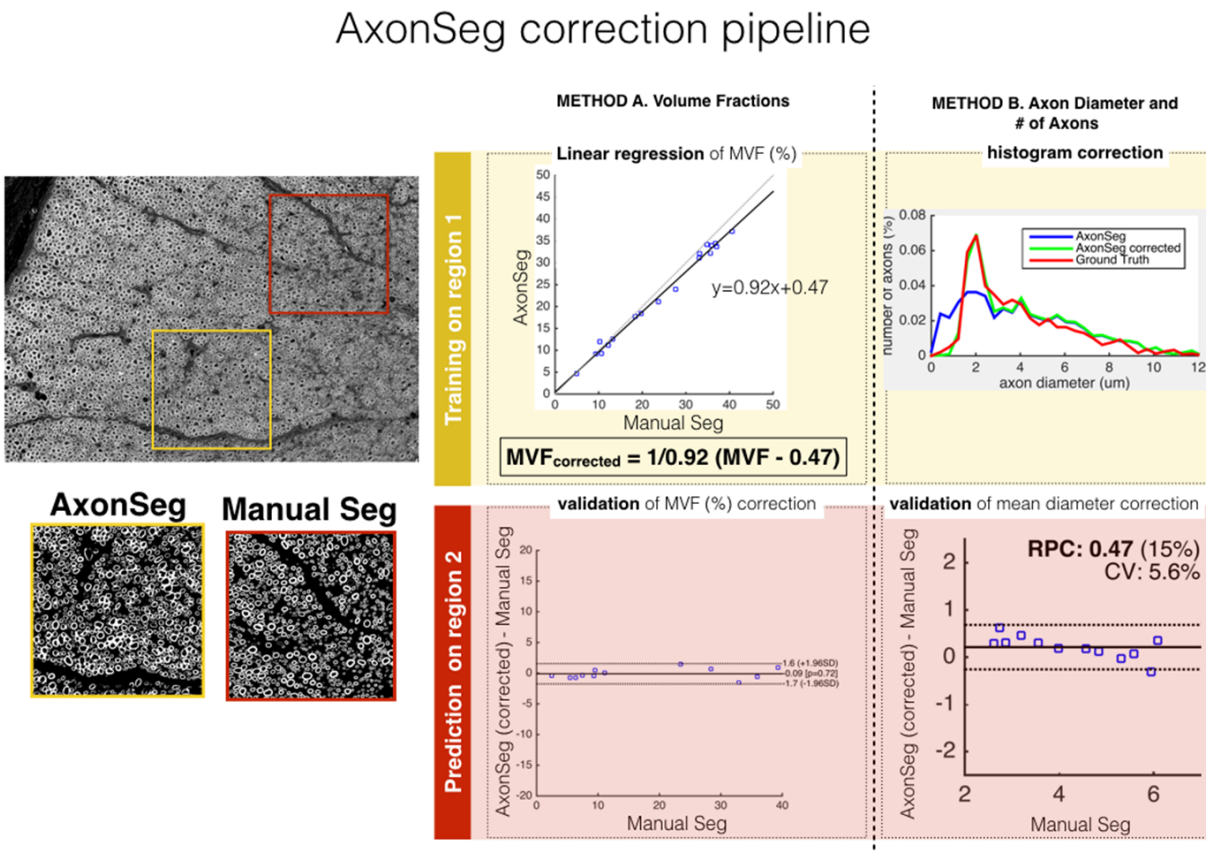

Figure 8.17: Pipeline de correction AxonSeg en utilisant deux méthodes distinctes pour différentes mesures.

Comme il est mentionné dans la section de traitement d'image, la limite de résolution a été jugée comme le logiciel de 1 pm AxonSeg serait positif pour la plupart des segments faux dans cette gamme de diamètre. En outre, de faire cette correction statistique, il a été observé (comme le montre la figure 7) du Groundtruth qu'il y avait beaucoup axones plus petits que lµm qui ne sont pas segmentée (faux négatifs).

La **Figure 8.18** ci-dessous montre une comparaison des statistiques corrigées avec le Groundtruth en utilisant des parcelles-Altman fade. Cela a été calculé en utilisant un intervalle de confiance de 95% (1,96 * ecart-type).

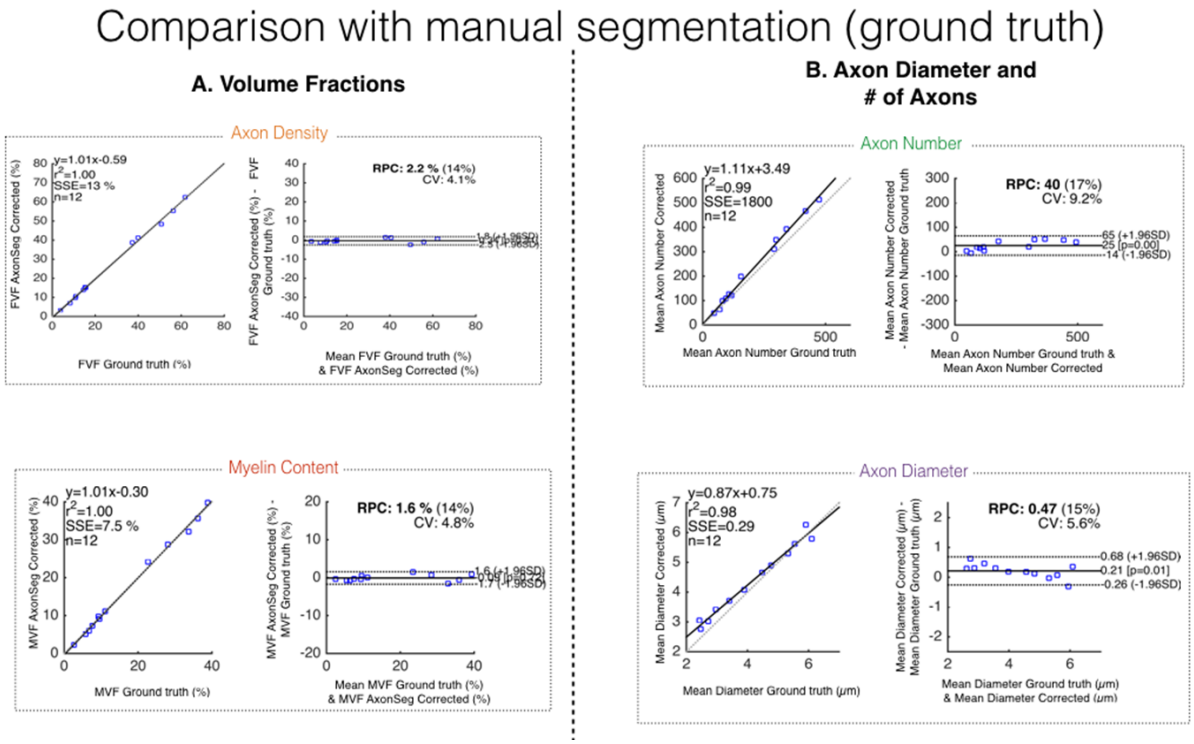

Figure 8.18: Les parcelles Bland-Altman comparant la segmentation AxonSeg (après correction) avec la segmentation manuelle. La première courbe représente la corrélation linéaire tandis que la seconde courbe représente l'accord entre la Groundtruth et la segmentation. Le RPC est le coefficient de reproductibilité avec le pourcentage de la valeur à côté. Le CV est le coefficient de variation, qui est essentiellement l'écart-type des valeurs moyennes pour cent en forme.

CHAPITRE 9 TRANSLATION CLINIQUE

9.1 600 mT/m par rapport au protocole optimisé 80 mT/m

La méthode AxCaliber (Assaf et al., 2008) se caractérise par l'utilisation d'une seule direction d'encodage de diffusion (perpendiculaire aux faisceaux de fibres neuronales) mais avec un échantillonnage fin de la force du gradient |G| et du temps de diffusion Δ. Nous avons montré que cette méthode peut être appliquée *in vivo* dans la moelle épinière humaine à 300mT/m (Duval et al., 2015). Malheureusement, les systèmes cliniques les plus puissants n'offrent que 60-80 mT / m dans chaque direction (c'est-à-dire 85-113 mT / m si l'on utilise deux gradients), et pour la plupart des techniques d'IRM de diffusion qui étudies la microstructure, cela a pour conséquence d'obtenir des mesures moins précises et moins exactes (Ferizi et al., 2015; Huang et al., 2015). Dans ce travail nous avons donc voulu (i) trouver le meilleur protocole AxCaliber à 80mT / m et (ii) quantifier le biais dans la métrique estimée.

9.1.1 Méthodes

L'optimisation du protocole utilise l'équation analytique du modèle CHARMED (Assaf et al., 2005). La direction d'encodage étant fixe (perpendiculaire au fibres nerveuses), les trois paramètres d'acquisition à optimiser sont δ, Δ et Gmax. Le processus d'optimisation tentera de maximiser la robustesse au bruit afin d'obtenir des valeurs plus précises. L'idée est de maximiser la dérivée du signal pondéré par diffusion en fonction des paramètres microstructuraux que nous essayons de mesurer (par exemple le diamètre axonal), de sorte qu'un petit changement de signal (par exemple dû au bruit thermique) ait peu d'impact sur ces paramètres, et en retour une petite différence de microstructure conduit à un changement de signal significatif.

9.1.1.1 Optimisation du protocole

Le protocole a été optimisé suivant la méthode proposé par (Alexander, 2008) : l'algorithme d'optimisation numérique SOMA (en mode « adaptatif tous-vers-un », population initiale

de 100 protocoles, 300 volumes par protocole, 1000 itérations) (Zelinka, 2004) a été utilisé. La fonction objective est la borne inférieure de Cramer-Rao (CRLB) du modèle. L'optimisation assume un tissue particulier (i.e. avec une combinaison particulière de paramètres microstructuraux et physiques) : S0 = 1, T2 = 70ms, *fr* = 0.5, d = 5µm, Dh = 0.2µm^2/ms et les contraintes d'acquisition suivantes : Gmax = 80 mT/m, $\delta > 3$ms, $\Delta + \delta + 17\text{ms} = TE < 80$ms et $\Delta > \delta + 7$ms. Le bruit est considéré Gaussian, avec un rapport signal sur bruit (SNR) à b=0 et TE=70ms de 50.

Un algorithme de kmeans a ensuite été appliqué sur le protocole optimal pour extraire seulement 10 combinaisons de Δ et δ. Cette optimisation SOMA a produit un protocole d'IRM de diffusion de 300 volumes.

9.1.1.2 Expérimentation IRM

Une moelle épinière de chat, perfusée et post-fixée avec 4% de PFA a été scannée sur un scanner IRM 7T Agilent, situé à l'Institut de cardiologie de Montréal, avec une séquence spin-écho EPI. Les gradients de diffusion ont été appliqués dans la direction de lecture, celle-ci étant perpendiculaire à la moelle épinière. Les paramètres d'acquisition suivant ont été utilisés : matrice 64x64x3, TE minimisée, résolution 0,16x0,16x2mm, SNR = 35 dans la substance blanche à TE = 55ms. L'espace (Δ, δ, G) a été échantillonné de trois manières différentes (voir Figure 9.2.a): (1) Gmax = 600mT / m, 204 volumes, Δ = 20,35,40ms, δ = 8ms; (2) Gmax = 80mT / m, 1326 volumes, 25 combinaisons de Δ / δ échantillonnées sur une grille; (3) Solution de l'optimisation SOMA (Gmax = 80mT / m, 300 volumes).

9.1.1.3 Ajustement de courbe

Les données ont été analysées avec qMRLab en utilisant (i) le modèle complet ou (ii) en négligeant la diffusion radiale du compartiment restreint (i.e. $S_{restricted}$ = 1, ou d=0µm) (ce qui est valable pour de petites valeurs b).

9.1.1.4 Statistiques

Simulation. Une analyse de la précision des mesures par approche Monte Carlo a été réalisée pour valider l'optimisation du protocole et étudier la précision de la métrique *fr* pour les

trois protocoles à différents SNR (5,10,20,30,40 à TE = 70ms). En utilisant l'équation du modèle, 200 jeux de données bruités ont été simulés puis analysées pour chaque configuration de SNR et de protocole.

Expériences IRM. Le protocole acquis avec Gmax = 600 mT/m a été utilisé comme vérité terrain. Le coefficient de corrélation et la régression linéaire avec cette vérité terrain ont été calculés pour la métrique *fr* obtenue en utilisant le (i) protocole optimisé, (ii) le protocole de 1326 volumes au complet et (iii) 10 sous-ensembles aléatoires (300 volumes sur 1326).

9.1.2 Résultats

9.1.2.1 Simulation

La Figure 9.1a montre la convergence du CRLB en utilisant l'optimisation SOMA. L'algorithme SOMA converge correctement vers un minimum de la CRLB. La figure 9.1b valide la conception du protocole optimisé en montrant la meilleure robustesse au bruit de la métrique *fr* en termes de précision et d'exactitude. Ainsi à SNR = 40, comparé à une configuration aléatoire de même durée (300 volumes), l'écart type de *fr* passe de 0.12 à 0.05, et la déviation de 0.06 à 0.02. Malgré l'optimisation, le protocole à haut gradient (Gmax = 600 mT/m) permet toujours d'avoir la meilleure performance avec un écart type de 0.007 et une déviation de - 3.10^{-5}.

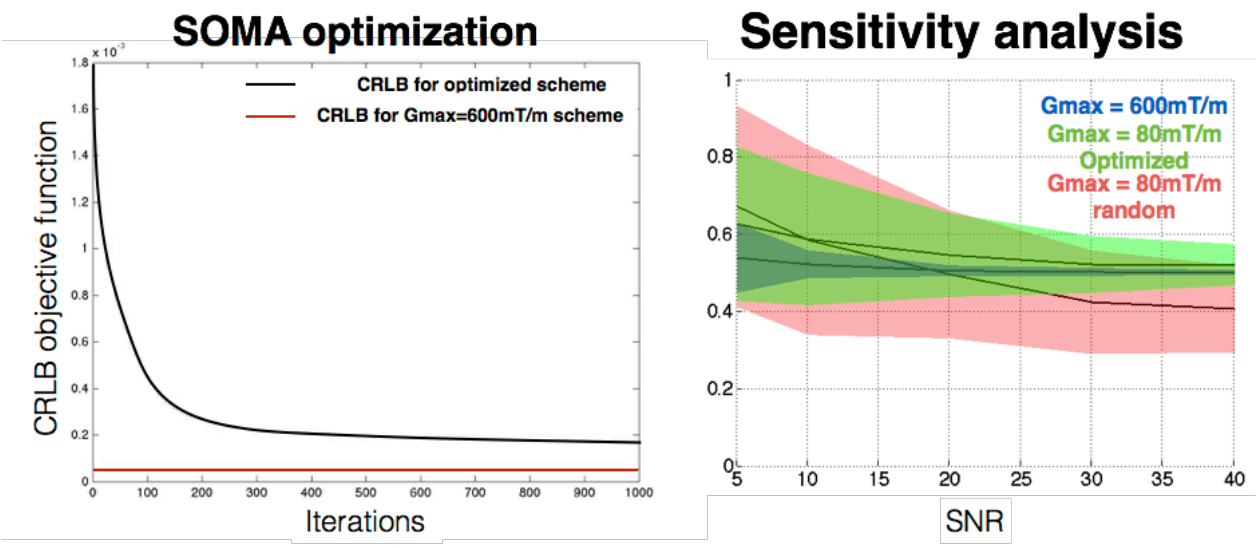

Figure 9.1: Résultats de l'optimisation SOMA. Gauche. Convergence du CRLB pour le protocole optimisé. Droite. Écart-type et erreur sur 200 simulations pour différents SNR.

9.1.2.2 Expériences IRM

La Figure 9.2b montre, qualitativement, que le modèle peut être correctement ajusté pour tous les jeux de données. La figure 9.2c montre les cartes des métriques *fr* et d (axon diameter index) pour les trois protocoles différents. Les cartes de 600 mT/m présentent un bon rapport de contraste au bruit (CNR) suggérant une bonne précision des mesures. Comme prévu, à un plus faible gradient, le diamètre des axones n'a pas pu être ajusté avec précision. Fixer $S_{restricted}$ = 1 (Fig 2d) améliore qualitativement la cohérence de la métrique *fr* dans les trois protocoles. De bons coefficients de corrélation (r^2 = 0,76) et de faible écart (-0,026) (voir la figure 9.2c) ont été trouvés en comparant la métrique *fr* optimisée à la vérité de terrain (protocole 600 mT/m). Les 10 sous-ensembles de 300 volumes aléatoires ont tous présenté une corrélation plus faible (r^2 <0,7).

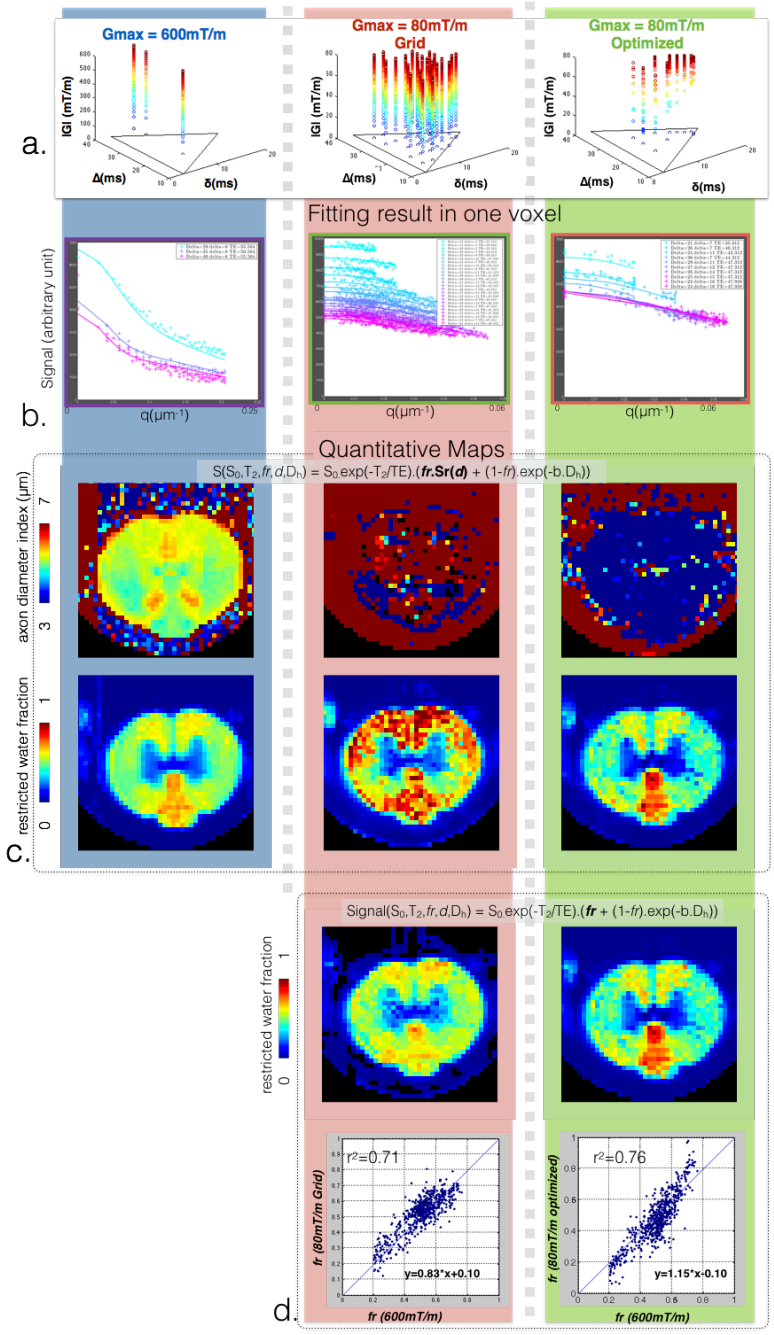

Figure 9.2: Comparaison expérimentale des mesures AxCaliber en utilisant des protocoles acquis à 600mT / m (colonne bleue), 80mT / m avec échantillonnage en grille de l'espace (| G |, Δ, δ) (colonne rouge) et 80mT / m optimisé (colonne verte). a. Visualisation des trois protocoles expérimentaux. b. exemple de fit dans un pixel de la matière blanche. c et d. cartes quantitatives avec (c) ou sans (d) estimation du diamètre axonal.

9.1.3 Conclusion

La fraction d'eau restreinte (*fr*) peut être mesurée de manière robuste sur des systèmes équipés de gradients de 80 mT/m, avec un faible biais (<3%) par rapport aux systèmes équipés de gradients plus élevés. Le CRLB optimise correctement la conception du protocole en améliorant la sensibilité aux différences de microstructure (corrélation améliorée). Cette étude ouvre la voie à l'utilisation des techniques d'IRM de diffusion quantitatives sur des systèmes cliniques pour mesurer les caractéristiques et l'intégrité de la microstructure de la moelle épinière *in vivo*.

9.2 Application sur un patient atteint de sclérose en plaques

La sclérose en plaques (SEP) est une cause majeure de paralysie ou déficience sensorielle non-traumatique chez les jeunes adultes (Miller et al., 2007). La moelle épinière est fréquemment impliquée dans la SEP (Bot and Barkhof, 2009 ; Tench et al., 2005 ; Gilmore et al., 2009) et contribue aux critères diagnostiques de la SEP (McDonald et al., 2001). La détection des lésions dans la moelle épinière améliore non seulement la certitude des diagnostiques de la SEP (Thorpe et al., 1996 ; Agosta et al. 2007 ; Lycklama et al. 2003 ; Simon, 2000), mais fournit également des informations supplémentaires sur les différents phénotypes MS et la progression de la maladie, ce qui n'est pas toujours facilement observable dans le cerveau (Bot et al. 2004). Actuellement, la routine clinique pour la détection des lésions est basée sur l'imagerie par résonance magnétique (IRM). Bien que les séquences anatomiques standard de l'IRM fournissent déjà une bonne sensibilité pour détecter les lésions, ces séquences manquent de spécificité à la pathologie sous-jacente. Par exemple, l'étendue relative de la démyélinisation et de la perte axonale dans les lésions individuelles est variable. Le développement de marqueurs plus spécifiques pour chaque pathologie peut permettre un diagnostic plus précis et précoce et l'évaluation de l'efficacité de nouveaux médicaments remyélinisants (Mekhail et al. 2012). L'application de l'IRM quantitative multimodale, combinant diffusion et densité protonique, a le potentiel d'évaluer spécifiquement la dégénérescence axonale et la démyélinisation chez les patients atteints de SEP. Pour preuve de concept, trois patients atteints de sclérose en plaques ont été scannés avec les protocoles des chapitres 5 et 6 sur le scanner Connectom (gradient de 300 mT/m).

9.2.1 Méthodes

Le protocole était le même que dans l'article du chapitre 5, ainsi que la méthodologie (analyse d'image de pointe incluant la correction des artefacts, enregistrement dans l'atlas de la boîte à outils de la moelle épinière). La sensibilité à la lésion de la SEP a été évaluée

en comparant, à l'aide du test t, les biomarqueurs quantitatifs dans un tract touché par des lésions de SEP, par opposition au groupe de sujets sains (N = 8). La valeur du tractus touché a été extraite en utilisant la méthode d'extraction métrique basée sur l'atlas de la boîte à outils de la moelle épinière (Levy et al., 2016).

9.2.2 Résultats

Les biomarqueurs quantitatifs sont sensibles aux lésions de SEP avec au moins deux biomarqueurs montrant une différence significative ($p < 0,05$) par rapport au groupe sain.

Ensemble, ces biomarqueurs sont capables de distinguer les lésions de SEP selon trois scénarios différents (voir **Figure 9.3**).

• Patient n ° 1 : réduction à la fois de la teneur en myéline et de la densité axonale, résultant en un rapport g normal. Interprétation possible : Inflammation.

• Patient n ° 3 : réduction de la densité axonale seulement, entraînant une diminution du rapport g. Interprétation possible : myéline perturbée.

• Patient n ° 2 : réduction de la teneur en myéline seulement, entraînant une augmentation du g-ratio. Interprétation possible : démyélinisation.

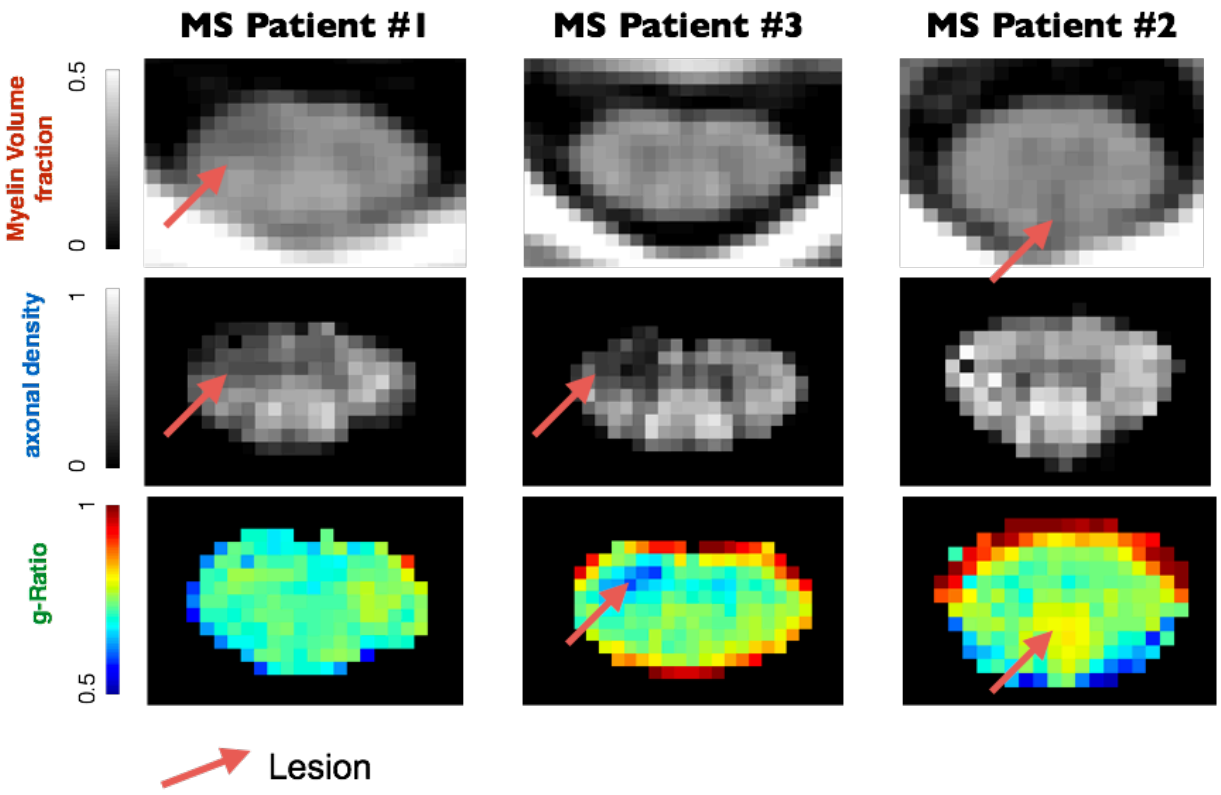

Figure 9.3: L'IRM quantitative est sensible aux lésions de SEP et permet de distinguer différents phénotypes. Haut. Fraction volumique de myéline (MVF) obtenue à partir de MTV. Milieu. Densité axonale obtenue à partir de l'IRM de diffusion en utilisant le modèle AxCaliber. Bas. Cartes pondérées par rapport au G obtenues en combinant la MVF et la densité axonale. Les flèches rouges mettent en évidence des valeurs anormales.

9.2.3 Conclusions

Comme indiqué aux chapitres 4-5-6, les nouveaux biomarqueurs IRM peuvent fournir des valeurs hautement reproductibles sensibles à la microstructure. Nous démontrons maintenant que ces biomarqueurs sont également sensibles à la lésion de la SEP et devraient aider à l'interprétation de l'intégrité tissulaire sous-jacente, et potentiellement trier les patients atteints de SEP dans différents phénotypes. Bien que l'on observe différent comportement entre les différentes lésions, une étude plus approfondie du comportement (augmentation, diminution, stagnation) de chaque métrique dans différent cas (œdème,

démyélination, cicatrice gliale) est nécessaire pour interpréter ces résultats. Une étude sur modèle animale de la SEP, avec histologie, pourra apporter des réponses.

Le protocole est maintenant appliqué longitudinalement sur les patients au laboratoire du Dr Klawiter.

9.2.4 Références

Bot, J.C.J., Barkhof, F., 2009. Spinal-cord MRI in multiple sclerosis: conventional and nonconventional MR techniques. Neuroimaging Clin. N. Am. 19, 81–99.

Bot, J.C.J., Barkhof, F., Polman, C.H., Lycklama à Nijeholt, G.J., de Groot, V., Bergers, E., Ader, H.J., Castelijns, J.A., 2004. Spinal cord abnormalities in recently diagnosed MS patients: added value of spinal MRI examination. Neurology 62, 226–233.

Gilmore, C.P., Donaldson, I., Bö, L., Owens, T., Lowe, J., Evangelou, N., 2009. Regional variations in the extent and pattern of grey matter demyelination in multiple sclerosis: a comparison between the cerebral cortex, cerebellar cortex, deep grey matter nuclei and the spinal cord. J. Neurol. Neurosurg. Psychiatry 80, 182–187.

Lycklama, G., Thompson, A., Filippi, M., Miller, D., Polman, C., Fazekas, F., Barkhof, F., 2003. Spinal-cord MRI in multiple sclerosis. Lancet Neurol. 2, 555–562.

McDonald, W.I., Compston, A., Edan, G., Goodkin, D., Hartung, H.P., Lublin, F.D., McFarland, H.F., Paty, D.W., Polman, C.H., Reingold, S.C., Sandberg-Wollheim, M., Sibley, W., Thompson, A., van den Noort, S., Weinshenker, B.Y., Wolinsky, J.S., 2001. Recommended diagnostic criteria for multiple sclerosis: guidelines from the International Panel on the diagnosis of multiple sclerosis. Ann. Neurol. 50, 121–127.

Mekhail, M., Almazan, G., Tabrizian, M., 2012. Oligodendrocyte-protection and remyelination post-spinal cord injuries: a review. Prog. Neurobiol. 96, 322–339.

Miller, D.H., Leary, S.M., 2007. Primary-progressive multiple sclerosis. Lancet Neurol. 6, 903–912.

Simon, J.H., 2000. The contribution of spinal cord MRI to the diagnosis and differential diagnosis of multiple sclerosis. J. Neurol. Sci. 172, S32–S35.

Tench, C.R., Morgan, P.S., Jaspan, T., Auer, D.P., Constantinescu, C.S., 2005. Spinal cord imaging in multiple sclerosis. J. Neuroimaging 15, 94S–102S.

Thorpe, J.W., Kidd, D., Moseley, I.F., Thompson, A.J., MacManus, D.G., Compston, D.A.,

McDonald, W.I., Miller, D.H., 1996. Spinal MRI in patients with suspected multiple sclerosis and negative brain MRI. Brain 119 (Pt 3), 709–714.

CHAPITRE 10 DISCUSSION GÉNÉRALE

Dans cette thèse, nous avons tout d'abord appliqué l'IRM de la microstructure sur des sujets humain puis sur des patients avec sclérose en plaques. Nous avons démontré la bonne précision et reproductibilité de cette méthode au sein d'un même site et la possibilité de l'appliquer sur des scanners cliniques. Cette méthode apporte bien plus d'information qu'un scan clinique basé sur un simple contraste. En effet, des centaines d'images sont acquises, basées sur des phénomènes physiques variés (e.g. relaxation T1, diffusion), et analysées avec les modèles biophysiques pour extraire quelques métriques seulement de la microstructure. Une mesure quantitative permet en outre de faire des études scientifiques objectives pour tester la performance d'un médicament ou pour améliorer les diagnostiques.

Comment exploiter l'IRM de la microstructure ?

Tout d'abord, il est nécessaire d'habituer les neurologues à ces cartes IRM quantitatives, en les affichant à côté d'un scan clinique avec un contraste fixe. Pour cela, il serait nécessaire de travailler en collaboration avec les constructeurs afin d'intégrer nos protocoles et nos méthodes de traitement (i.e. SCT, qMRLab) pour un traitement temps réel sur le scanner. En parallèle, les informations microstructurales (e.g. densité axonale, g-ratio) extraites automatiquement des différents tractus peuvent être traités par analyse discriminante, afin de diagnostiquer et pronostiquer les patients automatiquement.

IRM de la microstructure *versus* IRM quantitative

L'IRM quantitative permet d'obtenir des mesures reproductibles entre les scans. L'IRM de la microstructure permet d'interpréter ces valeurs et ainsi prédire l'intégrité d'un tissu de façon non-invasive. L'IRM quantitative peut être directement utilisé en étude clinique, les biomarqueurs IRM quantitatifs n'ont en effet pas besoin d'être interprété pour pouvoir classifier, et donc diagnostiquer et pronostiquer les différents phénotypes de sclérose en plaques. Les protocoles proposés dans cette thèse (voir chapitres 5 et 6), ainsi que le post-traitement développé (SCT et qMRLab), peuvent donc d'ores et déjà être appliqué pour des études longitudinales (scan IRM à intervalle régulier sur une cohorte de patients). À noter

qu'une une simple normalisation des scan (e.g. par une image b=0 en diffusion) permet d'obtenir un jeu de donnée quantitatif, et l'utilisation des modèles de microstructure n'est donc pas absolument nécessaire. La MRF (Magnetic Resonance Fingerprinting), qui propose d'obtenir une série de cartes quantitatives rapidement (e.g. T1, Proton density, diffusion coefficient), suscite d'ailleurs beaucoup d'intérêt (ESR, 2015).

Alors pourquoi donc développer des modèles bio-physiques complexes et des équations analytiques du signal IRM ?

Tout d'abord, les méthodes de classification assument une linéarité des prédicteurs. Dans le cas où de nombreux effets se combinent et se compensent (e.g. relaxation T1, densité du tissu, taille des fibres, transfert de magnétisation), les méthodes de classification sans aucune supervision peuvent être alors sous-performant. La désambiguïsation de ces effets non-linéaires par modélisation du signal (e.g. calcul du g-ratio) permet d'améliorer ces classifications.

D'autre part, la modélisation du signal IRM permet d'identifier tout biais potentiel et toute source ayant un impact sur le signal. Le biais Ricien, ou les effets de volumes partiel, d'orientation des fibres, de dépendance du coefficient de diffusion avec le temps, ont notamment été identifiés grâce au développement des modèles.

Aussi, et comme montré en chapitre 9.1, les équations analytiques permettent d'optimiser les protocoles IRM, et donc de réduire la durée des scans tout en améliorant la sensibilité à l'intégrité de la microstructure.

Enfin, les méthodes de classification dépendent des données d'entraînement. Un nouveau cas qui ne ferait pas parti des données d'entraînement ne pourra pas être correctement interprété avec des métriques quantitatives abstraites (e.g. temps de relaxation).

Ceci étant dit, la modélisation exhaustive de l'ensemble des effets sur le signal IRM est un immense défi, comme détaillé dans l'article 1 du chapitre 2.

Validation de l'IRM quantitative

Concernant la validation de l'IRM de la microstructure qui exploite l'histologie à large champ de vue, bien que les résultats obtenus soient riches en information, certaines limitations existent. Une grande partie de ces limitations ont été abordées en discussion de l'article 8 et nous allons ici mettre l'accent que sur les points les plus importants.

Qualité

Tout d'abord le g-ratio mesuré avec notre méthode est anormalement faible (surestimation de l'épaisseur de la myéline) à cause du flou de l'image d'une part et de la mauvaise préservation des axones dans les études *ex vivo* d'autre part.

En effet la fonction d'étalement du point (PSF) de la microscopie électronique est particulièrement importante à haut voltage lorsque les électrons pénètrent profondément dans le tissu. Une comparaison haut (~15 keV) versus bas (~3 keV) permettrait d'évaluer l'impact de la PSF sur nos mesures, et potentiellement de corriger les biais. L'utilisation du mode « high-magnification » permettrait aussi d'améliorer la PSF, mais cela se traduirait par une plus faible profondeur de champ (donc nécessité d'un autofocus) et d'un plus petit champ de vue (plus grand nombre de mosaïques). Une comparaison avec la microscopie électronique à transmission, considéré comme la vérité terrain de l'observation des axones, serait aussi intéressant. Finalement la préparation des tissus (notamment la vitesse de la perfusion) peut être améliorée. Le développement d'un système CARS, permettant l'imagerie de tissue frais (sans coloration par osmium) peut aussi être envisagé.

Histologie 2D

D'autre part les images obtenues sont 2D, et nous n'avons pas d'information directe sur l'orientation des fibres notamment. Bien que des méthodes de microscopie existent pour imager en 3D (e.g. tomographie par cohérence optique), la quantité de donnée à acquérir puis traiter rend difficile l'application sur des coupes complètent. Une solution intermédiaire serait d'utiliser la microscopie optique conventionnelle, très rapide (~1min) avec des numériseurs de coupes entière, pour imager une série de coupes sagittales et coronales afin d'extraire l'orientation des fibres dans ces directions.

Ex vivo

Une troisième limitation est le fait que l'imagerie IRM et l'histologie ont été faites *ex vivo*. Cela peut changer les propriétés du tissu (e.g. T1, T2, PD, coefficients de diffusion) et ne garantit donc pas la validité des modèles *in vivo*. Une comparaison *in vivo* versus *ex vivo* serait nécessaire pour démontrer que nous mesurons la même chose dans les deux cas. Une autre approche permettant de valider de façon la plus réaliste possible consistera à effectuer des scans *in vivo* juste avant biopsie ou sacrifice, puis de comparer l'histologie et l'IRM *in vivo*.

À noter aussi que la fixation du tissu lors de l'histologie *ex vivo* peut biaiser nos mesures de densité axonale à cause du rétrécissement globale du tissu. Une comparaison entre le CARS sur tissu frais et la microscopie électronique serait nécessaire.

CHAPITRE 11 CONCLUSION ET RECOMMANDATIONS

Cette thèse s'inscrit donc dans le développement de l'IRM quantitative pour usage clinique. Cette recherche s'accompagne tout d'abord de plusieurs retombées technologiques et méthodologique : le pipeline de post-traitement pour l'IRM quantitative de la moelle épinière, le logiciel libre AxonSeg pour la segmentation automatique des axons et de la myéline, et enfin qMRLab pour la simulation, la visualisation et le calcul des métriques quantitatives à partir d'images IRM.

Ces technologies ont permis l'application de l'IRM quantitative sur la moelle épinière humaine. Nous avons évalué la précision de ces mesures (scan-rescan <3%), leur exactitude, et enfin la sensibilité et la spécificité (comparaison avec l'histologie). Une optimisation du protocole de diffusion pour le transfert vers IRM clinique (80mT/m en XY) a été effectuée et ce protocole a été testé *ex vivo* : Les métriques quantitatives, sauf diamètre axonal, peuvent se mesurer sans biais particulier sur IRM clinique, avec un bon rapport contraste sur bruit, et avec un protocole plus court (300 volumes, 5-10min).

Nos résultats sur les patients atteints de sclérose en plaques montrent une capacité à différencier plusieurs lésions, et donc un gain en spécificité par rapport à l'IRM conventionnelle. Une étude longitudinale permettra d'évaluer le potentiel pronostique chez de futurs patients.

Beaucoup de travail reste à faire pour que l'IRM quantitative de la moelle arrive à maturité : (1) valider le protocole de diffusion optimisé sur l'humain (reproduire l'étude du chapitre **Erreur ! Nous n'avons pas trouvé la source du renvoi.** sur l'humain avec l'IRM Connectom), (2) évaluer le comportement des métriques quantitatives dans les lésions à l'aide de modèle animal *ex vivo* (les hypothèses des modèles sont-elles toujours valables dans les lésions ?), (3) effectuer des tests de reproductibilité inter-scanner, (4) utiliser ces nouveaux biomarqueurs pour une analyse discriminante des différents phénotypes.

Concernant les recherches plus fondamentales sur la compréhension de l'organisation de

Concernant les recherches plus fondamentales sur la compréhension de l'organisation de la microstructure de la moelle, les pistes de recherche pour aller dans la continuité de ce projet sont : (1) une amélioration de la qualité des images histologique afin de distinguer les axons <1µm, (2) l'utilisation d'autres modalités histologique pour cartographier le système vasculaire, la densité mitochondriale ou gliale, et l'orientation tridimensionnelle des fibres de la matière blanche, (3) application de modèles biophysique permettant d'expliquer les variations de microstructure.

Je souhaite donc bonne chance et bon courage à mes successeurs pour mener à terme ces recherches.

BIBLIOGRAPHIE

Ali M Neishabouri, A.A.F., 2011. The metabolic efficiency of myelinated vs unmyelinated axons. BMC Neurosci. 12, P100.

Bot, J.C.J., Barkhof, F., 2009. Spinal-cord MRI in multiple sclerosis: conventional and nonconventional MR techniques. Neuroimaging Clin. N. Am. 19, 81–99.

Bot, J.C.J., Barkhof, F., Polman, C.H., Lycklama à Nijeholt, G.J., de Groot, V., Bergers, E., Ader, H.J., Castelijns, J.A., 2004. Spinal cord abnormalities in recently diagnosed MS patients: added value of spinal MRI examination. Neurology 62, 226–233.

Branzoli, F., Ercan, E., Valabrègue, R., Wood, E.T., Buijs, M., Webb, A., Ronen, I., 2016. Differentiating between axonal damage and demyelination in healthy aging by combining diffusion-tensor imaging and diffusion-weighted spectroscopy in the human corpus callosum at 7 T. Neurobiol. Aging 47, 210–217.

Campbell, J.S.W., Leppert, I.R., Narayanan, S., Boudreau, M., Duval, T., Cohen-Adad, J., Pike, G.B., Stikov, N., 2017. Promise and pitfalls of g-ratio estimation with MRI. Neuroimage. https://doi.org/10.1016/j.neuroimage.2017.08.038

Cerghet, M., Skoff, R.P., Bessert, D., Zhang, Z., Mullins, C., Ghandour, M.S., 2006. Proliferation and death of oligodendrocytes and myelin proteins are differentially regulated in male and female rodents. J. Neurosci. 26, 1439–1447.

D'Arceuil, H.E., Westmoreland, S., de Crespigny, A.J., 2007. An approach to high resolution diffusion tensor imaging in fixed primate brain. Neuroimage 35, 553–565.

De Gail, P., Lance, J.W., Neilson, P.D., 1966. Differential effects on tonic and phasic reflex mechanisms produced by vibration of muscles in man. J. Neurol. Neurosurg. Psychiatry 29, 1–11.

De Leener, B., Fonov, V.S., Collins, D.L., Callot, V., Stikov, N., Cohen-Adad, J., 2017. PAM50: Unbiased multimodal template of the brainstem and spinal cord aligned with the ICBM152 space. Neuroimage 165, 170–179.

Duval, T., Leppert R, I., Cabana, J.-F., Boudreau, M., Gagnon, I., Berestovoy, G., Cohen-Adad, J., Stikov, N., 2018. Quantitative MRI made easy with qMRLab, in: Proceedings of the 26th Annual Meeting of ISMRM.

Duval, T., Smith, V., Stikov, N., Klawiter, E.C., Cohen-Adad, J., 2017. Scan-rescan of axcaliber, macromolecular tissue volume, and g-ratio in the spinal cord. Magn. Reson. Med. https://doi.org/10.1002/mrm.26945

File:Anatomy and physiology of animals The spinal cord.jpg - Wikimedia Commons [WWW Document], n.d. URL https://commons.wikimedia.org/wiki/File:Anatomy_and_physiology_of_animals_The_spinal_cord.jpg (accessed 12.17.17).

File:BodyPlanes.jpg - Wikimedia Commons [WWW Document], n.d. URL https://commons.wikimedia.org/wiki/File:BodyPlanes.jpg (accessed 12.17.17).

Flint, J.J., Hansen, B., Fey, M., Schmidig, D., King, M.A., Vestergaard-Poulsen, P., Blackband, S.J., 2010. Cellular-level diffusion tensor microscopy and fiber tracking in mammalian nervous tissue with direct histological correlation. Neuroimage 52, 556–561.

Gilmore, C.P., Donaldson, I., Bö, L., Owens, T., Lowe, J., Evangelou, N., 2009. Regional variations in the extent and pattern of grey matter demyelination in multiple sclerosis: a comparison between the cerebral cortex, cerebellar cortex, deep grey matter nuclei and the spinal cord. J. Neurol. Neurosurg. Psychiatry 80, 182–187.

Goto, N., Goto, J., 2006. Morphometric evaluations of the human nervous system. Hum. Cell 19, 49–64.

Khir, A.W., O'Brien, A., Gibbs, J.S., Parker, K.H., 2001. Determination of wave speed and wave separation in the arteries. J. Biomech. 34, 1145–1155.

Knösche, T.R., Anwander, A., Liptrot, M., Dyrby, T.B., 2015. Validation of tractography: Comparison with manganese tracing. Hum. Brain Mapp. 36, 4116–4134.

Laxminarayan, S., 1979. The calculation of forward and backward waves in the arterial system. Med. Biol. Eng. Comput. 17, 130.

Le Bihan, D., 2012. Cerveau de cristal (Le): Ce que nous révèle la neuro-imagerie. Odile Jacob.

Li, J.K., 1986. Time domain resolution of forward and reflected waves in the aorta. IEEE Trans. Biomed. Eng. 33, 783–785.

Lycklama, G., Thompson, A., Filippi, M., Miller, D., Polman, C., Fazekas, F., Barkhof, F., 2003. Spinal-cord MRI in multiple sclerosis. Lancet Neurol. 2, 555–562.

Macgowan, C.K., Stoops, S.J., Zhou, Y.-Q., Cahill, L.S., Sled, J.G., 2015. Evaluation of cerebrovascular impedance and wave reflection in mouse by ultrasound. J. Cereb. Blood Flow Metab. 35, 521–526.

Maier, F., Fuentes, D., Weinberg, J.S., Hazle, J.D., Stafford, R.J., 2015. Robust phase unwrapping for MR temperature imaging using a magnitude-sorted list, multi-clustering

algorithm. Magn. Reson. Med. 73, 1662–1668.

McDonald, W.I., Compston, A., Edan, G., Goodkin, D., Hartung, H.P., Lublin, F.D., McFarland, H.F., Paty, D.W., Polman, C.H., Reingold, S.C., Sandberg-Wollheim, M., Sibley, W., Thompson, A., van den Noort, S., Weinshenker, B.Y., Wolinsky, J.S., 2001. Recommended diagnostic criteria for multiple sclerosis: guidelines from the International Panel on the diagnosis of multiple sclerosis. Ann. Neurol. 50, 121–127.

Mekhail, M., Almazan, G., Tabrizian, M., 2012. Oligodendrocyte-protection and remyelination post-spinal cord injuries: a review. Prog. Neurobiol. 96, 322–339.

Miller, D.H., Leary, S.M., 2007. Primary-progressive multiple sclerosis. Lancet Neurol. 6, 903–912.

Polarlys, Mikael, H., n.d. File:Spinal cord tracts - English.svg - Wikimedia Commons [WWW Document]. URL https://commons.wikimedia.org/wiki/File:Spinal_cord_tracts_-_English.svg (accessed 12.17.17).

Ramani, A., Dalton, C., Miller, D.H., Tofts, P.S., Barker, G.J., 2002. Precise estimate of fundamental in-vivo MT parameters in human brain in clinically feasible times. Magn. Reson. Imaging 20, 721–731.

Reddy, A.K., Madala, S., Jones, A.D., Caro, W.A., Eberth, J.F., Pham, T.T., Taffet, G.E., Hartley, C.J., 2009. Multichannel pulsed Doppler signal processing for vascular measurements in mice. Ultrasound Med. Biol. 35, 2042–2054.

Saliani, A., Perraud, B., Duval, T., Stikov, N., Rossignol, S., Cohen-Adad, J., 2017. Axon and myelin morphology in animal and human spinal cord. Front. Neuroanat. 11, 129.

Schofield, M.A., Zhu, Y., 2003. Fast phase unwrapping algorithm for interferometric applications. Opt. Lett. 28, 1194–1196.

Setsompop, K., Fan, Q., Stockmann, J., Bilgic, B., Huang, S., Cauley, S.F., Nummenmaa, A., Wang, F., Rathi, Y., Witzel, T., Wald, L.L., 2017. High-resolution in vivo diffusion imaging of the human brain with generalized slice dithered enhanced resolution: Simultaneous multislice (gSlider-SMS). Magn. Reson. Med. https://doi.org/10.1002/mrm.26653

Simon, J.H., 2000. The contribution of spinal cord MRI to the diagnosis and differential diagnosis of multiple sclerosis. J. Neurol. Sci. 172, S32–S35.

Teh, I., McClymont, D., Zdora, M.-C., Whittington, H.J., Davidoiu, V., Lee, J., Lygate, C.A., Rau, C., Zanette, I., Schneider, J.E., 2017. Validation of diffusion tensor MRI measurements of cardiac microstructure with structure tensor synchrotron radiation imaging. J. Cardiovasc. Magn. Reson. 19, 31.

Tench, C.R., Morgan, P.S., Jaspan, T., Auer, D.P., Constantinescu, C.S., 2005. Spinal cord imaging in multiple sclerosis. J. Neuroimaging 15, 94S–102S.

Thorpe, J.W., Kidd, D., Moseley, I.F., Thompson, A.J., MacManus, D.G., Compston, D.A., McDonald, W.I., Miller, D.H., 1996. Spinal MRI in patients with suspected multiple sclerosis and negative brain MRI. Brain 119 (Pt 3), 709–714.

Wada, A., Goto, J., Goto, N., Kawamura, N., Matsumoto, K., 2001. Are there one million nerve fibres in the human medullary pyramid? Okajimas Folia Anat. Jpn. 77, 221–224.

Yarnykh, V.L., 2012. Fast macromolecular proton fraction mapping from a single off-resonance magnetization transfer measurement. Magn. Reson. Med. 68, 166–178.

Barth, M., Breuer, F., Koopmans, P.J., Norris, D.G., Poser, B.A., 2016. Simultaneous multislice (SMS) imaging techniques. Magn. Reson. Med. 75, 63–81.

Bieri, O., Scheffler, K., 2007. Optimized balanced steady-state free precession magnetization transfer imaging. Magn. Reson. Med. 58, 511–518.

Blamire, A.M., 2008. The technology of MRI--the next 10 years? Br. J. Radiol. 81, 601–617.

Block, K.T., Uecker, M., Frahm, J., 2008a. Suppression of MRI Truncation Artifacts Using Total Variation Constrained Data Extrapolation. Int. J. Biomed. Imaging 2008. https://doi.org/10.1155/2008/184123

Block, K.T., Uecker, M., Frahm, J., 2008b. Suppression of MRI truncation artifacts using total variation constrained data extrapolation. Int. J. Biomed. Imaging 2008, 184123.

Brandão, L.A., Domingues, R.C., 2004. MR Spectroscopy of the Brain. Lippincott Williams & Wilkins.

Cohen-Adad, J., Zhao, W., Wald, L.L., Oaklander, A.L., 2012. 7T MRI of spinal cord injury. Neurology 79, 2217.

Duval, T., Smith, V., Klawiter, E., Cohen-Adad, J., 2016. New Biomarkers for MS Lesions with Magnetic Resonance Imaging (MRI) Provide Quantitative Interpretation of Microstructural Integrity, in: Proceedings of the endMS Conference. Presented at the endMS Conference.

Evarts, E.V., 1965. RELATION OF DISCHARGE FREQUENCY TO CONDUCTION VELOCITY IN PYRAMIDAL TRACT NEURONS. J. Neurophysiol. 28, 216–228.

Figley, C.R., Yau, D., Stroman, P.W., 2008. Attenuation of lower-thoracic, lumbar, and

sacral spinal cord motion: implications for imaging human spinal cord structure and function. AJNR Am. J. Neuroradiol. 29, 1450–1454.

Firmin, L., Field, P., Maier, M.A., Kraskov, A., Kirkwood, P.A., Nakajima, K., Lemon, R.N., Glickstein, M., 2014. Axon diameters and conduction velocities in the macaque pyramidal tract. J. Neurophysiol. 112, 1229–1240.

Gochberg, D.F., Kennan, R.P., Robson, M.D., Gore, J.C., 1999. Quantitative imaging of magnetization transfer using multiple selective pulses. Magn. Reson. Med. 41, 1065–1072.

Guillery, R.W., Polley, E.H., Torrealba, F., 1982. The arrangement of axons according to fiber diameter in the optic tract of the cat. J. Neurosci. 2, 714–721.

Haralick, R.M., Shapiro, L.G., 1992. Computer and Robot Vision, 1st ed. Addison-Wesley Longman Publishing Co., Inc., Boston, MA, USA.

Hasenstaub, A., Otte, S., Callaway, E., Sejnowski, T.J., 2010. Metabolic cost as a unifying principle governing neuronal biophysics. Proc. Natl. Acad. Sci. U. S. A. 107, 12329–12334.

Jiang, Y.-Q., Zaaimi, B., Martin, J.H., 2016. Competition with Primary Sensory Afferents Drives Remodeling of Corticospinal Axons in Mature Spinal Motor Circuits. J. Neurosci. 36, 193–203.

Laird-Wa, J., 2015. Improving Spinal Cord Stimulation.

Lassek, A.M., Rasmussen, G.L., 1940. A comparative fiber and numerical analysis of the pyramidal tract. J. Comp. Neurol. 72, 417–428.

Le Bihan, D., 2012. Le Cerveau de cristal : Ce que nous révèle la neuro-imagerie. Odile Jacob.

MacKay, A., Whittall, K., Adler, J., Li, D., Paty, D., Graeb, D., 1994. In vivo visualization of myelin water in brain by magnetic resonance. Magn. Reson. Med. 31, 673–677.

Miller, J.P., Eldabe, S., Buchser, E., Johanek, L.M., Guan, Y., Linderoth, B., 2016. Parameters of Spinal Cord Stimulation and Their Role in Electrical Charge Delivery: A Review. Neuromodulation 19, 373–384.

More, H.L., Hutchinson, J.R., Collins, D.F., Weber, D.J., Aung, S.K.H., Donelan, J.M., 2010. Scaling of sensorimotor control in terrestrial mammals. Proc. Biol. Sci. 277, 3563–3568.

More, H.L., O'Connor, S.M., Brøndum, E., Wang, T., Bertelsen, M.F., Grøndahl, C., Kastberg, K., Hørlyck, A., Funder, J., Donelan, J.M., 2013. Sensorimotor responsiveness and resolution in the giraffe. J. Exp. Biol. 216, 1003–1011.

Niu, J., Ding, L., Li, J.J., Kim, H., Liu, J., Li, H., Moberly, A., Badea, T.C., Duncan, I.D., Son, Y.-J., Scherer, S.S., Luo, W., 2013. Modality-based organization of ascending somatosensory axons in the direct dorsal column pathway. J. Neurosci. 33, 17691–17709.

Noseworthy, J.H., 1994. Clinical scoring methods for multiple sclerosis. Ann. Neurol. 36 Suppl, S80–5.

Panov, A.V., Kubalik, N., Zinchenko, N., Ridings, D.M., Radoff, D.A., Hemendinger, R., Brooks, B.R., Bonkovsky, H.L., 2011. Metabolic and functional differences between brain and spinal cord mitochondria underlie different predisposition to pathology. Am. J. Physiol. Regul. Integr. Comp. Physiol. 300, R844–54.

Plonsey, R., Barr, R.C., 2007. Bioelectricity: A Quantitative Approach. Springer Science & Business Media.

Point, P., n.d. The Nervous System: Sensory and Motor Tracts of the Spinal Cord.

Pruessmann, K.P., Weiger, M., Scheidegger, M.B., Boesiger, P., 1999. SENSE: sensitivity encoding for fast MRI. Magn. Reson. Med. 42, 952–962.

Rossignol, S., Bouyer, L., Barthélemy, D., Langlet, C., Leblond, H., 2002. Recovery of locomotion in the cat following spinal cord lesions. Brain Res. Brain Res. Rev. 40, 257–266.

Saritas, E.U., Cunningham, C.H., Lee, J.H., Han, E.T., Nishimura, D.G., 2008. DWI of the spinal cord with reduced FOV single-shot EPI. Magn. Reson. Med. 60, 468–473.

Saritas, E.U., Lee, D., Çukur, T., Shankaranarayanan, A., Nishimura, D.G., 2014. Hadamard slice encoding for reduced-FOV diffusion-weighted imaging. Magn. Reson. Med. 72, 1277–1290.

Schneider, G., Prince, M.R., Meaney, J.F.M., Ho, V.B., 2006. Magnetic Resonance Angiography: Techniques, Indications and Practical Applications. Springer Science & Business Media.

Schwartz, E.D., Flanders, A.E., 2007. Spinal Trauma: Imaging, Diagnosis, and Management. Lippincott Williams & Wilkins.

Singleton, M.J., 2009. Functional Magnetic Resonance Imaging. Yale J. Biol. Med. 82, 233.

Stehling, M.K., Turner, R., Mansfield, P., 1991. Echo-planar imaging: magnetic resonance imaging in a fraction of a second. Science 254, 43–50.

Stephan, R., Goellner, B., Moreno, E., Frank, C.A., Hugenschmidt, T., Genoud, C., Aberle, H., Pielage, J., 2015. Hierarchical microtubule organization controls axon caliber and transport and determines synaptic structure and stability. Dev. Cell 33, 5–21.

Traub, R.D., Schmitz, D., Maier, N., Whittington, M.A., Draguhn, A., 2012. Axonal properties determine somatic firing in a model of in vitro CA1 hippocampal sharp wave/ripples and persistent gamma oscillations. Eur. J. Neurosci. 36, 2650–2660.

Wilm, B.J., Svensson, J., Henning, A., Pruessmann, K.P., Boesiger, P., Kollias, S.S., 2007. Reduced field-of-view MRI using outer volume suppression for spinal cord diffusion imaging. Magn. Reson. Med. 57, 625–630.

Wu, B., Warnock, G., Zaiss, M., Lin, C., Chen, M., Zhou, Z., Mu, L., Nanz, D., Tuura, R., Delso, G., 2016. An overview of CEST MRI for non-MR physicists. EJNMMI Phys 3, 19.

Apkarian, A.V., Hodge, C.J., 1989. Primate spinothalamic pathways: I. A quantitative study of the cells of origin of the spinothalamic pathway. J. Comp. Neurol. 288, 447–473.

Avants, B.B., Tustison, N.J., Song, G., Cook, P.A., Klein, A., Gee, J.C., 2011. A reproducible evaluation of ANTs similarity metric performance in brain image registration. Neuroimage 54, 2033–2044.

Ben Arous, J., Binding, J., Léger, J.-F., Casado, M., Topilko, P., Gigan, S., Boccara, A.C., Bourdieu, L., 2011. Single myelin fiber imaging in living rodents without labeling by deep optical coherence microscopy. J. Biomed. Opt. 16, 116012.

Boudreau, M., Stikov, N., Pike, G.B., 2017. B1-sensitivity analysis of quantitative magnetization transfer imaging. Magn. Reson. Med. https://doi.org/10.1002/mrm.26673

Boundless, 2016. Classification of Nerves, in: Boundless Physiology. Boundless.

Burgess, P.R., Horch, K.W., 1978. The distinction between the short and intermediate ascending pathways in the fasciculus gracilis of the cat. Brain Res. 151, 579–580.

Chen, H.S.-M., Holmes, N., Liu, J., Tetzlaff, W., Kozlowski, P., 2017. Validating myelin water imaging with transmission electron microscopy in a rat spinal cord injury model. Neuroimage 153, 122–130.

Damangir, S., Westman, E., Simmons, A., Vrenken, H., Wahlund, L.-O., Spulber, G., 2016. Reproducible segmentation of white matter hyperintensities using a new statistical definition. MAGMA. https://doi.org/10.1007/s10334-016-0599-3

Demyer, W., 1959. Number of axons and myelin sheaths in adult human medullary pyramids; study with silver impregnation and iron hematoxylin staining methods.

Neurology 9, 42–47.

Drobnjak, I., Zhang, H., Ianuş, A., Kaden, E., Alexander, D.C., 2016. PGSE, OGSE, and sensitivity to axon diameter in diffusion MRI: Insight from a simulation study. Magn. Reson. Med. 75, 688–700.

Duval, T., Perraud, B., Vuong, M.-T., Lopez Rios, N., Stikov, N., Cohen-Adad, J., 2016. Validation of Quantitative MRI Metrics Using Full Slice Histology with Automatic Axon Segmentation, in: Proceedings of the 24th Annual Meeting of ISMRM. p. 928.

Duval, T., Smith, V., Klawiter, E., Stikov, N., Cohen-Adad, J., 2017. Scan-Rescan of AxCaliber, Macromolecular Tissue Volume and G-Ratio in the Spinal Cord, in: Proceedings of the 25th Annual Meeting of ISMRM. p. 3472.

Gray, H., 1867. Anatomy, descriptive and surgical. Henry C. Lea.

Harms, R.L., Fritz, F.J., Tobisch, A., Goebel, R., Roebroeck, A., 2017. Robust and fast nonlinear optimization of diffusion MRI microstructure models. Neuroimage 155, 82–96.

Hwang, Y.C., Hinsman, E.J., Roesel, O.F., 1975. Caliber spectra of fibers in the fasciculus gracilis of the cat cervical spinal cord: a quantitative electron microscopic study. J. Comp. Neurol. 162, 195–203.

Ibrahim, T.S., Hue, Y.-K., Tang, L., 2009. Understanding and manipulating the RF fields at high field MRI. NMR Biomed. 22, 927–936.

Jelescu, I.O., Zurek, M., Winters, K.V., Veraart, J., Rajaratnam, A., Kim, N.S., Babb, J.S., Shepherd, T.M., Novikov, D.S., Kim, S.G., Fieremans, E., 2016. In vivo quantification of demyelination and recovery using compartment-specific diffusion MRI metrics validated by electron microscopy. Neuroimage 132, 104–114.

Kenna, L.A., 1959. Eccentricity in Ellipses. Math. Mag. 32, 133–135.

Knott, G., Marchman, H., Wall, D., Lich, B., 2008. Serial section scanning electron microscopy of adult brain tissue using focused ion beam milling. J. Neurosci. 28, 2959–2964.

Nudo, R.J., Frost, S.B., 2007. The Evolution of Motor Cortex and Motor Systems, in: Evolution of Nervous Systems. Elsevier, pp. 373–395.

Patience, G.S., Boffito, D.C., Patience, P., 2015. Communicate Science Papers, Presentations, and Posters Effectively. Academic Press.

Preibisch, S., Saalfeld, S., Tomancak, P., 2009. Globally optimal stitching of tiled 3D

microscopic image acquisitions. Bioinformatics 25, 1463–1465.

Ralston, D.D., Milroy, A.M., Ralston, H.J., 3rd, 1987. Non-myelinated axons are rare in the medullary pyramids of the macaque monkey. Neurosci. Lett. 73, 215–219.

Rayleigh, 1879. XXXI. Investigations in optics, with special reference to the spectroscope. Philos. Mag. 8, 261–274.

Schindelin, J., Arganda-Carreras, I., Frise, E., Kaynig, V., Longair, M., Pietzsch, T., Preibisch, S., Rueden, C., Saalfeld, S., Schmid, B., Tinevez, J.-Y., White, D.J., Hartenstein, V., Eliceiri, K., Tomancak, P., Cardona, A., 2012. Fiji: an open-source platform for biological-image analysis. Nat. Methods 9, 676–682.

Soh, L.K., Tsatsoulis, C., 1999. Texture analysis of SAR sea ice imagery using gray level co-occurrence matrices. IEEE Trans. Geosci. Remote Sens. 37, 780–795.

Sommer, C., Straehle, C., Köthe, U., Hamprecht, F.A., 2011. Ilastik: Interactive learning and segmentation toolkit, in: 2011 IEEE International Symposium on Biomedical Imaging: From Nano to Macro. pp. 230–233.

Souma, Y., Goto, N., Goto, J., Chiba, K., Ishida, Y., 2008. Morphological evaluation of the human pyramidal tract: gender and age differences. Okajimas Folia Anat. Jpn. 85, 107–109.

Souma, Y., Goto, N., Goto, J., Fujimoto, T., Fujiwara, T., 2009. Morphological evaluation of the human pyramidal tract: tapering of axons. Okajimas Folia Anat. Jpn. 85, 111–113.

Steck, K., Knaden, M., Hansson, B.S., 2010. Do desert ants smell the scenery in stereo? Anim. Behav. 79, 939–945.

Stevens, R.T., Apkarian, A.V., Hodge, C.J., Jr, 1991. The location of spinothalamic axons within spinal cord white matter in cat and squirrel monkey. Somatosens. Mot. Res. 8, 97–102.

Susaki, E.A., Ueda, H.R., 2016. Whole-body and Whole-Organ Clearing and Imaging Techniques with Single-Cell Resolution: Toward Organism-Level Systems Biology in Mammals. Cell Chem Biol 23, 137–157.

Thomas, A., Westrum, L.E., Devito, J.L., Biedenbach, M.A., 1984. Unmyelinated axons in the pyramidal tract of the cat. Brain Res. 301, 162–165.

Towe, A.L., 1973. Relative Numbers of Pyramidal Tract Neurons in Mammals of Different Sizes. Biotechnol. Bioprocess Eng. 7, 1–17.

Veenith, T.V., Carter, E., Grossac, J., Newcombe, V.F.J., Outtrim, J.G., Lupson, V.,

Williams, G.B., Menon, D.K., Coles, J.P., 2013. Inter subject variability and reproducibility of diffusion tensor imaging within and between different imaging sessions. PLoS One 8, e65941.

Verhaart, W.J., 1962. The pyramidal tract. Its structure and functions in man and animals. World Neurol. 3, 43–53.

Verhaart, W.J.C., 1947. ON THICK AND THIN FIBERS IN THE PYRAMIDAL TRACT. Acta Psychiatr. Scand. 22, 271–281.

Vuong, M.-T., Duval, T., Cohen-Adad, J., Stikov, N., 2017. On the Precision of Myelin Imaging: Characterizing Ex Vivo Dog Spinal Cord with MRI and Histology, in: Proceedings of the 25th Annual Meeting of ISMRM. p. 3760.

Watson, C., Paxinos, G., Kayalioglu, G., 2009. The Spinal Cord: A Christopher and Dana Reeve Foundation Text and Atlas. Academic Press.

Zhang, X., Wenk, H.N., Honda, C.N., Giesler, G.J., Jr, 2000. Locations of spinothalamic tract axons in cervical and thoracic spinal cord white matter in monkeys. J. Neurophysiol. 83, 2869–2880.

Åslund, I., Topgaard, D., 2009. Determination of the self-diffusion coefficient of intracellular water using PGSE NMR with variable gradient pulse length. J. Magn. Reson. 201, 250–254.

Balls, G.T., Frank, L.R., 2009. A simulation environment for diffusion weighted MR experiments in complex media. Magn. Reson. Med. 62, 771–778.

Budde, M.D., Annese, J., 2013. Quantification of anisotropy and fiber orientation in human brain histological sections. Front. Integr. Neurosci. 7, 3.

Cercignani, M., Giulietti, G., Dowell, N.G., Gabel, M., Broad, R., Leigh, P.N., Harrison, N.A., Bozzali, M., 2017. Characterizing axonal myelination within the healthy population: a tract-by-tract mapping of effects of age and gender on the fiber g-ratio. Neurobiol. Aging 49, 109–118.

De Leener, B., Lévy, S., Dupont, S.M., Fonov, V.S., Stikov, N., Louis Collins, D., Callot, V., Cohen-Adad, J., 2016. SCT: Spinal Cord Toolbox, an open-source software for processing spinal cord MRI data. Neuroimage. https://doi.org/10.1016/j.neuroimage.2016.10.009

de Mathematiques Pures et Appliquees Joseph Liouville, L., n.d. Dense Packings of Equal Spheres in a Cube.

Dellemann, G., Kemen, T., Eberle, A., Garbowski, T., Malloy, M., Bunday, B., Thiel, B.,

Zeidler, D., n.d. Advances in Multi-Beam SEM Technology for High-Throughput Defect Inspection.

Duval, T., Stikov, N., Cohen-Adad, J., 2016. Modeling white matter microstructure. Funct. Neurol. 31, 217–228.

Glasser, M.F., Coalson, T.S., Robinson, E.C., Hacker, C.D., Harwell, J., Yacoub, E., Ugurbil, K., Andersson, J., Beckmann, C.F., Jenkinson, M., Smith, S.M., Van Essen, D.C., 2016a. A multi-modal parcellation of human cerebral cortex. Nature 536, 171–178.

Glasser, M.F., Smith, S.M., Marcus, D.S., Andersson, J.L.R., Auerbach, E.J., Behrens, T.E.J., Coalson, T.S., Harms, M.P., Jenkinson, M., Moeller, S., Robinson, E.C., Sotiropoulos, S.N., Xu, J., Yacoub, E., Ugurbil, K., Van Essen, D.C., 2016b. The Human Connectome Project's neuroimaging approach. Nat. Neurosci. 19, 1175–1187.

Glasser, M.F., Van Essen, D.C., 2011. Mapping human cortical areas in vivo based on myelin content as revealed by T1- and T2-weighted MRI. J. Neurosci. 31, 11597–11616.

Grant, G., Koerber, H.R., 2004. CHAPTER 5 - Spinal Cord Cytoarchitecture A2 - Paxinos, George, in: The Rat Nervous System (THIRD EDITION). Academic Press, Burlington, pp. 121–128.

Guise, C., Fernandes, M.M., Nóbrega, J.M., Pathak, S., Schneider, W., Fangueiro, R., 2016. Hollow Polypropylene Yarns as a Biomimetic Brain Phantom for the Validation of High-Definition Fiber Tractography Imaging. ACS Appl. Mater. Interfaces 8, 29960–29967.

Jelescu, I.O., Veraart, J., Fieremans, E., Novikov, D.S., 2016. Degeneracy in model parameter estimation for multi-compartmental diffusion in neuronal tissue. NMR Biomed. 29, 33–47.

Kamiya, K., Irie, R., Kamagata, K., Hori, M., Suzuki, Y., Mori, H., Kunimatsu, A., Aoki, S., Ohtomo, K., 2015. Impact of axon undulation on the estimation of dMRI metrics: Monte-Carlo simulation study with conventional DTI and NODDI, in: European Congress of Radiology. European Congress of Radiology 2016.

Kaynig, V., Vazquez-Reina, A., Knowles-Barley, S., Roberts, M., Jones, T.R., Kasthuri, N., Miller, E., Lichtman, J., Pfister, H., 2015. Large-scale automatic reconstruction of neuronal processes from electron microscopy images. Med. Image Anal. 22, 77–88.

Kharbanda, H.S., Alsop, D.C., Anderson, A.W., Filardo, G., Hackney, D.B., 2006. Effects of cord motion on diffusion imaging of the spinal cord. Magn. Reson. Med. 56, 334–339.

Kipp, L., Cawley, N., Prados, F., Schneider, T., Ourselin, S., Wheeler-Kingshott, C.A., Miller, D.H., Thompson, A.J., Ciccarelli, O., 2015. Neurite orientation dispersion and

density imaging (NODDI) in RRMS. MULTIPLE SCLEROSIS JOURNAL 21, 9–9.

Li, K., Zu, Z., Xu, J., Janve, V.A., Gore, J.C., Does, M.D., Gochberg, D.F., 2010. Optimized inversion recovery sequences for quantitative T1 and magnetization transfer imaging. Magn. Reson. Med. 64, 491–500.

Mesri, H.Y., Novikov, D., Viergever, M.A., Leemans, A., 2016. Simulating Axon Packing for Investigating White Matter Tissue Characteristics with Diffusion MRI, in: Proceedings of the 24th Annual Meeting of ISMRM. p. 3084.

Mezer, A., Rokem, A., Berman, S., Hastie, T., Wandell, B.A., 2016. Evaluating quantitative proton-density-mapping methods. Hum. Brain Mapp. 37, 3623–3635.

Mingasson, T., Duval, T., Stikov, N., Cohen-Adad, J., 2017. AxonPacking: An Open-Source Software to Simulate Arrangements of Axons in White Matter. Front. Neuroinform. 11, 5.

Morell, P. (Ed.), 1984. Myelin: Springer US.

Morozov, D., Bar, L., Sochen, N., Cohen, Y., 2013. Modeling of the diffusion MR signal in calibrated model systems and nerves. NMR Biomed. 26, 1787–1795.

Ning, L., Setsompop, K., Westin, C.-F., Rathi, Y., 2016. New insights about time-varying diffusivity and its estimation from diffusion MRI. Magn. Reson. Med. https://doi.org/10.1002/mrm.26403

Novikov, D.S., Jespersen, S.N., Kiselev, V.G., Fieremans, E., 2016. Quantifying brain microstructure with diffusion MRI: Theory and parameter estimation. arXiv [physics.bio-ph].

Oh, J., Sotirchos, E.S., Saidha, S., Whetstone, A., Chen, M., Newsome, S.D., Zackowski, K., Balcer, L.J., Frohman, E., Prince, J., Diener-West, M., Reich, D.S., Calabresi, P.A., 2015. Relationships between quantitative spinal cord MRI and retinal layers in multiple sclerosis. Neurology 84, 720–728.

Otsu, N., 1979. A Threshold Selection Method from Gray-Level Histograms. IEEE Trans. Syst. Man Cybern. 9, 62–66.

Palacios, E.M., Martin, A.J., Boss, M.A., Ezekiel, F., Chang, Y.S., Yuh, E.L., Vassar, M.J., Schnyer, D.M., MacDonald, C.L., Crawford, K.L., Irimia, A., Toga, A.W., Mukherjee, P., TRACK-TBI Investigators, 2017. Toward Precision and Reproducibility of Diffusion Tensor Imaging: A Multicenter Diffusion Phantom and Traveling Volunteer Study. AJNR Am. J. Neuroradiol. 38, 537–545.

Price, W.S., 1998. Pulsed-field gradient nuclear magnetic resonance as a tool for studying

translational diffusion: Part II. Experimental aspects. Concepts Magn. Reson. 10, 197–237.

Price, W.S., 1997. Pulsed-field gradient nuclear magnetic resonance as a tool for studying translational diffusion: Part 1. Basic theory. Concepts Magn. Reson. 9, 299–336.

Ronen, I., Budde, M., Ercan, E., Annese, J., Techawiboonwong, A., Webb, A., 2014. Microstructural organization of axons in the human corpus callosum quantified by diffusion-weighted magnetic resonance spectroscopy of N-acetylaspartate and post-mortem histology. Brain Struct. Funct. 219, 1773–1785.

Ronneberger, O., Fischer, P., Brox, T., 2015. U-Net: Convolutional Networks for Biomedical Image Segmentation, in: Navab, N., Hornegger, J., Wells, W.M., Frangi, A.F. (Eds.), Medical Image Computing and Computer-Assisted Intervention – MICCAI 2015, Lecture Notes in Computer Science. Presented at the International Conference on Medical Image Computing and Computer-Assisted Intervention, Springer International Publishing, pp. 234–241.

Schröder, J.M., Bohl, J., von Bardeleben, U., 1988. Changes of the ratio between myelin thickness and axon diameter in human developing sural, femoral, ulnar, facial, and trochlear nerves. Acta Neuropathol. 76, 471–483.

Smith, S.A., Jones, C.K., Gifford, A., Belegu, V., Chodkowski, B., Farrell, J.A.D., Landman, B.A., Reich, D.S., Calabresi, P.A., McDonald, J.W., van Zijl, P.C.M., 2010. Reproducibility of tract-specific magnetization transfer and diffusion tensor imaging in the cervical spinal cord at 3 tesla. NMR Biomed. 23, 207–217.

Sullivan, D.C., Obuchowski, N.A., Kessler, L.G., Raunig, D.L., Gatsonis, C., Huang, E.P., Kondratovich, M., McShane, L.M., Reeves, A.P., Barboriak, D.P., Guimaraes, A.R., Wahl, R.L., RSNA-QIBA Metrology Working Group, 2015. Metrology Standards for Quantitative Imaging Biomarkers. Radiology 277, 813–825.

Talbott, J.F., Nout-Lomas, Y.S., Wendland, M.F., Mukherjee, P., Huie, J.R., Hess, C.P., Mabray, M.C., Bresnahan, J.C., Beattie, M.S., 2016. Diffusion-Weighted Magnetic Resonance Imaging Characterization of White Matter Injury Produced by Axon-Sparing Demyelination and Severe Contusion Spinal Cord Injury in Rats. J. Neurotrauma 33, 929–942.

Torquato, S., 2013. Random Heterogeneous Materials: Microstructure and Macroscopic Properties. Springer Science & Business Media.

West, K.L., Kelm, N.D., Carson, R.P., Gochberg, D.F., Ess, K.C., Does, M.D., 2016. Myelin volume fraction imaging with MRI. Neuroimage. https://doi.org/10.1016/j.neuroimage.2016.12.067

Zelinka, I., 2004. SOMA — Self-Organizing Migrating Algorithm, in: New Optimization Techniques in Engineering, Studies in Fuzziness and Soft Computing. Springer Berlin Heidelberg, pp. 167–217.

Arciénega, I.I., Brunet, J.F., Bloch, J., Badaut, J., 2010. Cell locations for AQP1, AQP4 and 9 in the non-human primate brain. Neuroscience 167, 1103–1114.

Assaf, Y., Cohen, Y., 1998. Non-mono-exponential attenuation of water and N-acetyl aspartate signals due to diffusion in brain tissue. J. Magn. Reson. 131, 69–85.

Bourne, G., 2012. The Structure and Function of Nervous Tissue V2: Structure I. Elsevier.

Cohen, Y., Anaby, D., Morozov, D., 2016. Diffusion MRI of the spinal cord: from structural studies to pathology. NMR Biomed. https://doi.org/10.1002/nbm.3592

Cohen-Adad, J., De Leener, B., Benhamou, M., Cadotte, D., Fleet, D., Cadotte, A., Fehlings, M.G., Pelletier Paquette, J.P., Thong, W., Taso, M., Collins, D.L., Callot, V., Fonov, V., 2014. Spinal Cord Toolbox: an open-source framework for processing spinal cord MRI data. Proceedings of the 20th Annual Meeting of OHBM, Hamburg, Germany 3633.

Deoni, S.C.L., Rutt, B.K., Peters, T.M., 2003. Rapid combined T1 and T2 mapping using gradient recalled acquisition in the steady state. Magn. Reson. Med. 49, 515–526.

Dortch, R.D., Moore, J., Li, K., Jankiewicz, M., Gochberg, D.F., Hirtle, J.A., Gore, J.C., Smith, S.A., 2013. Quantitative magnetization transfer imaging of human brain at 7 T. Neuroimage 64, 640–649.

Duong, T.Q., Ackerman, J.J., Ying, H.S., Neil, J.J., 1998a. Evaluation of extra- and intracellular apparent diffusion in normal and globally ischemic rat brain via 19F NMR. Magn. Reson. Med. 40, 1–13.

Duong, T.Q., Springer, C.S., Sotak, C.H., Bretthorst, G.L., Vetek, G., Palyka, I., Ackerman, J., Neil, J.J., 1998b. Evaluation of equilibrium transcytolemmal water exchange in intact rat brain, in: Proceedings of the 6th Annual Meeting of ISMRM. p. 208.

Dupont, S.M., De Leener, B., Taso, M., Le Troter, A., Stikov, N., Callot, V., Cohen-Adad, J., 2016. Fully-integrated framework for the segmentation and registration of the spinal cord white and gray matter. Neuroimage. https://doi.org/10.1016/j.neuroimage.2016.09.026

Duval, T., Lévy, S., Stikov, N., Campbell, J., Mezer, A., Witzel, T., Keil, B., Smith, V., Wald, L.L., Klawiter, E., Cohen-Adad, J., 2017. g-Ratio weighted imaging of the human spinal cord in vivo. Neuroimage 145, 11–23.

European Society of Radiology (ESR), 2015. Magnetic Resonance Fingerprinting - a

promising new approach to obtain standardized imaging biomarkers from MRI. Insights Imaging 6, 163–165.

Ferizi, U., Schneider, T., Witzel, T., Wald, L.L., Zhang, H., Wheeler-Kingshott, C.A.M., Alexander, D.C., 2015. White matter compartment models for in vivo diffusion MRI at 300mT/m. Neuroimage 118, 468–483.

Fields, R.D., 2008. White matter in learning, cognition and psychiatric disorders. Trends Neurosci. 31, 361–370.

Fieremans, E., Burcaw, L.M., Lee, H.-H., Lemberskiy, G., Veraart, J., Novikov, D.S., 2016. In vivo observation and biophysical interpretation of time-dependent diffusion in human white matter. Neuroimage 129, 414–427.

Fieremans, E., Jensen, J.H., Helpern, J.A., 2011. White matter characterization with diffusional kurtosis imaging. Neuroimage 58, 177–188.

Grussu, F., Schneider, T., Yates, R.L., Zhang, H., Wheeler-Kingshott, C.A.M.G., DeLuca, G.C., Alexander, D.C., 2016. A framework for optimal whole-sample histological quantification of neurite orientation dispersion in the human spinal cord. J. Neurosci. Methods 273, 20–32.

Henkelman, R.M., Huang, X., Xiang, Q.S., Stanisz, G.J., Swanson, S.D., Bronskill, M.J., 1993. Quantitative interpretation of magnetization transfer. Magn. Reson. Med. 29, 759–766.

Innocenti, G.M., Caminiti, R., Aboitiz, F., 2015. Comments on the paper by Horowitz et al. (2014). Brain Struct. Funct. 220, 1789–1790.

Isola, R., 2008. Packing of granular materials. University of Nottingham.

Johansen-Berg, H., Behrens, T.E.J., 2013. Diffusion MRI: From Quantitative Measurement to In vivo Neuroanatomy. Elsevier Science.

Kipp, L., Cawley, N., Prados, F., Schneider, T., Ourselin, S., Wheeler-Kingshott, C., Miller, D., Thompson, A., Ciccarelli, O., 2016. Neurite Orientation Dispersion and Density Imaging (NODDI) in RRMS (P4.159). Neurology 86, 4.

Lamantia, A.S., Rakic, P., 1990. Cytological and quantitative characteristics of four cerebral commissures in the rhesus monkey. J. Comp. Neurol. 291, 520–537.

Lulé, D., Diekmann, V., Müller, H.-P., Kassubek, J., Ludolph, A.C., Birbaumer, N., 2010. Neuroimaging of multimodal sensory stimulation in amyotrophic lateral sclerosis. J. Neurol. Neurosurg. Psychiatry 81, 899–906.

Ma, D., Gulani, V., Seiberlich, N., Liu, K., Sunshine, J.L., Duerk, J.L., Griswold, M.A., 2013. Magnetic resonance fingerprinting. Nature 495, 187–192.

Meier, C., Dreher, W., Leibfritz, D., 2003. Diffusion in compartmental systems. II. Diffusion-weighted measurements of rat brain tissue in vivo and postmortem at very large b-values. Magn. Reson. Med. 50, 510–514.

Meyers, S.M., Vavasour, I.M., Mädler, B., Harris, T., Fu, E., Li, D.K.B., Traboulsee, A.L., MacKay, A.L., Laule, C., 2013. Multicenter measurements of myelin water fraction and geometric mean T2 : intra- and intersite reproducibility. J. Magn. Reson. Imaging 38, 1445–1453.

Nielsen, S., Nagelhus, E.A., Amiry-Moghaddam, M., Bourque, C., Agre, P., Ottersen, O.P., 1997. Specialized membrane domains for water transport in glial cells: high-resolution immunogold cytochemistry of aquaporin-4 in rat brain. J. Neurosci. 17, 171–180.

Nunes, D., Cruz, T.L., Jespersen, S.N., Shemesh, N., 2016. Mapping axonal density and average diameter using non-monotonic time-dependent gradient-echo MRI. arXiv [physics.med-ph].

Olude, M.A., Mustapha, O.A., Aderounmu, O.A., Olopade, J.O., Ihunwo, A.O., 2015. Astrocyte morphology, heterogeneity, and density in the developing African giant rat (Cricetomys gambianus). Front. Neuroanat. 9, 67.

Pasternak, O., Sochen, N., Gur, Y., Intrator, N., Assaf, Y., 2009. Free water elimination and mapping from diffusion MRI. Magn. Reson. Med. 62, 717–730.

Pizzolato, M., Wassermann, D., Duval, T., Campbell, J.S.W., Boutelier, T., Cohen-Adad, J., Deriche, R., 2016. A Temperature Phantom to Probe the Ensemble Average Propagator Asymmetry: An In-Silico Study, in: Computational Diffusion MRI. Springer International Publishing, pp. 183–194.

Sled, J.G., Pike, G.B., 2001. Quantitative imaging of magnetization transfer exchange and relaxation properties in vivo using MRI. Magn. Reson. Med. 46, 923–931.

Syková, E., Vargová, L., Prokopová, S., Simonová, Z., 1999. Glial swelling and astrogliosis produce diffusion barriers in the rat spinal cord. Glia 25, 56–70.

Topfer, R., Starewicz, P., Lo, K.-M., Metzemaekers, K., Jette, D., Hetherington, H.P., Stikov, N., Cohen-Adad, J., 2016. A 24-channel shim array for the human spinal cord: Design, evaluation, and application. Magn. Reson. Med. https://doi.org/10.1002/mrm.26354

Trapp, B.D., Kidd, G.J., 2004. Structure of the myelinated axon. Myelin biology and disorders.

W. J., J.A., Arnold, J.M., Gilbert, D.L., 2013. Squid as Experimental Animals. Springer US.

Yarnykh, V.L., 2010. Optimal radiofrequency and gradient spoiling for improved accuracy of T1 and B1 measurements using fast steady-state techniques. Magn. Reson. Med. 63, 1610–1626.

Yu, A.B., Bridgwater, J., Burbidge, A., 1997. On the modelling of the packing of fine particles. Powder Technol.

Zaimi, A., Duval, T., Gasecka, A., Côté, D., Stikov, N., Cohen-Adad, J., 2016. AxonSeg: Open Source Software for Axon and Myelin Segmentation and Morphometric Analysis. Front. Neuroinform. 10, 37.

Aboitiz, F., Scheibel, A.B., Fisher, R.S., Zaidel, E., 1992. Fiber composition of the human corpus callosum. Brain Res. 598, 143–153.

Badaut, J., Ashwal, S., Adami, A., Tone, B., Recker, R., Spagnoli, D., Ternon, B., Obenaus, A., 2011. Brain water mobility decreases after astrocytic aquaporin-4 inhibition using RNA interference. J. Cereb. Blood Flow Metab. 31, 819–831.

Campbell, J.S.W., Leppert, I.R., Boudreau, M., Narayanan, S., Cohen-Adad, J., Pike, G.B., Stikov, N., 2016. Mapping the myelin g-ratio: promises and pitfalls, in: Proceedings of the 24th Annual Meeting of ISMRM. p. 1501.

Clare, S., Jezzard, P., 2001. Rapid T1 mapping using multislice echo planar imaging. Magn. Reson. Med. 45, 630–634.

Daducci, A., Canales-Rodríguez, E.J., Zhang, H., Dyrby, T.B., Alexander, D.C., Thiran, J.-P., 2015. Accelerated Microstructure Imaging via Convex Optimization (AMICO) from diffusion MRI data. Neuroimage 105, 32–44.

Duval, T., Mingasson, T., Klawiter, E., Stikov, N., Cohen-Adad, J., 2017. Translating AxCaliber on a Clinical System : 600mT/m Versus Optimized 80mT/m Protocol, in: Proceedings of the 25th Annual Meeting of ISMRM. p. 1760.

Einstein, A., 1956. Investigations on the Theory of the Brownian Movement, Dover Books on Physics Series. Dover Publications.

Fatouros, P.P., Marmarou, A., 1999. Use of magnetic resonance imaging for in vivo measurements of water content in human brain: method and normal values. J. Neurosurg. 90, 109–115.

Fieremans, E., De Deene, Y., Delputte, S., Ozdemir, M.S., D'Asseler, Y., Vlassenbroeck, J., Deblaere, K., Achten, E., Lemahieu, I., 2008. Simulation and experimental verification of the diffusion in an anisotropic fiber phantom. J. Magn. Reson. 190, 189–199.

FitzGibbon, T., Nestorovski, Z., 2013. Human intraretinal myelination: axon diameters and axon/myelin thickness ratios. Indian J. Ophthalmol. 61, 567–575.

Fujiyoshi, K., Hikishima, K., Nakahara, J., Tsuji, O., Hata, J., Konomi, T., Nagai, T., Shibata, S., Kaneko, S., Iwanami, A., Momoshima, S., Takahashi, S., Jinzaki, M., Suzuki, N., Toyama, Y., Nakamura, M., Okano, H., 2016. Application of q-Space Diffusion MRI for the Visualization of White Matter. J. Neurosci. 36, 2796–2808.

Giuliodori, M.J., DiCarlo, S.E., 2004. Myelinated vs. unmyelinated nerve conduction: a novel way of understanding the mechanisms. Adv. Physiol. Educ. 28, 80–81.

Golabchi, F.N., Brooks, D.H., Hoge, W.S., De Girolami, U., Maier, S.E., 2010. Pixel-based comparison of spinal cord MR diffusion anisotropy with axon packing parameters. Magn. Reson. Med. 63, 1510–1519.

Harrison, R., Bronskill, M.J., Henkelman, R.M., 1995. Magnetization transfer and T2 relaxation components in tissue. Magn. Reson. Med. 33, 490–496.

Helms, G., Dathe, H., Kallenberg, K., Dechent, P., 2008. High-resolution maps of magnetization transfer with inherent correction for RF inhomogeneity and T1 relaxation obtained from 3D FLASH MRI. Magn. Reson. Med. 60, 1396–1407.

Herculano-Houzel, S., 2014. The glia/neuron ratio: how it varies uniformly across brain structures and species and what that means for brain physiology and evolution. Glia 62, 1377–1391.

Koenig, S.H., Brown, R.D., 3rd, Spiller, M., Lundbom, N., 1990. Relaxometry of brain: why white matter appears bright in MRI. Magn. Reson. Med. 14, 482–495.

Lee, H.-H., Veraart, J., Novikov, D.S., Fieremans, E., 2016. What dominates the diffusivity time dependence transverse to axons: Intra- or extra-axonal water?, in: Proceedings of the 24th Annual Meeting of ISMRM. p. 656.

Levesque, I.R., Sled, J.G., Narayanan, S., Giacomini, P.S., Ribeiro, L.T., Arnold, D.L., Pike, G.B., 2010. Reproducibility of quantitative magnetization-transfer imaging parameters from repeated measurements. Magn. Reson. Med. 64, 391–400.

Liewald, D., Miller, R., Logothetis, N., Wagner, H.-J., Schüz, A., 2014. Distribution of axon diameters in cortical white matter: an electron-microscopic study on three human brains

and a macaque. Biol. Cybern. 108, 541–557.

Mangeat, G., Govindarajan, S.T., Mainero, C., Cohen-Adad, J., 2015. Multivariate combination of magnetization transfer, T2* and B0 orientation to study the myelo-architecture of the in vivo human cortex. Neuroimage 119, 89–102.

Marques, J.P., Gruetter, R., 2013. New developments and applications of the MP2RAGE sequence--focusing the contrast and high spatial resolution R1 mapping. PLoS One 8, e69294.

Marques, J.P., Kober, T., Krueger, G., van der Zwaag, W., Van de Moortele, P.-F., Gruetter, R., 2010. MP2RAGE, a self bias-field corrected sequence for improved segmentation and T1-mapping at high field. Neuroimage 49, 1271–1281.

Oh, S.-H., Bilello, M., Schindler, M., Markowitz, C.E., Detre, J.A., Lee, J., 2013. Direct visualization of short transverse relaxation time component (ViSTa). Neuroimage 83, 485–492.

Olivares, R., Montiel, J., Aboitiz, F., 2001. Species differences and similarities in the fine structure of the mammalian corpus callosum. Brain Behav. Evol. 57, 98–105.

Pelvig, D.P., Pakkenberg, H., Stark, A.K., Pakkenberg, B., 2008. Neocortical glial cell numbers in human brains. Neurobiol. Aging 29, 1754–1762.

Prasloski, T., Rauscher, A., MacKay, A.L., Hodgson, M., Vavasour, I.M., Laule, C., Mädler, B., 2012. Rapid whole cerebrum myelin water imaging using a 3D GRASE sequence. Neuroimage 63, 533–539.

Remahl, S., Hildebrand, C., 1982. Changing relation between onset of myelination and axon diameter range in developing feline white matter. J. Neurol. Sci. 54, 33–45.

Sacolick, L.I., Wiesinger, F., Hancu, I., Vogel, M.W., 2010. B1 mapping by Bloch-Siegert shift. Magn. Reson. Med. 63, 1315–1322.

Sheth, V., Shao, H., Chen, J., Vandenberg, S., Corey-Bloom, J., Bydder, G.M., Du, J., 2016. Magnetic resonance imaging of myelin using ultrashort Echo time (UTE) pulse sequences: Phantom, specimen, volunteer and multiple sclerosis patient studies. Neuroimage 136, 37–44.

Smith, S.M., Jenkinson, M., Woolrich, M.W., Beckmann, C.F., Behrens, T.E.J., Johansen-Berg, H., Bannister, P.R., De Luca, M., Drobnjak, I., Flitney, D.E., Niazy, R.K., Saunders, J., Vickers, J., Zhang, Y., De Stefano, N., Brady, J.M., Matthews, P.M., 2004. Advances in functional and structural MR image analysis and implementation as FSL. Neuroimage 23 Suppl 1, S208–19.

Spurr, A.R., 1969. A low-viscosity epoxy resin embedding medium for electron microscopy. J. Ultrastruct. Res. 26, 31–43.

Szafer, A., Zhong, J., Gore, J.C., 1995. Theoretical Model for Water Diffusion in Tissues. Magn. Reson. Med. 33, 697–712.

Taso, M., Girard, O.M., Duhamel, G., Le Troter, A., Feiweier, T., Guye, M., Ranjeva, J.-P., Callot, V., 2016. Tract-specific and age-related variations of the spinal cord microstructure: a multi-parametric MRI study using diffusion tensor imaging (DTI) and inhomogeneous magnetization transfer (ihMT). NMR Biomed. https://doi.org/10.1002/nbm.3530

Tofts, P., 2003. Quantitative MRI of the Brain: Measuring Changes Caused by Disease. John Wiley & Sons.

Vavasour, I.M., Laule, C., Li, D.K.B., Traboulsee, A.L., MacKay, A.L., 2011. Is the magnetization transfer ratio a marker for myelin in multiple sclerosis? J. Magn. Reson. Imaging 33, 713–718.

Vollmar, C., O'Muircheartaigh, J., Barker, G.J., Symms, M.R., Thompson, P., Kumari, V., Duncan, J.S., Richardson, M.P., Koepp, M.J., 2010. Identical, but not the same: intra-site and inter-site reproducibility of fractional anisotropy measures on two 3.0T scanners. Neuroimage 51, 1384–1394.

Ward, K., Schussheim, A.E., Balaban, R.S., 2003. Contribution of mitochondria to cardiac muscle water/macromolecule proton magnetization transfer. Magn. Reson. Med. 50, 1312–1316.

Weiskopf, N., Suckling, J., Williams, G., Correia, M.M., Inkster, B., Tait, R., Ooi, C., Bullmore, E.T., Lutti, A., 2013. Quantitative multi-parameter mapping of R1, PD(*), MT, and R2(*) at 3T: a multi-center validation. Front. Neurosci. 7, 95.

West, K.L., Kelm, N.D., Gochberg, D.F., Carson, R.P., Ess, K.C., Does, M.D., 2016. Quantitative Estimates of Myelin Volume Fraction from T2 and Magnetization Transfer, in: Proceedings of the 24th Annual Meeting of ISMRM. p. 1277.

Azevedo, F.A.C., Carvalho, L.R.B., Grinberg, L.T., Farfel, J.M., Ferretti, R.E.L., Leite, R.E.P., Jacob Filho, W., Lent, R., Herculano-Houzel, S., 2009. Equal numbers of neuronal and nonneuronal cells make the human brain an isometrically scaled-up primate brain. J. Comp. Neurol. 513, 532–541.

Baumann, N., Pham-Dinh, D., 2001. Biology of oligodendrocyte and myelin in the mammalian central nervous system. Physiol. Rev. 81, 871–927.

Bégin, S., Bélanger, E., Laffray, S., Vallée, R., Côté, D., 2009. In vivo optical monitoring of tissue pathologies and diseases with vibrational contrast. J. Biophotonics 2, 632–642.

Bélanger, E., Henry, F.P., Vallée, R., Randolph, M.A., Kochevar, I.E., Winograd, J.M., Lin, C.P., Côté, D., 2011. In vivo evaluation of demyelination and remyelination in a nerve crush injury model. Biomed. Opt. Express 2, 2698–2708.

Bot, J.C.J., Blezer, E.L.A., Kamphorst, W., Lycklama A Nijeholt, G.J., Ader, H.J., Castelijns, J.A., Ig, K.N., Bergers, E., Ravid, R., Polman, C., Barkhof, F., 2004. The spinal cord in multiple sclerosis: relationship of high-spatial-resolution quantitative MR imaging findings to histopathologic results. Radiology 233, 531–540.

Cabana, J.-F., Gu, Y., Boudreau, M., Levesque, I.R., Atchia, Y., Sled, J.G., Narayanan, S., Arnold, D.L., Pike, G.B., Cohen-Adad, J., Duval, T., Vuong, M.-T., Stikov, N., 2015. Quantitative magnetization transfer imaging made easy with qMTLab: Software for data simulation, analysis, and visualization. Concepts Magn. Reson. 44A, 263–277.

De Santis, S., Jones, D.K., Roebroeck, A., 2016. Including diffusion time dependence in the extra-axonal space improves in vivo estimates of axonal diameter and density in human white matter. Neuroimage 130, 91–103.

Fick, R.H.J., Wassermann, D., Caruyer, E., Deriche, R., 2016. MAPL: Tissue microstructure estimation using Laplacian-regularized MAP-MRI and its application to HCP data. Neuroimage. https://doi.org/10.1016/j.neuroimage.2016.03.046

Fox, R.J., Cronin, T., Lin, J., Wang, X., Sakaie, K., Ontaneda, D., Mahmoud, S.Y., Lowe, M.J., Phillips, M.D., 2011. Measuring myelin repair and axonal loss with diffusion tensor imaging. AJNR Am. J. Neuroradiol. 32, 85–91.

Hall, M.G., Alexander, D.C., 2009. Convergence and parameter choice for Monte-Carlo simulations of diffusion MRI. IEEE Trans. Med. Imaging 28, 1354–1364.

Harkins, K.D., Dula, A.N., Does, M.D., 2012. Effect of intercompartmental water exchange on the apparent myelin water fraction in multiexponential T2 measurements of rat spinal cord. Magn. Reson. Med. 67, 793–800.

Harkins, K.D., Xu, J., Dula, A.N., Li, K., Valentine, W.M., Gochberg, D.F., Gore, J.C., Does, M.D., 2016. The microstructural correlates of T1 in white matter. Magn. Reson. Med. 75, 1341–1345.

Hellerbach, A., Schuster, V., Jansen, A., Sommer, J., 2013. MRI phantoms - are there alternatives to agar? PLoS One 8, e70343.

Hilgetag, C.C., Barbas, H., 2009. Are there ten times more glia than neurons in the brain? Brain Struct. Funct. 213, 365–366.

Kawai, K., Itoh, T., Itoh, A., Horiuchi, M., Wakayama, K., Bannerman, P., Garbern, J.Y., Pleasure, D., Lindsten, T., 2009. Maintenance of the relative proportion of oligodendrocytes to axons even in the absence of BAX and BAK. Eur. J. Neurosci. 30, 2030–2041.

Kim, J.H., Song, S.-K., 2013. Diffusion tensor imaging of the mouse brainstem and cervical spinal cord. Nat. Protoc. 8, 409–417.

Kolind, S., Seddigh, A., Combes, A., Russell-Schulz, B., Tam, R., Yogendrakumar, V., Deoni, S., Sibtain, N.A., Traboulsee, A., Williams, S.C.R., Barker, G.J., Brex, P.A., 2015. Brain and cord myelin water imaging: a progressive multiple sclerosis biomarker. Neuroimage Clin 9, 574–580.

Kolind, S.H., Deoni, S.C., 2011. Rapid three-dimensional multicomponent relaxation imaging of the cervical spinal cord. Magn. Reson. Med. 65, 551–556.

Kucharczyk, W., Macdonald, P.M., Stanisz, G.J., Henkelman, R.M., 1994. Relaxivity and magnetization transfer of white matter lipids at MR imaging: importance of cerebrosides and pH. Radiology 192, 521–529.

Lajtha, A., 2013. Pathological Neurochemistry. Springer US.

Levesque, I.R., Pike, G.B., 2009. Characterizing healthy and diseased white matter using quantitative magnetization transfer and multicomponent T2 relaxometry: A unified view via a four-pool model. Magn. Reson. Med. 62, 1487–1496.

Lévy, S., n.d. CARACTÉRISATION DE LA MICROSTRUCTURE DES VOIES SPINALES HUMAINES PAR IRM MULTIPARAMÉTRIQUE. Polytechnique Montréal.

Li, Z., Du, J., Sun, H., Mang, J., He, J., Wang, J., Liu, H., Xu, Z., 2014. Effects of the combination of methylprednisolone with aminoguanidine on functional recovery in rats following spinal cord injury. Exp. Ther. Med. 7, 1605–1610.

MacKay, A., Whittall, K., Adler, J., Li, D., Paty, D., Graeb, D., 1994. In vivo visualization of myelin water in brain by magnetic resonance. Magn. Reson. Med. 31, 673–677.

Morell, P., 2013. Myelin.

Morell, P., Lipkind, R., Greenfield, S., 1973. Protein composition of myelin from brain and spinal cord of several species. Brain Res. 58, 510–514.

Nijeholt, G.J., Bergers, E., Kamphorst, W., Bot, J., Nicolay, K., Castelijns, J.A., van Waesberghe, J.H., Ravid, R., Polman, C.H., Barkhof, F., 2001. Post-mortem high-resolution MRI of the spinal cord in multiple sclerosis: a correlative study with conventional MRI, histopathology and clinical phenotype. Brain 124, 154–166.

Nishimoto, S., Tanaka, H., Okamoto, M., Okada, K., Murase, T., Yoshikawa, H., 2015. Methylcobalamin promotes the differentiation of Schwann cells and remyelination in lysophosphatidylcholine-induced demyelination of the rat sciatic nerve. Front. Cell. Neurosci. 9, 298.

Norton, W.T., Cammer, W., 1984. Isolation and Characterization of Myelin, in: Myelin. Springer US, pp. 147–195.

Saito, N., Watanabe, M., Sakai, O., Jara, H., 2012. Human lifespan age-related changes of the brain proton density by quantitative MRI, in: Proceedings of the 20th Annual Meeting of ISMRM. p. 780.

Santis, S., Assaf, Y., Evans, C.J., Jones, D.K., 2014. Improved precision in CHARMED assessment of white matter through sampling scheme optimization and model parsimony testing. Magn. Reson. Med. 71, 661–671.

Schmierer, K., Wheeler-Kingshott, C.A.M., Tozer, D.J., Boulby, P.A., Parkes, H.G., Yousry, T.A., Scaravilli, F., Barker, G.J., Tofts, P.S., Miller, D.H., 2008. Quantitative magnetic resonance of postmortem multiple sclerosis brain before and after fixation. Magn. Reson. Med. 59, 268–277.

Sepehrband, F., Alexander, D.C., Kurniawan, N.D., Reutens, D.C., Yang, Z., 2016. Towards higher sensitivity and stability of axon diameter estimation with diffusion-weighted MRI. NMR Biomed. 29, 293–308.

Tariq, M., Schneider, T., Alexander, D.C., Wheeler-Kingshot, C., Zhang, H., 2012. Scan-rescan reproducibility of neurite microstructure estimates using NODDI, in: Xie, X. (Ed.), Medical Image Understanding and Analysis 2012: Proceedings of the 16th Conference on Medical Image Understanding and Analysis. Presented at the 16th Conference on Medical Image Understanding and Analysis, The British Machine Vision Association and Society for Pattern Recognition, Swansea, UK, pp. 255–261.

Taso, M., Girard, O.M., Duhamel, G., Le Troter, A., Ribeiro, G., Feiweier, T., Guye, M., Ranjeva, J.-P., Callot, V., 2015. Regional and age-related variations of the healthy spinal cord structure assessed by multimodal MRI (diffusion, inhomogeneous magnetization transfer, ihMT), in: Proceedings of the 23th Annual Meeting of ISMRM. Toronto.

van der Knaap, M.S., Valk, J., 2013. Magnetic Resonance of Myelin, Myelination and Myelin Disorders. Springer Berlin Heidelberg.

Waehneldt, T.V., 1978. Density and protein profiles of myelin from two regions of young and adult rat CNS. Brain Res. Bull. 3, 37–44.

Wolff, S.D., Balaban, R.S., 1989. Magnetization transfer contrast (MTC) and tissue water proton relaxation in vivo. Magn. Reson. Med. 10, 135–144.

Albert, M., Antel, J., Brück, W., Stadelmann, C., 2007. Extensive cortical remyelination in patients with chronic multiple sclerosis. Brain Pathol. 17, 129–138.

Berthold, C.H., Nilsson, I., Rydmark, M., 1983. Axon diameter and myelin sheath thickness in nerve fibres of the ventral root of the seventh lumbar nerve in the adult and developing cat. J. Anat. 3).

Brander, A., Kataja, A., Saastamoinen, A., Ryymin, P., Huhtala, H., Ohman, J., Soimakallio, S., Dastidar, P., 2010. Diffusion tensor imaging of the brain in a healthy adult population: Normative values and measurement reproducibility at 3 T and 1.5 T. Acta radiol. 51, 800–807.

Chin, C.-L., Wehrli, F.W., Hwang, S.N., Takahashi, M., Hackney, D.B., 2002. Biexponential diffusion attenuation in the rat spinal cord: computer simulations based on anatomic images of axonal architecture. Magn. Reson. Med. 47, 455–460.

Chong, A.L., Chandra, R.V., Chuah, K.C., Roberts, E.L., Stuckey, S.L., 2016. Proton Density MRI Increases Detection of Cervical Spinal Cord Multiple Sclerosis Lesions Compared with T2-Weighted Fast Spin-Echo. AJNR Am. J. Neuroradiol. 37, 180–184.

Cohen-Adad, J., Wheeler-Kingshott, C., 2014. Quantitative MRI of the Spinal Cord. Elsevier Science.

Cragg, B., 1980. Preservation of extracellular space during fixation of the brain for electron microscopy. Tissue Cell 12, 63–72.

Dean, D.C., O'Muircheartaigh, J., Dirks, H., Travers, B.G., Adluru, N., Alexander, A.L., Deoni, S.C.L., 2016. Mapping an index of the myelin g-ratio in infants using magnetic resonance imaging. Neuroimage 132, 225–237.

Dean_NIMG-15-2596_revision.pdf, n.d.

Finean, J.B., 1960. Electron microscope and x-ray diffraction studies of the effects of dehydration on the structure of nerve myelin. II. Optic nerve. J. Biophys. Biochem. Cytol. 8, 31–37.

Franklin, R.J.M., 2002. Why does remyelination fail in multiple sclerosis? Nat. Rev.

Neurosci. 3, 705–714.

Frohman, E.M., Racke, M.K., Raine, C.S., 2006. Multiple Sclerosis — The Plaque and Its Pathogenesis. N. Engl. J. Med. 354, 942–955.

Guttmann, C.R., Ahn, S.S., Hsu, L., Kikinis, R., Jolesz, F.A., 1995. The evolution of multiple sclerosis lesions on serial MR. AJNR Am. J. Neuroradiol. 16, 1481–1491.

Hua, Y., Laserstein, P., Helmstaedter, M., 2015. Large-volume en-bloc staining for electron microscopy-based connectomics. Nat. Commun. 6, 7923.

Le Bihan, D., 2007. The “wet mind”: water and functional neuroimaging. Phys. Med. Biol. 52, R57–90.

Mezer, A., Rokem, A., Hastie, T., Wandell, B., 2015. Proton density mapping: Removing receive-inhomogeneity using multi-coil information and T1 regularization, in: Proceedings of the 23th Annual Meeting of ISMRM. Toronto.

Mikula, S., Binding, J., Denk, W., 2012. Staining and embedding the whole mouse brain for electron microscopy. Nat. Methods 9, 1198–1201.

Minty, E.P., Bjarnason, T.A., Laule, C., MacKay, A.L., 2009. Myelin water measurement in the spinal cord. Magn. Reson. Med. 61, 883–892.

Mohammadi, S., Carey, D., Dick, F., Diedrichsen, J., Sereno, M.I., Reisert, M., Callaghan, M.F., Weiskopf, N., 2015. Whole-Brain In-vivo Measurements of the Axonal G-Ratio in a Group of 37 Healthy Volunteers. Front. Neurosci. 9, 441.

Morell, P., Quarles, R.H., 1999. Myelin Formation, Structure and Biochemistry. Lippincott-Raven.

Morrell, G.R., Schabel, M.C., 2010. An analysis of the accuracy of magnetic resonance flip angle measurement methods. Phys. Med. Biol. 55, 6157–6174.

Mottershead, J.P., Schmierer, K., Clemence, M., Thornton, J.S., Scaravilli, F., Barker, G.J., Tofts, P.S., Newcombe, J., Cuzner, M.L., Ordidge, R.J., McDonald, W.I., Miller, D.H., 2003. High field MRI correlates of myelin content and axonal density in multiple sclerosis--a post-mortem study of the spinal cord. J. Neurol. 250, 1293–1301.

Norton, W.T., Autilio, L.A., 1966. The lipid composition of purified bovine brain myelin. J. Neurochem. 13, 213–222.

O’Brien, J.S., Sampson, E.L., 1965. Lipid composition of the normal human brain: gray matter, white matter, and myelin. J. Lipid Res. 6, 537–544.

O'Brien, J.S., Sampson, E.L., Stern, M.B., 1967. Lipid composition of myelin from the peripheral nervous system. Intradural spinal roots. J. Neurochem. 14, 357–365.

Ontaneda, D., Sakaie, K., Lin, J., Wang, X., Lowe, M.J., Phillips, M.D., Fox, R.J., 2014. Identifying the start of multiple sclerosis injury: a serial DTI study. J. Neuroimaging 24, 569–576.

Paus, T., Pesaresi, M., French, L., 2014. White matter as a transport system. Neuroscience 276, 117–125.

Pesaresi, M., Soon-Shiong, R., French, L., Kaplan, D.R., Miller, F.D., Paus, T., 2015. Axon diameter and axonal transport: In vivo and in vitro effects of androgens. Neuroimage 115, 191–201.

Prineas, J.W., Connell, F., 1979. Remyelination in multiple sclerosis. Ann. Neurol. 5, 22–31.

Rovira, A., Auger, C., Alonso, J., 2013. Magnetic resonance monitoring of lesion evolution in multiple sclerosis. Ther. Adv. Neurol. Disord. 6, 298–310.

Shemesh, N., Álvarez, G.A., Frydman, L., 2015. Size Distribution Imaging by Non-Uniform Oscillating-Gradient Spin Echo (NOGSE) MRI. PLoS One 10, e0133201.

Shepherd, V.A., 2006. The cytomatrix as a cooperative system of macromolecular and water networks. Curr. Top. Dev. Biol. 75, 171–223.

Smith, M.E., Sedgewick, L.M., 1975. Studies of the mechanism of demyelination. Regional differences in myelin stability in vitro. J. Neurochem. 24, 763–770.

Stikov, N., Campbell, J.S.W., Stroh, T., Lavelée, M., Frey, S., Novek, J., Nuara, S., Ho, M.-K., Bedell, B.J., Dougherty, R.F., Leppert, I.R., Boudreau, M., Narayanan, S., Duval, T., Cohen-Adad, J., Picard, P.-A., Gasecka, A., Côté, D., Pike, G.B., 2015. Quantitative analysis of the myelin g-ratio from electron microscopy images of the macaque corpus callosum. Data Brief 4, 368–373.

Stüber, C., Morawski, M., Schäfer, A., Labadie, C., Wähnert, M., Leuze, C., Streicher, M., Barapatre, N., Reimann, K., Geyer, S., Spemann, D., Turner, R., 2014. Myelin and iron concentration in the human brain: a quantitative study of MRI contrast. Neuroimage 93 Pt 1, 95–106.

Toews, A.D., Horrocks, L.A., King, J.S., 1976. Simultaneous isolation of purified microsomal and myelin fractions from rat spinal cord. J. Neurochem. 27, 25–31.

Tofts, P.S., 2003. PD: proton density of tissue water. Quantitative MRI of the brain. Wiley,

England 85–109.

Ueno, K., Ando, S., Yu, R.K., 1978. Gangliosides of human, cat, and rabbit spinal cords and cord myelin. J. Lipid Res. 19, 863–871.

Wu, Y., Alexander, A.L., Fleming, J.O., Duncan, I.D., Field, A.S., 2006. Myelin water fraction in human cervical spinal cord in vivo. J. Comput. Assist. Tomogr. 30, 304–306.

Yarnykh, V.L., 2007. Actual flip-angle imaging in the pulsed steady state: a method for rapid three-dimensional mapping of the transmitted radiofrequency field. Magn. Reson. Med. 57, 192–200.

Adluru, G., Gur, Y., Anderson, J.S., Richards, L.G., Adluru, N., DiBella, E.V.R., 2014. Assessment of white matter microstructure in stroke patients using NODDI. Conf. Proc. IEEE Eng. Med. Biol. Soc. 2014, 742–745.

Alexander, A.L., Lee, J.E., Lazar, M., Field, A.S., 2007. Diffusion tensor imaging of the brain. Neurotherapeutics 4, 316–329.

Balezeau, F., Eliat, P.-A., Cayamo, A.B., Saint-Jalmes, H., 2011. Mapping of low flip angles in magnetic resonance. Phys. Med. Biol. 56, 6635–6647.

Barral, J.K., Gudmundson, E., Stikov, N., Etezadi-Amoli, M., Stoica, P., Nishimura, D.G., 2010. A robust methodology for in vivo T1 mapping. Magn. Reson. Med. 64, 1057–1067.

Beirowski, B., Adalbert, R., Wagner, D., Grumme, D.S., Addicks, K., Ribchester, R.R., Coleman, M.P., 2005. The progressive nature of Wallerian degeneration in wild-type and slow Wallerian degeneration (WldS) nerves. BMC Neurosci. 6, 6.

Benninger, Y., Colognato, H., Thurnherr, T., Franklin, R.J.M., Leone, D.P., Atanasoski, S., Nave, K.-A., Ffrench-Constant, C., Suter, U., Relvas, J.B., 2006. Beta1-integrin signaling mediates premyelinating oligodendrocyte survival but is not required for CNS myelination and remyelination. J. Neurosci. 26, 7665–7673.

Byrd, R.H., Gilbert, J.C., Nocedal, J., 2000. A trust region method based on interior point techniques for nonlinear programming. Math. Program. 89, 149–185.

Carvlin, M.J., Asato, R., Hackney, D.B., Kassab, E., Joseph, P.M., 1989. High-resolution MR of the spinal cord in humans and rats. AJNR Am. J. Neuroradiol. 10, 13–17.

Cohen-Adad, J., Lévy, S., Avants, B., 2015. Slice-by-slice regularized registration for spinal cord MRI: SliceReg, in: Proceedings of the 23th Annual Meeting of ISMRM. Toronto.

De Leener, B., Kadoury, S., Cohen-Adad, J., 2014. Robust, accurate and fast automatic

segmentation of the spinal cord. Neuroimage 98, 528–536.

Donell, B.M., n.d. Spinal Cord Axon Segmentation.

Fonov, V.S., Le Troter, A., Taso, M., De Leener, B., Lévêque, G., Benhamou, M., Sdika, M., Benali, H., Pradat, P.-F., Collins, D.L., Callot, V., Cohen-Adad, J., 2014. Framework for integrated MRI average of the spinal cord white and gray matter: the MNI-Poly-AMU template. Neuroimage 102 Pt 2, 817–827.

Fram, E.K., Herfkens, R.J., Johnson, G.A., Glover, G.H., Karis, J.P., Shimakawa, A., Perkins, T.G., Pelc, N.J., 1987. Rapid calculation of T1 using variable flip angle gradient refocused imaging. Magn. Reson. Imaging 5, 201–208.

Guttmann, C.R.G., n.d. Spine [WWW Document]. spinevirtuallab.org. URL https://spinevirtuallab.org/public/#/index

Hartline, D.K., Colman, D.R., 2007. Rapid conduction and the evolution of giant axons and myelinated fibers. Curr. Biol. 17, R29–35.

Holland, G.R., 1982. The effect of buffer molarity on the size, shape and sheath thickness of peripheral myelinated nerve fibres. J. Anat. 135, 183–190.

Hursh, J.B., 1939. Conduction velocity and diameter of nerve fibers. Am. J. Physiol.

Huxley, A.F., Stämpfli, R., 1949. Evidence for saltatory conduction in peripheral myelinated nerve fibres. J. Physiol. 108, 315–339.

Ikeda, M., Oka, Y., 2012. The relationship between nerve conduction velocity and fiber morphology during peripheral nerve regeneration. Brain Behav. 2, 382–390.

Insko, E.K., Bolinger, L., 1993. Mapping of the Radiofrequency Field. J. Magn. Reson. A 103, 82–85.

Jensen, J.H., Helpern, J.A., Ramani, A., Lu, H., Kaczynski, K., 2005. Diffusional kurtosis imaging: The quantification of non-gaussian water diffusion by means of magnetic resonance imaging. Magn. Reson. Med. 53, 1432–1440.

Lévy, S., Benhamou, M., Naaman, C., Rainville, P., Callot, V., Cohen-Adad, J., 2015. White matter atlas of the human spinal cord with estimation of partial volume effect. Neuroimage 119, 262–271.

Lisanti, C., Carlin, C., Banks, K.P., Wang, D., 2007. Normal MRI appearance and motion-related phenomena of CSF. AJR Am. J. Roentgenol. 188, 716–725.

Metwalli, N.S., Benatar, M., Nair, G., Usher, S., Hu, X., Carew, J.D., 2010. Utility of axial and radial diffusivity from diffusion tensor MRI as markers of neurodegeneration in amyotrophic lateral sclerosis. Brain Res. 1348, 156–164.

MS Symptoms [WWW Document], n.d.. National Multiple Sclerosis Society. URL http://www.nationalmssociety.org/Symptoms-Diagnosis/MS-Symptoms (accessed 12.11.15).

Nilsson, M., Lätt, J., Ståhlberg, F., van Westen, D., Hagslätt, H., 2012. The importance of axonal undulation in diffusion MR measurements: a Monte Carlo simulation study. NMR Biomed. 25, 795–805.

Niven, J.E., Farris, S.M., 2012. Miniaturization of nervous systems and neurons. Curr. Biol. 22, R323–9.

Noback, C.R., Strominger, N.L., Demarest, R.J., Ruggiero, D.A., 2005. The Human Nervous System: Structure and Function, SpringerLink: Springer e-Books. Humana Press.

Perrault, W., Duval, T., Cohen-Adad, J., 2015. Comparison of NOGSE and PGSE Sequences for Axon Diameter Estimation, in: Proceedings of the 23th Annual Meeting of ISMRM, 2884. Toronto.

Pohmann, R., Scheffler, K., 2013. A theoretical and experimental comparison of different techniques for B1 mapping at very high fields. NMR Biomed. 26, 265–275.

Raff, M.C., Whitmore, A.V., Finn, J.T., 2002. Axonal self-destruction and neurodegeneration. Science 296, 868–871.

Rowland, L.P., Shneider, N.A., 2001. Amyotrophic lateral sclerosis. N. Engl. J. Med. 344, 1688–1700.

Saba, L., 2015. Imaging in Neurodegenerative Disorders. OUP Oxford.

Schultz, R.L., Case, N.M., 1970. A modified aldehyde perfusion technique for preventing certain artifacts in electron microscopy of the central nervous system. J. Microsc. 92, 69–84.

Venkatesan, R., Lin, W., Haacke, E.M., 1998. Accurate determination of spin-density and T1 in the presence of RF-field inhomogeneities and flip-angle miscalibration. Magn. Reson. Med. 40, 592–602.

Verma, T., Cohen-Adad, J., 2014. Effect of respiration on the B0 field in the human spinal cord at 3T. Magn. Reson. Med. 72, 1629–1636.

Vincent, L., 1998. Minimal path algorithms for the robust detection of linear features in gray images. Amsterdam.

Waller, A., 1850. Experiments on the Section of the Glossopharyngeal and Hypoglossal Nerves of the Frog, and Observations of the Alterations Produced Thereby in the Structure of Their Primitive Fibres. Philosophical Transactions of the Royal Society of London Series I 140, 423–429.

West, K.L., Kelm, N.D., Carson, R.P., Does, M.D., 2015a. A revised model for estimating g-ratio from MRI. Neuroimage. https://doi.org/10.1016/j.neuroimage.2015.08.017

West, K.L., Kelm, N.D., Carson, R.P., Does, M.D., 2015b. Quantitative analysis of mouse corpus callosum from electron microscopy images. Data Brief 5, 124–128.

Abbas, Z., Gras, V., Möllenhoff, K., Oros-Peusquens, A.-M., Shah, N.J., 2015. Quantitative water content mapping at clinically relevant field strengths: a comparative study at 1.5 T and 3 T. Neuroimage 106, 404–413.

Abdel-Aziz, K., Schneider, T., Solanky, B.S., Yiannakas, M.C., Altmann, D.R., Wheeler-Kingshott, C.A.M., Peters, A.L., Day, B.L., Thompson, A.J., Ciccarelli, O., 2015. Evidence for early neurodegeneration in the cervical cord of patients with primary progressive multiple sclerosis. Brain. https://doi.org/10.1093/brain/awv086

Arbuthnott, E.R., Ballard, K.J., Boyd, I.A., Kalu, K.U., 1980. Quantitative study of the non-circularity of myelinated peripheral nerve fibres in the cat. J. Physiol. 308, 99–123.

Biedenbach, M.A., De Vito, J.L., Brown, A.C., 1986. Pyramidal tract of the cat: axon size and morphology. Exp. Brain Res. 61, 303–310.

Burcaw, L.M., Fieremans, E., Novikov, D.S., 2015. Mesoscopic structure of neuronal tracts from time-dependent diffusion. Neuroimage 114, 18–37.

Caruyer, E., 2012. Q-space Diffusion MRI: Acquisition and Signal Processing.

Chavez, S., Xiang, Q.-S., An, L., 2002. Understanding phase maps in MRI: a new cutline phase unwrapping method. IEEE Trans. Med. Imaging 21, 966–977.

Cohen, N., Yang, S., Andalman, A., Broxton, M., Grosenick, L., Deisseroth, K., Horowitz, M., Levoy, M., 2014. Enhancing the performance of the light field microscope using wavefront coding. Opt. Express 22, 24817–24839.

Dagher, J., Nael, K., 2015. MAGPI: A framework for maximum likelihood MR phase imaging using multiple receive coils. Magn. Reson. Med. https://doi.org/10.1002/mrm.25756

Denk, C., Hernandez Torres, E., MacKay, A., Rauscher, A., 2011. The influence of white matter fibre orientation on MR signal phase and decay. NMR Biomed. 24, 246–252.

Duval, T., McNab, J.A., Setsompop, K., Witzel, T., Schneider, T., Huang, S.Y., Keil, B., Klawiter, E.C., Wald, L.L., Cohen-Adad, J., 2015. In vivo mapping of human spinal cord microstructure at 300mT/m. Neuroimage 118, 494–507.

Farrell, J.A.D., University, T.J.H., 2009. Q-space Diffusion Imaging of Axon and Myelin Damage in the Human and Rat Spinal Cord. Johns Hopkins University.

Fu, Y., Huff, T.B., Wang, H.-W., Wang, H., Cheng, J.-X., 2008. Ex vivo and in vivo imaging of myelin fibers in mouse brain by coherent anti-Stokes Raman scattering microscopy. Opt. Express 16, 19396–19409.

Gray, H., Standring, S., Ellis, H., Berkovitz, B.K.B., 2005. Gray's Anatomy: The Anatomical Basis of Clinical Practice, Gray's Anatomy. Elsevier Churchill Livingstone.

Hargreaves, B.A., 2012. Rapid gradient-echo imaging. J. Magn. Reson. Imaging 36, 1300–1313.

Henkelman, R.M., Stanisz, G.J., Graham, S.J., 2001. Magnetization transfer in MRI: a review. NMR Biomed. 14, 57–64.

Horowitz, A., Barazany, D., Tavor, I., Bernstein, M., Yovel, G., Assaf, Y., 2014. In vivo correlation between axon diameter and conduction velocity in the human brain. Brain Struct. Funct. https://doi.org/10.1007/s00429-014-0871-0

Jacobs, J.M., Love, S., 1985. Qualitative and quantitative morphology of human sural nerve at different ages. Brain 108 (Pt 4), 897–924.

Jones, D.K., Knösche, T.R., Turner, R., 2013. White matter integrity, fiber count, and other fallacies: the do's and don'ts of diffusion MRI. Neuroimage 73, 239–254.

Kearney, H., Miller, D.H., Ciccarelli, O., 2015. Spinal cord MRI in multiple sclerosis[mdash]diagnostic, prognostic and clinical value. Nat. Rev. Neurol. 11, 327–338.

Keil, B., Blau, J.N., Biber, S., Hoecht, P., Tountcheva, V., Setsompop, K., Triantafyllou, C., Wald, L.L., 2013. A 64-channel 3T array coil for accelerated brain MRI. Magn. Reson. Med. 70, 248–258.

Kerschensteiner, M., Schwab, M.E., Lichtman, J.W., Misgeld, T., 2005. In vivo imaging of axonal degeneration and regeneration in the injured spinal cord. Nat. Med. 11, 572–577.

Le Bihan, D., Johansen-Berg, H., 2012. Diffusion MRI at 25: exploring brain tissue structure and function. Neuroimage 61, 324–341.

Leenen, L.P., Meek, J., Posthuma, P.R., Nieuwenhuys, R., 1985. A detailed morphometrical analysis of the pyramidal tract of the rat. Brain Res. 359, 65–80.

Ma, D., Pierre, E.Y., Jiang, Y., Schluchter, M.D., Setsompop, K., Gulani, V., Griswold, M.A., 2015. Music-based magnetic resonance fingerprinting to improve patient comfort during MRI examinations. Magn. Reson. Med. https://doi.org/10.1002/mrm.25818

Mikula, S., Denk, W., 2015. High-resolution whole-brain staining for electron microscopic circuit reconstruction. Nat. Methods. https://doi.org/10.1038/nmeth.3361

Mohammadi, S., Freund, P., Feiweier, T., Curt, A., Weiskopf, N., 2013. The impact of post-processing on spinal cord diffusion tensor imaging. Neuroimage 70, 377–385.

Novikov, D.S., Jensen, J.H., Helpern, J.A., Fieremans, E., 2014. Revealing mesoscopic structural universality with diffusion. Proc. Natl. Acad. Sci. U. S. A. 111, 5088–5093.

Oh, J., Saidha, S., Chen, M., Smith, S.A., Prince, J., Jones, C., Diener-West, M., van Zijl, P.C.M., Reich, D.S., Calabresi, P.A., 2013. Spinal cord quantitative MRI discriminates between disability levels in multiple sclerosis. Neurology 80, 540–547.

Paus, T., Toro, R., 2009. Could Sex Differences in White Matter be Explained by g ratio? Front. Neuroanat. 3, 14.

Rauscher, A., Sedlacik, J., Barth, M., Mentzel, H.-J., Reichenbach, J.R., 2005. Magnetic susceptibility-weighted MR phase imaging of the human brain. AJNR Am. J. Neuroradiol. 26, 736–742.

Rushton, W.A.H., 1951. A theory of the effects of fibre size in medullated nerve. J. Physiol. 115, 101–122.

Schmierer, K., Scaravilli, F., Altmann, D.R., Barker, G.J., Miller, D.H., 2004. Magnetization transfer ratio and myelin in postmortem multiple sclerosis brain. Ann. Neurol. 56, 407–415.

Shackelford, K., n.d. Multiple Sclerosis: New Diagnostic Criteria [WWW Document]. Healthline. URL http://www.healthline.com/health/multiple-sclerosis/new-diagnostic-criteria#3 (accessed 6.16.15).

Stikov, N., Campbell, J.S.W., Stroh, T., Lavelée, M., Frey, S., Novek, J., Nuara, S., Ho, M.-K., Bedell, B.J., Dougherty, R.F., Leppert, I.R., Boudreau, M., Narayanan, S., Duval, T., Cohen-Adad, J., Picard, P.-A., Gasecka, A., Côté, D., Pike, G.B., 2015. In vivo histology of the

myelin g-ratio with magnetic resonance imaging. Neuroimage 118, 397–405.

Uranova, N., Orlovskaya, D., Vikhreva, O., Zimina, I., Kolomeets, N., Vostrikov, V., Rachmanova, V., 2001. Electron microscopy of oligodendroglia in severe mental illness. Brain Res. Bull. 55, 597–610.

Xu, J., Li, H., Harkins, K.D., Jiang, X., Xie, J., Kang, H., Does, M.D., Gore, J.C., 2014. Mapping mean axon diameter and axonal volume fraction by MRI using temporal diffusion spectroscopy. Neuroimage 103, 10–19.

Zhang, J., Kolind, S.H., Laule, C., Mackay, A.L., 2014. Comparison of myelin water fraction from multiecho T2 decay curve and steady-state methods. Magn. Reson. Med. https://doi.org/10.1002/mrm.25125

Anaby, D., Duncan, I.D., Smith, C.M., Cohen, Y., 2013. q-Space diffusion MRI (QSI) of the disease progression in the spinal cords of the Long Evans shaker: diffusion time and apparent anisotropy. NMR Biomed. 26, 1879–1886.

Bar-Shir, A., Cohen, Y., 2008. High b-value q-space diffusion MRS of nerves: structural information and comparison with histological evidence. NMR Biomed. 21, 165–174.

Beaulieu, C., Fenrich, F.R., Allen, P.S., 1998. Multicomponent water proton transverse relaxation and T2-discriminated water diffusion in myelinated and nonmyelinated nerve. Magn. Reson. Imaging 16, 1201–1210.

Bégin, S., Dupont-Therrien, O., Bélanger, E., Daradich, A., Laffray, S., De Koninck, Y., Côté, D.C., 2014. Automated method for the segmentation and morphometry of nerve fibers in large-scale CARS images of spinal cord tissue. Biomed. Opt. Express, BOE 5, 4145–4161.

Biton, I.E., Duncan, I.D., Cohen, Y., 2007. q-Space diffusion of myelin-deficient spinal cords. Magn. Reson. Med. 58, 993–1000.

Clark, C.A., Le Bihan, D., 2000. Water diffusion compartmentation and anisotropy at high b values in the human brain. Magn. Reson. Med. 44, 852–859.

Clayden, J.D., Nagy, Z., Weiskopf, N., Alexander, D.C., Clark, C.A., 2015. Microstructural parameter estimation in vivo using diffusion MRI and structured prior information. Magn. Reson. Med. https://doi.org/10.1002/mrm.25723

Decay, T.R., n.d. Kenneth P. Whittall, Alex L. MacKay, Douglas A. Graeb, Robert A. Nugent, David K. B. Li, Donald W. Paty.

Deoni, S.C.L., 2011. Magnetic resonance relaxation and quantitative measurement in the

brain. Methods Mol. Biol. 711, 65–108.

Deoni, S.C.L., Rutt, B.K., Arun, T., Pierpaoli, C., Jones, D.K., 2008. Gleaning multicomponent T1 and T2 information from steady-state imaging data. Magn. Reson. Med. 60, 1372–1387.

Does, M.D., Beaulieu, C., Allen, P.S., Snyder, R.E., 1998. Multi-component T1 relaxation and magnetisation transfer in peripheral nerve. Magn. Reson. Imaging 16, 1033–1041.

Duval, T., Gasecka, A., Pouliot, P., Côté, D., Stikov, N., Cohen-Adad, J., 2015. Validation of MRI microstructure measurements with Coherent Anti-Stokes Raman Scattering (CARS), in: Proceedings of the 23th Annual Meeting of ISMRM. Toronto, p. 682.

Duval, T., Lévy, S., Stikov, N., Mezer, A., Witzel, T., Keil, B., Smith, V., Wald, L.L., Klawiter, E., Cohen-Adad, J., 2015a. In vivo mapping of myelin g-ratio in the human spinal cord, in: Proceedings of the 23th Annual Meeting of ISMRM. Toronto, p. 0005.

Duval, T., Witzel, T., Keil, B., Wald, L.L., Smith, V., Klawiter, E., Cohen-Adad, J., 2015b. Impact of noise bias with parallel imaging for axon diameter estimation with q-space MRI, in: Proceedings of the 23th Annual Meeting of ISMRM, 2950. Toronto.

Ferizi, U., Schneider, T., Panagiotaki, E., Nedjati-Gilani, G., Zhang, H., Wheeler-Kingshott, C.A.M., Alexander, D.C., 2014. A ranking of diffusion MRI compartment models with in vivo human brain data. Magn. Reson. Med. 72, 1785–1792.

Gareau, P.J., Rutt, B.K., Bowen, C.V., Karlik, S.J., Mitchell, J.R., 1999. In vivo measurements of multi-component T2 relaxation behaviour in guinea pig brain. Magn. Reson. Imaging 17, 1319–1325.

Grussu, F., Schneider, T., Zhang, H., Alexander, D.C., Wheeler-Kingshott, C.A.M., 2015. Neurite orientation dispersion and density imaging of the healthy cervical spinal cord in vivo. Neuroimage 111, 590–601.

Hildebrand, C., Remahl, S., Persson, H., Bjartmar, C., 1993. Myelinated nerve fibres in the CNS. Prog. Neurobiol. 40, 319–384.

Hooshmand, M.J., Anderson, A.J., Cummings, B.J., 2014. Improved pre-embedded immuno-electron microscopy procedures to preserve myelin integrity in mammalian central nervous tissue, in: Center, F.R. (Ed.), Microscopy: Advances in Scientific Research and Education. pp. 59–65.

Huang, S.Y., Nummenmaa, A., Witzel, T., Duval, T., Cohen-Adad, J., Wald, L.L., McNab, J.A., 2015. The impact of gradient strength on in vivo diffusion MRI estimates of axon diameter. Neuroimage 106, 464–472.

Huisman, T.A.G.M., Loenneker, T., Barta, G., Bellemann, M.E., Hennig, J., Fischer, J.E., Il'yasov, K.A., 2006. Quantitative diffusion tensor MR imaging of the brain: field strength related variance of apparent diffusion coefficient (ADC) and fractional anisotropy (FA) scalars. Eur. Radiol. 16, 1651–1658.

Johansen-Berg, H., Behrens, T.E.J., 2013. Diffusion MRI: From Quantitative Measurement to In vivo Neuroanatomy. Elsevier Science.

Kolasinski, J., Stagg, C.J., Chance, S.A., Deluca, G.C., Esiri, M.M., Chang, E.-H., Palace, J.A., McNab, J.A., Jenkinson, M., Miller, K.L., Johansen-Berg, H., 2012. A combined post-mortem magnetic resonance imaging and quantitative histological study of multiple sclerosis pathology. Brain 135, 2938–2951.

Kunz, N., Sizonenko, S.V., Hüppi, P.S., Gruetter, R., van de Looij, Y., 2013. Investigation of field and diffusion time dependence of the diffusion-weighted signal at ultrahigh magnetic fields. NMR Biomed. 26, 1251–1257.

Laule, C., Vavasour, I.M., Kolind, S.H., Li, D.K.B., Traboulsee, T.L., Moore, G.R.W., MacKay, A.L., 2007. Magnetic resonance imaging of myelin. Neurotherapeutics 4, 460–484.

Mackay, A., Whittall, K., Adler, J., Li, D., Paty, D., Graeb, D., 1994. In vivo visualization of myelin water in brain by magnetic resonance. Magn. Reson. Med. 31, 673–677.

MacMillan, E.L., Mädler, B., Fichtner, N., Dvorak, M.F., Li, D.K.B., Curt, A., MacKay, A.L., 2011. Myelin water and T(2) relaxation measurements in the healthy cervical spinal cord at 3.0T: repeatability and changes with age. Neuroimage 54, 1083–1090.

Mulkern, R.V., Zengingonul, H.P., Robertson, R.L., Bogner, P., Zou, K.H., Gudbjartsson, H., Guttmann, C.R., Holtzman, D., Kyriakos, W., Jolesz, F.A., Maier, S.E., 2000. Multi-component apparent diffusion coefficients in human brain: relationship to spin-lattice relaxation. Magn. Reson. Med. 44, 292–300.

Pfeuffer, J., Provencher, S.W., Gruetter, R., 1999. Water diffusion in rat brain in vivo as detected at very large b values is multicompartmental. MAGMA 8, 98–108.

Reese, T.G., Heid, O., Weisskoff, R.M., Wedeen, V.J., 2003. Reduction of eddy-current-induced distortion in diffusion MRI using a twice-refocused spin echo. Magn. Reson. Med. 49, 177–182.

Smith, S.A., Edden, R.A.E., Farrell, J.A.D., Barker, P.B., Van Zijl, P.C.M., 2008. Measurement of T1 and T2 in the cervical spinal cord at 3 tesla. Magn. Reson. Med. 60, 213–219.

Sotiropoulos, S.N., Jbabdi, S., Xu, J., Andersson, J.L., Moeller, S., Auerbach, E.J., Glasser, M.F., Hernandez, M., Sapiro, G., Jenkinson, M., Feinberg, D.A., Yacoub, E., Lenglet, C., Van Essen, D.C., Ugurbil, K., Behrens, T.E.J., WU-Minn HCP Consortium, 2013. Advances in diffusion MRI acquisition and processing in the Human Connectome Project. Neuroimage 80, 125–143.

Stanisz, G.J., Henkelman, R.M., 1998. Diffusional anisotropy of T2 components in bovine optic nerve. Magn. Reson. Med. 40, 405–410.

Stepišnik, J., 1993. Time-dependent self-diffusion by NMR spin-echo. Physica B Condens. Matter 183, 343–350.

Stikov, N., Boudreau, M., Levesque, I.R., Tardif, C.L., Barral, J.K., Pike, G.B., 2015. On the accuracy of T1 mapping: searching for common ground. Magn. Reson. Med. 73, 514–522.

Vaithianathar, L., Tench, C.R., Morgan, P.S., Constantinescu, C.S., 2003. Magnetic resonance imaging of the cervical spinal cord in multiple sclerosis--a quantitative T1 relaxation time mapping approach. J. Neurol. 250, 307–315.

Volz, S., Nöth, U., Deichmann, R., 2012. Correction of systematic errors in quantitative proton density mapping. Magn. Reson. Med. 68, 74–85.

von dem Hagen, E.A.H., Henkelman, R.M., 2002. Orientational diffusion reflects fiber structure within a voxel. Magn. Reson. Med. 48, 454–459.

Whittall, K.P., MacKay, A.L., Graeb, D.A., Nugent, R.A., Li, D.K., Paty, D.W., 1997. In vivo measurement of T2 distributions and water contents in normal human brain. Magn. Reson. Med. 37, 34–43.

Altman, J., Bayer, S.A., 2001. Development of the Human Spinal Cord: An Interpretation Based on Experimental Studies in Animals. Oxford University Press.

Alvarez, G.A., Shemesh, N., Frydman, L., 2013. Coherent dynamical recoupling of diffusion-driven decoherence in magnetic resonance. arXiv [quant-ph].

Bammer, R., Fazekas, F., 2003. Diffusion imaging of the human spinal cord and the vertebral column. Top. Magn. Reson. Imaging 14, 461–476.

Basser, P.J., Jones, D.K., 2002. Diffusion-tensor MRI: theory, experimental design and data analysis - a technical review. NMR Biomed. 15, 456–467.

Brightman, M.W., Klatzo, I., Olsson, Y., Reese, T.S., 1970. The blood-brain barrier to proteins under normal and pathological conditions. J. Neurol. Sci. 10, 215–239.

Campbell, J.S.W., Stikov, N., Dougherty, R.F., Bruce Pike, G., 2014. Combined NODDI and qMT for full-brain g-ratio mapping with complex subvoxel microstructure, in: Proceedings of the 22th Annual Meeting of ISMRM, Milan. p. 393.

Chomiak, T., Hu, B., 2009. What is the optimal value of the g-ratio for myelinated fibers in the rat CNS? A theoretical approach. PLoS One 4, e7754.

Christensen, P.C., Brideau, C., Poon, K.W.C., Döring, A., Yong, V.W., Stys, P.K., 2014. High-resolution fluorescence microscopy of myelin without exogenous probes. Neuroimage 87, 42–54.

Chung, J.-Y., Han, Y., Cho, Z.-H., Park, H., 2012. A correction method for streak artifacts in gradient-echo EPI using spin-echo EPI reference data. MAGMA 25, 205–213.

Dietrich, O., Raya, J.G., Reeder, S.B., Reiser, M.F., Schoenberg, S.O., 2007. Measurement of signal-to-noise ratios in MR images: Influence of multichannel coils, parallel imaging, and reconstruction filters. J. Magn. Reson. Imaging 26, 375–385.

Fonov, V.S., Le Troter, A., Taso, M., De Leener, B., Lévêque, G., Benhamou, M., Sdika, M., Benali, H., Pradat, P.-F., Collins, D.L., Callot, V., Cohen-Adad, J., 2014. Framework for integrated MRI average of the spinal cord white and gray matter: The MNI-Poly-AMU template. Neuroimage 102P2, 817–827.

Griswold, M.A., Jakob, P.M., Heidemann, R.M., Nittka, M., Jellus, V., Wang, J., Kiefer, B., Haase, A., 2002. Generalized autocalibrating partially parallel acquisitions (GRAPPA). Magn. Reson. Med. 47, 1202–1210.

Histology at the University of Michigan [WWW Document], n.d. URL http://histology.med.umich.edu/medical/central-nervous-system (accessed 8.24.14).

Horowitz, A., Barazany, D., Tavor, I., Bernstein, M., Yovel, G., Assaf, Y., 2014. In vivo correlation between axon diameter and conduction velocity in the human brain. Brain Struct. Funct. https://doi.org/10.1007/s00429-014-0871-0

Horsfield, M.A., Jones, D.K., 2002. Applications of diffusion-weighted and diffusion tensor MRI to white matter diseases - a review. NMR Biomed. 15, 570–577.

Ingram, P., Shelburne, J.D., Roggli, V.L., LeFurgey, A., 1999. Biomedical Applications of Microprobe Analysis. Elsevier Science.

Kameyama, T., Hashizume, Y., Ando, T., Takahashi, A., Yanagi, T., Mizuno, J., 1995. Spinal cord morphology and pathology in ossification of the posterior longitudinal ligament. Brain 118 (Pt 1), 263–278.

Keil, B., Cohen-Adad, J., Porter, D.A., Biber, S., Heberlein, K., Triantafyllou, C., Wald, L.L., 2013. Simultaneous Diffusion-Weighted MRI of Brain and Cervical Spinal Cord using a 64-Channel Head-Neck Array Coil at 3T. Proc. Intl. Soc. Mag. Reson. Med. 21, 1210–1210.

Kim, T.H., Zollinger, L., Shi, X.F., Kim, S.E., Rose, J., Patel, A.A., Jeong, E.K., 2010. Quantification of diffusivities of the human cervical spinal cord using a 2D single-shot interleaved multisection inner volume diffusion-weighted echo-planar imaging technique. AJNR Am. J. Neuroradiol. 31, 682–687.

Klawiter, E.C., Schmidt, R.E., Trinkaus, K., Liang, H.-F., Budde, M.D., Naismith, R.T., Song, S.-K., Cross, A.H., Benzinger, T.L., 2011. Radial diffusivity predicts demyelination in ex vivo multiple sclerosis spinal cords. Neuroimage 55, 1454–1460.

Lassek, A.M., 1945. The human pyramidal tract: xi. Correlation of the babinski sign and the pyramidal syndrome. Arch NeurPsych 53, 375–377.

Lätt, J., Nilsson, M., Malmborg, C., Rosquist, H., Wirestam, R., Ståhlberg, F., Topgaard, D., Brockstedt, S., 2007. Accuracy of q-space related parameters in MRI: simulations and phantom measurements. IEEE Trans. Med. Imaging 26, 1437–1447.

Le Bihan, D., Breton, E., Lallemand, D., Grenier, P., Cabanis, E., Laval-Jeantet, M., 1986. MR imaging of intravoxel incoherent motions: application to diffusion and perfusion in neurologic disorders. Radiology 161, 401–407.

Liberman, G., Louzoun, Y., Ben Bashat, D., 2014. T1 Mapping using variable flip angle SPGR data with flip angle correction. J. Magn. Reson. Imaging 40, 171–180.

McNab, J.A., Edlow, B.L., Witzel, T., Huang, S.Y., Bhat, H., Heberlein, K., Feiweier, T., Liu, K., Keil, B., Cohen-Adad, J., Tisdall, M.D., Folkerth, R.D., Kinney, H.C., Wald, L.L., 2013. The Human Connectome Project and beyond: Initial applications of 300 mT/m gradients. Neuroimage 80, 234–245.

Pajevic, S., Basser, P.J., 2013. An optimum principle predicts the distribution of axon diameters in normal white matter. PLoS One 8, e54095.

Setsompop, K., Kimmlingen, R., Eberlein, E., Witzel, T., Cohen-Adad, J., McNab, J.A., Keil, B., Tisdall, M.D., Hoecht, P., Dietz, P., Cauley, S.F., Tountcheva, V., Matschl, V., Lenz, V.H., Heberlein, K., Potthast, A., Thein, H., Van Horn, J., Toga, A., Schmitt, F., Lehne, D., Rosen, B.R., Wedeen, V., Wald, L.L., 2013. Pushing the limits of in vivo diffusion MRI for the Human Connectome Project. Neuroimage 80, 220–233.

Sled, J.G., Pike, G.B., 2000. Quantitative interpretation of magnetization transfer in spoiled gradient echo MRI sequences. J. Magn. Reson. 145, 24–36.

Song, S.-K., Yoshino, J., Le, T.Q., Lin, S.-J., Sun, S.-W., Cross, A.H., Armstrong, R.C., 2005. Demyelination increases radial diffusivity in corpus callosum of mouse brain. Neuroimage 26, 132–140.

Stikov, N., Campbell, J.S.W., Lavallée, M., Stroh, T., Frey, S., Novek, J., Nuara, S., Ho, M.-K., Bedell, B., Bruce Pike, G., 2014. In vivo measurement of the myelin g-ratio with histological validation, in: Proceedings of the 22th Annual Meeting of ISMRM, Milan. p. 102.

Syková, E., Nicholson, C., 2008. Diffusion in brain extracellular space. Physiol. Rev. 88, 1277–1340.

Trobe, J.D., 2010. The Human Brain. An Introduction to Its Functional Anatomy, 6th Edition. J. Neuroophthalmol. 30, 107.

Walsh, D.O., Gmitro, A.F., Marcellin, M.W., 2000. Adaptive reconstruction of phased array MR imagery. Magn. Reson. Med. 43, 682–690.

Wang, L.Z., Caprihan, A., Fukushima, E., 1995. The Narrow-Pulse Criterion for Pulsed-Gradient Spin-Echo Diffusion Measurements. J. Magn. Reson. A 117, 209–219.

Waxman, S.G., Kocsis, J.D., Stys, P.K., 1995. The Axon: Structure, Function, and Pathophysiology. Oxford University Press.

Wheeler-Kingshott, C.A., Stroman, P.W., Schwab, J.M., Bacon, M., Bosma, R., Brooks, J., Cadotte, D.W., Carlstedt, T., Ciccarelli, O., Cohen-Adad, J., Curt, A., Evangelou, N., Fehlings, M.G., Filippi, M., Kelley, B.J., Kollias, S., Mackay, A., Porro, C.A., Smith, S., Strittmatter, S.M., Summers, P., Thompson, A.J., Tracey, I., 2014. The current state-of-the-art of spinal cord imaging: applications. Neuroimage 84, 1082–1093.

Wilhelm, M.J., Ong, H.H., Wehrli, S.L., Li, C., Tsai, P.-H., Hackney, D.B., Wehrli, F.W., 2012. Direct magnetic resonance detection of myelin and prospects for quantitative imaging of myelin density. Proc. Natl. Acad. Sci. U. S. A. 109, 9605–9610.

Wyndaele, M., Wyndaele, J.-J., 2006. Incidence, prevalence and epidemiology of spinal cord injury: what learns a worldwide literature survey? Spinal Cord 44, 523–529.

Aja-Fernández, S., Tristán-Vega, A., Hoge, W.S., 2011. Statistical noise analysis in GRAPPA using a parametrized noncentral Chi approximation model. Magn. Reson. Med. 65, 1195–1206.

Avants, B.B., Epstein, C.L., Grossman, M., Gee, J.C., 2008. Symmetric diffeomorphic image registration with cross-correlation: evaluating automated labeling of elderly and

neurodegenerative brain. Med. Image Anal. 12, 26–41.

Basser, P.J., Pierpaoli, C., 1996. Microstructural and physiological features of tissues elucidated by quantitative-diffusion-tensor MRI. J. Magn. Reson. B 111, 209–219.

Beaulieu, C., Allen, P.S., 1994. Determinants of anisotropic water diffusion in nerves. Magn. Reson. Med. 31, 394–400.

Benhamou, M., Fonov, V., Taso, M., Le Troter, A., Sdika, M., Collins, L., Callot, V., Cohen-Adad, J., 2014. Atlas of white-matter tracts in the human spinal cord, in: Proceedings of the 22th Annual Meeting of ISMRM, Milan. p. 13.

Bodammer, N., Kaufmann, J., Kanowski, M., Tempelmann, C., 2004. Eddy current correction in diffusion-weighted imaging using pairs of images acquired with opposite diffusion gradient polarity. Magn. Reson. Med. 51, 188–193.

Callaghan, P.T., 1995. Pulsed-Gradient Spin-Echo NMR for Planar, Cylindrical, and Spherical Pores under Conditions of Wall Relaxation. J. Magn. Reson. A 113, 53–59.

Callaghan, P.T., Eccles, C.D., Xia, Y., 1988. NMR microscopy of dynamic displacements: k-space and q-space imaging. J. Phys. E 21, 820.

Carpenter, M.B., 1976. Human neuroanatomy.

Cluskey, S., Ramsden, D.B., 2001. Mechanisms of neurodegeneration in amyotrophic lateral sclerosis. Mol. Pathol. 54, 386–392.

Cohen-Adad, J., Descoteaux, M., Rossignol, S., Hoge, R.D., Deriche, R., Benali, H., 2008. Detection of multiple pathways in the spinal cord using q-ball imaging. Neuroimage 42, 739–749.

Cohen-Adad, J., El Mendili, M.-M., Lehéricy, S., Pradat, P.-F., Blancho, S., Rossignol, S., Benali, H., 2011. Demyelination and degeneration in the injured human spinal cord detected with diffusion and magnetization transfer MRI. Neuroimage 55, 1024–1033.

Cohen-Adad, J., Descoteaux, M., 2011a. Impact of outliers on diffusion tensor and Q-ball imaging: Clinical implications and correction strategies. Resonance Imaging.

Cohen-Adad, J., Descoteaux, M., 2011b. Quality assessment of high angular resolution diffusion imaging data using bootstrap on Q-ball reconstruction. Resonance Imaging.

DeLuca, G.C., Ebers, G.C., Esiri, M.M., 2004. Axonal loss in multiple sclerosis: a pathological survey of the corticospinal and sensory tracts. Brain 127, 1009–1018.

Dijkers, M., Bryce, T., Zanca, J., 2009. Prevalence of chronic pain after traumatic spinal cord injury: a systematic review. J. Rehabil. Res. Dev. 46, 13–29.

Duval, T., Mc Nab, J.A., Setsompop, K., Witzel, T., Schneider, T., Huang, S.Y., Keil, B., Klawiter, E., Wald, L.L., Cohen-Adad, J., 2014. In vivo estimation of axon diameter in the human spinal cord using 300 mT/m gradients, in: Proceedings of the 22th Annual Meeting of ISMRM, Milan. p. 99.

Fonov, V.S., Le Troter, A., Taso, M., Leveque, G., Benhamou, M., Sdika, M., Louis Collins, D., Callot, V., Adad, J.C.-, 2014. MNI-Poly-AMU average anatomical template for automatic spinal cord measurements, in: Proceedings of the 22th Annual Meeting of ISMRM, Milan. p. 1713.

Huang, S.Y., Nummenmaa, A., Witzel, T., Duval, T., Cohen-Adad, J., Wald, L.L., Mc Nab, J.A., 2014. The impact of gradient strength on in vivo diffusion MRI estimates of axon diameter, in: Proceedings of the 22th Annual Meeting of ISMRM, Milan. p. 791.

Jenkinson, M., Bannister, P., Brady, M., Smith, S., 2002. Improved optimization for the robust and accurate linear registration and motion correction of brain images. Neuroimage 17, 825–841.

Keil, B., Cohen-Adad, J., Porter, D.A., Biber, S., Heberlein, K., 2013. Simultaneous diffusion-weighted MRI of brain and cervical spinal cord using a 64-channel head-neck array coil at 3T. International Society for.

Lätt, J., Nilsson, M., Wirestam, R., Johansson, E., Larsson, E.-M., Stahlberg, F., Brockstedt, S., 2008. In vivo visualization of displacement-distribution-derived parameters in q-space imaging. Magn. Reson. Imaging 26, 77–87.

Lundell, H., Nielsen, J.B., Ptito, M., Dyrby, T.B., 2011. Distribution of collateral fibers in the monkey cervical spinal cord detected with diffusion-weighted magnetic resonance imaging. Neuroimage 56, 923–929.

Nieuwenhuys, R., Voogd, J., van Huijzen, C., 2007. The Human Central Nervous System: A Synopsis and Atlas. Springer.

Nilsson, M., Alexander, D., 2012. Investigating tissue microstructure using diffusion MRI: How does the resolution limit of the axon diameter relate to the maximal gradient strength? Proc. Intl. Soc. Mag. Reson. Med. 20, 3567.

Paus, T., 2010. Growth of white matter in the adolescent brain: myelin or axon? Brain Cogn. 72, 26–35.

Perge, J.A., Koch, K., Miller, R., Sterling, P., Balasubramanian, V., 2009. How the optic

nerve allocates space, energy capacity, and information. J. Neurosci. 29, 7917–7928.

Perge, J.A., Niven, J.E., Mugnaini, E., Balasubramanian, V., Sterling, P., 2012. Why do axons differ in caliber? J. Neurosci. 32, 626–638.

Peters, A., Palay, S.L., Webster, H.F., 1991. The fine structure of the nervous system: neurons and their supporting cells. Oxford University Press.

Piché, M., Cohen-Adad, J., Nejad, M.K., Perlbarg, V., Xie, G., Beaudoin, G., Benali, H., Rainville, P., 2009. Characterization of cardiac-related noise in fMRI of the cervical spinal cord. Magn. Reson. Imaging 27, 300–310.

Richardson, S., Siow, B., Batchelor, A.M., Lythgoe, M.F., Alexander, D.C., 2013. A viable isolated tissue system: a tool for detailed MR measurements and controlled perturbation in physiologically stable tissue. Magn. Reson. Med. 69, 1603–1610.

Richardson, S., Siow, B., Panagiotaki, E., Schneider, T., Lythgoe, M.F., Alexander, D.C., 2013. Viable and fixed white matter: Diffusion magnetic resonance comparisons and contrasts at physiological temperature. Magn. Reson. Med. https://doi.org/10.1002/mrm.25012

Rossignol, S., Dubuc, R., Gossard, J.-P., 2006. Dynamic sensorimotor interactions in locomotion. Physiol. Rev. 86, 89–154.

Schr Oder, J.M., Bohl, J., von Bardeleben 2', U., 1988. Changes of the ratio between myelin thickness and axon diameter in human developing sural, femoral, ulnar, facial, and trochlear nerves*'*. Acta Neuropathol. 76, 471–483.

Schwartz, E.D., Duda, J., Shumsky, J.S., Cooper, E.T., Gee, J., 2005. Spinal cord diffusion tensor imaging and fiber tracking can identify white matter tract disruption and glial scar orientation following lateral funiculotomy. J. Neurotrauma 22, 1388–1398.

Stejskal, E.O., Tanner, J.E., 1965. Spin Diffusion Measurements: Spin Echoes in the Presence of a Time-Dependent Field Gradient. J. Chem. Phys. 42, 288–292.

Stikov, N., Perry, L.M., Mezer, A., Rykhlevskaia, E., Wandell, B.A., Pauly, J.M., Dougherty, R.F., 2011. Bound pool fractions complement diffusion measures to describe white matter micro and macrostructure. Neuroimage 54, 1112–1121.

Summers, P., Staempfli, P., Jaermann, T., Kwiecinski, S., Kollias, S., 2006. A preliminary study of the effects of trigger timing on diffusion tensor imaging of the human spinal cord. AJNR Am. J. Neuroradiol. 27, 1952–1961.

Wheeler-Kingshott, C.A.M., Cercignani, M., 2009. About "axial" and "radial" diffusivities.

Magn. Reson. Med. 61, 1255–1260.

Callaghan, P.T., 1996. NMR imaging, NMR diffraction and applications of pulsed gradient spin echoes in porous media. Magn. Reson. Imaging 14, 701–709.

Callaghan, P.T., Arns, C.H., Galvosas, P., Hunter, M.W., Qiao, Y., Washburn, K.E., 2007. Recent Fourier and Laplace perspectives for multidimensional NMR in porous media. Magn. Reson. Imaging 25, 441–444.

Callaghan, P.T., Godefroy, S., Ryland, B.N., 2003a. Use of the second dimension in PGSE NMR studies of porous media. Magn. Reson. Imaging 21, 243–248.

Callaghan, P.T., Godefroy, S., Ryland, B.N., 2003b. Diffusion–relaxation correlation in simple pore structures. J. Magn. Reson. 162, 320–327.

Cheng, C.-J., Chu, L.-Y., Zhang, J., Zhou, M.-Y., Xie, R., 2008. Preparation of monodisperse poly(N-isopropylacrylamide) microspheres and microcapsules via Shirasu-porous-glass membrane emulsification. Desalination 234, 184–194.

Codd, Callaghan, 1999. Spin Echo Analysis of Restricted Diffusion under Generalized Gradient Waveforms: Planar, Cylindrical, and Spherical Pores with Wall Relaxivity. J. Magn. Reson. 137, 358–372.

Di Scipio, F., Raimondo, S., Tos, P., Geuna, S., 2008. A simple protocol for paraffin-embedded myelin sheath staining with osmium tetroxide for light microscope observation. Microsc. Res. Tech. 71, 497–502.

Dyrby, T.B., Baaré, W.F.C., Alexander, D.C., Jelsing, J., Garde, E., Søgaard, L.V., 2011. An ex vivo imaging pipeline for producing high-quality and high-resolution diffusion-weighted imaging datasets. Hum. Brain Mapp. 32, 544–563.

Fox, C.H., Johnson, F.B., Whiting, J., Roller, P.P., 1985. Formaldehyde fixation. J. Histochem. Cytochem. 33, 845–853.

Godefroy, S., Callaghan, P.T., 2003. 2D relaxation/diffusion correlations in porous media. Magn. Reson. Imaging 21, 381–383.

Gore, J.C., Xu, J., Colvin, D.C., Yankeelov, T.E., Parsons, E.C., Does, M.D., 2010. Characterization of tissue structure at varying length scales using temporal diffusion spectroscopy. NMR Biomed. 23, 745–756.

Hunter, M.W., Jackson, A.N., Callaghan, P.T., 2010. PGSE NMR measurement of the non-local dispersion tensor for flow in porous media. J. Magn. Reson. 204, 11–20.

Hutchinson, N.A., Koles, Z.J., Smith, R.S., 1970. Conduction velocity in myelinated nerve fibres of Xenopus laevis. J. Physiol. 208, 279–289.

Ianuş, A., Siow, B., Drobnjak, I., Zhang, H., Alexander, D.C., 2013. Gaussian phase distribution approximations for oscillating gradient spin echo diffusion MRI. J. Magn. Reson. 227, 25–34.

Li, H., Gore, J.C., Xu, J., 2014. Fast and robust measurement of microstructural dimensions using temporal diffusion spectroscopy. J. Magn. Reson. 242, 4–9.

Lovas, G., Szilágyi, N., Majtényi, K., Palkovits, M., Komoly, S., 2000. Axonal changes in chronic demyelinated cervical spinal cord plaques. Brain 123 (Pt 2), 308–317.

Lundell, H., Sønderby, C.K., Dyrby, T.B., 2014. Diffusion weighted imaging with circularly polarized oscillating gradients. Magn. Reson. Med. https://doi.org/10.1002/mrm.25211

Mahmood, N.S., Kadavigere, R., Avinash, K.R., Ramesh, A.K., Rao, V.R., 2008. Magnetic resonance imaging in acute cervical spinal cord injury: a correlative study on spinal cord changes and 1 month motor recovery. Spinal Cord 46, 791–797.

Mercadé-Prieto, R., Allen, R., York, D., Preece, J.A., Goodwin, T.E., Zhang, Z., 2012. Determination of the shell permeability of microcapsules with a core of oil-based active ingredient. J. Microencapsul. 29, 463–474.

More, H.L., Chen, J., Gibson, E., Donelan, J.M., Beg, M.F., 2011. A semi-automated method for identifying and measuring myelinated nerve fibers in scanning electron microscope images. J. Neurosci. Methods 201, 149–158.

Murday, J.S., Cotts, R.M., 1968. Self-Diffusion Coefficient of Liquid Lithium. J. Chem. Phys. 48, 4938–4945.

Nakashima, T., Shimizu, M., Kukizaki, M., 2000. Particle control of emulsion by membrane emulsification and its applications. Adv. Drug Deliv. Rev. 45, 47–56.

Pattany, P.M., Puckett, W.R., Klose, K.J., Quencer, R.M., Bunge, R.P., Kasuboski, L., Weaver, R.G., 1997. High-resolution diffusion-weighted MR of fresh and fixed cat spinal cords: evaluation of diffusion coefficients and anisotropy. AJNR Am. J. Neuroradiol. 18, 1049–1056.

Price, W.S., Barzykin, A.V., Hayamizu, K., Tachiya, M., 1998. A model for diffusive transport through a spherical interface probed by pulsed-field gradient NMR. Biophys. J. 74, 2259–2271.

Rane, S., Duong, T.Q., 2011. Comparison of in vivo and ex vivo diffusion tensor imaging in

rhesus macaques at short and long diffusion times. Open Neuroimag. J. 5, 172–178.

Rane, S., Nair, G., Duong, T.Q., 2010. DTI at long diffusion time improves fiber tracking. NMR Biomed. 23, 459–465.

Shemesh, N., Alvarez, G.A., Frydman, L., 2013. Measuring small compartment dimensions by probing diffusion dynamics via Non-uniform Oscillating-Gradient Spin-Echo (NOGSE) NMR. J. Magn. Reson. 237, 49–62.

Shemesh, N., Ozarslan, E., Basser, P.J., Cohen, Y., 2010. Detecting diffusion-diffraction patterns in size distribution phantoms using double-pulsed field gradient NMR: Theory and experiments. J. Chem. Phys. 132, 034703.

Shepherd, T.M., Blackband, S.J., Wirth, E.D., 3rd, 2002. Simultaneous diffusion MRI measurements from multiple perfused rat hippocampal slices. Magn. Reson. Med. 48, 565–569.

Shepherd, T.M., Thelwall, P.E., Stanisz, G.J., Blackband, S.J., 2009. Aldehyde fixative solutions alter the water relaxation and diffusion properties of nervous tissue. Magn. Reson. Med. 62, 26–34.

Siow, B., Drobnjak, I., Ianus, A., Christie, I.N., Lythgoe, M.F., Alexander, D.C., 2013. Axon radius estimation with Oscillating Gradient Spin Echo (OGSE) Diffusion MRI. diffusion-fundamentals.org 18.

Stepisnik, J., Lasic, S., Mohoric, A., Sersa, I., Sepe, A., 2006. Spectral characterization of diffusion in porous media by the modulated gradient spin echo with CPMG sequence. J. Magn. Reson. 182, 195–199.

Stroman, P.W., Kornelsen, J., Bergman, A., Krause, V., Ethans, K., Malisza, K.L., Tomanek, B., 2004. Noninvasive assessment of the injured human spinal cord by means of functional magnetic resonance imaging. Spinal Cord 42, 59–66.

Summers P. Staempfli T. Jaermann S. Kwiecinski S. Kollias, 2006. A Preliminary Study of the Effects of Trigger Timing on Diffusion Tensor Imaging of the Human. AJNR 27.

Van, A.T., Holdsworth, S.J., Bammer, R., 2014. In vivo investigation of restricted diffusion in the human brain with optimized oscillating diffusion gradient encoding. Magn. Reson. Med. 71, 83–94.

Yong-Hing, C.J., Obenaus, A., Stryker, R., Tong, K., Sarty, G.E., 2005. Magnetic resonance imaging and mathematical modeling of progressive formalin fixation of the human brain. Magn. Reson. Med. 54, 324–332.

Alexander, A.L., Tsuruda, J.S., Parker, D.L., 1997. Elimination of Eddy Current Artifacts in Diffusion-Weighted Echo-Planar Images: The IJse of Bipolar Gradients. MRM 38.

Avram, L., Assaf, Y., Cohen, Y., 2004. The effect of rotational angle and experimental parameters on the diffraction patterns and micro-structural information obtained from q-space diffusion NMR: implication for diffusion in white matter fibers. J. Magn. Reson. 169, 30–38.

Bar-Shir, A., Avram, L., Ozarslan, E., Basser, P.J., Cohen, Y., 2008. The effect of the diffusion time and pulse gradient duration ratio on the diffraction pattern and the structural information estimated from q-space diffusion MR: experiments and simulations. J. Magn. Reson. 194, 230–236.

Chin, C.-L., Wehrli, F.W., Fan, Y., Hwang, S.N., Schwartz, E.D., Nissanov, J., Hackney, D.B., 2004. Assessment of axonal fiber tract architecture in excised rat spinal cord by localized NMR q-space imaging: simulations and experimental studies. Magn. Reson. Med. 52, 733–740.

Coupé, P., Manjón, J.V., Gedamu, E., Arnold, D., Robles, M., Collins, D.L., 2010. Robust Rician noise estimation for MR images. Med. Image Anal. 14, 483–493.

Descoteaux, M., Wiest-Daesslé, N., Prima, S., Barillot, C., Deriche, R., 2008. Impact of Rician adapted Non-Local Means filtering on HARDI. Med. Image Comput. Comput. Assist. Interv. 11, 122–130.

Dula, A.N., Gochberg, D.F., Valentine, H.L., Valentine, W.M., Does, M.D., 2010. Multiexponential T2, magnetization transfer, and quantitative histology in white matter tracts of rat spinal cord. Magn. Reson. Med. 63, 902–909.

Ebara, S., Kumamoto, K., Matsuura, T., Mazurkiewicz, J.E., Rice, F.L., 2002. Similarities and differences in the innervation of mystacial vibrissal follicle–sinus complexes in the rat and cat: A confocal microscopic study. J. Comp. Neurol. 449, 103–119.

Gudbjartsson, H., Patz, S., 1995. The Rician distribution of noisy MRI data. Magn. Reson. Med. 34, 910–914.

Koay, C.G., Basser, P.J., 2006. Analytically exact correction scheme for signal extraction from noisy magnitude MR signals. J. Magn. Reson. 179, 317–322.

Koay, C.G., Ozarslan, E., Basser, P.J., 2009a. A signal transformational framework for breaking the noise floor and its applications in MRI. J. Magn. Reson. 197, 108–119.

Koay, C.G., Ozarslan, E., Pierpaoli, C., 2009b. Probabilistic Identification and Estimation of Noise (PIESNO): a self-consistent approach and its applications in MRI. J. Magn. Reson.

199, 94–103.

Landman, B., Bazin, P.-L., Prince, J., 2007. Diffusion Tensor Estimation by Maximizing Rician Likelihood. Proc. IEEE Int. Conf. Comput. Vis. 1–8.

Lavdas, I., Behan, K.C., Papadaki, A., McRobbie, D.W., Aboagye, E.O., 2013. A phantom for diffusion-weighted MRI (DW-MRI). J. Magn. Reson. Imaging 38, 173–179.

Manjón, J.V., Coupé, P., Concha, L., Buades, A., Collins, D.L., Robles, M., 2013. Diffusion Weighted Image Denoising Using Overcomplete Local PCA. PLoS One 8, e73021.

Mc Gregor, J.E., Wang, Z., ffrench-Constant, C., Donald, A.M., n.d. Microscopy of myelination.

Nagashima, Ando, Makino, Tsukamoto, Ohshima, 1998. Size Dependence of Polymer Composition in the Surface Layer of Poly(acrylamide-co-acrylic acid) Hydrogel Microspheres. J. Colloid Interface Sci. 197, 377–382.

Nyska, A., Horowitz, M., Anaby, D., Sabban, A., Leizerman, I., Blaugrund, E., Mayk, A., Behar, V., 2006. A new method of wet scanning electron microscopy for the analysis of myelination in EAE mouse model of multiple sclerosis. Exp. Toxicol. Pathol. 57, 291–297.

Omi, S., 1996. Preparation of monodisperse microspheres using the Shirasu porous glass emulsification technique. Colloids Surf. A Physicochem. Eng. Asp. 109, 97–107.

Özarslan, E., Shemesh, N., Koay, C.G., Cohen, Y., Basser, P.J., 2011. Nuclear magnetic resonance characterization of general compartment size distributions. New J. Phys. 13, 015010.

Peled, S., 2007. New perspectives on the sources of white matter DTI signal. IEEE Trans. Med. Imaging 26, 1448–1455.

Perrin, M., Poupon, C., Rieul, B., Leroux, P., Constantinesco, A., Mangin, J.-F., Lebihan, D., 2005. Validation of q-ball imaging with a diffusion fibre-crossing phantom on a clinical scanner. Philos. Trans. R. Soc. Lond. B Biol. Sci. 360, 881–891.

Pullens, P., Roebroeck, A., Goebel, R., 2010. Ground truth hardware phantoms for validation of diffusion-weighted MRI applications. J. Magn. Reson. Imaging 32, 482–488.

Sannes", A., Skjak-BrÒk!, G., 1999. Microcapsules of alginate–chitosan. II. A study of capsule stability and permeability. Biomaterials 20, 773–783.

Schneider, T., Lundell, H., Dyrby, T.B., Alexander, D.C., Wheeler-Kingshott, C.A., 2010. Optimized diffusion MRI protocols for estimating axon diameter with known fibre

orientation. Proc. Intl. Soc. Mag. Reson. Med. 18, 1561.

Sen, P.N., Basser, P.J., 2005. A model for diffusion in white matter in the brain. Biophys. J. 89, 2927–2938.

Shemesh, N., Cohen, Y., 2011. Microscopic and compartment shape anisotropies in gray and white matter revealed by angular bipolar double-PFG MR. Magn. Reson. Med. 65, 1216–1227.

Siow, B., Drobnjak, I., Chatterjee, A., Lythgoe, M.F., Alexander, D.C., 2012. Estimation of pore size in a microstructure phantom using the optimised gradient waveform diffusion weighted NMR sequence. J. Magn. Reson. 214, 51–60.

Stanisz, G.J., Szafer, A., Wright, G.A., Henkelman, R.M., 1997. An analytical model of restricted diffusion in bovine optic nerve. Magn. Reson. Med. 37, 103–111.

Stroman, P.W., Wheeler-Kingshott, C., Bacon, M., Schwab, J.M., Bosma, R., Brooks, J., Cadotte, D., Carlstedt, T., Ciccarelli, O., Cohen-Adad, J., Curt, A., Evangelou, N., Fehlings, M.G., Filippi, M., Kelley, B.J., Kollias, S., Mackay, A., Porro, C.A., Smith, S., Strittmatter, S.M., Summers, P., Tracey, I., 2014. The current state-of-the-art of spinal cord imaging: methods. Neuroimage 84, 1070–1081.

Wang, L.-Y., Ma, G.-H., Su, Z.-G., 2005. Preparation of uniform sized chitosan microspheres by membrane emulsification technique and application as a carrier of protein drug. J. Control. Release 106, 62–75.

Wright, A.C., Bataille, H., Ong, H.H., Wehrli, S.L., Song, H.K., Wehrli, F.W., 2007. Construction and calibration of a 50 T/m z-gradient coil for quantitative diffusion microimaging. J. Magn. Reson. 186, 17–25.

Zhang, H., Barazany, D., Assaf, Y., Lundell, H.M., Alexander, D.C., Dyrby, T.B., 2011. A comparative study of axon diameter imaging techniques using diffusion MRI, in: Proceedings of the 19th Annual Meeting of ISMRM, Montréal.

Zhang, H., Hubbard, P.L., Parker, G.J.M., Alexander, D.C., 2011. Axon diameter mapping in the presence of orientation dispersion with diffusion MRI. Neuroimage 56, 1301–1315.

Zhang, H., Schneider, T., Wheeler-Kingshott, C.A., Alexander, D.C., 2012. NODDI: practical in vivo neurite orientation dispersion and density imaging of the human brain. Neuroimage 61, 1000–1016.

Zhou, F.-L., Hubbard, P.L., Eichhorn, S.J., Parker, G.J.M., 2012. Coaxially electrospun axon-mimicking fibers for diffusion magnetic resonance imaging. ACS Appl. Mater. Interfaces 4, 6311–6316.

Ziemecka, I., van Steijn, V., Koper, G.J.M., Rosso, M., Brizard, A.M., van Esch, J.H., Kreutzer, M.T., 2011. Monodisperse hydrogel microspheres by forced droplet formation in aqueous two-phase systems. Lab Chip 11, 620–624.

Aboitiz_1992_Individual differences in brain asymmetries.pdf, n.d.

Alexander, D.C., 2008. A general framework for experiment design in diffusion MRI and its application in measuring direct tissue-microstructure features. Magn. Reson. Med. 60, 439–448.

Alexander, D.C., Dyrby, T.B., 2013. Diffusion imaging with stimulated echoes: signal models and experiment design. arXiv [physics.med-ph].

Alexander, D.C., Hubbard, P.L., Hall, M.G., Moore, E.A., Ptito, M., Parker, G.J.M., Dyrby, T.B., 2010. Orientationally invariant indices of axon diameter and density from diffusion MRI. Neuroimage 52, 1374–1389.

Assaf, Y., 2008. Can we use diffusion MRI as a bio-marker of neurodegenerative processes? Bioessays 30, 1235–1245.

Assaf, Y., Basser, P.J., 2005. Composite hindered and restricted model of diffusion (CHARMED) MR imaging of the human brain. Neuroimage 27, 48–58.

Assaf, Y., Blumenfeld-Katzir, T., Yovel, Y., Basser, P.J., 2008. AxCaliber: a method for measuring axon diameter distribution from diffusion MRI. Magn. Reson. Med. 59, 1347–1354.

Assaf, Y., Freidlin, R.Z., Rohde, G.K., Basser, P.J., 2004. New modeling and experimental framework to characterize hindered and restricted water diffusion in brain white matter. Magn. Reson. Med. 52, 965–978.

Assaf, Y., Mayk, A., Cohen, Y., 2000. Displacement imaging of spinal cord using q-space diffusion-weighted MRI. Magn. Reson. Med. 44, 713–722.

Barazany, D., Basser, P.J., Assaf, Y., 2009. In vivo measurement of axon diameter distribution in the corpus callosum of rat brain. Brain 132, 1210–1220.

Barazany, D., Jones, D., Assaf, Y., 2011. AxCaliber 3D, in: Proceedings of the 19th Annual Meeting of ISMRM, Montréal.

Biton, I.E., Duncan, I.D., Cohen, Y., 2007. q-Space diffusion of myelin-deficient spinal cords. Magn. Reson. Med. 58, 993–1000.

Biton, I.E., Duncan, I.D., Cohen, Y., 2006. High b-value q-space diffusion MRI in myelin-deficient rat spinal cords. Magn. Reson. Imaging 24, 161–166.

Drobnjak, I., Siow, B., Alexander, D.C., 2010. Optimizing gradient waveforms for microstructure sensitivity in diffusion-weighted MR. J. Magn. Reson. 206, 41–51.

Dyrby, T.B., Søgaard, L.V., Hall, M.G., Ptito, M., Alexander, D.C., 2012. Contrast and stability of the axon diameter index from microstructure imaging with diffusion MRI. Magn. Reson. Med. 70, 711–721.

Farrell, J.A.D., Zhang, J., Jones, M.V., Deboy, C.A., Hoffman, P.N., Landman, B.A., Smith, S.A., Reich, D.S., Calabresi, P.A., van Zijl, P.C.M., 2010. q-space and conventional diffusion imaging of axon and myelin damage in the rat spinal cord after axotomy. Magn. Reson. Med. 63, 1323–1335.

Ferizi, U., Schneider, T., Panagiotaki, E., Nedjati-Gilani, G., Zhang, H., Wheeler-Kingshott, C.A.M., Alexander, D.C., 2013. Using in-vivo human brain data to select diffusion MRI compartment models. Proc. Intl. Soc. Mag. Reson. Med. 21, 3128.

Grussu, F., Schneider, T., Kearney, H., Zhang, H., Miller, D.H., Ciccarelli, O., Alexander, D.C., Wheeler-, C.A., 2013. Towards spinal cord microstructure mapping with the neurite orientation dispersion and density imaging. Proc. Intl. Soc. Mag. Reson. Med. 21, 2095.

Jespersen, S.N., Lundell, H., Sønderby, C.K., Dyrby, T.B., 2013. Rotationally invariant double pulsed field gradient diffusion imaging. Proc. Intl. Soc. Mag. Reson. Med. 21, 2071.

Johnston, L.A., Wright, D., Philipsen, R.H., Kolbe, S.C., Bourne, J.A., Mareels, I.M., Egan, G.F., 2011. Inferring micron-scale tissue structure using extreme value theory for cylindrically- restricted diffusion, in: Proceedings of the 19th Annual Meeting of ISMRM, Montréal.

Landman, B.A., Farrell, J.A., Smith, S.A., Calabresi, P.A., van Zijl, P.C., Prince, J.L., 2008. Exploring the Information Content of q-Space Diffusion Weighted Imaging: Application to Multiple Sclerosis (MS) Spinal Cord Lesions. Proc. Intl. Soc. Mag. Reson. Med. 16, 2298.

Lätt, J., Nilsson, M., Wirestam, R., Johansson, E., Larsson, E.-M., Ståhlberg, F., Brockstedt, S., 2008. In vivo visualization of displacement-distribution-derived parameters in q-space imaging. Magn. Reson. Imaging 26, 77–87.

Lundell, H., Sønderby, C.K., Dyrby, T.B., 2013. Increasing the sensitivity of temporal diffusion spectroscopy with circularly polarized oscillating gradient spin echo. Proc. Intl. Soc. Mag. Reson. Med. 21, 2073.

McNab, J.A., Witzel, T., Bhat, H., Heberlein, K., Keil, B., Cohen-Adad, J., Dylan T, M.,

Wald, L.L., 2012. In Vivo Human Brain Measurements of Axon Diameter Distributions in the Corpus Callosum using 300 mT/m Maximum Gradient Strengths, in: Proceedings of the 22th Annual Meeting of ISMRM, Melbourne.

Mezer, A., Yeatman, J.D., Stikov, N., Kay, K.N., Cho, N.-J., Dougherty, R.F., Perry, M.L., Parvizi, J., Hua, L.H., Butts-Pauly, K., Wandell, B.A., 2013. Quantifying the local tissue volume and composition in individual brains with magnetic resonance imaging. Nat. Med. 19, 1667–1672.

Nilsson, M., Alexander, D., 2012. Investigating tissue microstructure using diffusion MRI: How does the resolution limit of the axon diameter relate to the maximal gradient strength? Proc. Intl. Soc. Mag. Reson. Med. 20, 3567.

Nilsson, M., Lätt, J., Nordh, E., Wirestam, R., Ståhlberg, F., Brockstedt, S., 2009. On the effects of a varied diffusion time in vivo: is the diffusion in white matter restricted? Magn. Reson. Imaging 27, 176–187.

Nilsson, M., van Westen, D., Ståhlberg, F., Sundgren, P.C., Lätt, J., 2013. The role of tissue microstructure and water exchange in biophysical modelling of diffusion in white matter. Magn. Reson. Mater. Phys. Biol. Med. 26, 345–370.

Nossin-Manor, R., Duvdevani, R., Cohen, Y., 2002. q-Space high b value diffusion MRI of hemi-crush in rat spinal cord: evidence for spontaneous regeneration. Magn. Reson. Imaging 20, 231–241.

Ong, H.H., Wehrli, F.W., 2011. Assessment of axon diameter distribution in mouse spinal cord with q-space imaging, in: Proceedings of the 20th Annual Meeting of ISMRM, Montréal.

Ong, H.H., Wehrli, F.W., 2010. Quantifying axon diameter and intra-cellular volume fraction in excised mouse spinal cord with q-space imaging. Neuroimage 51, 1360–1366.

Ong, H.H., Wright, A.C., Wehrli, S.L., Souza, A., Schwartz, E.D., Hwang, S.N., Wehrli, F.W., 2008. Indirect measurement of regional axon diameter in excised mouse spinal cord with q-space imaging: simulation and experimental studies. Neuroimage 40, 1619–1632.

Panagiotaki, E., Schneider, T., Siow, B., Hall, M.G., Lythgoe, M.F., Alexander, D.C., 2012. Compartment models of the diffusion MR signal in brain white matter: a taxonomy and comparison. Neuroimage 59, 2241–2254.

Schneider, T., Choong, X., Kachramanoglou, C., Thomas, D.L., Choi, D., Wheeler-Kingshott, C.A.M., Ciccarelli, O., 2013. CONVENTIONAL DTI AND Q-SPACE IMAGING IN BRACHIAL PLEXUS ROOT RE-IMPLANTATION. Proc. Intl. Soc. Mag. Reson. Med. 21, 1126.

Schneider, T., Wheeler-Kingshott, C.A.M., Alexander, D.C., 2012. MAPPING THE AXON DIAMETER INDEX IN THE CORPUS CALLOSUM IS CLINICALLY FEASIBLE. Proc. Intl. Soc. Mag. Reson. Med. 20, 350.

Tariq, M., Schneider, T., Alexander, D.C., Wheeler-Kingshott, C.A.M., Zhang, H., 2013. Assessing scan-rescan reproducibility of the parameter estimates from NODDI. Proc. Intl. Soc. Mag. Reson. Med. 21, 31